

Sea State measurements using TerraSAR-X/TanDEM-X data

Dissertation

Dissertation zur Erlangung des Doktorgrades der Mathematisch-Naturwissenschaftlichen
Fakultät der Christian-Albrechts-Universität zu Kiel

vorgelegt von
Miguel Bruck

Kiel, 2015

Referent: Prof. Dr. Roberto Mayerle

Koreferent: Dr. Susanne Lehner

Datum der Disputation: 11.06.2015

Zum Druck genehmigt: 11.06.2015

Erklärung

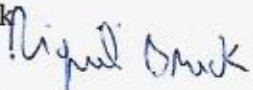
Hiermit bestätige ich, dass die vorliegende Dissertation mit dem Titel: „Sea State measurements using TerraSAR-X/TanDEM-X data“, von mir selbstständig verfasst worden ist und keine weiteren Quellen und Hilfsmittel als die angegebenen verwendet wurden.

Die vorliegende Arbeit ist unter Einhaltung der Regeln guter wissenschaftlicher Praxis der Deutschen Forschungsgemeinschaft entstanden. Ich versichere, dass diese Arbeit noch nicht zur Erlangung eines Doktorgrades an anderer Stelle vorgelegen hat.

Ich erkläre mich einverstanden, dass diese Arbeit an die Bibliothek des GEOMAR und die Universitätsbibliothek der CAU weitergeleitet wird.

München, 4 März , 2015

Miguel Bruck



Contents

Contents.....	I
List of figures.....	IV
List of tables.....	XIII
Chapter 1: Introduction	1
1.1 Introduction and motivation.....	1
1.2 Objectives.....	2
1.3 Outline of the thesis.....	4
1.4 Summary of the thesis	5
Chapter 2: Ocean waves	7
2.1 Linear theory	7
2.2 Wind generated sea surface ocean waves.....	9
2.3 Conversion from time to spatial domain	13
Chapter 3: Radar Remote sensing	15
3.1 Real Aperture Radar (RAR)	15
3.2 Spatial resolution.....	17
3.2 Synthetic Aperture Radar (SAR).....	17
3.2.1 Range processing	19
3.2.2 Azimuth processing	19
Chapter 4: State of the art	20
4.1 Ocean waves imaging mechanism by SAR.....	20
4.2 Historical SAR data.....	22
4.2.1 ERS ½	22
4.2.2 ENVISAT	22
4.3 Ocean wave analysis algorithms for C-band SAR data	23
4.3.1 MPI scheme	23
4.3.2 SAR cross-spectral algorithm	24
4.3.3 PARSA	24
4.3.4.1 CWAVE and CWAVE_ENV.....	25

Chapter 5: DATA	26
5.1 <i>In-situ</i> buoy wave measurements	26
5.2 TS-X/TD-X SAR	28
5.2.1 Calibration	31
5.3 Numerical Wave model data.....	32
5.4.1 Wave model DWD data.....	32
5.4.2 K-model data (coastal wave model)	33
Chapter 6: TS-X/TD-X Sea Surface observation	34
6.1 TS-X/TD-X data acquired over the ocean.....	34
6.2 Phenomena sea surface signatures observed in TS-X/TD-X data.....	40
Chapter 7: Data Analysis.....	43
7.1 The 2D Fourier analysis.....	43
7.2 Homogeneous and inhomogeneous wave fields observed TS-X/TD-X SAR.....	45
7.3 Ocean waves peak wavelength and direction derived from TS-X/TD-X data.....	49
7.4 Azimuth <i>cut-off</i>	52
7.5 Azimuth <i>cut-off</i> effect on TS-X/TD-X data	54
7.6 Dependency of azimuth <i>cut-off</i> wavelength from TS-X/TD-X with significant wave height and wind speed	55
7.7 Dependency of azimuth <i>cut-off</i> wavelength with incidence angle.....	60
Chapter 8: Empirical algorithm to estimate H_s from TS-X/TD-X data: XWA.....	62
8.1 Background	62
8.2 Data selection	64
8.3 Algorithm discussion.....	68
8.4 Dependencies taken into account in the algorithm	69
8.4.1 Incidence angle	69
8.4.2 Sea surface wind speed U_{10}	71
8.4.3 Ocean wave propagation direction in relation to satellite path (azimuth).....	73
8.5 Validation of the algorithm	74
Chapter 9: Case studies	76
9.1 Case studies over <i>in-situ</i> wave measurements.....	76
Chapter 10: Coastal wave field extraction	90
10.1 Coastal wave field extraction using TS-X/TD-X data.....	90
10.2 Case studies	91
Case study I: Coastal wave field extraction in high sea state conditions	92

Case study II: Comparison with numerical wave model data.....	98
Case Study III: Analyzing sea state variability in the TS-X derived wave field with <i>in-situ</i> wave measurements.....	103
Chapter 11: Summary and Conclusions	105
Outlook.....	108
Appendix A	110
Appendix B	116
Appendix C	129
Appendix D	132
References	138
List of Symbols	143
List of acronyms	145

List of Figures

Figure 2.1: Representation of a linear ocean wave propagating with speed c , wavelength λ , amplitude a and modulating the sea surface η at height h	7
Figure 2.2: Frequency and period of the vertical motions of the ocean surface (after Munk., 1950).....	9
Figure 2.3: Diagram showing the predicted H_s according to the wind speed duration of the wind speed and the fetch distance (adapted from Van Dorn, W.G, Oceanography and Seamanship, 1974).....	10
Figure 2.4: The sea surface $\eta(t)$, is composed of a large sum of wave components which propagate at different periods, directions, amplitudes and phases.(after [Pierson <i>et al.</i> , 1955], in Holthuijsen, L.H., Waves in Oceanic and Coastal Waters, 2007).....	11
Figure 2.5: Two dimensional wave number spectrum.....	11
Figure 2.6: Representation of the one dimensional (1D) wave spectrum. It corresponds to the distribution of the energy density of ocean waves with frequency.....	12
Figure 3.1: The electromagnetic spectrum (in ASAR Product Handbook, 2007 © ESA).....	15
Figure 3.2: Representation of the SAR imaging system. The SAR is moving with velocity V along the x – axis; azimuth direction, and the sensor is looking into the y -axis; range direction.....	18
Figure 3.3: Representation of how the SAR system achieves its high resolution coverage by synthesizing a virtual longer antenna: During the flight of the satellite the echoes of the illuminated area by the radar are stored, by analysing the Doppler shift (the change in the frequency/wavelength of the echo is comparison to the original remitted radar pulse, the location of each echo is computed (Figure © ESA).....	18
Figure 4.1: Representation of a simplified view of the sea surface imaging mechanism by SAR. The radar cross section peak value does not correspond to the sea surface elevation peak but rather to the surface perpendicular to the radar signal.....	20
Figure 5.1: Ocean waves (sea surface elevation) measurements devices commonly known as buoys: 6 meter NOMAD aluminium hulled boat shaped buoy (left). 3-meter aluminium hulled discus buoy (center). Data well Directional Waverider buoy (left).....	26
Figure 5.2: Visualization of standard one dimensional wave spectra provided by ocean wave measurement buoys .In this case the energy density is located in the lower frequencies, which corresponds to long wavelength waves, probably <i>swell</i> conditions. Significant wave height calculated from the spectrum is for this case 3.1 m and a wave peak period of 12.9s.....	27
Figure 5.3: The TerraSAR-X and his twin Tandem-X satellite.	28

Figure 5.4: Representation of the different modes imaged by the TS-X/TD-X ©DLR.....	29
Figure 5.5: TS-X VV polarized StripMap acquired on February 26, 2013 at 19:48 UTC over the Dixon Entrance, west coast of Canada.....	31
Figure 5.6: H_s field (left) and the <i>Swell</i> wave height field (right) given by the DWD wave model on November 21, 2008 at 17:01 UTC.....	33
Figure 6.1: TS-X VV pol. StripMap acquired on April 9 th 2012 at 1:51 UTC. Inlet: TS-X SpotLight acquired on June 13, 2013 at 1:51 UTC on the west coast of USA.	35
Figure 6.2: TS-X VV pol. SpotLight data image acquired on June 12, 2013 at 1:51 UTC (inlet Fig.6.1).....	35
Figure 6.3: TS-X VV polarized ScanSAR data taken on 3th Oktober, 2012 at 8:22 UTC over the Tropical Storm Nadine on the North Atlantic Ocean (left) Sub-scenes taken from different positions on the data image (right).	36
Figure 6.4: TS-X VV polarized StripMap data taken on the Oktober 31, 2012 at 11:28 UTC near the Gulf of Mexico. The image data is taken under low sea state and moderate wind conditions (left) TS-X VV polarized StripMap data taken on the 18 Dezember 2012 at 22:20 UTC. The image data is taken under low sea state conditions with influence of wind, which created signatures visible in the data (right).....	37
Figure 6.5: TS-X VV polarized StripMap data taken on October 20, 2012 at 15:55 UTC. The data is acquired under high sea state conditions.....	38
Figure 6.6: TS-X HH polarized StripMap image acquired over the Elbe estuary on November 21, 2008 at 17:00 UTC (a), sub-scene of the TS-X (b), and sub-scene zoom (c), background image, Google Maps©.	38
Figure 6.7: TS-X combined dual (HH and VV) polarized StripMap data image acquired on February 4, 2012 at 22:05 UTC over the North Atlantic Ocean.....	39
Figure 6.8: Sub-scene taken from the HH polarized data from the TS-X dual polarized StripMap data image shown on figure 6.7 (left). Sub-scene taken from the VV polarized data from the TS-X dual polarized StripMap data image shown on figure 6.7 (right).....	40
Figure 6.9: TS-X VV polarized StripMap data image acquired in the Pacific Ocean near the coast of Japan on September 21, 2012 at 8:12 UTC. The examples shows internal Ocean waves probably formed by the underwater terrain (left). TD-X VV polarized StripMap data image acquired over the North Pacific Ocean, off the west of Canada on December 10, 2011 5:05 UTC. A set of internal ocean waves are visible in the TS-X images (right).....	41
Figure 6.10: TS-X VV polarized StripMap data image taken in the Indian Ocean, south from India on September 19, 2012 at 13:20 UTC. The image shows an atmospheric signature visible in the middle of the image (left). TS-X VV polarized StripMap data image acquired in the North Pacific Ocean near Canada on March 13, 2012 3:23 UTC. The image shows cloud signatures (right).....	41
Figure 6.11: TS-X VV polarized StripMap data image acquired off the east coast of the USA on March 16, 2012 at 10:49 UTC. The case shows an example of surface oil slicks (algae blooms) (left). TS-X VV	

polarized StripMap image acquired over the Gulf of Mexico on August 28, 2011 at 23:48 UTC. This case shows an oil spill in the right side of the image (right).....42

Figure 6.12: TS-X VV polarized StripMap data image taken over the coast of Oman, North Africa, on the March 2, 2012 at 2:14 UTC. The example shows a fleet of ship, and wind blowing from land to the sea bringing dust from the mainland dune (left).TS-X VV polarized StripMap image acquired over Lake Huron, Canada on December 13, 2011 at 23:10 UTC. The image appears black in most of the upper part because the wind speed is too low to provide enough roughness to reflect the radar signal back to the antenna (right).42

Figure 7.1: TS-X sub-scene (left) 2D spectrum derived from the left sub-scene using the methodology described in this section (right).....44

Figure 7.2: Example of TS-X data presenting homogeneous wind generated ocean wave field; TS-X VV polarized StripMap data image taken over the Pacific Ocean near Canada on November 24, 2011 at 3:21 UTC.....46

Figure 7.3: Sub-scene (2048 by 2048 pixel => (5.1 km x 5.1 km) taken from data presented in (figure 7.2) is divided into 4 smaller 1024 pixel sub-scenes of equal size (2.6km x 2.6 km) (left). For each of the smaller sub-scenes the spectrum is derived (right).46

Figure 7.4: Example of an Inhomogeneous data image; the data presents an atmospheric signature visible in the middle of the image. TS-X VV polarized StripMap taken in the Indian Ocean, south from India on September 19, 2012 at 13:20 UTC.....47

Figure 7.5: TS-X StripMap sub-scene (2048 by 2048 pixel => (4.6 km x 4.6 km) is divided into 4 smaller 1024 pixel sub-scenes of equal size (2.6km x 2.6 km). For each of the smaller sub-scenes the spectrum is derived.....47

Figure 7.6: Location of the NDBC buoys used in the analysis of TS-X/TD-X data.....50

Figure 7.7: The distribution of the wave peak wavelength and direction for the analysed 200 collocated, wave peak wavelength versus wave peak direction; red: *in-situ*, blue: TS-X/TD-X.....50

Figure 7.8: Comparison of the wave peak wavelength λ_p derived from TS-X/TD-X VV polarized StripMap data against peak wavelength λ_p derived from buoy data using the dispersion relationship for deep waters (left). Comparison of ocean wave peak direction θ_p derived from TS-X/TD-X data against θ_p given by the buoy. Each color corresponds to different a wavelengths range; Orange wavelengths >120 m; Green: wavelengths between 120 to 75 m, purple wavelengths between 55 and 75 m (right)..... 51

Figure 7.9: Visualization in 3D of the 2D spectrum derived from a sub-scene taken from TS-X VV polarized StripMap data over a wave field with *in-situ* meteo-marine information; wave height: 5.9 m and wind speed: 5.4 m/s.53

Figure 7.10: 3D view of the 2D spectrum derived from TS-X data. The yellow lines correspond approximately to the wavelengths where the gradient between consecutive azimuth bins is higher. The azimuth wavelength of the line is the estimated azimuth *cut-off* wavelength. The red line indicates that the

line is affected by the presence of the wave peak, which moves the prediction line away from the center range axis.....	55
Figure 7.11: The 3D visualization of the 2D spectrum derived from TS-X data. The case A is taken over high sea state. <i>In-situ</i> information: H_s : 5.9 m, wind speed: 5.4 m/s. The derived azimuth <i>cut-off</i> wavelength is 160m. The case B is taken over low sea state conditions. <i>In-situ</i> information: H_s : 0.9 m, wind speed: 3.2 m/s. The derived azimuth <i>cut-off</i> wavelength is 46 m.....	56
Figure 7.12: Azimuth <i>cut-off</i> wavelength derived from TS-X/TD-X data and the corresponding <i>in-situ</i> values of H_s given by the buoy (left) and wind speed (right) given by the anemometer.....	57
Figure 7.13: Derived <i>cut-off</i> wavelength from TS-X/TD-X data (red) and the predicted azimuth <i>cut-off</i> wavelength given by the empirical (formula 7.19) with $R = 514$ km, and $V = 7.2$ km/s with <i>in-situ</i> wave height and wind speed as input (blue) the same formula but assuming $R = 800$ km and $V = 7$ km/s, the case of ENVISAT and ERS satellites (violet) and the predicted azimuth <i>cut-off</i> wavelength assuming the relationship found in figure 7.12 left, using <i>in-situ</i> wave height as input (green)	58
Figure 7.14: Azimuth <i>cut-off</i> wavelength for data from TS-X/TD-X acquisitions over sea states classified as <i>wind sea</i> by the parameter a_{wind} (left). Azimuth <i>cut-off</i> wavelength from TD-X/TS-X acquisitions taken under sea state classified as <i>swell</i> by the parameter a_{wind}	60
Figure 7.15: Azimuth <i>cut-off</i> wavelength derived from TD-X/TS-X data-set according to the incidence angle of the acquisition.....	61
Figure 7.16: Azimuth <i>cut-off</i> wavelength derived from TS-X/TD-X collocated data-set with <i>in-situ</i> wave measurements against H_s measured buoy.....	61
Figure 8.1: H_s given by the wave model WAM running at DWD, against the parameter E derived from HH and VV dual polarized data from TS-X/TD-X StripMap and SpotLight acquisitions taken over the Ekofisk oil platform in the second semester of the year 2009. Only observations for wave height above 0.9 m and wind speed above 3.5 m/s are considered.....	65
Figure 8.2: Histogram showing the distribution of measured H_s by the buoy for the TS-X/TD-X tuning data-set.....	67
Figure 8.3: Distribution of H_s against the peak wavelength derived from the peak frequency from buoy data using the dispersion relationship, assuming deep water (formula 2.19) in the tuning data-set.....	67
Figure 8.4: Distribution of the measured <i>in-situ</i> wind with measured <i>in-situ</i> H_s in the tuning data-set....	67
Figure 8.5: Parameter E derived from TS-X/TD-X data acquired at different incidence angles and wave heights. The colours correspond to the different wave height ranges. Blue: wave height: [1.9-2.1] m, red: wave height: [2.9-3.1] m, green: wave height: [3.9-4.1] m.....	70
Figure 8.6: Significant wave height estimation using (8.6) with <i>in-situ</i> wave data.....	71
Figure 8.7: Scatterplot with the bias found on the H_s given by the buoy and values of H_s derived by using (formula 8.6).	71
Figure 8.8: H_s derived from TS-X/TD-X data using (8.5) against <i>in-situ</i> H_s	72

Figure 8.9: Bias of the wave height estimated by (8.5) for ocean waves higher than 4.5 m compared to wave propagation direction relative to the satellite path (azimuth direction).....	74
Figure 8.10: Validation of H_s derived from TS-X/TD-X data using the developed empirical algorithm XWAVE against <i>in-situ</i> wave measurements The data used for verification of the algorithm corresponds to 100 homogenous TS-X/ TD-X VV polarized StripMap data acquired with incidence angles between 20° and 37° collocated with buoys with water depth higher than 100 m.....	75
Figure 8.11: Comparison of values of H_s given by the wave model WAM running at the DWD and the values H_s derived from TS-X/TD-X data.....	75
Figure 9.1: TanDem-X VV polarized StripMap image acquired on November 17, 2010 at 4:14 UTC over buoy 51000 near the Hawaii Archipelago in the Pacific Ocean (left). Sub-scene (5.1 x 5.1 km) taken from the left image (right).....	78
Figure 9.2: 2D spectrum derived from TS-X VV polarized StripMap image acquired on November 17, 2010 at 4:14 UTC over buoy 51000 (left). Comparison of the 1D spectrum derived from TS-X data (blue) and the buoy 1D spectrum (red). The black vertical line represents the derived <i>cut-off</i> frequency: 0.111 H_z (125 m wavelength) (right).....	79
Figure 9.3: H_s wave field (left) and <i>swell</i> wave height (right) on November 17, 2010 at 4:14 UTC given by the WAM wave model running at DWD.....	80
Figure 9.4: <i>Wind sea</i> height (left) and wind field (right) on November 17, 2010 at 4:14 UTC given by the WAM wave model running at DWD.....	80
Figure 9.5: TD-X VV polarized StripMap data image acquired on November 13, 2011 at 3:23 UTC over buoy 46001 near the west coast of Canada (left). Sub-scene (5.1 x 5.1 km), taken from the left image (right).....	81
Figure 9.6: 2D spectrum derived from TS-X VV polarized StripMap image acquired on November 13, 2011 at 3:23 UTC over buoy 46001 (left). Comparison of the 1D spectrum derived from TD-X data (blue) and the buoy 1D spectrum (red). The black vertical line represents the derived <i>cut-off</i> frequency: 0.078 H_z (256 m wavelength) (right).....	81
Figure 9.7: H_s wave field (left) and <i>swell</i> wave height (right) on November 13, 2011 at 3:23 UTC given by the WAM wave model running at DWD.....	83
Figure 9.8: <i>Wind sea</i> height (left) and wind field (right) on November 13, 2011 at 3:23 UTC given by the WAM wave model running at DWD.....	83
Figure 9.9: TS-X VV polarized StripMap data image acquired on November 16, 2010 at 14:32 UTC over buoy 46014 located near the west coast of USA (left). Sub-scene (5.1 x 5.1 km) taken from the image left (right).....	84
Figure 9.10: 2D spectrum derived from the TS-X VV polarized StripMap image acquired on November 16, 2010 at 14:32 UTC over buoy 46014 (left). Comparison of the 1D spectrum derived from TS-X data (blue) and the buoy 1D spectrum (red). The black vertical line represents the derived <i>cut-off</i> frequency: 0.109 H_z (131 m wavelength) (right).....	85

Figure 9.11: H_s wave field (left) and <i>swell</i> wave height (right) on November 16, 2010 at 14:32 UTC given by the WAM wave model running at DWD.....	86
Figure 9.12: <i>Wind sea</i> height (left) and wind field (right) on November 16, 2010 at 14:32 UTC given by the WAM wave model running at DWD.....	86
Figure 9.13: TS-X VV polarized StripMap data image acquired on July 1, 2010 at 11:36 UTC over buoy 42056 located near the west coast of Cuba (left). Sub-scene (5,1 x 5.1 km) taken from the left image (right).....	87
Figure 9.14: 2D spectrum derived from TS-X VV polarized StripMap image acquired on 1 st July, 2010 at 11:36 UTC over buoy 42056 (left) Comparison of the 1D spectrum derived from TS-X data (blue) and the buoy 1D spectrum (red). The black vertical line represents the derived <i>cut-off</i> frequency: 0.117 Hz (114 m wavelength) (right).....	88
Figure 9.15: H_s wave field (left) and <i>swell</i> wave height (right) on July 1, 2010 at 11:36 UTC given by the WAM wave model running at DWD.....	89
Figure 9.16: <i>Wind sea</i> height (left) and wind field (right) on July 1, 2010 at 11:36 UTC given by the WAM wave model running at DWD.....	89
Figure 10.1: Bathymetry with a resolution of 1 nautical mile for the North Sea area near the coast of Germany.....	92
Figure 10.2: TS-X VV polarized StripMap image acquired on December 9, 2011 at 5:42 UTC near the island of Helgoland located in the North Sea, near the coast of Germany, Google earth ©.....	93
Figure 10.3: View of the respective underlying bathymetry for the same area shown in figure 10.2. The red box corresponds to the area of the TS-X acquisition.....	93
Figure 10.4: H_s wave field (left) and <i>swell</i> wave height (right) given by the WAM wave model at DWD on December 9, 2011 at 6:00 UTC.....	94.
Figure 10.5: <i>Wind sea</i> height (left) and wind field (right) given by the WAM wave model at DWD on December 9, 2011 at 6:00 UTC.....	94
Figure 10.6: Sea surface wind field derived applying the XMOD algorithm on the TS-X VV polarized StripMap acquired on December 9, 2011 at 5:42 UTC.....	96
Figure 10.7: H_s wave field (left) and peak wavelength field (right) derived from TS-X VV polarized StripMap image acquired on December 9, 2011 at 5:42 UTC using a 2.6 km x 2.6 km size box. The red boxes and black circle (location of the buoy) are sub-scenes presented in figure 10.8.....	96
Figure 10.8: Sub-scenes (2.6 × 2.6) km from the TS-X VV polarized StripMap data image acquired on December 9, 2011, at 5:42 UTC.....	97
Figure 10.9: Zoom into the TS-X VV polarized StripMap mage acquired on December 9, 2011, at 5:42 UTC (black rectangle figure 10.7), shown on Google Earth©.....	98

Figure 10.10: High tide situation acquired on TS-X StripMap taken on November 21, 2008 at 17:01 UTC (left). Low tide situation acquired on TS-X StripMap taken on November 26, 2008 at 17:10 UTC (right).....	98
Figure 10.11: TS-X sub-scenes from the TS-X StripMap data taken on November 21, 2008 at 17:01 UTC showing high tide (left) and low tide situation taken on November 26, 2008 at 17:10 UTC (right).....	99
Figure 10.12 TS-X HH polarized StripMap image acquired on November 21, 2008, at 17:01 UTC over the Elbe estuary, and respective underlying bathymetry , Google Earth ©.....	99
Figure 10.13: H_s wave field (left) and <i>swell</i> wave height (right) given by the WAM wave model running at the DWD on November 21, 2008 at 17:01 UTC.	100
Figure 10.14: <i>Wind sea</i> height (right) and wind field (left) given by the WAM wave model running DWD on November 21, 2008 at 17:01 UTC.....	100
Figure 10.15: Sea surface wind field derived from the TS-X HH polarized StripMap data acquired over the Elbe Estuary on November 21, 2008 at 17:01 UTC.....	101
Figure 10.16: Coastal wave model H_s results (<i>K</i> -model) for the North Sea, near the coast of Germany, with a resolution of 1 nautical mile on November 21, 2008 at 18:00 UTC (left). Zoom into the area of the inside the red box shown on the right image, the black box corresponds to the area of the TS-X acquisition (right).....	102
Figure 10.17: Significant wave height wave field derived from the TS-X HH polarized StripMap image acquired over the Elbe estuary on November 21, 2008 at 17:01 UTC (left) and the corresponding peak wave length (right).....	102
Figure 10.18: TS-X VV polarized StripMap image acquired over the south coast of USA, near Santa Barbara (California) acquired on April 9, 2012 at 1:51 UTC (left). Significant wave height wave field (box size 2.6 km) derived from the image shown left (right).....	103
Figure A.1: TD-X VV polarized StripMap data image acquired on December 4, 2011 at 2:02 UTC over buoy 46089 located near the west coast of the USA (left). Sub-scene (4.6 x 4.6 km), taken from the left image (right).....	110
Figure A.2: 2D spectrum derived from TD-X VV polarized StripMap image acquired on December 4, 2011 at 2:02 UTC over buoy 46089 (left). Comparison of the 1D spectrum derived from TD-X data (blue) and the buoy 1D spectrum (red). The black vertical line represents the derived cut-off frequency: $0.124 H_z$ (102 m wavelength) (right).....	111
Figure A.3: H_s wave field (left) and <i>swell</i> wave height (right) on December 4, 2011 at 2:02 UTC given by the WAM wave model running at the DWD.....	112
Figure A.4: <i>Wind sea</i> height (left) and wind field (right) on December 4, 2011 at 2:02 UTC given by the WAM wave model running at the DWD.....	112
Figure A.5: TS-X VV polarized StripMap image acquired on December 4, 2011 at 15:04 UTC over buoy 46005 (left). Sub-scene (4.6 x 4.6 km) taken from the image left (right).	113
Figure A.6: 2D spectrum derived from TS-X VV polarized StripMap image acquired on December 4,	

2011 at 15:04 UTC over buoy 46005 (left). Comparison of the 1D spectrum derived from TS-X data (blue) and the buoy 1D spectrum (red). The black vertical line represents the derived <i>cut-off</i> frequency: $0.110 H_z$ (127 m wavelength) (right).....	114
Figure A.7: H_s wave field (left) and <i>swell</i> wave height (right) on December 4, 2011 at 15:04 UTC given by the WAM wave model running at DWD.....	115
Figure A.8: <i>Wind sea</i> height (left) and wind field (right) on December 4, 2011 at 15:04 UTC given by the WAM wave model running at DWD.....	115
Figure B.1: Marine Radar located at the top of the pole (left) Radar image (right) © DLR.....	116
Figure B.2: Sequence of marine radar WaMoS data images of the sea surface taken for the same location over time, as seen in [Nieto Borges et al., 2004].....	117
Figure B.3: Ekofisk oil platform located the North Sea. The marine radar WaMoS is located in the platform, measuring the sea state conditions of the ocean area surrounding the platform (~5km).....	118
Figure B.4: Distribution of different TS-X data image mode acquired over the Ekofisk oil platform with valid <i>in-situ</i> and marine radar WaMoS measurements.....	119
Figure B.5: Comparison of H_s derived from a single marine radar image with H_s derived from marine radar WaMoS images.....	120
Figure B.6: Comparison of H_s given by the marine radar WaMoS with <i>in-situ</i> buoy wave measurements.....	120
Figure B.7: Comparison of H_s derived from TS-X data with <i>in-situ</i> buoy wave measurements.....	121
Figure B.8: Comparison of H_s derived from TS-X data with H_s given by the marine radar WaMoS.....	121
Figure B.9: Comparison of the peak period derived from the TS-X data against the peak period given by the buoy.....	122
Figure B.10: Comparison of the peak period derived from TS-X data against the peak period measured by the marine radar WaMos.....	122
Figure B.11: Comparison of the peak wave direction derived from TS-X data against the wave peak direction derived from the marine radar WaMoS data.....	123
Figure B.12: TS-X VV polarized SpotLight data image taken over Ekofisk oil platform on May 15, 2009 at 17:19 UTC (left). Sub-scene from image showed left (right).....	124
Figure B.13: 2D spectrum derived from the image data sub-scene (figure 11.10 right) (left) 2D spectrum derived from marine radar WaMoS data on May 15, 2009 at 17:19 UTC (right).....	125
Figure B.14: TS-X VV polarized SpotLight image data taken over Ekofisk oil platform on May 4, 2009 at 17:19 UTC (left). Sub-scene from image showed left (right).....	126

Figure B.15: 2D spectrum derived from sub-scene in figure B.14 (left). 2D spectrum derived from marine radar WaMoS data on May 4, 2009 at 17:19 UTC (right).....	126
Figure B.16: TS-X dual polarized (HH-VV) StripMap image data taken over Ekofisk oil platform on August 16, 2009 at 17:27 UTC (left). TS-X Sub-scene from image showed left (right).....	127
Figure B.17: 2D spectrum derived from sub-scene from TS-X dual polarized StripMap on August 16, 2009 at 17:27 UTC (figure 10.13) (left). 2D spectrum derived from marine radar WaMoS data for the same date and time (right).....	128
Figure C.1: Graphic representation of the sea surface wind speed U_{10} estimation from TS-X/TD-X SAR data by the XMOD function [<i>Ren et al., 2012</i>].....	130
Figure C.2: Sea surface Wind fields U_{10} derived by the XMOD algorithm on the TanDEM-X VV polarized StripMap data image acquired on November 17, 2010 at 4:14 UTC over buoy 51000 near the Hawaii Archipelago.....	131
Figure C.3: Comparison of the derived sea surface wind speed at 10 m height, U_{10} , given by the XMOD algorithm and wind speed measured by anemometers.....	131
Figure D.1: TanDEM-X VV polarized StripMap image acquired on November 17, 2010 at 4:14 UTC over buoy 51000 near the Hawaiian Archipelago. Sub-scenes are analysed and results are shown in Table D.1 and from figure D.2 to figure D .5.....	132
Figure D.2: Sub-scenes from the TanDEM-X StripMap VV polarized image acquired on November 17, 2010 at 4:14 UTC over buoy 51000 near the Hawaii Island at position A and their respective derived 2D image spectrum and the meteo-marine parameters. On top the 2048 pixel sub-scene results are shown, in the centre a 1024 pixel sub-scene results are shown and on the bottom a 512 pixel sub-scene results are shown.....	134
Figure D.3: Sub-scenes from the TanDEM-X StripMap VV polarized image acquired on November 17, 2010 at 4:14 UTC over buoy 51000 near the Hawaii Island at position B and their respective derived 2D image spectrum and the meteo-marine parameters. On top the 2048 pixel sub-scene results are shown, in the centre a 1024 pixel sub-scene results are shown and on the bottom a 512 pixel sub-scene results are shown.....	135
Figure D.4: Sub-scenes from the TanDEM-X VV polarized StripMap data image acquired on November 17, 2010 at 4:14 UTC over buoy 51000 near the Hawaii Island at position C and their respective derived image spectrum and the meteo-marine parameters. On top the 2048 pixel sub-scene results are shown, in the centre a 1024 pixel sub-scene results are shown and on the bottom a 512 pixel sub-scene results are shown.....	136
Figure D.5: Sub-scenes from the TanDEM-X VV polarized StripMap data image acquired on November 17, 2010 at 4:14 UTC over buoy 51000 near the Hawaii Island at position D and their respective derived image spectrum and the meteo-marine parameters. On top the 2048 pixel sub-scene results are shown, in the centre a 1024 pixel sub-scene results are shown and on the bottom a 512 pixel sub-scene results are shown.....	137

List of Tables

Table 5.1: General specifications of the TS-X satellite	28
Table 5.2: Overview of TS-X acquisition standard modes products.....	29
Table 9.1: Summary of the case studies.....	77
Table 9.2: Sea state parameters provided by buoy 51000, the wave model at DWD, and derived from the collocated TD-X image.....	79
Table 9.3: Sea state parameters provided by buoy 46001, the wave model at DWD, and derived from the collocated TD-X image.....	83
Table 9.4: Sea state parameters provided by buoy 46014, the WAM wave model at DWD, and derived from the collocated TS-X image.....	86
Table 9.5: Sea state parameters provided by buoy 42056, the WAM wave model at DWD, and derived from the collocated TS-X image.....	88
Table 10.1: Sea state parameters given by the buoy, the DWD wave model (grid point 54 N 8.2 E) and derived from the collocated TS-X StripMap image taken on December 9, 2011 at 5:42 UTC.....	95
Table 10.2: Summary of <i>in-situ</i> data (waves and wind) at the location of the TS-X StripMap data acquired on April 9, 2012 at 1:51 UTC, south coast of USA near Santa Barbara (California).	104
Table A.1: Sea state parameters provided by buoy 46089, the WAM wave model at the DWD, and derived from the collocated TD-X image.....	111
Table A.2: Sea state parameters provided by buoy 46005, the WAM wave model at DWD, and derived from the collocated TS-X image.....	114
Table B.1: Sea state parameters given by the buoy, the WaMoS and derived from the collocated TS-X SpotLight data taken on May 15, 2009 at 17:19 UTC.....	125
Table B.2: Sea state parameters given by the buoy, the WaMoS and derived from the collocated TS-X SpotLight data taken on May 4, 2009 at 17:19 UTC.....	126
Table B.3: Sea state parameters given by the buoy, the WaMoS and derived from the collocated TS-X StripMap data taken on August 16, 2009 at 17:27 UTC.....	128
Table D.1: Summary of the sea state parameters results obtained for the different sized sub-scenes from the TD-X data acquired on November 17, 2010 at 4:14 UTC over buoy 51000 near Hawaii Archipelago.....	133

Chapter 1

Introduction

1.1 Introduction and motivation

The first space-borne Synthetic Aperture Radar (SAR) observation of ocean surface waves that provided ocean surface wave information was achieved by the SEASAT satellite in 1978, (e.g. [Vesecky *et al.*, 1982], [Alpers *et al.*, 1981], [Beal *et al.*, 1983] [Alpers *et al.*, 1986]). SEASAT was followed by other SAR satellites launched over the years and the ocean surface continued to be observed and analyzed (e.g.[Hasselmann and Hasselmann, 1991], [Krogstad *et al.*, 1992], [Hasselmann *et al.*, 1996], [Kerbaol *et al.*, 1998], [Lehner *et al.*, 2000] and [Schulz-Stellenfleth, and Lehner, 2004]).

As an active sensor, SAR illuminates the ground with a radar beam and unlike optical sensors it is able to image the surface independent of sunlight (e.g.[Curlander and McDonough, 1991]). The roughness of the sea surface due to wind allows the radar beam to reflect back to the antenna. The radar signal is able to penetrate clouds and therefore SAR is called an “all weather conditions” sensor. SAR is able to provide two dimensional (2D) ocean surface information. However, the ocean wave information derived from SAR data is more accurate for the longer waves (*swell*) than in the high frequency wave spectra domain (*wind sea*) [Alpers *et al.*, 1981]. Methods to compensate the limitations on the high frequency domain (short ocean waves) were developed considering a priori information from numerical wave models [Hasselmann *et al.*, 1996], [Schulz-Stellenfleth *et al.*, 2005] or from other sensors like scatterometers [Mastenbroek and de Valk., 2000].

Empirical wave height algorithms (e.g. [Schulz-Stellenfleth, *et al.*, 2007], [Li *et al.*, 2011a]) and also algorithms to derive 2D wave spectra (e.g. [Engen *et al.*, 1995], [Mastenbroek and de Valk., 2000], [Johnsen *et al.*, 2002], [Schulz-Stellenfleth *et al.*, 2005], [Collard *et al.*, 2005]) have been developed for C-band SAR missions and SAR has been used continuously to image the ocean surface for global applications and inter-comparison with wave models (e.g. [Heimbach *et al.*, 1998] and [Abdalla *et al.*, 2006]).

The X-band satellites, TerraSAR-X/TanDEM-X (TS-X/TD-X), provide higher resolution data than conventional space-borne SAR's and achieve resolutions of up to 1 m and

2 m respectively at high resolution SpotLight mode, and for standard SpotLight and StripMap acquisition mode [Breit et al., 2010].

The TS-X/TD-X has a low orbit (513 km) in comparison to conventional C-band satellites, usually orbiting at about 800 km. This should reduce some of the limitations of imaging moving targets by SAR. These limitations cause for instance, short wavelength ($\sim < 150$ m) ocean waves propagating in the azimuth direction to not be imaged properly. In the TS-X/TD-X the displacement of an imaged target by SAR in azimuth direction $dx = V/R$ [Lyzenga et al., 1985], is about 73m for TS-X/TD-X, against 115 m for ENVISAT due to different platform velocity V (7.2 km/s for TS-X/TD-X and 7.55 km/s for ENVISAT) and slant range R (ENVISAT altitude is 800 km and TS-X/TD-X altitude is 513 km).

Therefore TS-X/TD-X SAR data provides better sea surface as previous SAR missions, especially regarding the imaging of ocean waves [Alpers et al., 1986]. TS-X/TD-X data has been used for ocean waves applications, focusing on sea surface wind, ocean wave refraction, and underwater topography estimation (e.g. [Brusch et al., 2010], [G. Diaz Mendez et al., 2010], [Li et al., 2010], [Ren et al., 2012], [Li et al., 2013], [Bruck et al., 2011]). The development of an algorithm to derive sea state from TS-X/TD-X data was also initiated, [Bruck et al., 2010] and continued to be developed [Lehner et al., 2012] into a mature stage [Bruck et al., 2014]. This thesis focuses on the development of the algorithm to obtain significant wave height H_s estimation from TS-X/TD-X SAR data. It is an empirical based algorithm and it was constructed by analyzing the correlations of different SAR derived parameters with the underlying sea state conditions, using *in-situ* wave measurements.

1.2 Objectives

It is the first time that TS-X/TD-X data is analyzed for sea state information. The objective of this thesis aims first to answer the following fundamental questions, which were of course asked on previous SAR missions:

- How much information is it possible to extract from TS-X/TD-X SAR data regarding ocean waves?
- How reliable is this information?
- What is the shortest ocean wave wavelength one can measure from TS-X/TD-X data?

- What is the shortest wavelength measured from TS-X/TD-X SAR data according to underlying sea state conditions, wave height, and sea surface wind?
- Does it depend on the incidence angle of the acquisition?
- What is the quality of the 2D spectrum derived from TS-X/TD-X using Fourier analysis?
- Does the 2D peak spectral information obtained have better quality than the one derived from previous SAR data?
- How does the one dimensional (1D) spectrum derived from TS-X/TD-X data compares with buoy wave spectrum?
- How do parameters derived from SAR data correlate with the imaged sea state?
- Is it possible to develop an algorithm to estimate significant wave height H_s from TS-X/TD-X data? If yes, is it possible using only SAR data as input?

To answer these main questions, the following objectives are to be accomplished:

- The main objective of this PhD thesis is the development of an algorithm able to derive sea state information, namely significant wave height from SAR data acquired by the TS-X and its twin brother TD-X.
- The TS-X/TD-X SAR data is for the first time used to the analysis of sea state. It is necessary to accomplish several sub-objectives previous to proceed to the main objective. The first steps necessary are the so-called sensitive studies, which were also performed for C-band SAR data, but were not yet performed to the new TS-X/TD-X X-band SAR data. These are:
 - Determination of the minimum correctly observable ocean waves wavelength propagating in the satellite path (azimuth cut-off wavelength) by the TS-X/TD-X in relation to the underlying meteo-marine conditions (sea state and sea surface wind).
 - Development of a method to derive the azimuth *cut-off* wavelength from the 2D spectrum and the analysis of the azimuth cut-off wavelength correlation with the underlying meteo-marine conditions.
 - To assert the quality of the 2D and 1D spectrum and the derived spectral parameters, ocean wave wavelength and direction derived from TS-X/TD-X data compared to *in-situ* or wave numerical wave data.

- To investigate parameters extracted from the TS-X/TD-X SAR data which give information regarding the underlying meteo-marine conditions.
- The second main objective is to assess the performance of the developed algorithm on TS-X/TD-X SAR data, as well as, its ability to analyze sea state spatial variability. Due to its high resolution TS-X/TD-X data is most suitable for the analysis of ocean waves in coastal areas, where sea state variability is high. The sub-objectives are
 - The developed algorithm is applied to coastal TS-X/TD-X imagery in order to analyze the performance of the algorithm to measure sea state variability in highly variable conditions.
 - H_s and peak wavelength wave fields derived from the TS-X/TD-X data are analyzed and compared to *in-situ* and wave measurements and to numerical wave model results not only to check the

1.3 Outline of the thesis

The thesis is structured as follows: the current chapter gives an overview regarding the topic of observation of the ocean sea surface by SAR and the motivation to develop an algorithm to derive sea state from TS-X/TD-X SAR data. The objectives of this thesis are described after. The outline of the thesis is given and a summary of the PhD is given as last.

Chapter 2 provides the basic theory on ocean waves. Chapter 3 includes the fundamental information regarding radar and SAR. The state of the art of ocean waves imaging by SAR, the description of the most important algorithms regarding sea state developed for C-band SAR data are given in Chapter 4. In Chapter 5 the different types of data used for this thesis are described. An introduction of the visualization of the ocean by the TS-X/TD-X is given in Chapter 6. TS-X/TD-X imagery acquired over the ocean, including different ocean phenomena are presented and shortly described.

In Chapter 7 the ocean wave analysis methods used prior to and necessary for the development of algorithms are described and applied. These include Fourier analysis, SAR data quality test and determination and analysis of the azimuth *cut-off* wavelength, which is the minimum detectable ocean wavelength in azimuth direction (satellite path) by the SAR. In Chapter 8, the new empirical algorithm (named XWAVE) developed which is the main

objective of this thesis is described. The validation results of the performance assessment with *in-situ* deep water buoy ocean wave measurements are discussed.

Chapter 9 presents case studies of TS-X/TD-X collocated data images with deep *in-situ* wave measurements. Sea state integrated parameters and 1D spectrum derived from SAR data are compared to *in-situ* measurements. Chapter 10 presents case studies where the developed algorithm is applied on TS-X/TD-X coastal imagery. The sea state variability on the spatial domain on SAR data acquired in coastal areas is analyzed and its performance is described. The contents of Chapter 10 are based on the results published in [Bruck *et al.*, 2013]. The final conclusions of this thesis are in the last chapter, Chapter 12.

1.4 Summary of the thesis.

The main objective of this PhD thesis, as referred previously, is to develop an algorithm to provide sea state information and perform ocean wave analysis. For this purpose TS-X/TD-X data is acquired over *in-situ* wave measurements buoys. The TS-X/TD-X data acquired was analyzed and a relationship between parameters derived from the SAR data and the sea state information provided by the buoys was pursued.

The first step consisted, in developing a method to discard TS-X/TD-X data which are contaminated by artefacts unrelated to wind generated ocean waves, as internal waves, algae blooms, oil spills, man-made structures, etc. After that, using data which passed the previously referred criterion, the spectrum from TS-X/TD-X data was derived and analyzed. An assessment of the quality of the spectrum derived parameters, wave peak wavelength and peak direction was pursued. This task was accomplished by comparing the derived results with *in-situ* wave measurements. The next step for the quality assessment is the determination of the minimum observable ocean wavelength (azimuth *cut-off* wavelength) which is associated to the azimuth *cut-off* effect influence on the 2D spectrum. The *cut-off* effect is related to the distortion present on SAR data acquired over moving field of targets, like the ocean. The *cut-off* effect changes the 2D spectrum shape according to the underlying meteo-marine conditions. An analysis of this effect on TS-X/TD-X data is performed. The parameter associated with the strength of the effect, the azimuth *cut-off* wavelength is derived from the TS-X/TD-X data and an analysis of its correlation with the underlying meteo-marine conditions was performed.

After the first ocean wave analysis steps described here, further ocean wave analysis is performed. Several parameters were derived from the TS-X/TD-X data with the objective of

searching correlations of the parameters retrieved from the data and the meteo-marine conditions (wind and ocean waves) of the sea surface where the TS-X/TD-X data is acquired. The goal was to combine the parameters into an algorithm to provide estimation of significant wave height from the TS-X/TD-X data. The collocated TS-X/TD-X data with the buoy is processed, and several parameters are extracted.

The parameters found suitable for the model are the integrated wavenumber spectrum energy parameter E , which is obtained by integrating the spectrum derived by Fourier analysis of the TS-X/TD-X data. The sea surface wind speed U_{10} , derived from the TS-X/TD-X data by an algorithm named XMOD [Ren *et al.*, 2012], the incidence angle θ_i , the ocean wave peak propagation direction in relation to satellite heading α , and the azimuth *cut-off* wavelength. The algorithm developed is applied to TS-X/TD-X data which is acquired globally over the ocean to retrieve sea state information. It was tuned and validated using deep water *in-situ* wave measurements. Comparisons are performed, analyzed and discussed.

As the TS-X/TD-X imagery has higher resolution than was previously possible with conventional SAR satellites, the performance assessment of an algorithm to derive sea state and its capability to measure spatial sea state variability is of great expectation and importance. If successful, sea state information derived from TS-X/TD-X coastal imagery gives valuable information about the variability of sea state properties in coastal areas. Therefore the last studies included in this thesis are the analysis of wave fields derived from TS-X/TD-X imagery acquired in coastal areas. These results are analyzed and verified with *in-situ* wave measurements or data from numerical wave model designed for coastal applications. TS-X/TD-X derived coastal wave fields can be used to verify coastal wave models results and/or vice versa in order to optimize both methods. The combination of both methods proved to be a powerful tool to analyze coastal waters and to study the sea state variability. The results are obtained by a software toolbox programmed for the aim of this PhD thesis which is designed to read all types of TS-X/TD-X products and to derive sea state parameters from the data.

Chapter 2

Ocean Waves

This chapter provides an overview of the theory of ocean waves and sea state. First the linear ocean wave theory is described. Then focus is given to wind generated ocean waves, which are of special interest for the work presented in this thesis. After that, a short introduction regarding sea state and analysis of ocean waves in the frequency and spatial domains is given. The data used here is from wave measurements devices, buoys that measure in the time (frequency) domain and in the spatial domain, TS-X/TD-X and from marine radar data.

2.1. Linear theory

The most simple sinusoidal wave can be defined by H (distance from the bottom to the top), period T (time between two consecutive wave crests or bottoms) and length λ (figure 2.1).

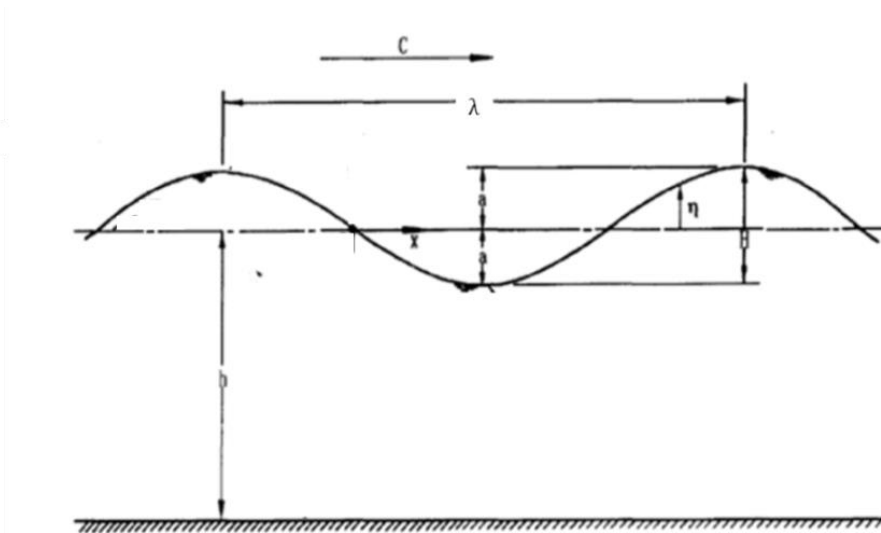


Figure 2.1: Representation of a linear ocean wave propagating with speed c , wavelength λ , amplitude a and modulating the sea surface η at height h .

The wave amplitude a is related to H by:

$$a = \frac{H}{2}. \quad (2.1)$$

The frequency f is the inverse of the wave period:

$$f = \frac{1}{T}. \quad (2.2)$$

The wavenumber k is defined by:

$$k = \frac{2\pi}{\lambda} \quad (2.3)$$

and the angular frequency ω is defined by:

$$\omega = \frac{2\pi}{T}. \quad (2.4)$$

The ocean waves phase speed c is related with the period T and wavelength λ or wavenumber k by:

$$c = \frac{\lambda}{T} = \frac{\omega}{k} \quad (2.5)$$

Gravity waves angular frequency ω is related with the k through the dispersion relationship e.g. [Goda, 1985] :

$$\omega^2 = gk \tanh kh. \quad (2.6)$$

Where g is gravity acceleration and h is the water depth. The phase speed is given by:

$$c^2 = \frac{g}{k} \tanh(kh). \quad (2.7)$$

For deep water the function $\tanh(kh)$ with depth $h \rightarrow \infty$ leads $\tanh(kh) \rightarrow 1$, the relationships can be simplified to:

$$\omega^2 = gk. \quad (2.8)$$

And the phase speed c can be calculated by:

$$c = \sqrt{\frac{g}{k}} . \quad (2.9)$$

2.2 Wind generated sea surface ocean waves

In the ocean, different types of propagating waves exist: wind waves, internal waves, tide waves, tsunamis, etc. (figure .2.2). These waves have different generation mechanisms; wind, bathymetry, sun-moon gravity and earthquakes. Wind generated ocean waves are as the name suggests generated by wind. When dominated by gravity (period above $\frac{1}{4}$ s), they are called surface gravity waves. These are the most common ocean waves and they are related to marine climate or sea state. The work presented in this thesis focuses on surface gravity ocean waves.

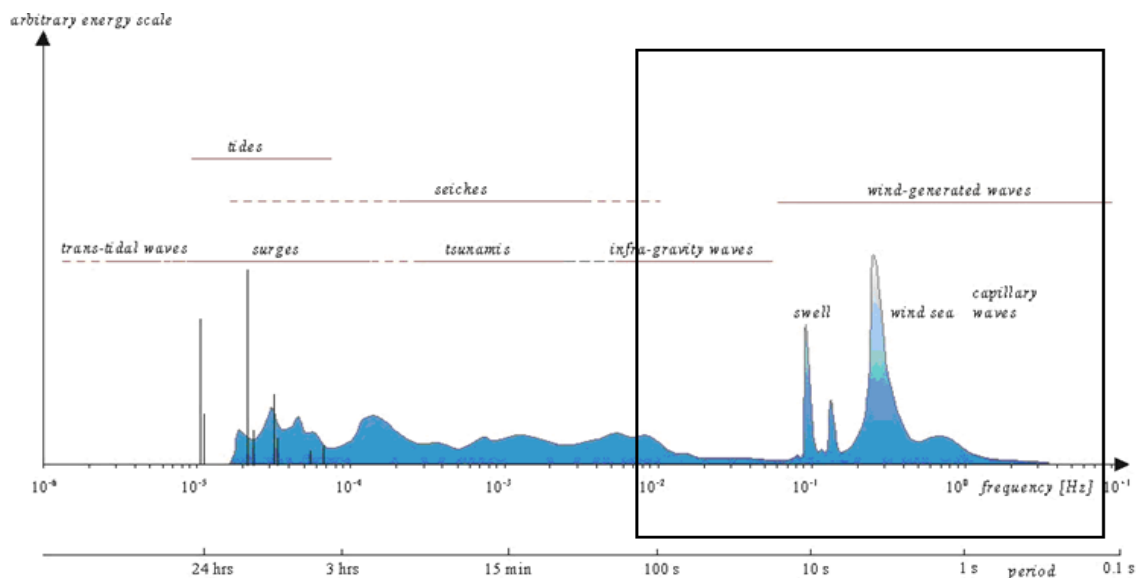


Figure 2.2: Frequency and period of the vertical motions of the ocean surface (after Munk., 1950).

The growth rate of these ocean waves' is related to wind stress on the sea surface proportional to wind speed, duration of the wind blowing over the sea surface and the length of the sea surface area swept by the wind, commonly known in oceanography by fetch length.

The wind ocean waves generated by the friction of the wind on the sea surface; the tension of the wind on the surface creates at first capillary waves, which are very short wavelength waves with only a few millimeters wavelength. As the wind continues to blow over

the sea surface, energy is transferred to the ocean waves through the tension created between the air (by wind) and the sea surface, and the wavelength of capillary waves increases. This type of ocean waves, which now have wavelengths in the order of centimeters to a few meters are called *wind sea* waves, because they are generated by the local wind. At some point the ocean waves have collected all the energy they can collect from the wind. They are considered fully developed. The wavelength of those ocean waves is usually in the order of meters, usually in the order of hundreds meters and they are called *swell* waves. The ocean wave's speed is high enough to escape the local wind field and they propagate outside the generation area. *Swell* waves can propagate over several hundred or thousands of kilometers and even circle the earth. As H_s and wave period are related to the wind speed, wind duration and fetch distance, it is possible to estimate roughly the peak period and wave height of ocean waves as a function of those parameters (figure 2.3).

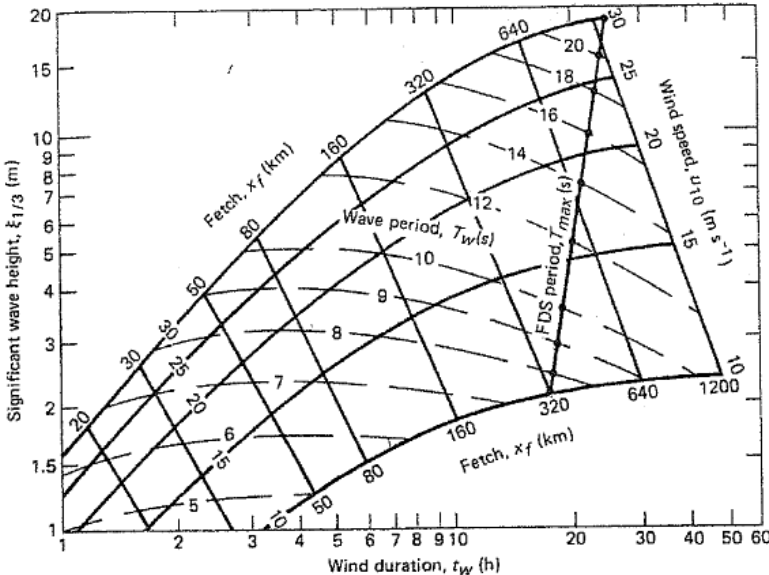


Figure 2.3: Diagram showing the predicted significant wave height related to the wind speed duration of the wind speed and the fetch distance (adapted from Van Dorn, W.G, Oceanography and Seamanship, 1974).

The ocean sea surface $\eta(t)$, is composed of waves propagating with different frequencies f (or wavelength in the spatial domain) and wave directions θ (figure 2.4). At time t , the sea surface can be defined mathematically by the sum of harmonic waves each one with different amplitude a , frequency f and phase ph , as follows:

$$\eta(t) = \sum_{i=1}^N a_i \cos(2\pi f_i t + \phi_i) \quad (2.10)$$

The ocean wave information represented in figure 2.4 and defined by (formula 2.10) is usually described by the wave spectrum which is defined in the time domain by $S(f, \theta)$ or in the spatial domain by $S(k, \theta)$ or $S(k_x, k_y)$ (figure 2.5). Where $\bar{k} = \frac{2\pi}{\lambda} = \frac{2\pi}{\sqrt{k_x^2 + k_y^2}}$ is the wavenumber and $\theta = \tan^{-1} \frac{k_x}{k_y}$ is the wave direction.

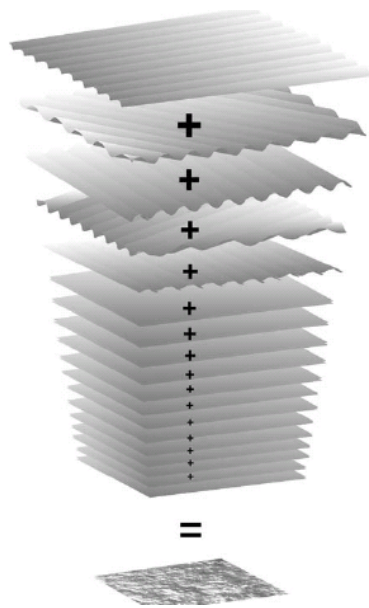


Figure 2.4: The sea surface $\eta(t)$, is composed of a large sum of wave components which propagate at different periods, directions, amplitudes and phases (after [Pierson *et al.*, 1955], in Holthuijsen, L.H., Waves in Oceanic and Coastal Waters, 2007).

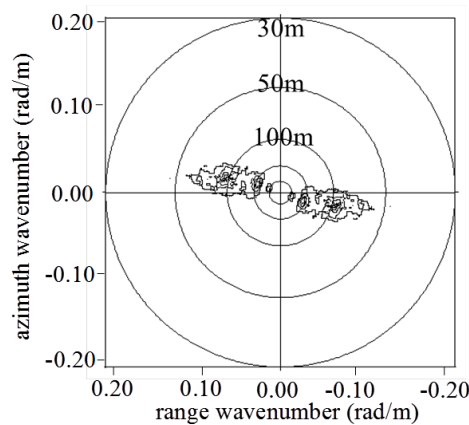


Figure 2.5: Two dimensional wave number spectrum.

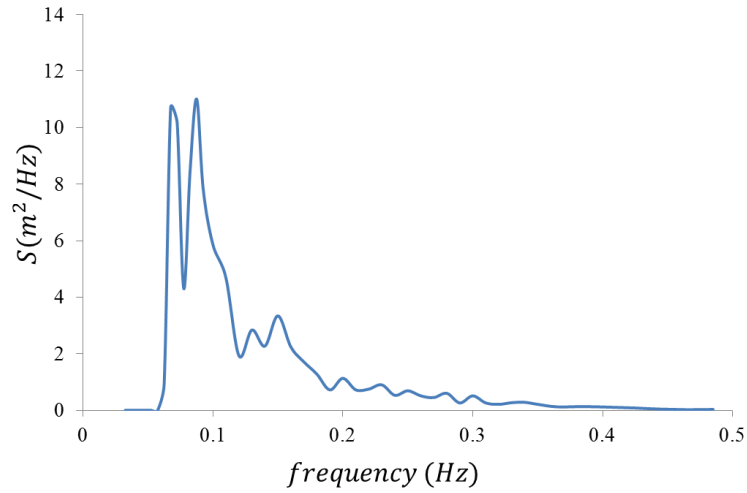


Figure 2.6: Representation of the one dimensional (1D) wave spectrum. It corresponds to the distribution of the energy density of ocean waves with frequency.

The wave spectrum $S(f, \theta)$ or $S(\lambda, \theta)$ gives the distribution of the energy density of the ocean waves for each frequency/wavelength and direction. The directional spectrum can be condensed into the one dimensional (1D) frequency spectrum $S(f)$ as shown in (figure 2.6). It is related to the directional spectrum $S(f, \theta)$ through the formula:

$$S(f) = \int_0^{2\pi} S(f, \theta) d\theta . \quad (2.11)$$

As the frequency spectrum is obtained by (formula 2.11) in the spatial domain the ocean waves are related with the wave number which is related with the wavelength, the wavenumber spectrum as follows:

$$S(k) = \int_0^{2\pi} S(k, \theta) d\theta . \quad (2.12)$$

As stated previously the ocean waves propagating in the ocean surface are generated by the wind. They are called wind generated wind waves, as referred previously.

Usually the information contained in the directional spectrum $S(f, \theta)$ or frequency spectrum $S(f)$ is summarized into parameters which describe the sea state in the form of parameters such as height, period, and direction in the case of $S(f, \theta)$.

These parameters are in their majority obtained from the spectral moments m_n of order n , defined by:

$$m_n = \int_0^{\infty} f^n S(f) df . \quad (2.13)$$

The significant wave height H_s , which can be defined as the average wave height of the third highest waves, more precisely defined as the mean of the highest one-third of waves in the wave record. It can be calculated from the wave spectrum and is then noted as H_{m0} . It is calculated by $H_{m0} = 4m_0^{1/2}$. Significant wave height is also approximately four times the square root of the variance of the surface elevation $\eta(t)$, $H_s \approx 4\sigma$ $H_s \approx 4\sigma_s$, where σ_s is the standard deviation.

2.3 Conversion from time to spatial domain wave analysis

Wave analysis can be performed in the spatial domain or in the time domain. For the case of the sea surface measurement device buoys the analysis is performed in the time domain. The average time of these buoy measurements is between 20 min and 40 min. The frequency spectrum can be derived from the wave number spectrum by:

$$E(f) = E(k) \cdot \left(\frac{1}{C_g} \right) . \quad (2.14)$$

Where C_g is the group speed which for deep water is half of the phase speed c , where $c = \frac{g}{2\pi} T$ and T is the period which is the inverse of the frequency, $T = \frac{1}{f}$.

The angular frequencies are obtained through the dispersion relationship:

$$\omega^2 = gk \tanh kh . \quad (2.15)$$

For deep water it can be simplified to:

$$f = \frac{1}{2\pi} \sqrt{gk}. \quad (2.16)$$

Taking as example the case of a single ocean wave with wavelength of 100 m, corresponding to a period of 8 s using the deep water relationship, the phase speed is 12.5 m/s. This means that a single wave takes about 6.1 minutes to travel about 4.6 km.

Chapter 3

Radar remote sensing

In this chapter an introduction to radar remote sensing is given. Initially, basic principles of radar and radar imaging theory are introduced. After that, a more advanced form of radar system called the Synthetic Aperture Radar (SAR) is described. The SAR is the remote sensing sensor used to image the sea surface, in the work presented in this thesis.

3.1 Real Aperture Radar (RAR)

The radar (**RA**dio **D**etection and **R**anging) is a remote sensing method which basically measures the distance to an object. The radar system uses as the name suggests radio waves which are electromagnetic waves with wavelengths between about 0.75 cm and 30 cm. The radio waves are a class, of electromagnetic waves, with different sub-classes according to their wavelengths. Their place in the full electromagnetic spectrum can be visualized in figure 3.1. The most basic radar system is defined as the Real Aperture Radar (RAR). The term “aperture” means for common photo cameras, the opening which is used to receive the light from outside to enable the photo camera device to produce an image photograph.

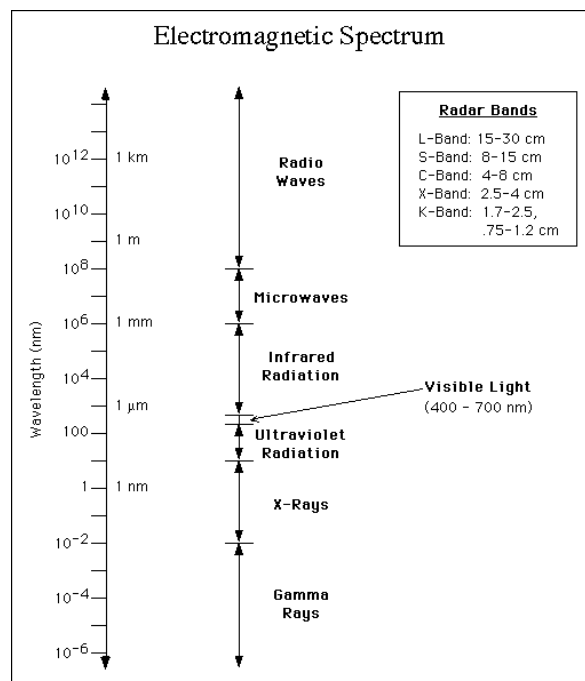


Figure 3.1: The electromagnetic spectrum (in ASAR Product Handbook, 2007 © ESA).

In the RAR system, the “aperture” or “opening” is the antenna, which is used to receive the backscattered radio pulse, sent previously by the antenna. The basic radar concept consists in sending a single radio pulse by an antenna to a target. The distance to the target can be calculated by measuring the time it takes the radio pulse to return back to the antenna. Electromagnetic waves have polarization properties, which means therefore the radar signal can be transmitted and received in any polarization. For both transmit and receive can be vertical (VV) or horizontal (HH).

Present days, RAR systems follow this principle, but are more complex. They can provide information of several large number of targets in a single measurement. By sweeping with radio waves (illuminating) an certain area size, which contains a large number of targets and knowing the time duration of each radio pulse sent and returned for each target, it is possible to know the distance and position of each target, and from this information derive an artificial image of the targets (radar image) of the area imaged by the RAR. Additional information is contained in the radio wave signal strength reflected back to the antenna. For the case that the radio signal transmitter antenna and the receiver antenna are the same location the power returning to the antenna can be given by the equation:

$$P_r = \frac{P_t G_t A_r \sigma F^4}{(4\pi)^2 R^4}. \quad (3.1)$$

Where P_t is the transmitted power (watts). G_t is the gain of the transmitted antenna (dimensionless). A_r is the effective aperture (area) of the receiving antenna. σ is the radar cross section. F is the pattern propagation factor. R is the distance from the transmitter to the target. The radar cross section σ is the measure of the ability of the target to reflect radar signals. Because it depends on the area of the target, it is usually normalized by the area. The normalized radar cross section (or sigma naught) σ_0 is defined by

$$\sigma_0 = 10 \log_{10} \left(\frac{\sigma}{A} \right). \quad (3.2)$$

Where σ is the energy backscattered and A is the area illuminated by the radar pulse.

3.1.1 Spatial resolution

The spatial resolution of the radar image is mainly determined by the antenna length and radio wave wavelength used. For any given wavelength, the bigger the antenna, the higher the resolution. Other factors that contribute to the spatial resolution are the pulse length and the antenna beam width. The beam width of the antenna is the radiation pattern present in the antenna. Similar to a flashlight, it can beam the light with different widths or patterns. Some flashlights have a more focused beam of light; others have a wider beam of light. The same applies to the radar antenna; the radar beam can have different widths or patterns. The range resolution is dependent of the fact that two distinct targets which are close together, their reflected signal is received separately by the antenna. An overlap of the two signals will cause the targets to appear blurred in the image. The azimuth resolution is affected by the beam width. The beam width is directly proportional to the wavelength of the pulse and inversely proportional to the length of the antenna. Antenna beam width can be adjusted by the length of the antenna or synthesizing the length of the antenna (next section).

3.2 Synthetic Aperture Radar (SAR)

SAR is a coherent microwave active method which enables to achieve high resolution for great distances that normal radar systems cannot achieve. It is usually used on board airplanes or satellites. Although this method is quite effective for imaging non-moving objects, like houses, trees, mountains, it does not perform so well for the case of moving objects. Moving objects will appear in the SAR image shifted and displaced and it will appear blurred in the case of multiple moving objects.

As ocean waves are a field of moving objects, the waves tend not to be correctly imaged, they will tend to appear blurred (multiple shifts and displacement of the imaged water particles) on the SAR data image the more complex the marine conditions are (higher waves, higher wind speed).

The SAR system has different methods to process the range and the azimuth resolution of a detected target. The method to synthesize the larger antenna is in the azimuth processing of the data. The Synthetic Aperture radar (SAR) is a method to achieve higher resolution without the actual need of having a larger antenna. The SAR system is different from a normal radar system because it synthesizes a longer antenna in order to cover a larger area. The method consists in illuminating a surface during the forward movement of the sensor with successive

pulses of signal and acquiring the echoes (more precisely the Doppler history) which are then combined together.

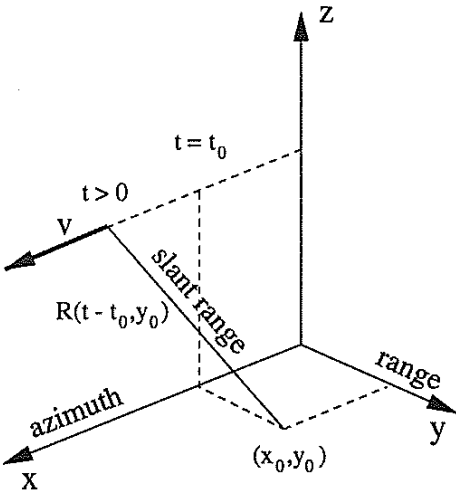


Figure 3.2: Representation of the SAR imaging system. The SAR is moving with velocity V along the x -axis; azimuth direction, and the sensor is looking into the y -axis; range direction.

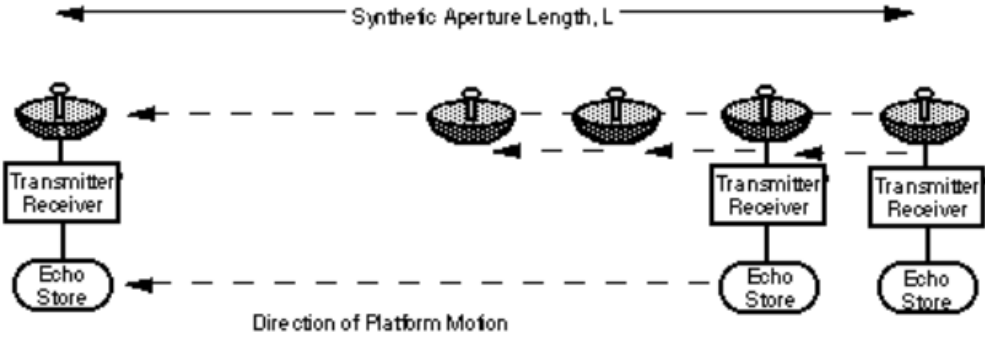


Figure 3.3: Representation of how the SAR system achieves its high resolution coverage by synthesizing a virtual longer antenna. During the flight of the satellite the echoes of the illuminated area by the radar are stored, by analysing the Doppler shift (the change in the frequency/wavelength of the echo is compared to the original remitted radar pulse, the location of each echo is computed (Figure © ESA).

The return echoes signals from the center portion of the beam width are separated by detecting the Doppler frequency shifts. The Doppler shift is the change in frequency resulting of the relative velocities of the transmitter and reflector. By processing the return signals according to their Doppler shifts it is possible to obtain a very narrow beam width (figure 3.2) and (figure

3.3). In summary the signals are recorded over a large period of time which becomes the length of the antenna.

3.2.1 Range processing:

The range resolution R_r of a SAR image is given by the bandwidth B of the signal [Cumming and Wong, 2004].

$$R_r = \frac{c_{light}}{2B}. \quad (3.3)$$

Where B is the bandwidth and c_{light} is the speed of light.

The corresponding ground range resolution g_r , which is dependent on the incidence angle θ_i , is given by:

$$g_r = \frac{R_r}{\sin\theta} \quad (3.4)$$

where R_r is the slant range.

3.2.2 Azimuth processing

The azimuth resolution for a RAR is given by the length of the antenna beam A_B [Massonnet and Souyris, 2008] which depends on the wavelength of the signal λ_r and the antenna length L_A . The 3db width of the antenna beam is given by [Bamler and Schättler 1993]:

$$B_{3db} = 0.64 \frac{\lambda}{L_A}. \quad (3.5)$$

The azimuth resolution a_r of the SAR data image is given by:

$$a_r = \frac{L}{2} \quad (3.6)$$

where L is the length of the antenna.

Chapter 4

State of the art

In this chapter, the state of the art of SAR ocean observation regarding ocean wind waves is briefly described. The chapter starts with the description of the theoretical ocean waves imaging mechanism by SAR and the simple equations related with the imaging geometry of a simple wave field (single sinusoidal wave). After that, a description of the SAR data and of the satellites which acquired it is provided. At the end a short description of the most important sea state algorithm developed for SAR data is given.

4.1 Ocean waves imaging mechanism by SAR

Figure 4.1 shows a simplified representation of the radar imaging mechanism of ocean waves. The signal backscattered from a single sinusoidal sea surface looking towards the antenna is strongest; this will appear as a bright strip in the radar image. In sea surface perpendicular to the radar signal, the signal will not reflect back to the antenna, and this surface will appear black in the radar image. The returned backscatter, as seen in figure 4.1, has a variation on sigma naught (σ_0) which follows to some extent the variation of the height of the ocean waves.

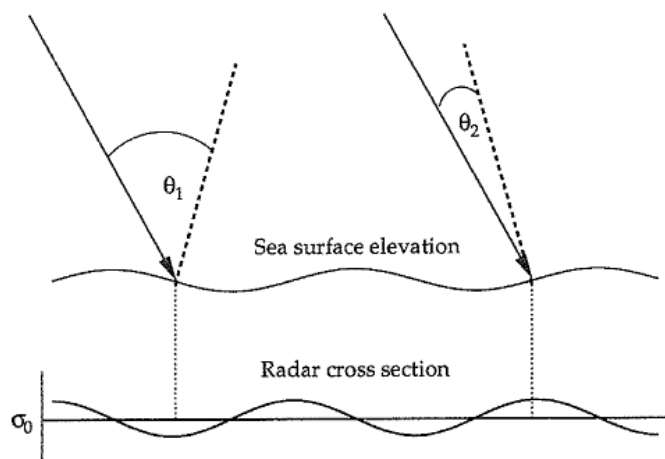


Figure 4.1: Simplified view of the sea surface imaging mechanism by SAR. Note that the radar cross section (sigma naught) σ_0 peak values does not correspond to the sea surface elevation peaks but rather to the surface perpendicular to the radar signal.

The imaging mechanism is sensitive both to the sigma naught σ_0 values, and also to the modulation and the sea surface motion associated with ocean waves. The detection of the

longer waves is only possible because shorter waves modulate the surface of the longer waves, making it possible to detect them.

The shorter ocean waves are the roughness in the sea surface that allows the signal to be reflected to the antenna, rather than being reflected away. In a flat surface, radar images appear as black, because the signal is scattered away from the antenna like a mirror. Even if longer waves are present there, without roughness created by the wind blowing on the sea surface, the long ocean waves would be seen merely as white stripes in a black background as the signal would only be reflected back where the ocean wave surface is exactly perpendicular to the antenna.

In the imaging mechanism of ocean waves three modulation processes are present: tilt, hydrodynamic and orbital. The RAR modulation dominates the imaging of ocean waves with longer wavelengths (*swell*) traveling in the range direction (perpendicular to satellite flight direction). This process can be assumed as a linear process [Hasselmann and Hasselmann., 1991]. The modulation of the sea surface $\frac{(x,t)-\langle\sigma_0\rangle}{\langle\sigma_0\rangle}$ can be given by:

$$\frac{(x,t)-\langle\sigma_0\rangle}{\langle\sigma_0\rangle} = 2(\sum_k T_K^R S \exp[kx - \omega t]). \quad (4.1)$$

Where S is the spectrum of the sea surface. k is the wavenumber and ω is the angular frequency. T_K^R is the so called transfer function, which is expressed by the sum of the three surface modulations functions, i.e: tilt, hydrodynamic and orbital [Schmidt, 1995] :

$$T_K^R = T_k^{tilt} + T_k^{hydro} + T_k^{orb}. \quad (4.2)$$

Where the tilt modulation is defined as:

$$T_K^{tilt} = -4ik_y \frac{\cot\theta}{1+\sin^2\theta}. \quad (4.3)$$

Where k_y is the looking direction of the SAR system (the right looking direction is negative). θ_i is the incidence angle. The hydrodynamic modulation is defined as:

$$T_k^{hydro} = 4.5\omega \frac{k_y^2(\omega - i\mu)}{|k|(\omega^2 + \mu^2)}. \quad (4.4)$$

μ is the hydrodynamic relaxation rate equal to 0.5 s [Hasselmann and Hasselmann., 1991]. The orbital wave's modulation is defined as:

$$T_k^{rb} = -ik_y \frac{\cos\theta}{\sin\theta}. \quad (4.5)$$

4.2 Historical SAR data

Almost all research studies on ocean wave applications on SAR data were done using mainly C-band SAR data from the European satellite missions ENVISAT and ERS-1/2 data. Even though they are not used in the frame of this work, a description of the data is given for historical reasons and to explain the difference in the data characteristics used in all previous studies and the data used in the current research study.

4.2.1 ERS-1/2

The ERS-1 and ERS-2 missions were two European satellites launched to the same orbit, polar, sun-synchronous, 785 km, in 1991 and 1995 respectively. They were equipped with different sensors, including a SAR. For ocean observation regarding the extraction of sea state parameters these satellites had a special mode called “wave mode”. The wave mode data covers an area of 5 x 10 km. In this mode the data was acquired automatically every 100 km along the satellite track at the same incidence angle ($\sim 23^\circ$), which is considered optimal for ocean observation. This provided a huge global data set of SAR data acquired over the ocean in the order of over a million per year. The pixel resolution of the wave mode SAR data is 20 x 20 m. Detailed information regarding the ERS-1 and ERS-2 satellite missions can be found in <https://earth.esa.int/web/guest/missions/esa-operational-eo-missions/ers> .

4.2.2 ENVISAT

The ENVISAT satellite was the follow-up mission for the ERS-1 and ERS-2 satellites. It was launched in the 1st of March, 2002 and the mission ended in April 2012. It was the first satellite mission to provide global measurements on the atmosphere, ocean, land and ice. The satellite had a sun-synchronous orbit at 800 km height with an inclination of 98.5° . The satellite was equipped with 10 instruments and is the heaviest civilian satellite to date, with 8 tons. One of the instruments was the ASAR sensor (Advanced Synthetic Aperture Radar). This satellite

had the “wave mode” with the same characteristics as the ERS mission did. Ongoing research on ocean waves and wind using C-band “wave mode” SAR data, continued with ENVISAT “wave mode” data. Algorithms to obtain sea state information were developed using this data and are described in the next section.

4.3 Ocean wave analysis algorithms for *C-band* SAR data

In this section the different algorithms developed for ocean wave analysis for C-band SAR data are described. The first algorithm described (MPI) is the basis of the following algorithms. It is based on the linear and nonlinear approximation model to describe the sea surface imaged by SAR. As the model is based on approximation of an ideal sea surface, it could only describe longer ocean waves, such as swell waves, excluding *wind sea* waves. Therefore it was unable to predict the total significant wave height of ocean waves.

The second model described here is the cross-spectral algorithm which can be seen as an extension of the previous one, including the possibility to derive the ocean wave’s propagation direction. The third algorithm, PARSA, is an extension of the previous algorithm, and focuses on the correction of the 2D spectrum derived from SAR data by using wave numerical model data to improve it. The last algorithms described were the first empirically based algorithms CWAVE and CWAVE_ENV, whose purpose was to derive not only *swell height* but significant wave height using only SAR data as input.

4.3.1 MPI scheme (Sea surface description)

The MPI linear and nonlinear scheme is an inversion algorithm based on theoretical assumptions of the sea surface geometry of the ocean waves related to the SAR signal. This algorithm intends to simulate the wave spectrum from the SAR data. A linear approximation of the ocean wave imaging mechanism by the SAR system was introduced by [Hasselmann and Hasselmann., 1991]. It is defined as follows:

$$\phi_{i^2}^{\Delta t} \approx 0.5 \exp[-k_x^2 \beta^2 \rho^u(0)] (|T_k^S|^2 \exp(i\omega\Delta t) F_k + |T_{-k}^S|^2 \exp(-i\omega\Delta t) F_{-k}). \quad (4.6)$$

The SAR transfer function is defined by:

$$T_k^S = T_k^R + i \frac{R}{V} k_x T_k^u. \quad (4.7)$$

Where T_k^R is defined in (formula 4.2) and $T_k^u = -\omega \left(\frac{k_y}{k} \sin\theta_i + i \cos\theta_i \right)$, being θ_i the incidence angle, k the wave number, ω the angular frequency. This algorithm is a geometry imaging of an “ideal“ sea surface, which better describes long ocean waves as swell waves. It is unable to describe wind sea waves, and as a result the total significant wave height cannot be obtained.

4.3.2 SAR cross-spectral algorithm

The SAR cross-spectra algorithm [Engen *et al.*, 1995] takes into account the theoretical ocean waves imaging mechanism. It can be seen as an extension of the previously described algorithm. It was developed to take advantage of a particular type of SAR data (complex data), where not only the amplitude (or sigma naught) but also the phase of signal is available, making it possible to extract two sub-scenes for the same imaged location by the SAR, separated by very short time differences between them (~ 0.33 s). Standard SAR data is a static image, which means that the 2D spectrum derived from standard SAR data has a 180° ambiguity regarding the ocean wave propagation direction. From “complex SAR data” a cross-spectrum from the two sub-images can be derived making it possible to obtain the ocean waves propagation direction.

4.3.3 PARSA (Partitioning Rescaling and Shift algorithm)

PARSA [Schulz-Stellenfleth *et al.*, 2005] focuses on the optimization of the retrieval of the 2-D cross-spectrum. It is an extension of the cross-spectral algorithm described before. PARSA uses the 2D spectrum and wind data from the numerical wave model to reshape the 2D spectrum derived from SAR data in order to obtain a 2D spectrum which approximates a real wave spectrum. A Levenberg-Marquardt method is used to find a numerical solution to retrieve a minimization of the cost function. By using the combined information of the SAR and the numerical model the algorithm tries to reshape the derived spectrum into a more reliable and approximate to the real wave spectrum.

4.3.4 CWAVE and CWAVE_ENV

The CWAVE [Schultz-Stellenfleth *et al.*, 2007] is an empirical algorithm whose purpose is to derive integrated sea state parameters from C-band SAR data e.g. H_s , and ocean wave periods. The algorithm is tuned with ERS-1/2 data and can estimate the integral sea state parameters without the need to derive the 2D spectrum as an intermediate step. It is based on a quadratic function with 22 input parameters. The parameters include the radar cross section σ_0 , the sea surface modulation, and 20 spectral parameters computed from the SAR spectrum using a set of orthonormal functions. It uses a step wise regression method. It is tuned using 12,000 globally distributed ERS-2 wave mode image spectra together with collocated ECMWF (European center Medium Weather Forecast) and the WAM wave model ocean wave spectra. The derivation of the model is based on the least squares minimization procedure. The algorithm is defined as

$$W = a_0 + \sum_{i=1}^N a_i Q_i + \sum_{i=1}^N \sum_{j=1}^i a_{i,j} Q_i Q_j \quad (4.8)$$

where the parameter W is a sum of linear fittings of parameters Q . The factors Q can be however nonlinear functions of other variables.

The validation of this algorithm, against H_s of 6000 collocated WAM model data points, gives an RMS of 0.44 m and a correlation R of 0.92 and when validated with *in-situ* wave measurements (21 data -pairs) it achieved a performance with an RMS of 0.39 m and a correlation R of 0.95 [Schulz-Stellenfleth *et al.*, 2007]. The CWAVE algorithm was tuned and validated for sea conditions with H_s below 6 m.

The CWAVE_ENV [Li *et al.*, 2011] is based on the CWAVE algorithm but tuned using ENVISAT SAR data, instead of ERS SAR data, resulting in a different set of coefficients. Furthermore, unlike the CWAVE algorithm, CWAVE_ENV is tuned and validated for a higher range of wave conditions including those where H_s is above 6 m.

The performance of this algorithm for the estimation of H_s compared to 55884 ECMWF wave model data points achieved a correlation R of 0.93, RMS of 0.43 m and a Scatter index S_i of 0.16.

Chapter 5

Data

This chapter describes the different types of data analyzed in this work. First a description of the ocean wave measurements devices, commonly named as buoys, and the data obtained by them are described. Second the TS-X/TD-X satellites and the data acquired by them and basic calibrations steps are described. At the end a description of the numerical wave model data is provided.

5.1 *In-situ* buoy wave measurements



Figure 5.1: Ocean waves (sea surface elevation) measurements devices commonly known as buoys: 6 meter NOMAD aluminium hulled boat shaped buoy (left). 3-meter aluminium hulled discus buoy (center). Data well Directional Waverider buoy (left).

Data from *in-situ* wave measurements, commonly known as buoys, is provided by the National Oceanic and Atmospheric Administration (NOAA) at the National Data Buoy Center www.ndbc.noaa.gov/, the Environment Canada <http://www.ec.gc.ca/>, the Scripps Institution of Oceanography through the Coastal Data Information Program (CDIP) <http://cdip.ucsd.edu/>. Sea state information is also provided by the North West European Shelf Operational Oceanographic System (NOOS) <http://www.noos.cc>. The NOOS buoy network covers the North European waters. Ocean wave data obtained from this source is presented as integrated sea state parameters; significant wave height, peak period and direction. The NOAA, the Environment Canada and the Scripps Institution of Oceanography all combined count with over 300 wave measurement devices (figure 5.1) providing free quality *in-situ* data for a large ocean area. The buoy network spreads over the entire west and east coast of the North American continent (USA and Canada) and also the Hawaii Archipelago situated in the middle of the

Pacific Ocean. The wave data from this data sources is provided in the form of wave spectra. The wave spectra are 1D energy density spectra which provide the energy density distribution of the ocean waves for each frequency (figure 5.2).

The minimum and maximum ocean wave frequency which can be measured depends on the type of wave measurement device. According to official information available at <http://www.ndbc.noaa.gov/rsa.shtml>, for example, the 3-meter discuss buoy with an ARES payload, (payload refers to specific on-board wave analysis software), (figure 5.1 center) is able to measure wave height from 0 to 35 m with an accuracy of 0.2 m, wave periods from 0 to 30 s with an accuracy of 1s and with a spectrum resolution of 0.01. The measured wave spectrum has usually a minimum frequency $f_{min} = 0.02 H_z$ and a maximum frequency of $f_{max} = 0.4850 H_z$, with a frequency resolution of $0.005 H_z$ at low frequencies, and up to $0.02 H_z$ in the high frequencies. Furthermore some buoys have the capacity to measure the wave field propagation direction like the Datawell directional buoys (figure 5.1 right). The buoy information is given each hour or each 30 minutes. Additionally most of the buoys used for our study are equipped with anemometers to measure wind speed and direction. This information is given each 10 minutes. More details regarding processing buoy data can be found in [Steele, K.E. and T.R. Mettlach, 1993], [Steele, K.E. et al., 1992], [Steele, K.E., 1998] and in [Brown et al., 1996].

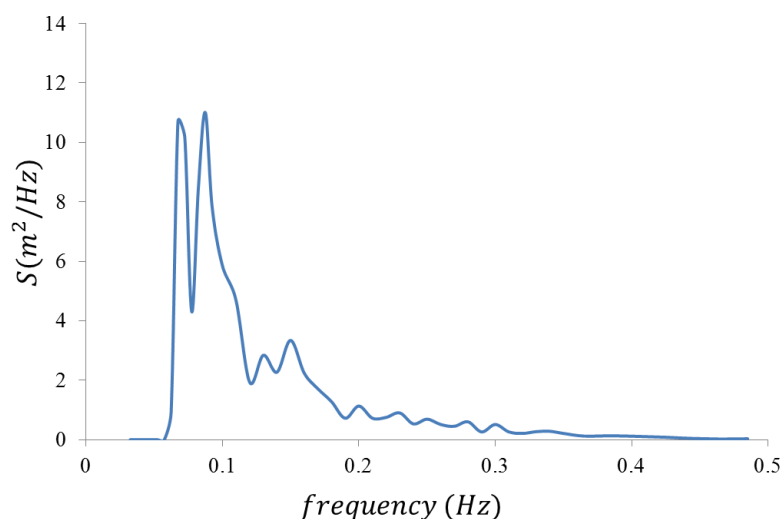


Figure 5.2: Visualization of standard 1D wave spectra provided by ocean wave measurement buoys .In this case the energy density is located in the lower frequencies, which corresponds to long wavelength waves, probably *swell* conditions. Significant wave height calculated from the spectrum is for this case 3.1 m and a wave peak period of 12.9 s.

5.2 TS-X/D-X SAR

The SAR data used in this study is acquired by the German Earth observation satellite TerraSAR-X (TS-X) and the Tandem-X(TD-X) satellite (figure 5.3). The TS-X satellite was launched in June 2007 and has been operational since January 2008. Its twin satellite TD-X was launched in 2010. The TS-X and TD-X satellites have a sun synchronous orbit with an inclination of 97.4° to the equator with altitude of sensibly 514 km. The TS-X and TD-X are equipped with an active phased X-band SAR antenna with a nominal frequency of 9.65 GHZ which corresponds to 3.1 cm wavelength. The TS-X/TD-X satellites acquire high resolution SAR images over land and ocean globally. The TS-X/TD-X are designed to work for at least 5 years, but they will probably last a few years longer.



Figure 5.3: The TerraSAR-X and his twin Tandem-X satellite.

The sun synchronous dusk–dawn orbit allows the satellite to move along the day night boundary presenting always the same side of the satellite to the sun which ensures the optimal configuration for providing sun light for the solar cells of the TS-X satellite. A summary of the main characteristics of the TS-X satellite are shown in Table 5.1.

Table 5.1: General specifications of the TS-X satellite

Height:	4,88 Meters
Width:	2,4 Meters
Weight:	1.230 Kilograms
frequency:	9,65 Gigahertz
Power consumption:	800 Watt ~
Resolution of the data:	1 Meter, 3 Meters, 16 Meters (depending on the image mode)
Start:	15. June 2007
Launch site:	Baikonur, Kazakhstan
Altitude:	514 Kilometers
Inclination with equator:	97,4 ° (Sun-synchronous)
Lifespan:	Minimum 5 years

The TS-X/TD-X scans the earth surface currently in four different modes, each one with a different scan area and resolution.

The current modes available for the TS-X/TD-X mission are the ScanSAR, StripMap, SpotLight and High-resolution SpotLight mode. The high resolution SpotLight mode has the highest resolution, up to 1m, but smallest coverage area of only 5 km by 10 km. The SpotLight mode has a pixel resolution up to 2 m and area coverage of about 10 km by 10 km. The StripMap mode covers an area of 30 km by 40 km with a resolution of about 2.5 m, offering the imaging mode with the best balance of spatial resolution and coverage area. The fourth mode is ScanSAR which covers an area of 100 by 100 km, with a resolution up to 18 m. A fifth mode is currently being planned, wide ScanSAR, which covers an area of about 400 km by 400 km with 18 m resolution. A summary of the TS-X/TD-X different imaging modes characteristics is given in Table 5.2. A representation of the TS-X/TD-X imaging modes on the earth surface is shown in figure 5.4.

Table 5.2: Overview of TS-X acquisition standard modes products

Product	<i>ScanSAR</i>	<i>StripMap</i>	<i>SpotLight</i>	<i>HrSpotLight</i>
Area	100 kmx150km	30 km x50km	10 kmx10km	5 kmx10 km
Incidence angle	20°-45°	20°-45°	20°-55°	20°-55°
Pixel spacing	8.25 m	1.25 m	0.75 m	0.75m
Azimuth Resolution	16 m	3 m	2 m	1 m
Range Resolution	1.7 m-3.5 m	1.7 -3.5 m	1.5 m -3.5 m	1.5 m -3.5 m
Polarization	VV or HH or dual	VV or HH or dual	VV or HH or dual	VV or HH or dual

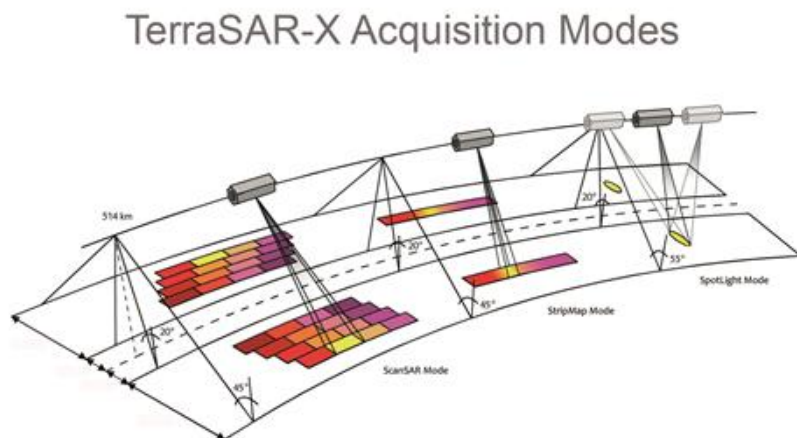


Figure 5.4: Representation of the different modes imaged by the TS-X/TD-X ©DLR.

For the different imaging modes there are still several sub-characteristics as the polarization. The polarization option can be single VV or HH or VH. Furthermore to cover larger areas or different locations, the different modes are acquired at different incidence angles. This changes some characteristics in the imaging of the underlying surface, of which the ocean sea surface is no exception.

The TS-X/TD-X SAR data is different in some aspects in relation to the SAR data provided by the European satellites ENVISAT and ERS missions. The first difference is of course the radar frequency, which is the X-band radar domain, being of shorter wavelength than the C-band. This allows to measure finer scale processes. The spatial resolution of the TS-X/TD-X data compared to previous SAR missions is much higher, e.g. for the case of TS-X/TD-X StripMap product resolution is about 3 m, which is a great improvement when compared to the resolution of C-band ENVISAT SAR “imaggettes” product, which the highest resolution product available is only about 20 m.

Another difference not related to the data, but to the operation method is; the ENVISAT and ERS data (wave mode), which was taken automatically by the satellite, with a predefined distance of 100km within each acquisition. The locations to be imaged by the TS-X/TD-X satellite are selected previously by the user. The TS-X/TD-X data used for the present study are the standard Multi-Look Ground Range Detected (MGD) product, which means only the intensity/amplitude is given not the phase as in complex SAR products. [Figure 5.5](#) shows a quick look of a MGD product, in this case acquired by the StripMap mode VV polarization.

The MGD product is delivered as an *Geotiff* image which is a matrix of pixels with values that can be transformed into values of the signal intensity σ_0 , which is the radar backscatter from the earth surface sent by the SAR antenna. The signal strength which is returned back to the antennas depends on the surface properties, mostly on the surface roughness and also electric dielectric properties. Over the ocean, if the sea surface is flat the impulse signal tends to be reflected away and therefore less signal power will return to the antenna and the image will appear black. In a non-flat sea surface with the presence of ocean waves and wind blowing, the sea surface roughness will increase. In this case the radar signal is not scatter away from the antenna, but instead is reflected back to the antenna. The sea surface where roughness is higher will appear bright. This means that is necessary that wind blows over the sea surface (usually over about 3 m/s) in order for the data to be useful for analysis.

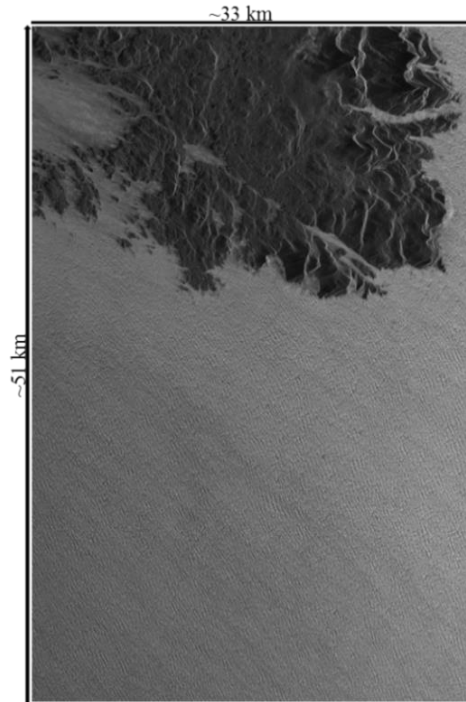


Figure 5.5: TS-X VV polarized StripMap acquired on February 26, 2013 at 19:48 UTC over the Dixon Entrance, west coast of Canada.

5.2.1 Calibration

TS-X/TD-X data have to be ordered in advance and are first calibrated by the following steps. Each value of the matrix of the SAR data needs to be transformed according to:

$$\sigma_0 = I \cdot 2 \cdot k_s \cdot \sin(\theta_i). \quad (5.1)$$

With I being the pixel digital number, k_s is the calibration factor (different for every acquisition and given in the product) and θ_i the incidence angle. For the wind algorithm the normalized radar cross section NRCS (σ_0) is used. NRCS (sigma nought) is given in dB values and calculated as follows:

$$\sigma_o^{dB} = 10 \cdot \log(\sigma_o). \quad (5.2)$$

The values of σ_0 on the TS-X/TD-X MGD SAR data are visualized as a matrix of grey values. An example of the TS-X VV polarized StripMap MGD data product is presented in figure 5.5. Further information regarding TS-X/TD-X data can be found in [Breit *et al.*, 2010] and on <http://sss.terrasar-x.dlr.de/>.

5.3 Numerical wave model data

5.3.1 Wave model DWD data

The wave model data provided by the DWD (German Weather Center) is obtained from the application of the third-generation Wave Prediction Model (WAM) model cycle 4 [Günther *et al.*, 1992]. The model was developed by the WAMDI group between 1984 -1994. Third generations models integrate the dynamical equations that describe the evolution of the wave field. Earlier versions of this model neglected nonlinear wave-wave interactions (first generation) or were described in a parametric form (second generation). The model is computed for the global ocean surface with a horizontal resolution of 0.75° and the model data output for all parameters is given every 3 hours. The scatter index for the model is about 20% with a bias of 0.1 m for the prediction of H_s [Komen *et al.*, 1994]. The wave model is defined by the transport equation as follows:

$$\frac{dF}{dt} + \frac{\partial}{\partial \vartheta} (\dot{\vartheta}F) + \frac{\partial}{\partial \lambda} (\dot{\lambda}F) + \frac{\partial}{\partial \theta} (\dot{\theta}F) = S \quad (5.3)$$

Where F represents the spectral density, θ is the direction, ϑ the latitude and λ the longitude. The terms $\dot{\vartheta}$, $\dot{\lambda}$, $\dot{\theta}$ are the variation of the position and wave propagation direction on the circle. The net source term S is composed by the sum of the source terms, defined as follows:

$$S = S_{in} + S_{nl} + S_{ds} \quad (5.4)$$

Where the term S_{in} is the wind energy input term, S_{ds} is the white capping dissipation [Komen *et al.*, 1994] and S_{nl} is the nonlinear energy transfer. The non-linear energy transfer is caused by four resonantly interacting waves which obey to the resonance conditions for the angular frequency and the wave number. The approach used in the model to describe the term S_{nl} is the one followed by [Hasselmann *et al.*, 1985]. An example of wave model data output, provided from the DWD, for a section of the North Sea on the November 21, 2008 is given in figure 5.6. It presents a wave field propagating south, with visible decrease of values of significant wave height from about 5m in the west, to very low values in the east grid points of the area shown. For our purposes, only integrated sea state parameters are used. Those are significant wave height H_s , swell wave height, wind sea height and the corresponding peak period and direction.

The wave direction corresponds to the direction where the waves come from. The wind fields (speed and direction) values used as input in the numerical wave model are also provided.

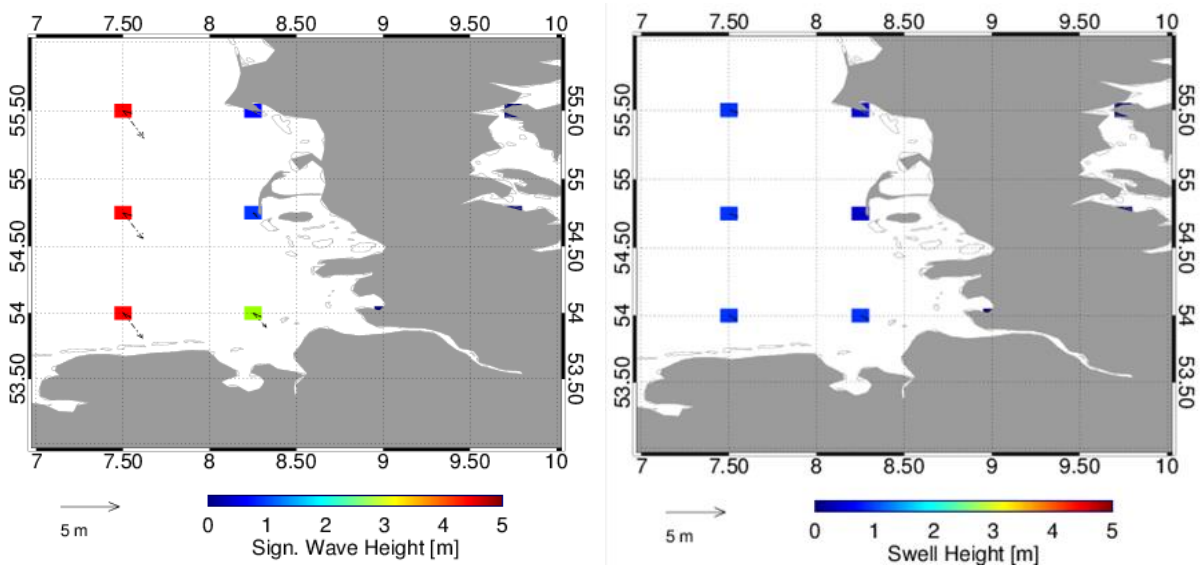


Figure 5.6: H_s field (left) and the *Swell* wave height field (right) given by the DWD wave model on November 21, 2008 at 17:01 UTC.

5.3.2 *K*-model data (coastal wave model)

The *K*-model is a discrete spectral wave prediction model for coastal areas developed at the former GKSS, now the Helmholtz-Zentrum Geesthacht. It is a third generation non-stationary spectral surface wave prediction model based on the action balance equation in *k*-space. The wave model includes a nonlinear white capping dissipation term. It was developed especially for small scale shallow waters areas e.g. German Bight, with non-stationary currents and water depths. The wave model uses as input a fine resolution bathymetry of the area to be analyzed and wave spectra information at the boundaries of the area in question. Additionally, wind fields, water currents and water level fields can also be used as input.

Further information about the numerical wave model *k-model* can be found in [Schneggenburger., 1998] and [Schneggenburger, et al., 2000].

Chapter 6

TS-X/TD-X Sea Surface observation

The aim of this Chapter is to introduce the data acquired over the ocean and to present image signatures of oceanographic phenomena on TS-X/TD-X data. The visual inspection and analysis of SAR data is an important step for ocean waves SAR analysis. Initially the sea surface acquisition by the different TS-X/TD-X modes, taken in different sea state conditions is presented. Then a description of several oceanographic phenomena signatures observed on TS-X/TD-X data, like internal waves, algae bloom, is provided.

6.1 TS-X/TD-X data acquired over the ocean

Wave fields imaged in TD-X/TS-X data give the impression that we are viewing a real ocean wave field. However one must keep in mind, that this is not the case. The radar data image is a representation of the imaged wave field. The variation of the radar signal in the image does not correspond to the real signal variation (Chapter 4). The sea surface imaged by the SAR radar is distorted because the SAR imaging method has limitations in case of moving targets, such as the ocean waves. The first step for ocean wave analysis of the SAR data is the visualization of signatures present in the data. Our own eyes are the first algorithm to infer information regarding ocean waves, such as ocean wave direction, wavelength, and even approximate wave height.

As discussed in Chapter 5, TS-X/TD-X offers four imaging modes, each with different resolution and spatial coverage. Figure 6.1 shows three TS-X/TD-X data images acquired over the same location, on the west coast of the USA in different modes: ScanSAR with the largest coverage (~100 x 150km) and the lowest resolution (~18m), with pixel spacing of 6m, StripMap, medium coverage (~30-50x30 km) and high resolution (~3 m), and pixel spacing of 1.25 m, and 3) SpotLight, with much smaller coverage (~10x10 km) but high resolution (~2 m) with pixel spacing of 0.75 m and high resolution SpotLight with the smallest coverage (~5x10 km) and resolution of about 1 m (figure 6.2).

For our applications, StripMap fits the coverage area requirements and has a resolution quite similar to SpotLight, which is comfortably sufficient to resolve short ocean wind waves. In all the four modes it is possible to observe the imaged wave field, although it is obvious that for StripMap and SpotLight the resolution is visibly higher, than for the ScanSAR mode. From

visual observation of the StripMap data one can infer that the wave propagation direction, is south east, as waves are generated in the open ocean. For the SpotLight data one can observe a cross sea situation where two wave systems with different propagation direction are present.

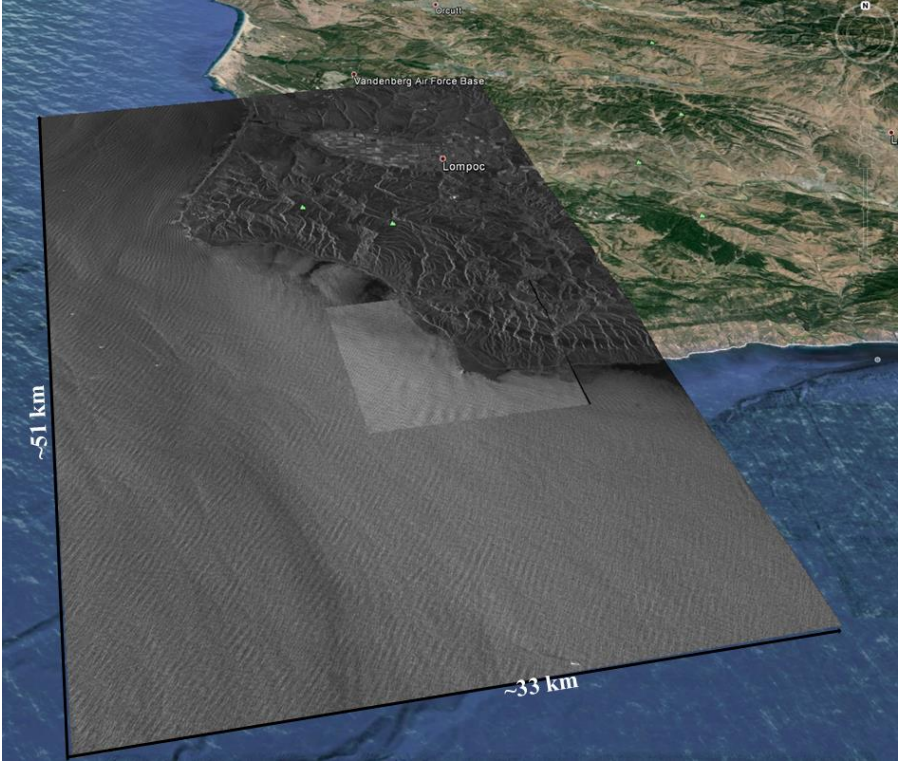


Figure 6.1: TS-X VV polarized StripMap acquired on April 9, 2012 at 1:51 UTC. Inlet: TS-X SpotLight acquired on June 13, 2013 at 1:51 UTC on the west coast of USA.

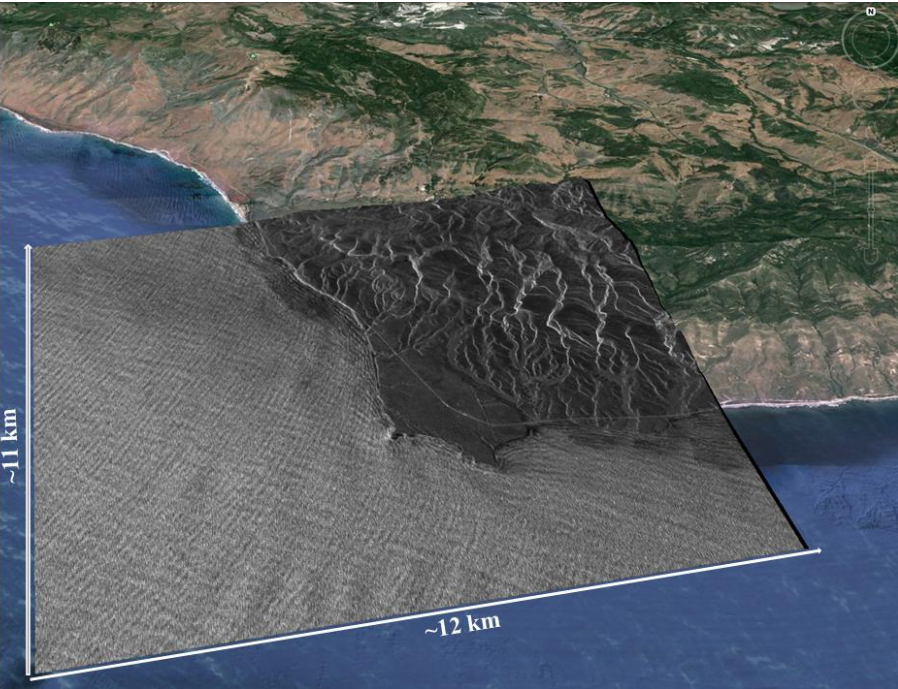


Figure 6.2: TS-X VV polarized SpotLight data image acquired on June 12, 2013 at 1:51 UTC (inlet Fig.6.1).

The spatial resolution of the TS-X/TD-X ScanSAR mode data is lower than StripMap. However its resolution is higher than the one from ENVISAT or ERS “imagerettes”, which was about 30 m. Furthermore, its high coverage area (~100 x 100 km) is an advantage for observing larger scale phenomena as hurricanes or tropical storms, as is the case of the Tropical Storm Nadine in the middle of the North Atlantic on the 3rd of October, 2012 at 8:22 UTC, which is partially imaged in ScanSAR data (figure 6.3). It is possible to observe the change in direction in the wave field from the sub-scenes taken from different locations of the image. Even though the TS-X/TD-X ScanSAR data, has a lower resolution than the other TS-X/TD-X modes, it can be used for ocean wave analysis, extraction of the 2D spectrum and estimation of the wave peak direction and wavelength.

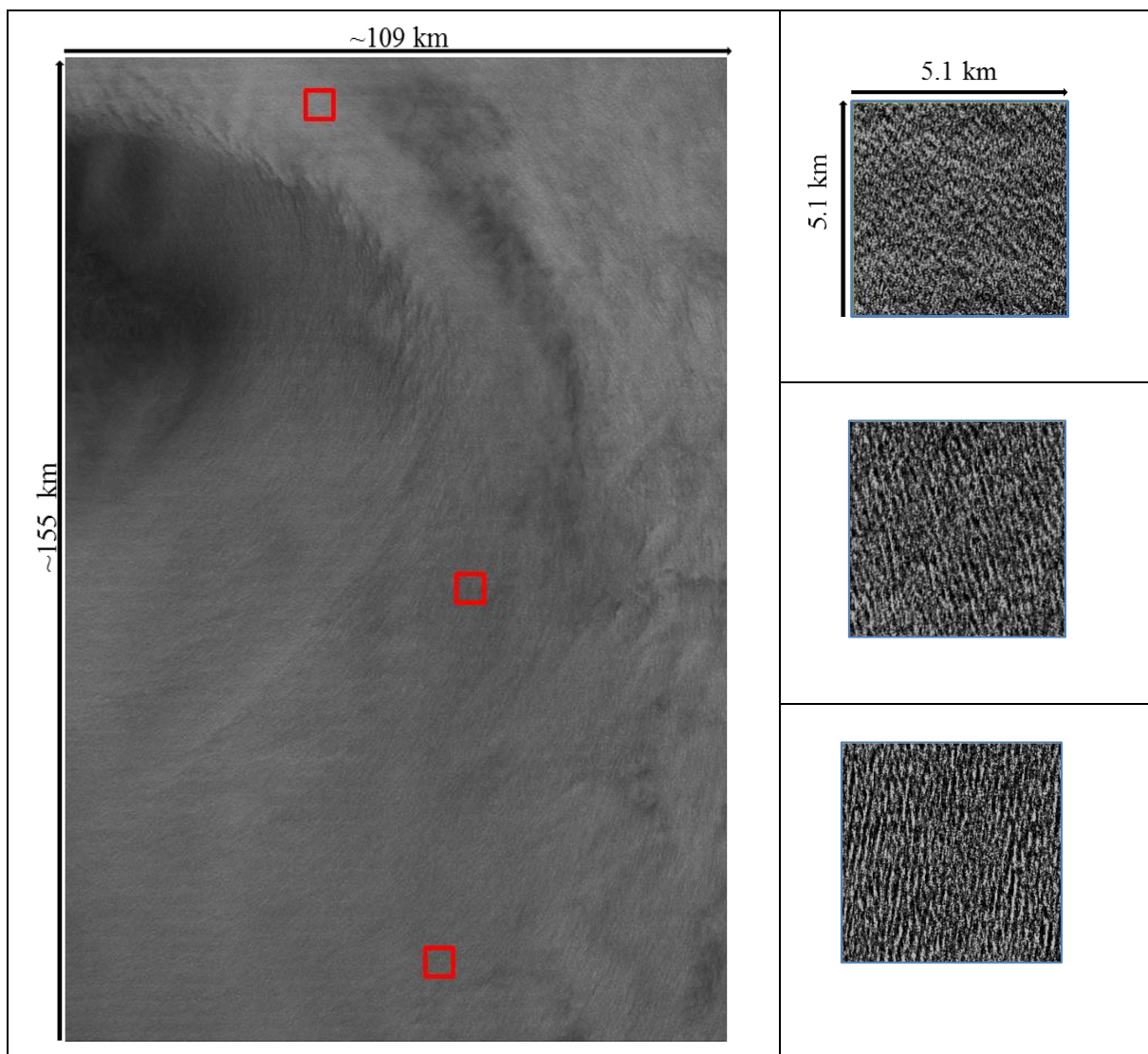


Figure 6.3: TS-X VV polarized ScanSAR data taken on October 3, 2012 at 8:22 UTC over the Tropical Storm Nadine in the middle of the North Atlantic Ocean (left) Sub-scenes taken from different positions on the data image (right).

Figures 6.4 and figure 6.5 are examples showing TS-X/TD-X StripMap data acquisitions over different sea states. Figure 6.4 left shows a TS-X VV polarized StripMap data image acquired under low sea state conditions. In this case it is difficult to assert visually the propagation of the wave field. Information regarding peak wavelength and direction are probably only possible through Fourier analysis. Besides, due to low sea state conditions, spectral peak information will not be so stable.

Figure 6.4 right, shows a TS-X VV polarized data image acquired over low sea and high wind speed conditions, which led to wind signatures in the data image. Due to the additional limitations caused by low sea state conditions, we would expect the Fourier analysis lead to the derivation of spectral peaks related to the wind signatures. Most of these peaks can be filtered out from the spectrum. Wind generated spectral peaks were usually above 1000 m wavelength for the case the case of C-band ENVISAT, ERS-1/2 data. For the case of TS-X/TD-X, by analysis done on data, this wavelength range was found to be much lower than 600 m. Higher resolution gives the ability to image finer scale wind signatures.

Figure 6.5 shows a TS-X Stripmap VV polarized an imaged wave field acquired in higher sea state conditions. It shows a clear defined wave field and consequently it is easy to observe that, the propagation direction is from north-west, even in the presence of wind signatures.

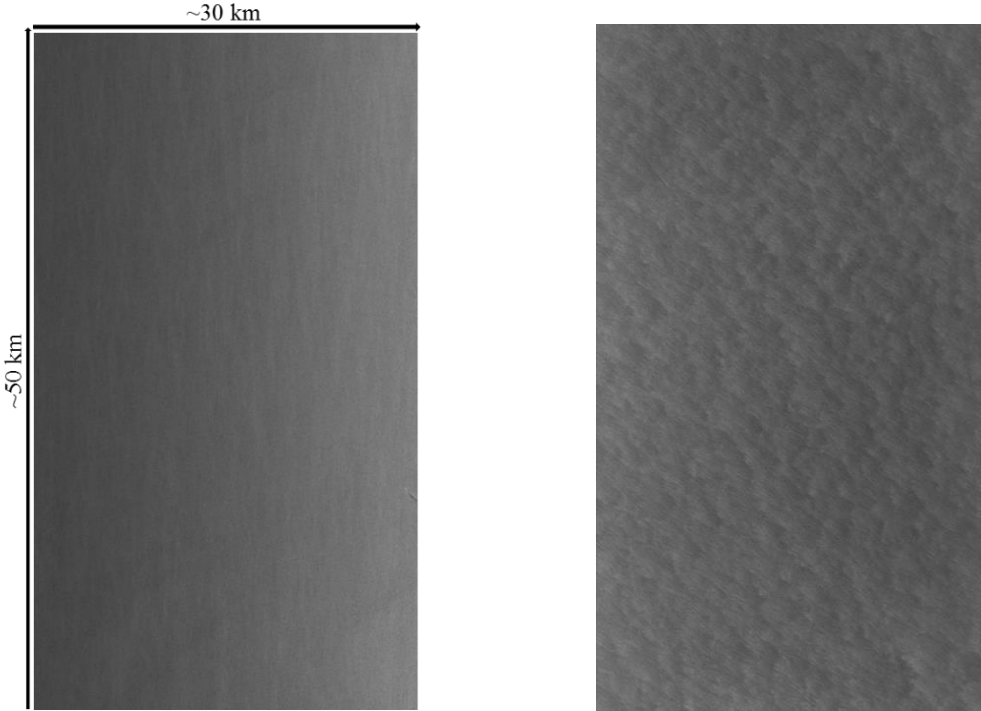


Figure 6.4: TS-X VV polarized StripMap data taken on October 31, 2012 at 11:28 UTC near the Gulf of Mexico. The image data is taken under low sea state and moderate wind conditions (left). TS-X VV polarized StripMap data taken on December 18, 2012 at 22:20 UTC. The image data is taken under low sea state conditions with influence of wind, which created signatures visible in the data (right).

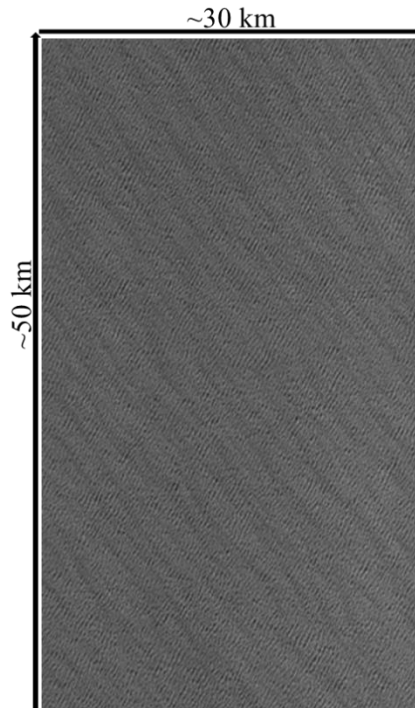


Figure 6.5: TS-X VV polarized StripMap data taken on October 20, 2012 at 15:55 UTC. The data is acquired under high sea state conditions.

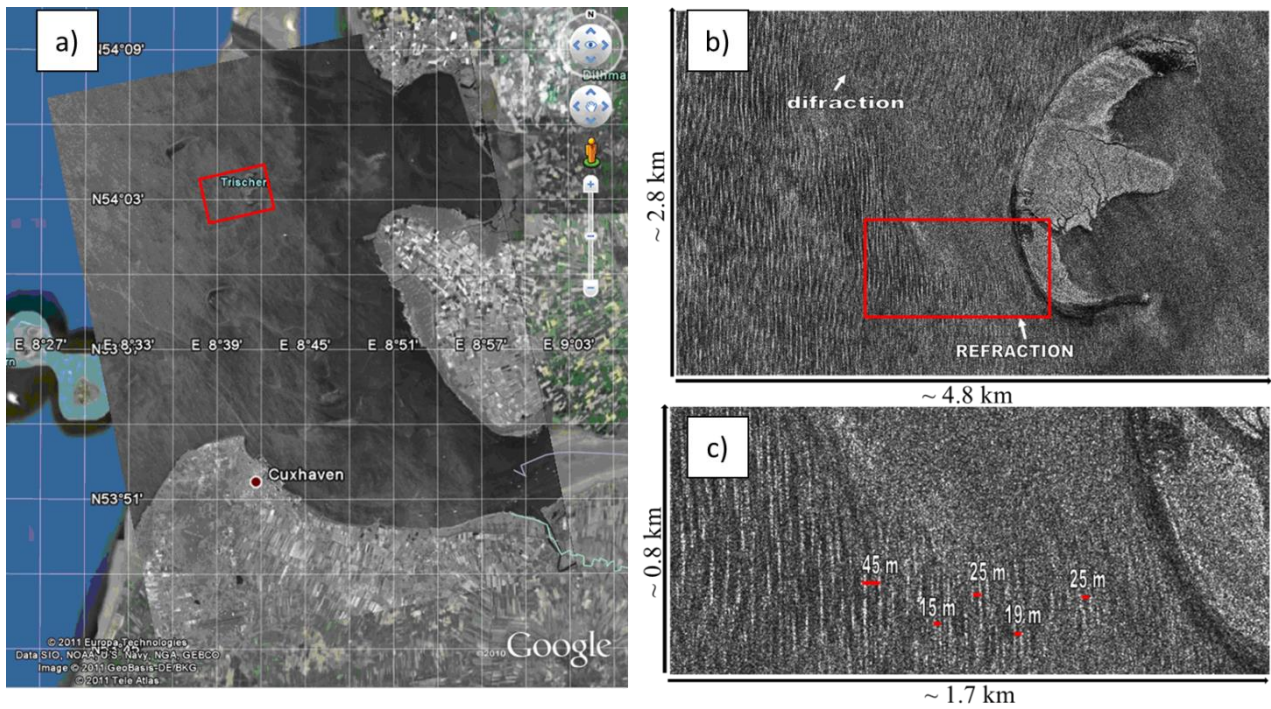


Figure 6.6: TS-X HH polarized StripMap image acquired over the Elbe estuary on November 21, 2008 at 17:00 UTC (a), sub-scene of the TS-X (b), and sub-scene zoom (c), background image, Google Maps©.

Figure 6.6 a) shows a TS-X HH polarized StripMap data image acquired over a complex coastal area in the Elbe Estuary in the north of Germany. The sub-scenes shown on (figure 6.6 b) and (figure 6.6 c), are examples of the capability of TS-X data to capture very small-scale ocean effects. In this case, diffraction and refraction of very short wavelength ocean waves, from 50 m down to 13 m. This indicates that TS-X StripMap data is useful to measure spatial variability. A subject is discussed in Chapter10.

TS-X/TD-X data has the possibility to be taken in HH or VV polarization (Chapter 5). Figure 6.7 shows an example of a wave field imaged in dual polarization TS-X StripMap data. The data shown is a combined set of both HH and VV polarization. As the sea surface is acquired on both polarizations, data has only half of the coverage in range as the standard StripMap data (Chapter 5). The HH and VV polarized data are shown separately in figure 6.8. There are differences between the HH and VV polarization which can be visually identified. The HH polarization wave field (figure 6.8 left), is sharper than the VV polarization wave field (figure 6.8 right). The “sharpness” on HH polarized SAR data can be an advantage for some applications, as ship-detection [Brusch *et al.*, 2011], where a threshold of the values of σ_0 is the key factor of the ship-detection algorithm. However for the case of ocean wave analysis, VV is the most suitable for ocean wave analysis, as it will be discussed in Chapter 8.

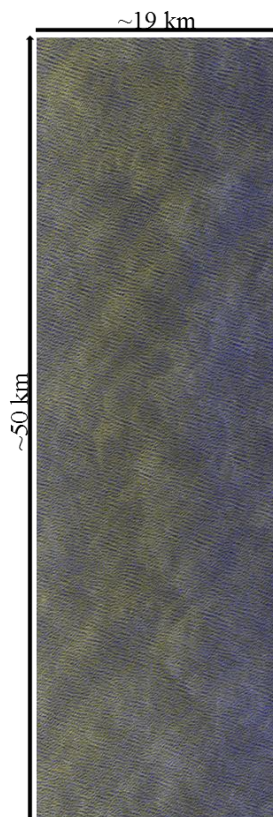


Figure 6.7: TS-X combined dual (HH and VV) polarized StripMap data image acquired on February 4, 2012 at 22:05 UTC over the North Atlantic Ocean.

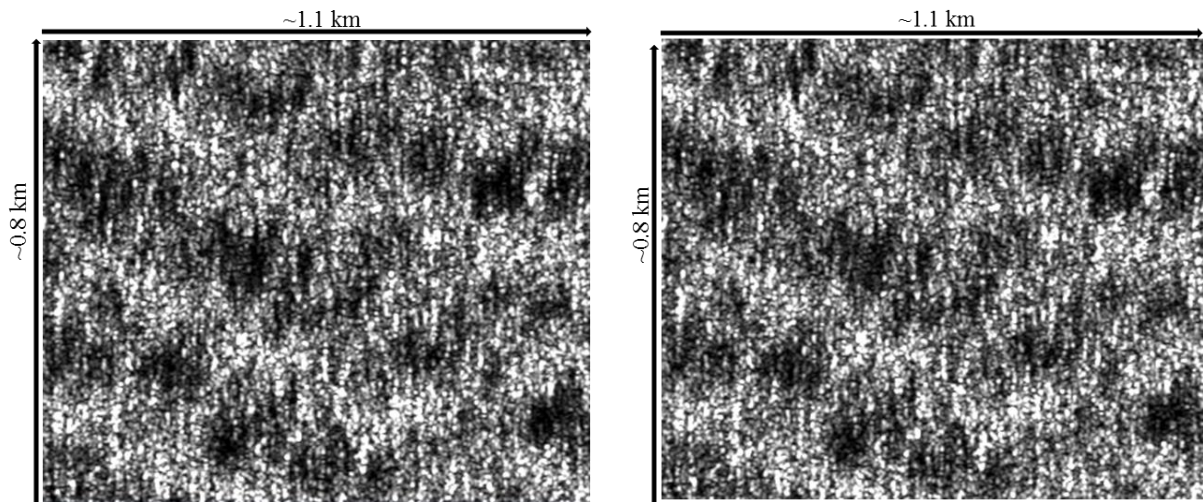


Figure 6.8: Sub-scene taken from the HH polarized data from the TS-X dual polarized StripMap data image shown on figure 6.7 (left). Sub-scene taken from the VV polarized data from the TS-X dual polarized StripMap data image shown on figure .6.7 (right).

6.2 Phenomena sea surface signatures observed in TS-X/TD-X data

There are a number of oceanic phenomena, which are not related directly to sea state or sea surface wind waves that can be observed in SAR data. Such types of phenomena have been studied by means of SAR data, since the beginning of the first C-band SAR missions [Vesecky *et al.*, 1983]. Those phenomena can be: internal waves, atmospheric or oceanic, cloud signatures, atmospheric disturbances, algae blooms or oil slicks.

This section presents a selection of examples of these phenomena observed in TS-X/TD-X data (figure 6.9 to figure 6.12). Figure 6.9 shows an example of internal ocean waves. Figure 6.10 shows an example of atmospheric disturbances signatures. Figure 6.11 left shows examples of man-made oil slicks signatures (oil tanker discharge or platform) and figure 6.11 right shows biological oil slick signatures (algae blooms). Figure 6.12 left shows an example of wind influence, where dust is carried out from the mainland to the sea surface. Figure 6.12 right shows an example of the absence of wind, causing the data to be partially black.

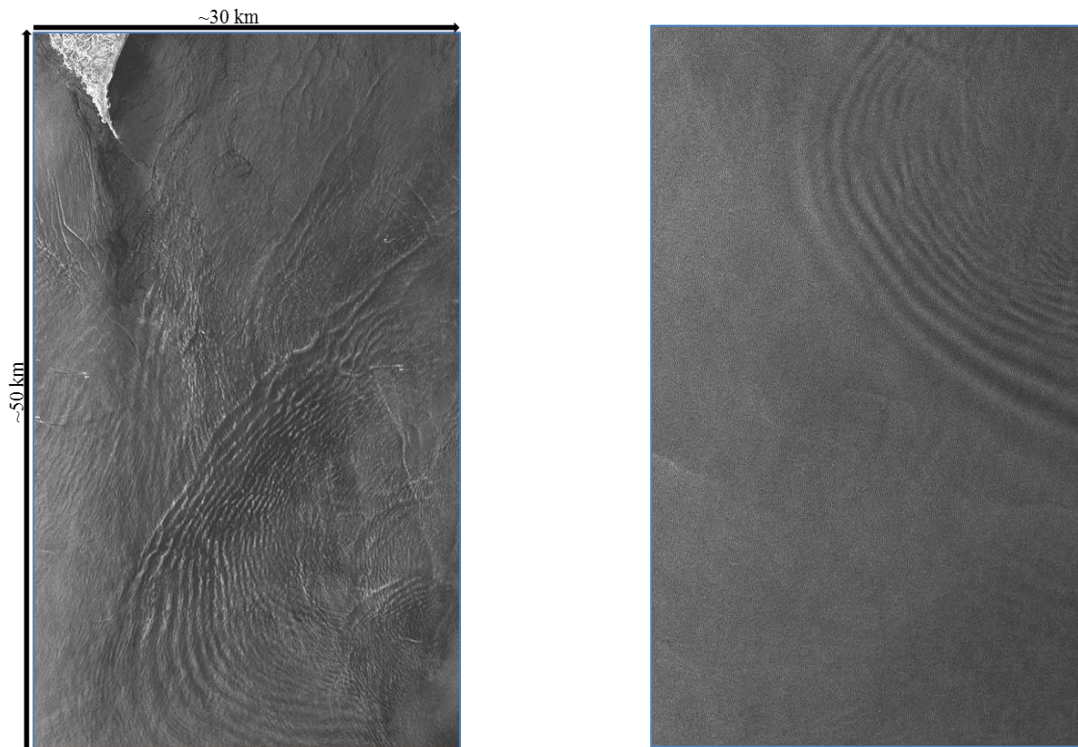


Figure 6.9: TS-X VV polarized StripMap data image acquired in the Pacific Ocean near the coast of Japan on September 21, 2012 at 8:12 UTC. The examples shows internal Ocean waves probably formed by the underwater terrain (left). TD-X VV polarized StripMap data image acquired over the North Pacific Ocean, off the west of Canada on December 10, 2011 5:05 UTC. A set of internal ocean waves are visible in the TS-X images (right).

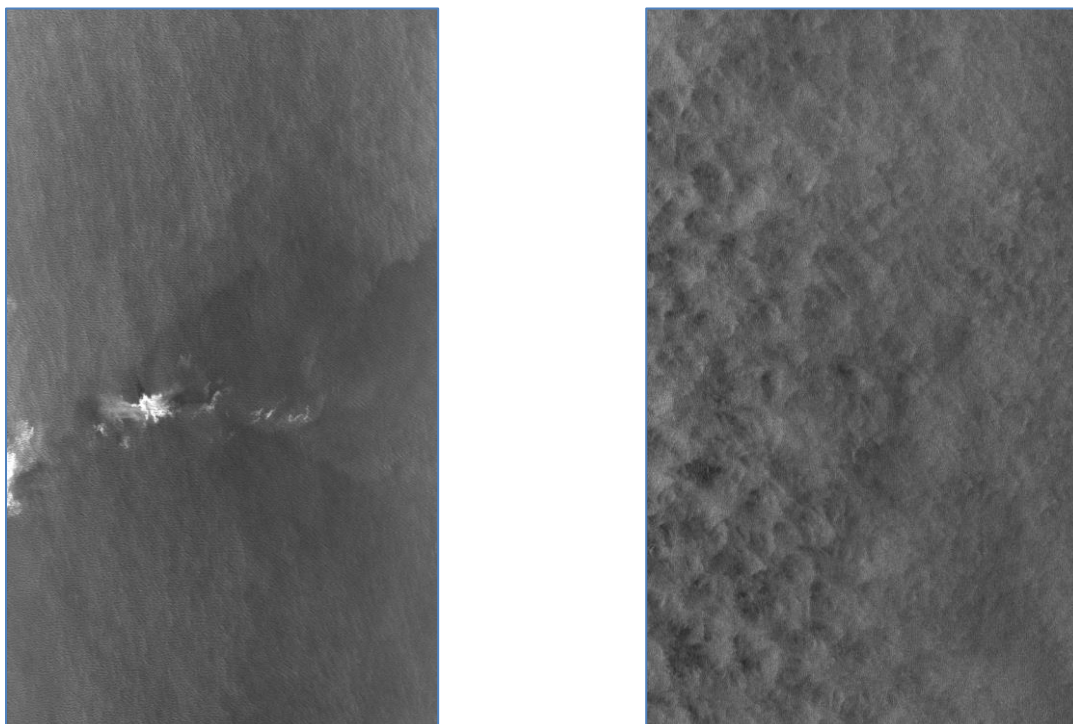


Figure 6.10: TS-X VV polarized StripMap data image taken in the Indian Ocean, south from India on September 19, 2012 at 13:20 UTC. The image shows an atmospheric signature visible in the middle of the image (left). TS-X VV polarized StripMap data image acquired in the North Pacific Ocean near Canada on March 13, 2012 3:23 UTC. The image shows cloud signatures (right).

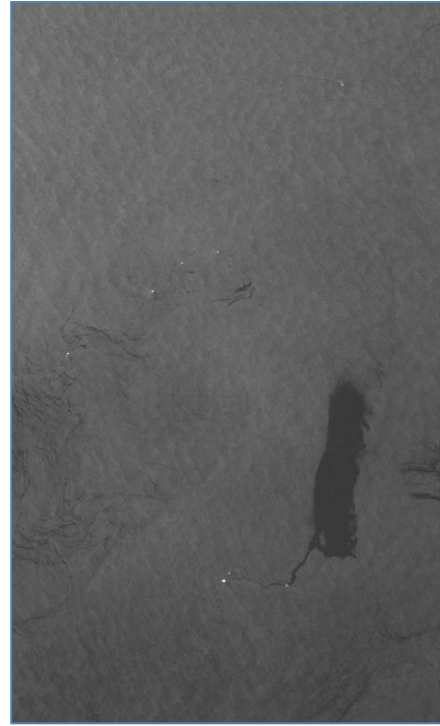
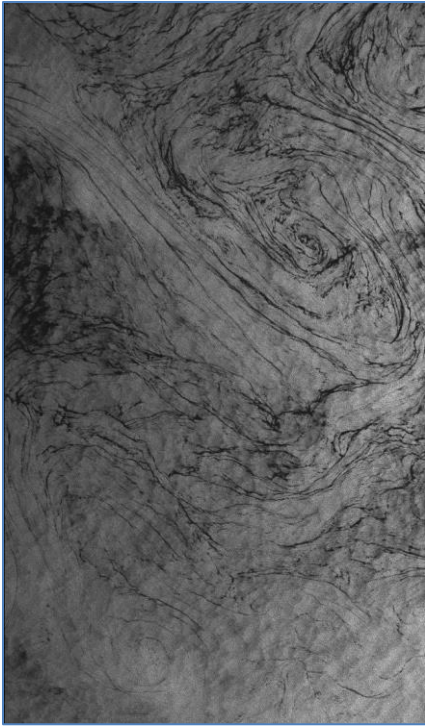


Figure 6.11: TS-X VV polarized StripMap data image acquired off the east coast of the USA on March 16, 2012 at 10:49 UTC. The case shows an example of surface oil slicks (algae blooms) (left). TS-X VV polarized StripMap image acquired over the Gulf of Mexico on August 28, 2011 at 23:48 UTC. This case shows an oil spill in the right side of the image (right).

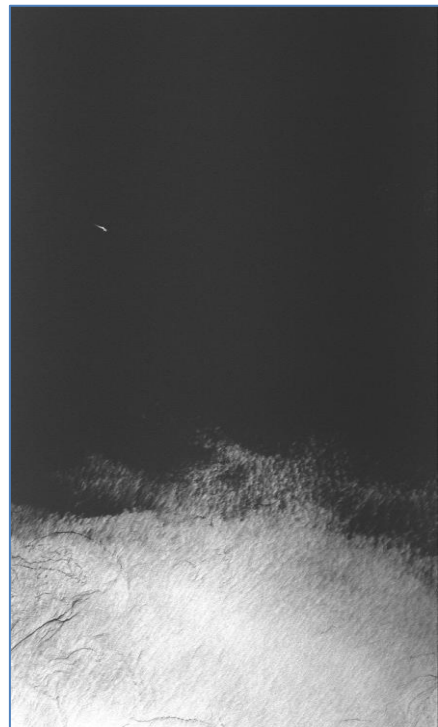
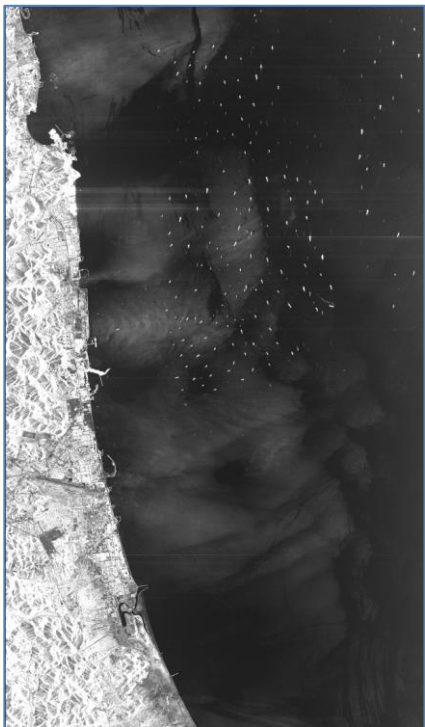


Figure 6.12: TS-X VV polarized StripMap data image taken over the coast of Oman, North Africa, on the March 2, 2012 at 2:14 UTC. The example shows a fleet of ship, and wind blowing from land to the sea bringing dust from the mainland dune (left). TS-X VV polarized StripMap image acquired over Lake Huron, Canada on December 13, 2011 at 23:10 UTC. The image appears black in most of the upper part because the wind speed is too low to provide enough roughness to reflect the radar signal back to the antenna (right).

Chapter 7

Data Analysis

This chapter contains a description of the ocean wave analysis done. A Fourier analysis was performed on TS-X/TD-X data, which is described first. Using the FFT algorithm methodology, one is able to derive the 2D spectrum from the TS-X/TD-X data. However, before the analysis, the SAR data has to be asserted for quality. Therefore a method, named homogeneity test, to identify TS-X/TD-X data which presents homogeneous wind generated ocean wave fields is presented, which is described after. This method is useful to discard TS-X/TD-X data which presents unwanted signatures in the data unrelated to wind generated ocean waves, such as internal waves, atmospheric disturbances, man-made structures, etc.

After the description of the methodology to derive 2D spectrum and to assert the quality of SAR data, the results of the ocean wave analysis are presented. The sea state parameters (peak wavelength and direction) inferred from the 2D spectrum derived from TS-X/TD-X data by Fourier analysis are compared to *in-situ* wave measurements. The objective is to assert the quality of the derived peak wavelength and direction from TS-X/TD-X data. As the SAR spectrum is being regarded as linear using the described methodology, the objective is to assert how good is the comparison of the derived parameters with the *in-situ* wave measurements.

The chapter ends with the study of the minimum detectable ocean wave wavelength by the SAR propagating in the satellite path, known as the azimuth *cut-off* wavelength. This parameter gives a level of capability of the SAR to image ocean waves. The lower the value of the azimuth *cut-off* wavelength, the lower is the ocean wavelength imaged by the SAR in azimuth direction, and therefore the higher is the quality of the SAR observation.

7.1 The 2D Fourier analysis

The first basic step of ocean wave analysis on SAR data is obtained by Fourier analysis. The steps of the FFT algorithm methodology used for the ocean wave analysis are as follow:

First, the TS-X/TD-X data is spatially averaged by a factor of 2. This provides a first level degree of correction to reduce speckle noise, and pixel errors. Each sub-scene has dimensions given in number of pixels in range dimension n_x and in azimuth dimension n_y . For the case of TS-X/TD-X StripMap data using $n_x = n_y = 2048$ corresponds to a box size of approximately 5.1 km, as the original standard pixel spacing for this mode is of 1.25 m (figure 7.1 left).

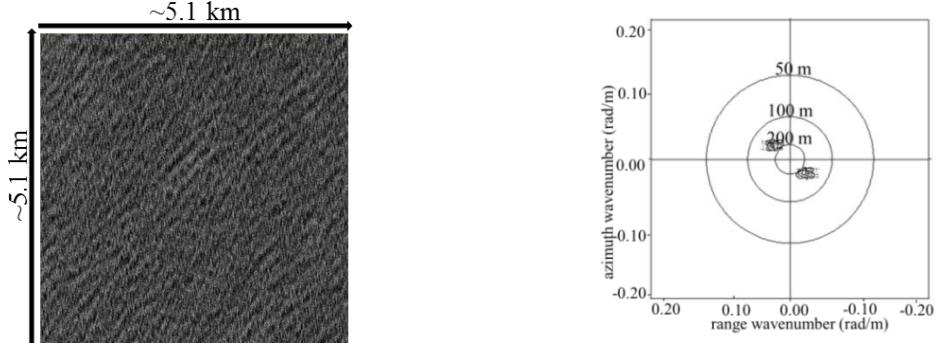


Figure 7.1: TS-X sub-scene (left) 2D spectrum derived from the left sub-scene using the methodology described in this section (right).

Each sub-scene S_S is then calibrated so that each pixel value $\sigma_0(x, y)$ of the sub-scene is modified by:

$$\sigma_c = \frac{\sigma_0(x, y) - \langle \sigma_0 \rangle}{\langle \sigma_0 \rangle}. \quad (7.1)$$

Where $\langle \sigma_0 \rangle$ is the mean value of σ_0 in the sub-scene resulting in a calibrated sub-scene S_S^* with pixel value σ_c . This is the so-called image modulation, a calibrated representation of the variation of the radar signal which approximates the sea surface elevation (Chapter 4). The next step of the process is to obtain the power spectrum P (figure 7.1, right) for each sub-scene S_S^* with pixel value σ_c . The power spectrum P is obtained by Fourier analysis using the FFT as follows:

$$P = (FFT(S_S^*))^2 \quad (7.2)$$

The spectrum P , derived in the spatial domain, has wavenumber spacing dkx and dky for the range and azimuth directions of the sub-scene obtained by:

$$dkx = \frac{2\pi}{(nx * dx)} \quad dky = \frac{2\pi}{(ny * dy)} \quad (7.4)$$

where dx and dy are the pixel spacing of the sub-scene and nx and ny are the number of pixels. For the case of standard TS-X/TD-X StripMap data, the image pixel of each sub-scene is 2.5 m, resulting in a wavenumber spacing dkx and $dky = 0.001227$.

The spectrum P defined as a function of the wavenumber can be represented best by:

$$P = S(k_x, k_y) \quad (7.5)$$

where $k_x = k \cos \theta$ and $k_y = k \sin \theta$, given that the wavenumber $k = \sqrt{k_x^2 + k_y^2}$ and $\theta = \arctan(k_y / k_x)$. An equivalent two-dimensional spectra in both the wavenumber and direction domain is related to the previous spectra by:

$$P(k, \theta) = P(k_x, k_y) J \quad (7.6)$$

J is the Jacobean matrix to transform the spectrum from the 2D wavenumber domain k_x, k_y into a 2D spectrum in both wavenumber k and direction θ domain. The Jacobean for this transformation is simply k . The two dimensional spectrum P can also be represented in the form of $\bar{P}(L, \theta)$, as k is related to wavelength by $k = 2\pi / L$. In this form it provides information about energy density distribution related to wavelength of the ocean waves.

7.2 Homogeneous and inhomogeneous wave fields observed by TS-X/TD-X

In Chapter 6 several examples of signatures caused by phenomena observed in TS-X/TD-X data acquired over the sea surface which are not related to wind generated ocean waves were presented. Although those phenomena are interesting, this thesis is focused on wind generated ocean waves and those phenomena signatures are considered artefacts on the data as they interfere with ocean wind wave analysis. TS-X/TD-X data can be inspected visually for the presence of these signatures, and discarded if there are detected. However visual inspection is not practical when dealing with large amount of data.

Examples of TS-X/TD-X StripMap VV polarized data presenting homogeneous wind generated ocean waves wave field is shown on figure 7.2 and contaminated wave field is shown on figure 7.4. A method to filter TS-X/TD-X data containing unwanted signatures is discussed below. The objective of the method is to analyze sub-scenes of the TS-X/TD-X data and check for unwanted signatures. Even if the TS-X/TD-X data image contains signatures, sub-scenes where signatures are not present can be kept for further analysis. The method consists on checking the variation of spectral properties within the sub-scene. On the open sea, the sea surface ocean wave statistics (e.g., significant wave height, wave period, wave direction) in

non-storm situations remain constant over a distance of a few kilometers. These wave fields can be considered homogeneous. For a homogeneous wave field, free of artefacts, the spectral properties of the wave field area do not change significantly over the imaged area. Following this idea, to assert that a TS-X/TD-X sub-scene is homogeneous, equally sized sub-scenes fragments are analyzed by Fourier analysis (figure 7.2, figure 7.3, figure 7.4 and figure 7.5).

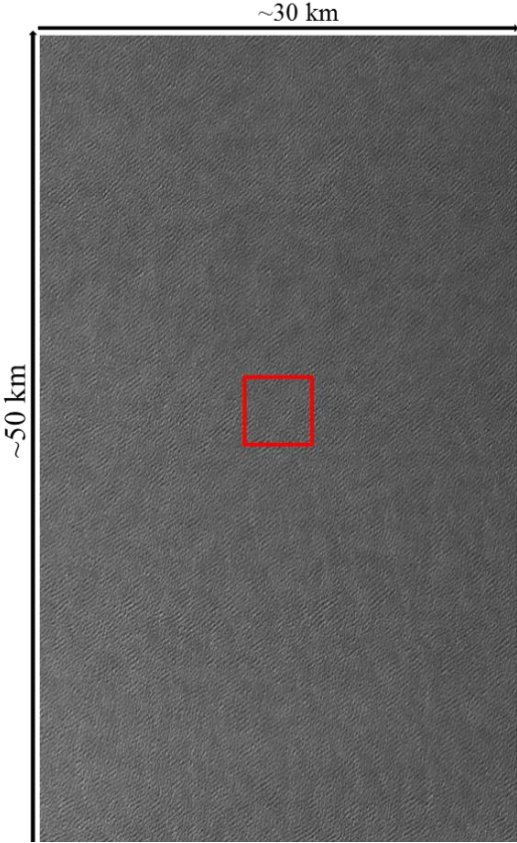


Figure 7.2: Example of TS-X data presenting homogeneous wind generated ocean wave field; TS-X VV polarized StripMap data image taken over the Pacific Ocean near Canada on November 24, 2011 at 3:21 UTC.

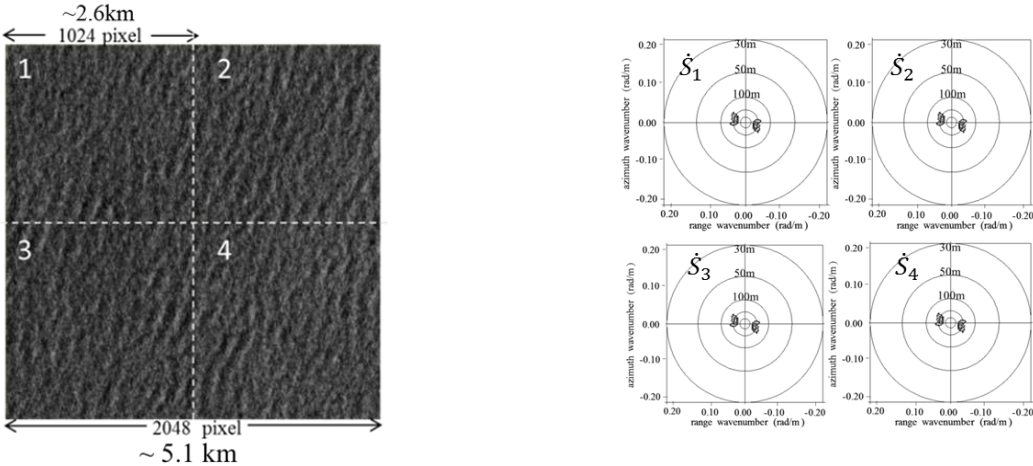


Figure 7.3: Sub-scene (2048 by 2048 pixel => (5.1 km x 5.1 km) taken from data presented in (figure 7.2) is divided into 4 smaller 1024 pixel sub-scenes of equal size (2.6km x 2.6 km) (left). For each of the smaller sub-scenes the spectrum is derived (right).

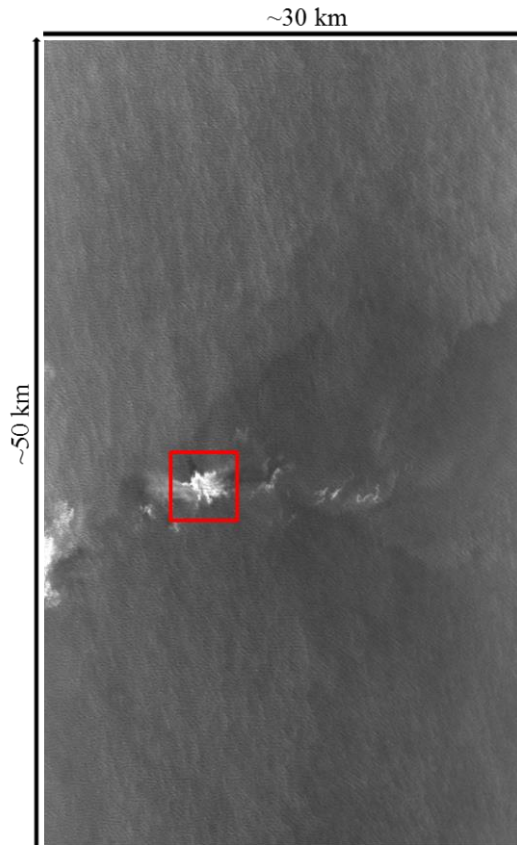


Figure 7.4: Example of an Inhomogeneous data image; the data presents an atmospheric signature visible in the middle of the image. TS-X VV polarized StripMap taken in the Indian Ocean, south from India on September 19, 2012 at 13:20 UTC.

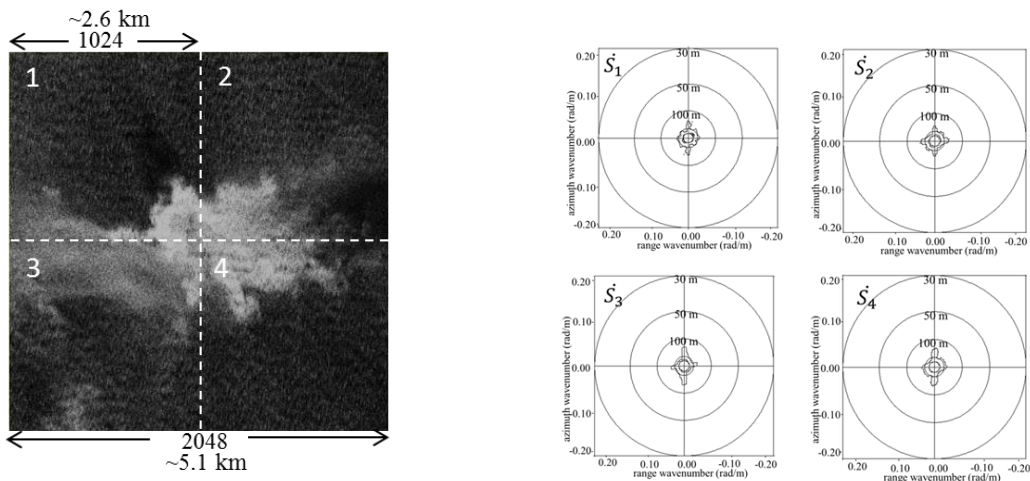


Figure 7.5: TS-X StripMap sub-scene (2048 by 2048 pixel \Rightarrow (4.6 km x 4.6 km) is divided into 4 smaller 1024 pixel sub-scenes of equal size (2.6km x 2.6 km). For each of the smaller sub-scenes the spectrum is derived.

The spectral densities of each spectrum obtained from the different sub-scenes fragment \hat{S}_1 to \hat{S}_4 are compared. More precisely the difference in spectral energy between each spectrum is calculated. If the difference between spectra is higher than a certain threshold, it means that the

spectral properties of the sub-scene are not similar. In other words, the analyzed sub-scene contains unwanted signature. The exact procedure to achieve the previously described objective is as follows: the derived spectra are normalized according to the maximum spectral value of each sub-scene. The spectra are inter-compared and the difference of the spectral values between each spectrum is calculated. The result is a matrix which contains the spectral differences between each spectrum as defined below:

$$S_{T12} = \dot{S}_1 - \dot{S}_2 \quad (7.7)$$

$$S_{T13} = \dot{S}_1 - \dot{S}_3 \quad (7.8)$$

$$S_{T14} = \dot{S}_1 - \dot{S}_4 \quad (7.9)$$

$$S_{T23} = \dot{S}_2 - \dot{S}_3 \quad (7.10)$$

$$S_{T24} = \dot{S}_2 - \dot{S}_4 \quad (7.11)$$

$$S_{T34} = \dot{S}_3 - \dot{S}_4 \quad (7.12)$$

A sensitive study using over 350 TS-X/TD-X data-sets was used to analyze the spectral properties on the data. On the basis of visual inspection and Fourier analysis of the TS-X/TD-X data, an empirical threshold value for the maximum difference between spectra was determined to identify TS-X/TD-X data presenting homogenous wave fields free of any signatures. The conditions of TS-X/TD-X data homogeneity can thus be summarized by:

$$\text{If } \overline{S_{T12}}, \overline{S_{T13}}, \overline{S_{T14}}, \overline{S_{T23}}, \overline{S_{T24}}, \overline{S_{T34}} < 0.08 : \text{ Homogenous wave field} \quad (7.13)$$

$$\text{If } (\overline{S_{T12}}, \overline{S_{T13}}, \overline{S_{T14}}, \overline{S_{T23}}, \overline{S_{T24}}, \overline{S_{T34}} > 0.08 : \text{ Inhomogeneous wave field.} \quad (7.14)$$

The threshold value set is able to discard all TS-X/TD-X contaminated data images and to keep data images visually free of signatures unrelated to wind ocean waves. The data selected is considered suitable for further ocean wave analysis. Only the data selected using the method described above is used in the tuning and validation of the algorithm developed for the aim of this thesis.

7.3. Ocean waves peak wavelength and direction derived from TS-X/TD-X data

In this section the peak wavelength derived from TS-X/TD-X data is verified against *in-situ* wave measurements. The data analyzed is free of unwanted signatures unrelated with wind generated ocean waves by applying the quality test described previously. Although SAR data visually seems to show ocean waves, the data only gives a representation of the imaged wave field (Chapters 4 and 6). Therefore, the 2D spectrum does not represent a real wave spectrum.

A first assessment of the quality of the derived 2D spectrum derived from SAR data, is accomplished by comparing the peak wavelength and direction derived from the SAR 2D spectrum with *in-situ* wave measurements. The statistical performance parameters used for the verification of the correlation of the derived SAR parameter X_{SAR} , with the *in-situ* wave measurements or numerical wave model data X_i , are the standard parameters correlation, Scatter index, Root mean square and bias. The correlation coefficient R defined by:

$$R = \left(\frac{\sum (X_i - \bar{X}_i)(X_{SAR} - \bar{X}_{SAR})}{\left(\sum (X_i - \bar{X}_i)^2\right)^{1/2} \left(\sum (X_{SAR} - \bar{X}_{SAR})^2\right)^{1/2}} \right). \quad (7.15)$$

The bias B given as follows:

$$B = \overline{X_{SAR} - X_i}. \quad (7.16)$$

The root means square RMS is given by:

$$E_{rms} = \sqrt{\overline{E_i^2}} = \sqrt{\overline{(X_{SAR} - X_i)^2}}, \quad (7.17)$$

and the scatter index Si is given by:

$$Si = \frac{E_{rms}}{\bar{X}_{SAR}}. \quad (7.18)$$

Given that the TS-X/TD-X has a lower orbit (513 km) than conventional SAR satellites, (approximately 800 km) it presents fewer limitations to image moving targets. Hence the imaging of ocean waves by the TS-X/TD-X is improved in comparison to previous SAR

satellites. Therefore a good performance for the derived peak parameters wavelength and direction from TS-X/TD-X data with *in-situ* data is expected.

A TS-X/TD-X collocated data-set with *in-situ* wave data from the NOAA buoy network is used for the comparison of the spectral peak parameter (figure 7.6). The buoys are located in deep water (we assume in our case deep water as $>100\text{m}$, for the range of wavelengths analyzed). This data-set is also used for the tuning and validation of the empirical algorithm to derive wave height discussed later in Chapter 8. The distribution of the wave peak direction (figure 7.7) shows that in the data analyzed, azimuthally traveling waves [between $\sim 0^\circ$ and $\sim 180^\circ$] are less frequent than the cases of near range travelling ocean waves [between $\sim 90^\circ$ and $\sim 270^\circ$].



Figure 7.6: Location of the NDBC buoys used in the analysis of TS-X/TD-X data.

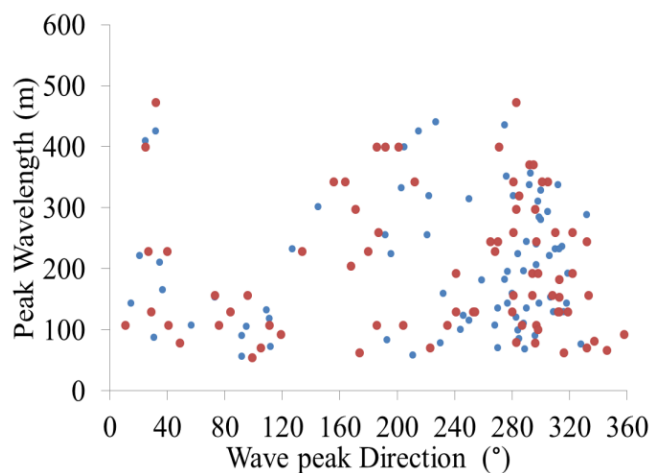


Figure 7.7: The distribution of the wave peak wavelength and direction for the analysed 200 collocated, wave peak wavelength versus wave peak direction; red: *in-situ*, blue: TS-X/TD-X.

This means that most of the measurements represent wave fields traveling perpendicular to the satellite flight path. However, this corresponds to the common ocean wave propagating conditions around the world, where ocean waves in mid-latitudes usually propagate West–East/East–West, except during storm conditions, or due to land mass interference. For the analyzed acquisitions the wave propagation direction West–East ($\sim 270^\circ$) predominates. The wave fields in question were acquired on the west coast of the USA. Most of the waves propagate from east, as they cannot be originated in the west where land is. Following the same line of thought, for the east coast of the USA, wave fields are predominantly propagating from east. The reason why there is more valid data acquired in the west than of the east side of the USA, is that although TS-X/TD-X data was acquired randomly covering a certain list of buoy locations equally distributed on both sides, in the North Atlantic many images were discarded due to frequent algae blooms. This is also the reason of the limited number of acquisitions taken over the Hawaii Archipelago.

Another reason for the difference in the number measurements in the west and east was the presence of the atmospheric disturbances in the east side. Hurricanes and tropical cyclones, caused not only contamination by unwanted signatures, but also due to the severity of the storms, buoys usually stop functioning for a certain period of time. In the west side, *swell* waves were mostly generated from weather systems not near the coast but located in the middle of the Pacific, so the data was free of atmospheric disturbances.

Results of the comparisons of the derived wave peak wavelength from TS-X/TD-X and *in-situ* wave measurements (buoy) are shown in figure 7.8 left.

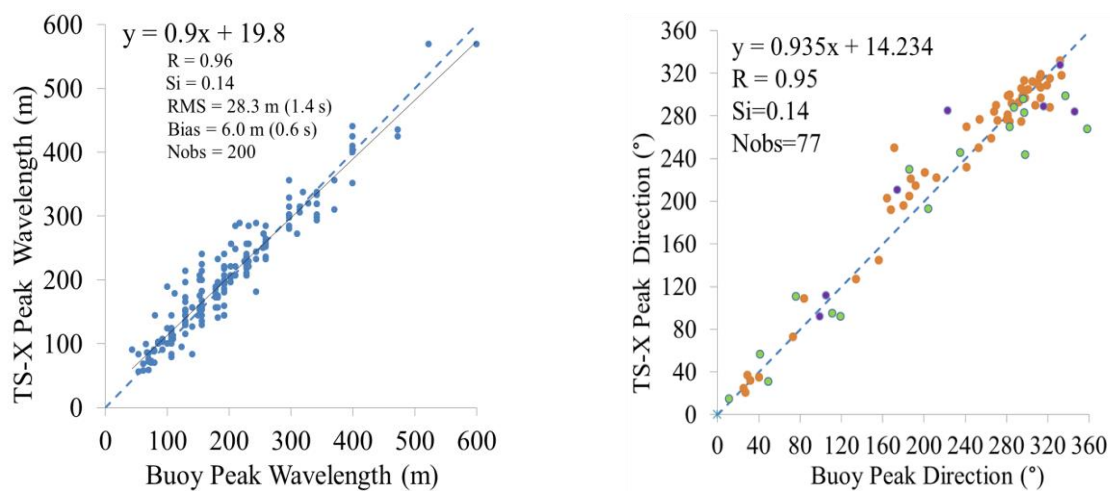


Figure 7.8: Comparison of the wave peak wavelength λ_p derived from TS-X/TD-X VV polarized StripMap data against peak wavelength λ_p derived from buoy data using the dispersion relationship for deep waters (left). Comparison of ocean wave peak direction θ_p derived from TS-X/TD-X data against θ_p given by the buoy. Each color corresponds to different a wavelengths range; Orange wavelengths >120 m; Green: wavelengths between 120 to 75 m, purple wavelengths between 55 and 75 m (right).

The data-set analyzed contains wave peak wavelengths ranging between 55 m and 600 m. The comparison with *in-situ* data shows good agreement, with a correlation R of 96 %, RMS of 28 m and a bias of 0.6 m, which is equivalent to 1.4 s and 0.6 s in the frequency domain, and a scatter index Si of 0.14. The good correlation and low scatter index is mainly due to the low orbit of the satellite. This enables ocean waves to be better imaged.

Only 77 out of the 200 buoys collocated with the TS-X/TD-X data deliver directional information. The comparison of the wave peak direction derived from TS-X/TD-X data with *in-situ* data shows a good agreement. The overall correlation R is of 95%, and the scatter index Si is about 0.14 (figure.7.8 right). The derived wave peak direction is identified with different colors associated to the different wavelengths bands. Blue for the shorter wavelengths band, set to be between 55m and 75m, green for wavelengths between 75 m and 120 m, and orange for wavelengths between 120 m and 600m. Given that shorter ocean wavelengths, tend to be more difficult to measure, and distortions can occur, in this way is possible is easily identifiable the quality for each range of wavelengths.

Figure 7.8 shows that in general, despite the different number of sample points between each band, it seems that for longer wavelengths wave peak direction estimates are better. Shorter ocean wavelengths tend to be more influenced by the distortion which happens when SAR images moving objects. The following section presents the next step of the analysis of the 2D spectrum. The distortion caused on the spectrum is analyzed and quantified.

7.4 Azimuth *cut-off*

In this section the azimuth *cut-off* effect on the 2D spectrum derived from TS-X/TD-X data is analyzed and discussed. The azimuth *cut-off* effect is seen as a distortion of the spectral shape, which can be seen in the spectrum as a shift of the spectral density into the range axis (figure 7.9). This leads to a clear gradient of higher spectral values against very low background spectral values.

The *cut-off* effect is associated by the distortion present on SAR data acquired over the sea surface. This distortion is caused due to miss-registrations of the Doppler radar signal caused by the motion of the imaged wave field. This distortion seen on the SAR data is often referred to as velocity bunching effect of moving targets, where moving targets are shifted from the original positions (Chapter 3).

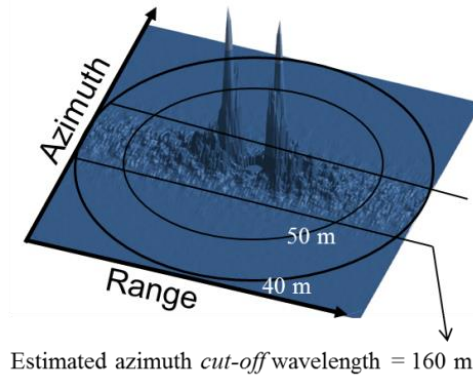


Figure 7.9: Visualization in 3D of the 2D spectrum derived from a sub-scene taken from TS-X VV polarized StripMap data over a wave field with *in-situ* meteo-marine information; wave height: 5.9 m and wind speed: 5.4 m/s.

The higher the motion of the object in question (in our case ocean waves), the stronger the distortion will be. Strong distortion is expected where movement on the wave field is high, high sea states and high wind speed conditions.

Distortion of the SAR data has generated debate over the last 25 years regarding the imaging of ocean waves by SAR. The bunching effect related to imaging moving targets, is seen as an important limitation. As a result the SAR system is unable to retrieve the full ocean wave's information e.g. [Alpers *et al.*, 1986]. For the cases of ERS-1/2 SAR data, the shortest detectable wavelength in azimuth direction was no less than 200 m [Kerbaol *et al.*, 1998]. The *cut-off* effect increases for SAR satellites orbiting at higher altitudes. More precisely increases with the ratio R/V , where R is the sensor altitude and V its velocity [Kerbaol *et al.*, 1998].

The *cut-off* effect, is also correlated to increasing wave height and wind speed [Beal *et al.*, 1983], [Vachon *et al.*, 1994], and to waves orbital motions [Vachon *et al.*, 1994], [Kerbaol *et al.*, 1998].

To quantify the *cut-off* effect, the azimuth *cut-off* wavelength derived from the spectrum of the SAR data can be used. More importantly, the azimuth *cut-off* wavelength is defined as the minimum detectable ocean wave wavelength propagating in azimuth direction (satellite path) by the SAR system [Beal *et al.*, 1983]. This topic has been extensively discussed for C-band SAR (e.g. [Kerbaol *et al.*, 1998], [Vachon *et al.*, 1997] and [Hasselmann *et al.*, 1996]). It is important to mention that this limitation is just for the azimuth component of imaged ocean waves. Ocean waves propagating in range direction (perpendicular to satellite path) are observed and measured theoretically up to the resolution of the pixel (2 m in the case of TS-X/TD.-X).

Several methods are available to derive the azimuth *cut-off* wavelength empirically (e.g. [Kerbaol et al., 1998], [Vachon et al., 1997] and [Hasselmann et al., 1996]). A two parameter fit model based on both H_s and wind speed U is defined by [Vachon et al., 1994] as follows:

$$\lambda_{cut} = \left(\frac{R}{V}\right) \sqrt{a_1 H_s + a_2 U^2} \quad (7.19)$$

Where R is the platform (sensor) altitude, V its velocity, and a_1 and a_2 are fitting coefficients. For the case of TS-X/TD-X $R = 513$ km and $V = 7.1$ km/s. [Vachon et al., 1994] pointed out that no obvious outliers were present when comparing the derived azimuth *cut-off* wavelength with this model. This strongly suggests that after, satellites altitude, H_s and wind speed are the most important factors to influence the *cut-off* effect on SAR data.

However TS-X/TD-X data is taken at different incidence angles and this formula does not include the dependence of incidence angle. In the next subsections the method used in this thesis to derive the azimuth *cut-off* wavelength from the TS-X/TD-X data is described. The dependency of this parameter with the underlying meteo-marine conditions and the incidence angle of the imaged sea surface are also assessed.

7. 5 Azimuth *cut-off* effect on TS-X/TD-X data

As described previously, the *cut-off* effect can be observed in the derived 2D spectrum from SAR data, as a band of higher spectral values in the range direction of the image spectrum in relation to the lower background spectral values (figure 7.9). In the derived 2D spectrum there is a gradient of higher against low background of spectral values. The border line between high spectral values and the low background values parallel to the range axis has azimuth *cut-off* wavelength coordinates.

One method to easily calculate the azimuth *cut-off* wavelength is to check for the highest spectral gradient in the 2D spectrum. However this line is not completely straight, mainly due to the imaged wave systems which influence behavior of this line (figure 7.10). The interference (red line in figure 7.10) caused by the presence of the wave spectral peak(s) near the azimuth *cut-off* wavelength line (yellow line in figure 7.10) is quite visible. Therefore to estimate the path of this line (azimuth *cut-off* wavelength), the 2D spectrum is divided into azimuth bands, with different range coordinates. For each band the azimuth coordinate of the bin with high spectral gradient is determined. The azimuth *cut-off* wavelength of the 2D

spectrum will be the azimuth coordinate, which in general terms, is the average of all the coordinates determined for each of the bins. More precisely the average of the coordinates estimated previously is calculated. After discarding the coordinates values beyond the limit of 0.7 times the standard deviation (threshold set by analysis of the 2D spectrum), a new average of the remaining coordinates is calculated. The resulting value is the estimated azimuth *cut-off* wavelength.

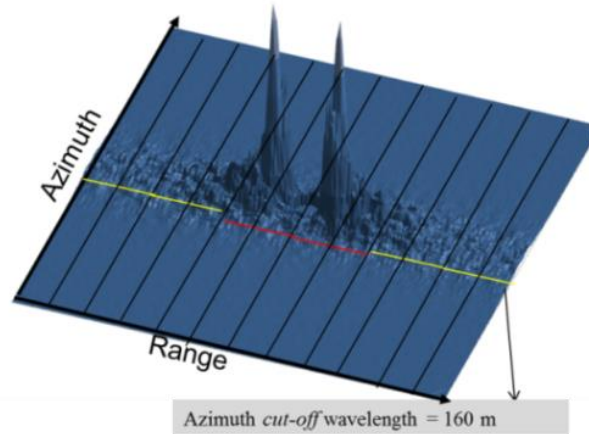


Figure 7.10: 3D view of the 2D spectrum derived from TS-X data. The yellow lines correspond approximately to the wavelengths where the gradient between consecutive azimuth bins is higher. The azimuth wavelength of the line is the estimated azimuth *cut-off* wavelength. The red line indicates that the line is affected by the presence of the wave peak, which moves the prediction line away from the center range axis.

7.6 Dependency of azimuth *cut-off* with significant wave height and sea surface wind speed

As stated previously, the *cut-off* effect on the SAR data increases with increasing H_s and wind speed. In this section the analysis of the dependency of the azimuth *cut-off* wavelength with H_s and wind speed is given. The azimuth *cut-off* wavelength is analysed in TS-X/TD-X StripMap data acquired over *in-situ* wave measurements.

A 3D representation of two examples of 2D spectrums derived from TS-X/TD-X VV polarized StripMap data are shown in figure 7.11. Case A shows the 2D spectrum derived from TS-X data acquired over high sea state conditions with an *in-situ* H_s of 5.9 m. The measured *in-situ* wind speed is about 5.4 m/s. It is observed that the 2D spectrum appears compressed along

the middle range axis. The gradient between higher spectral values against very low background spectral values is also visible.

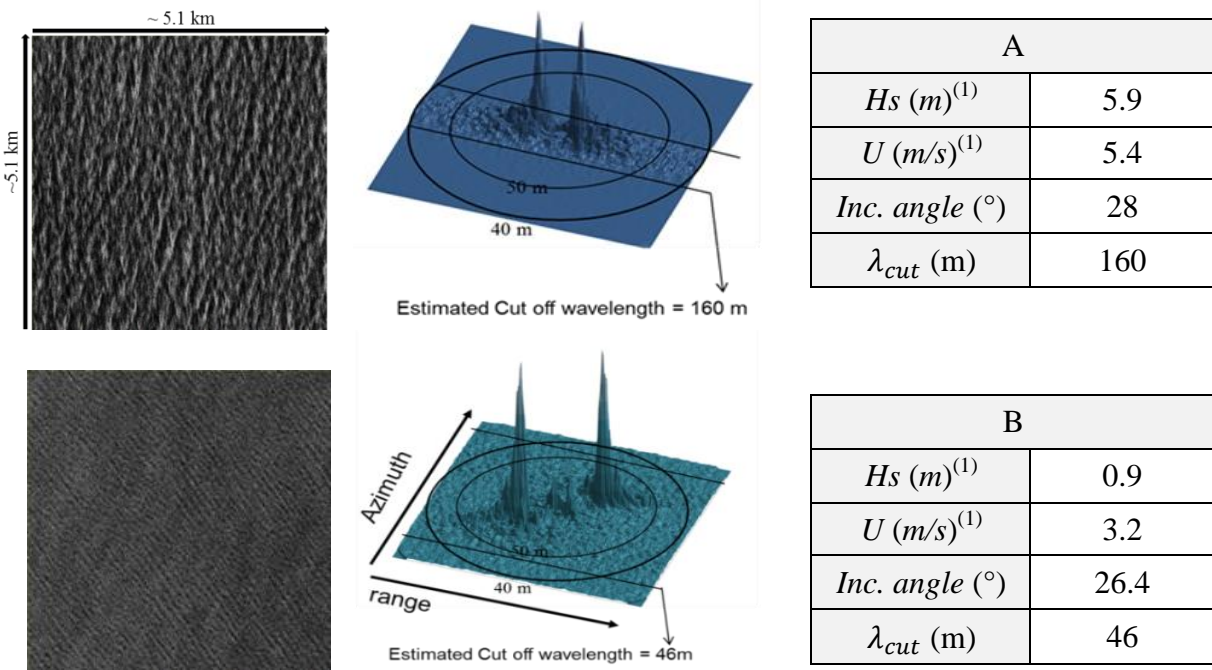


Figure 7.11: The 3D visualization of the 2D spectrum derived from TS-X data. The case A is taken over high sea state. *In-situ* information: H_s : 5.9 m, wind speed: 5.4 m/s. The derived azimuth *cut-off* wavelength is 160m. The case B is taken over low sea state conditions. *In-situ* information: H_s : 0.9 m, wind speed: 3.2 m/s. The derived azimuth *cut-off* wavelength is 46 m.

The derived azimuth *cut-off* wavelength for this case is of 160 m. The high value of the wavelength is to be expected, the higher the waves are and the stronger wind speed, the stronger the *cut-off* effect will be, and therefore the longer will be the *cut-off* wavelength.

Case B shows the 2D spectrum derived from TS-X data acquired over low sea state conditions with an *in-situ* H_s of 0.9 m. The measured *in-situ* wind speed is about 3.2 m/s. In this case there is almost no distortion in the spectrum. However there is slight gradient in the spectral values near the boundary of the spectrum, corresponding to higher wavenumbers, shorter wavelengths.

Through analysis the azimuth *cut-off* wavelength derived using the method described before, is 46 m. The derived azimuth *cut-off* wavelength is very low, almost the same as the minimum wavelength limit (30 m) used for the Fourier analysis limits. This means that (almost) the full spectrum of ocean wavelengths is imaged. The low value of the azimuth *cut-off*

wavelength was expected, because H_s value is very low, which means less particle motion. In this case the sea surface can be imaged near to the linear domain by the SAR.

In order to evaluate the dependency of the azimuth *cut-off* wavelength with the underlying meteo-marine conditions, this parameter is derived for a set of 200 TS-X/TD-X StripMap VV polarized data images collocated with *in-situ* wave measurements.

The TS-X/TD-X data considered for analysis was classified as homogeneous by the homogeneity test described in the previous section. The results of the analysis are given in figure 7.12. The azimuth *cut-off* wavelength resulted in a high correlation with significant wave height, with an R of 0.80, and with wind speed a correlation R of 0.58. The shortest azimuth *cut-off* wavelength derived from this data-set is 46 m, which corresponds to the case of a TS-X acquisition taken with a incidence angle of 26° over sea state conditions with H_s of 0.9 m and wind speed of 3.2 m/s.

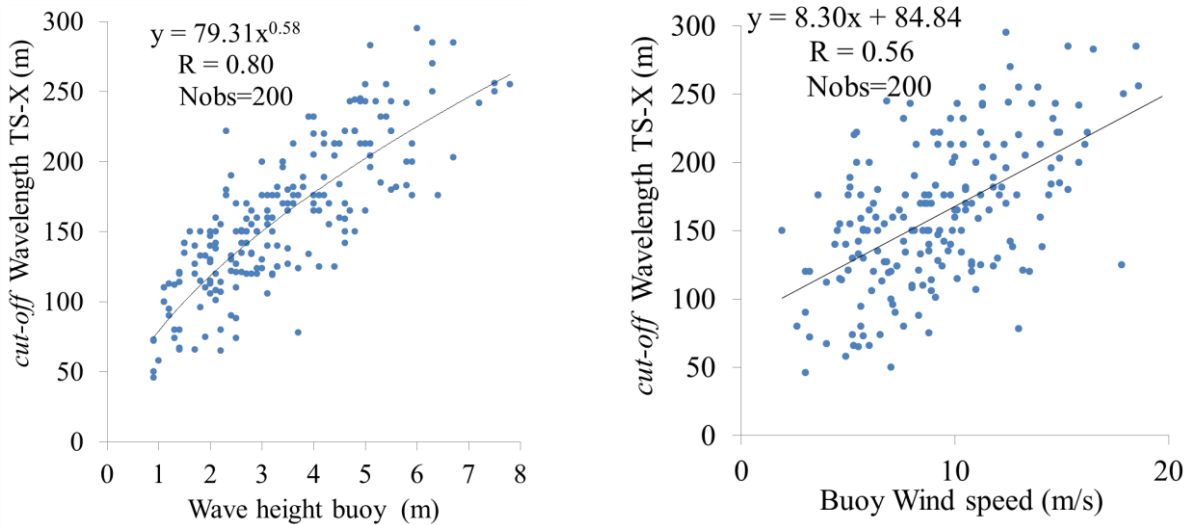


Figure 7.12: Azimuth *cut-off* wavelength derived from TS-X/TD-X data and the corresponding *in-situ* values of H_s given by the buoy (left) and wind speed (right) given by the anemometer.

In figure 7.13 the derived azimuth *cut-off* wavelength from TS-X/TD-X data, the same as in figure 7.12, is shown in red. The predicted estimation of azimuth *cut-off* wavelength obtained using (formula 7.19), assuming satellite altitude $R = 514$ km and velocity $V = 7.2$ km/s (TS-X/TD-X conditions) and using as input the buoy wind and wave height information, is plotted in blue.

The predicted estimation of azimuth *cut-off* wavelength obtained using (formula 7.19), but assuming satellite altitude $R = 800$ km and velocity $V = 7$ km/s and using as input the buoy wind and wave height information, is plotted in violet.

The estimation of the azimuth *cut-off* wavelength using the fitted correlation function given in (figure 7.12 left), using buoy wave height as input, is plotted in green. The bias between the values obtained by this formula and the values measured from the TS-X/TD-X data (red) can show the influence of the wind speed influence in the cut-off wavelength.

The estimation of the azimuth *cut-off* wavelength using (formula 7.19) with $R=514$ km shows an estimation slightly overestimated to the one derived directly from the data. Reasons for that can be several; difference in the type of data analysed TS-X/TD-X vs ENVISAT/ERS C-band, difference in the measuring method used for the cut-off wavelength estimation, higher influence of wind in the azimuth cut-off wavelength for X-band SAR data, and measurement errors.

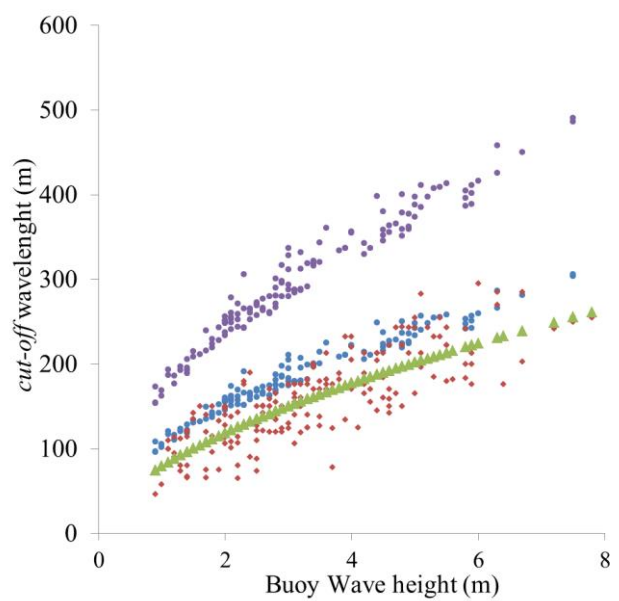


Figure 7.13: Derived *cut-off* wavelength from TS-X/TD-X data (red) and the predicted azimuth *cut-off* wavelength given by the empirical (formula 7.19) with $R = 514$ km, and $V = 7.2$ km/s with *in-situ* wave height and wind speed as input (blue) the same formula but assuming $R = 800$ km and $V = 7$ km/s, the case of ENVISAT and ERS satellites (violet) and the predicted azimuth *cut-off* wavelength assuming the relationship found in figure 7.12 left, using *in-situ* wave height as input (green).

In a further step, the azimuth *cut-off* wavelength was analysed regarding the different sea state climates, classified as *wind sea*, *swell*, and *old wind sea*. According to the classification method introduced by [Hasselmann *et al.*, 1996], the sea surface sea state conditions imaged by the TS-X/TD-X are classified as *wind sea*, *old wind sea* or *swell*.

The parameter $a_{wind} = \frac{c_{phase}}{u_{10}}$ is used to distinguish between the various sea states climates as follows:

$$a_{wind} \leq 1.3 \Rightarrow \textit{wind sea} \quad (7.20)$$

$$1.3 < a_{wind} < 2.0 \Rightarrow \textit{old wind sea} \quad (7.21)$$

$$a_{wind} \geq 2.0 \Rightarrow \textit{swell}. \quad (7.22)$$

Where U_{10} is the sea surface wind speed, which can be obtained by the XMOD algorithm, and c_{phase} is the ocean waves phase defined as follows:

$$c_{phase} = \sqrt{\frac{g \cdot \lambda_p}{2\pi}} \quad (7.23)$$

Where λ_p the peak wavelength and g is the earth's gravity. From the 200 TS-XTD-X observations analyzed, 35 are classified as *wind sea* and 35 as *swell*. The remaining observations are classified as *old wind sea*. Figure 7.14 shows the results for the derived azimuth *cut-off* wavelength values for sea state conditions classified as *wind sea* or *swell*. The correlation of the derived azimuth *cut-off* wavelength for *wind sea* cases is about 80%, corresponding to 35 observations, and it is of 74 % for the *swell* cases. It can be seen in figure.7.14 that the derived azimuth *cut-off* wavelength values are higher for *wind sea*, and lower for *swell*, when assuming the same wave height. The shortest azimuth *cut-off* wavelength derived is 46 m for a case of *swell* conditions. The H_s measured by the buoy for that case is 0.9 m. The shortest derived azimuth *cut-off* wavelength for cases considered *wind sea* is of 93 m, corresponding to approximately the same value of significant wave height (1.1m). These results were also predictable, as *wind sea* waves are generated locally by the wind, which means more contribution to the increase of the *cut-off* effect.

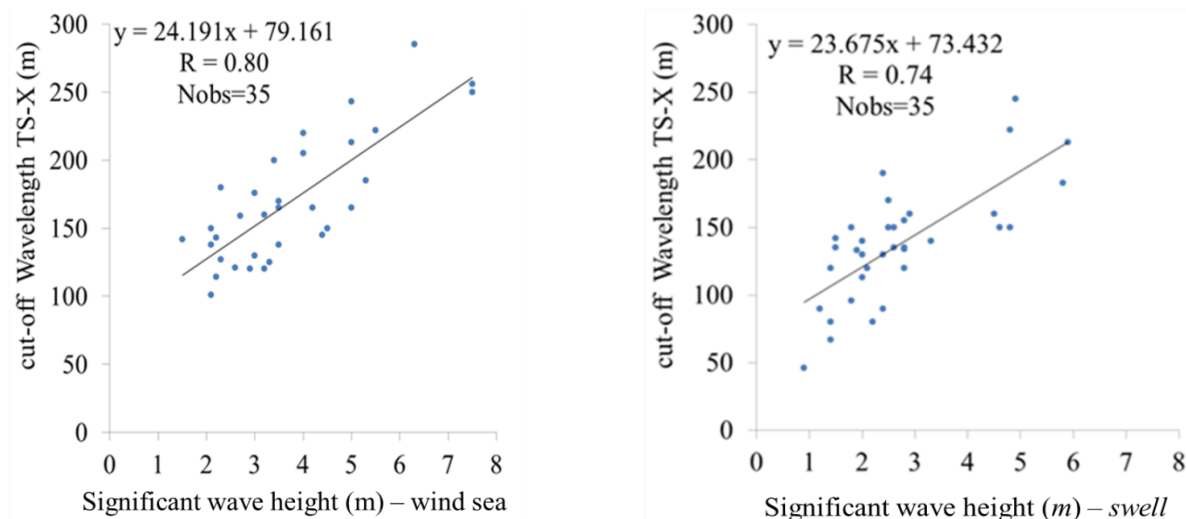


Figure 7.14: Azimuth *cut-off* wavelength for data from TS-X/TD-X acquisitions over sea states classified as *wind sea* by the parameter a_{wind} (left). Azimuth *cut-off* wavelength from TD-X/TS-X acquisitions taken under sea state classified as *swell* by the parameter a_{wind} .

7.7 Dependency of azimuth *cut-off* wavelength with incidence angle

TS-X/TD-X data is acquired with different incidence angles. Consequently for each acquisition the sea surface is imaged at different distances from the SAR. Additionally the geometry of the imaging process is also different. It is to be expected that wave fields imaged by the TS-X/TD-X with increasing incidence angles will have less quality. This is not only due to increasing distance but also due to the different imaging geometry, where shadowing of smaller wavelength ocean waves will occur for higher incidence angles.

Therefore an analysis of the azimuth *cut-off* wavelength regarding the incidence angle of the acquisitions seems necessary. The derived azimuth *cut-off* wavelength for the TS-X/TD-X acquisitions according to the incidence angle is shown in figure 7.15. The steps of the incidence angles (of about 2° to 2.5°) for *cut-off* wavelength seen in figure 7.15 are related to the fact that the center incidence angle of the acquisition, depends of the inclination of the beam in relation to the planet's surface. The SAR antenna rotates in order to obtain different swaths on the planet surface from the same orbit. The centre incidence angle at each swath acquisition is separated by an incidence angle of approximately 2° to 2.5° .

Figure 7.15 shows that for TS-X/TD-X data acquired at small incidence angles (up to $\sim 30^\circ$), shorter azimuth *cut-off* wavelengths are derived. For incidence angles over approximately 38° , azimuth *cut-off* wavelength below 100 are inexistent and for incidence angles of approximately 45° the lowest azimuth *cut-off* wavelength is approximately 180 m. The shortest possible azimuth *cut-off* wavelength for any wave conditions increases rapidly for

TS-X/TD-X acquisitions taken with incidence angles above 38°. At acquisitions taken at 40° incidence angle the shortest azimuth *cut-off* wavelength derived is 125m. For acquisitions taken at 45° incidence angle, the shortest derived azimuth *cut-off* wavelength is 193 m. In figure 7.16 the distribution of the azimuth *cut-off* wavelength against wave height is given. The distribution is represented in colours which identify the different range of incidence angles of the acquisitions. This distribution shows the dependency on wave height and incidence angle.

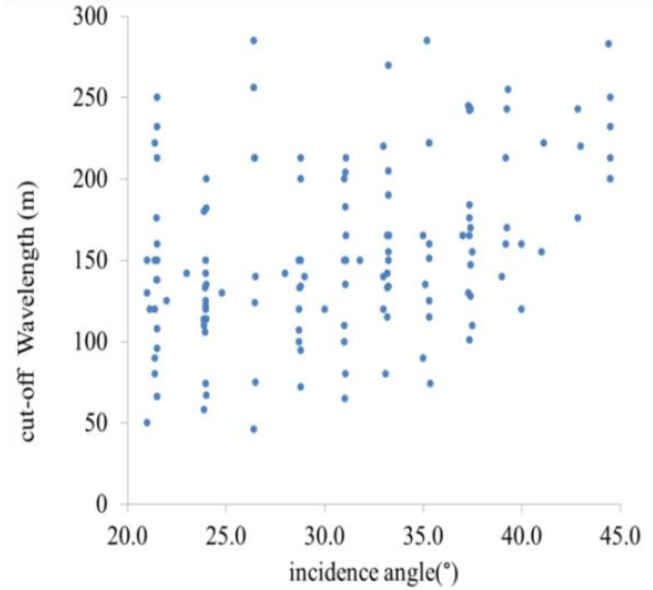


Figure 7.15: Azimuth *cut-off* wavelength derived from TD-X/TS-X data-set according to the incidence angle of the acquisition.

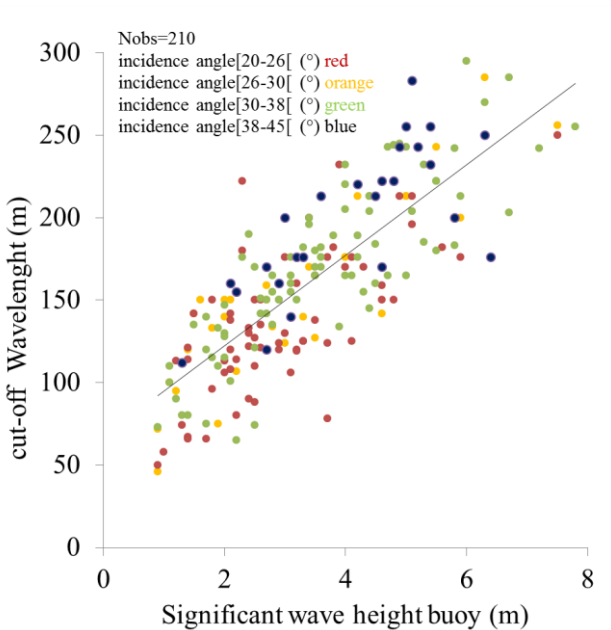


Figure 7.16: Azimuth *cut-off* wavelength derived from TS-X/TD-X collocated data-set with *in-situ* wave measurements against H_s measured buoy.

Chapter 8

XWAVE: An empirical algorithm to estimate significant wave height from TerraSAR-X/TanDem-X synthetic aperture radar data

This chapter describes XWAVE, the new empirical algorithm to derive H_s from TS-X/TD-X data, which was developed for the aim of this thesis. The chapter starts by explaining the idea behind the development of the algorithm. After that the various factors taken into consideration in the algorithm are described and discussed.

8.1 Background

An algorithm based on empirical approach to obtain H_s from X-band TS-X/TD-X SAR data is the aim of this thesis. The idea is not to simulate the sea surface or correct the spectrum obtain from the SAR data, as other algorithms developed, but to obtain only the information in the form of integrated sea state parameters; significant wave height, peak period and direction.

The empirical approach developed previously for C-band data, named CWAVE (Chapter 4), able to give an estimation of significant wave height, is based on empirical functions with parameters which are fitted with a large number of data samples (in the order of tens of thousands). The large number of data was fundamental for the tuning procedure algorithm, to obtain a good performance.

The algorithm was able to provide an estimation of significant wave height from SAR data, although the SAR data limitations. This was possible because not all ocean wave information is lost during the imaging process of ocean waves, and information as significant wave height, peak period and direction can be retrieved by proper algorithms.

There are several differences between the initial conditions for C-band and X-band SAR. First, the amount of available TS-X/TD-X data-set is about 100 times smaller than the amount of data which was used to tune the CWAVE algorithm. Besides, the previous SAR data was acquired over the ocean automatically by the ERS and ENVISAT continuously, each 100 km, leading to total data-set in the order of several millions of data images. Second, the TS-X/TD-X data is bigger in digital size than the previous SAR data by a factor of 200 (~10 MB vs ~2.2

GB). This makes it computationally very demanding. Third, there is also an organization problem, as the C-band data was already available when the CWAVE algorithm started to be developed. For the case of TS-X/TD-X data, it was acquired during the development phase. And these data acquisitions needed to be carefully planned due to operational reasons. Forth, and most important, is the fact that prior to the C-band algorithm development, extensive sensitive studies were already performed on C-band data acquired over ocean. These studies provided important a priori knowledge regarding C-band data characteristics and performance.

Regarding the TS-X/TD-X data the situation was the following: TS-X/TD-X data is not acquired automatically and the satellite needs to be previously commanded to acquire data at a specific location, with careful planning. No sensitive studies regarding X-band SAR TS-X/TD-X data acquired over sea surface were done, leading to all sort of unanswered questions which need to be answered first.

From the knowledge obtained from C-band SAR data and from the analysis of TS-X/TD-X data acquired over ocean, part of this information (Chapter 6 and 7) lead to the development of the algorithm described in this thesis. A completely new algorithm, needed to be developed for the case of X-band TS-X/TD-X SAR data, due to the difference in the number of data samples and characteristics between the SAR data (different band, different type of data, variable incidence angle, closer to linear domain, etc.). The algorithm described in this thesis, is an improved version of the algorithm described in [Bruck *et al.*, 2010] and [Lehner *et al.*, 2012].

However a very important advantage comes with the new TS-X/TD-X data. It has higher resolution and lower orbit. This allows the analysis of ocean waves with improved accuracy. The minimum observable ocean wavelength by the TS-X/TD-X is much smaller due to its lower orbit; being possible to observe shorter wavelength ocean waves, and image ocean closer to the linear domain and therefore with less distortion (Chapter 7).

Therefore, if closer to linear domain the previous SAR data, the first approach to be attempted to obtain an estimation of H_s or the total energy, is that the integral of the derived spectrum from the TS-X/TD-X data can be related to the spectrum derived from the sea surface elevation time series of a measurement device (buoy). The estimation of the integral of the spectrum derived from TS-X/TD-X data is given by the parameter E .

If the SAR imaging of the sea surface would be completely linear, this step would be practically enough. A similar approach, but using SNR instead of the parameter E , is used for example in standard radar data by ground marine radars, where the imaging is close to linear. The sea surface is a few meters to a few kilometers distance to the marine radar [Nieto Borges, *et al.*, 2008]

The parameter E is than the first parameter taken into account into the new algorithm and is defined as:

$$E = \int_0^{2\pi} \int_{30}^{600} I(k, \theta) dk d\theta \quad (8.1)$$

The Fourier algorithm used is the one described in Chapter 7. The integration limits of the derived spectrum are set to be $k_{max} = 0.21$ and $k_{min} = 0.01$ which corresponds to wavelength limits in deep water of $L_{min} = 30\text{m}$ and $L_{max} = 600\text{m}$. These limits were defined as they are the most important range of wavelengths for our study. Besides, the higher limit of 600 m also avoids most of the influence of wind streaks signatures on the SAR data.

8.2 Data selection

For the development and validation of the empirical algorithm XWAVE, the TS-X/TD-X data selected is the VV polarized StripMap data, acquired over *in-situ* wave measurements (buoys). The *in-situ* data (ocean waves and wind information) chosen to tune and validate the algorithm, as mentioned before, is obtained from the NOAA buoy network. The data is already described in detail in Chapter 6.

The TS-XTD-X data polarization was chosen to be VV, not only because previous studies showed that SAR VV polarization to be more suitable for ocean waves analysis e.g. [Alpers *et al.*, 1981], but also because analysis of TS-X/TD-X data showed that SAR VV polarization data is preferable. This can be seen for example in one sensitive study of the analysis of dual polarized TS-X/TD-X data (figure 8.1). It is observed for HH polarized data, that the fitting curve of the parameter E with *in-situ* significant wave height measurements has a higher slope. However, and important, is the fact that the correlation of the parameter E with *in-situ* significant wave height measurements is higher for VV polarized data.

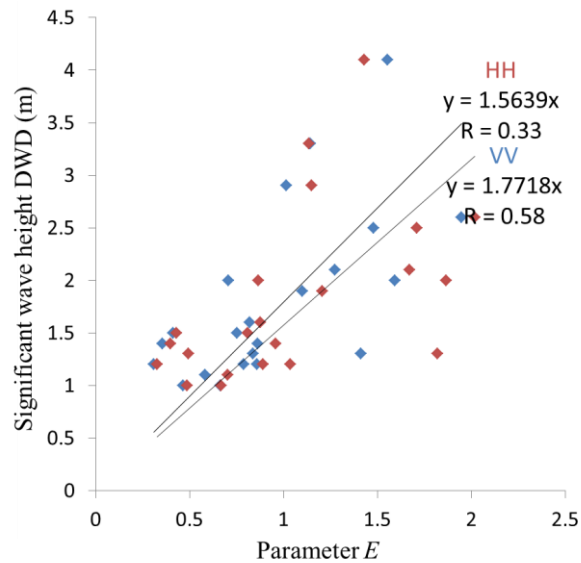


Figure 8.1: H_s given by the wave model WAM running at DWD, against the parameter E derived from HH and VV dual polarized data from TS-X/TD-X StripMap and SpotLight acquisitions taken over the Ekofisk oil platform in the second semester of the year 2009. Only observations for wave height above 0.9 m and wind speed above 3.5 m/s are considered.

The TS-XTTD-X data was pre-ordered over selected buoy locations. These locations were previously chosen according to these criteria:

- The buoys need to be in deep water, open ocean, away from river estuaries (river plumes can affect the ocean sea surface over several kilometres).
- The buoys selected were also not taken in locations in which is known that algae blooms are highly predominant, or near oil spill predominant sites, as the Gulf of Mexico.

Over 400 TS-X/TD-X VV polarized StripMap images from buoys were acquired considering these conditions. However, only 200 data pairs are used for the tuning/validation of the algorithm. Those measurements were not used due to the following reasons:

- The TS-X/TD-X data did not pass the quality/homogeneity described in Chapter 7 (about 35%).

- There are no *in-situ* wave measurements from the buoy available at the time of the TS-X/TD-X acquisition. This situation can happen when an error in the transmitter occurs or the buoy is absent due to maintenance, was stolen, or is adrift.
- TS-X/TD-X acquisitions over high waves situations were of particularly interest for the aim of this work, as high wave height measurements are very valuable for a better tuning of the algorithm, unfortunately about half of cases taken under very high sea state conditions during storms, lead to the buoy to go adrift or stop transmitting.
- Only TS-X/TD-X acquisitions with incidence angles between 20° and 37° were used for the tuning of the algorithm. This because, as it was mentioned in Chapter 7, ocean waves imaging performance decreases rapidly for incidence angles above 37° .
- The measured wind speed by the anemometer at the buoy location must be higher than 3.2 m/s. The reason for this criterion is that we need a minimum wind speed value over the surface imaged by the SAR, in order to have a minimum backscatter power signal that provides readable, reliable data.

Additionally conditions of the TS-X/TD-X tuning/validation data set, which were not imposed and occurred naturally worth mention, are:

- The maximum wind speed measured is 18.7 m/s.
- The maximum and minimum measured wave heights (by the buoy) are 7.7 m and 0.9 m respectively.

The tuning and the validation data-set have similar sea state distribution. The significant wave height distribution of the tuning data-set has a Rayleigh type distribution with average wave heights of about 3.6 m and a standard deviation of about 2.1 m (figure 8.2).

Other sea state parameters distributions of tuning data-set, can be seen in figure 8.3 and figure 8.4. Recalling Chapter 7, we also know that the tuning data-set has about 18% *swell* and ~18% *wind sea* conditions and the remaining 60% are old wind sea (mixed) sea state conditions.

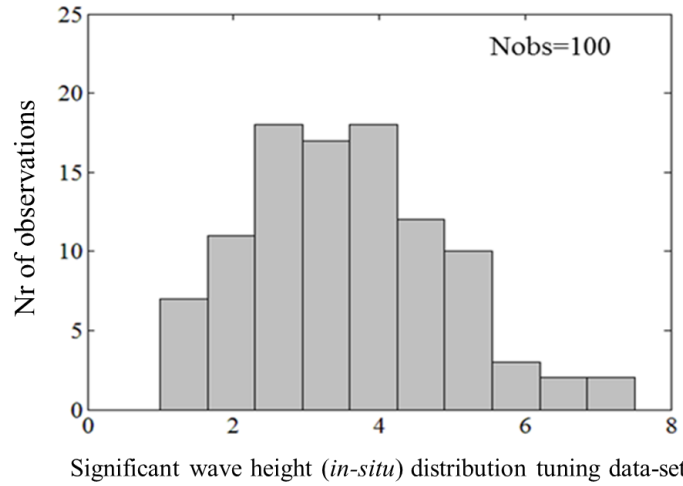


Figure 8.2: Histogram showing the distribution of measured H_s by the buoy for the TS-X/TD-X tuning data-set.

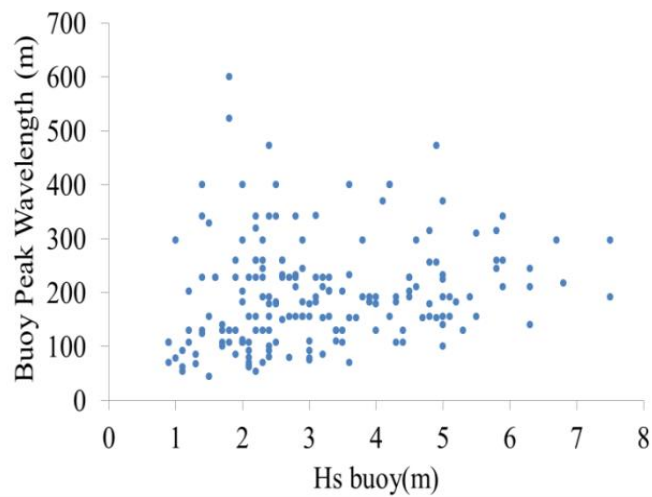


Figure 8.3: Distribution of H_s against the peak wavelength derived from the peak frequency from buoy data using the dispersion relationship, assuming deep water (formula 2.19) in the tuning data-set.

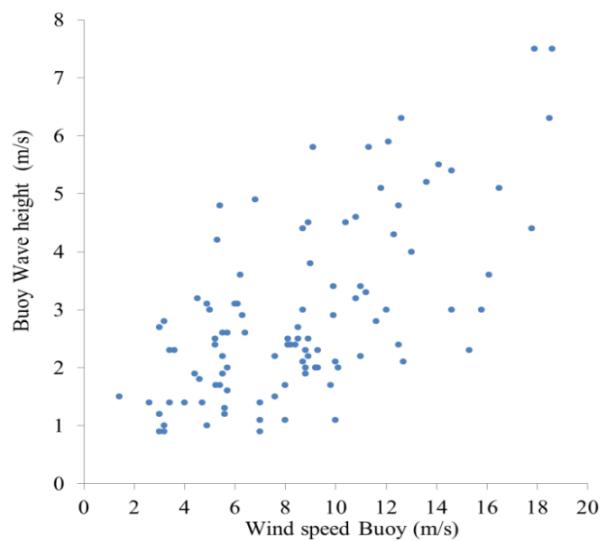


Figure 8.4: Distribution of the measured *in-situ* wind with measured *in-situ* H_s in the tuning data-set.

8.3 Algorithm discussion

The XWAVE algorithm is a two-step function with (formula 8.2) and (formula 8.3), with a simple buffer region between the two (formula 8.3). The different functions are used according to the range of H_s of the wave field acquired in the TS-X/TD-X data. In order to estimate the range of H_s of the imaged ocean area in advance, a first guess estimation of H_s is obtained by the relationship between the *cut-off* wavelength and the wave height (figure 7.12). As discussed in Chapter 7, the *cut-off* wavelength is related to wave height and wind speed. From this correlation it is possible to obtain a rough estimation of H_s . This in turn enables to predict if the H_s of the imaged sea state is low ($\sim < 3$ m) or high ($> \sim 4$ m).

For an imaged sea surface estimated to have an H_s below 3.5 m, roughly estimated by the correlation to the *cut-off* wavelength, the following formula is used to obtain an optimum estimation of H_s :

$$H_{s1} = a_1 \cdot \sqrt{E \cdot \tan\theta_i} + v \cdot a_2 \cdot U_{10} x_{mod} + a_3 \quad (8.2)$$

For an imaged sea surface estimated to have an H_s above 4 m, roughly estimated by the correlation to the *cut-off* wavelength, the following function is used to obtain an optimum estimation of H_s :

$$H_{s2} = a_4 \cdot \sqrt{E \cdot \tan\theta_i} + v \cdot a_5 \cdot U_{10} x_{mod} + a_6 \cdot \cos(\alpha) + a_7. \quad (8.3)$$

The coefficients a_1 to a_7 are obtained by linear fitting with *in-situ* wave measurements. v is an unitary coefficient with unit [s] to correct units, U_{10} is the sea surface wind speed at 10 m height, which is obtained from SAR data by applying the XMOD algorithm. α is the peak wave direction related to the azimuth direction ($0^\circ \leq \alpha \leq 90^\circ$) (in the case of two wave peaks the direction is averaged if at the second peak has at least half the energy, of the first one). For H_s between 3.5 m and 4.5 m (roughly estimated by the correlation to the azimuth *cut-off* wavelength), the optimum H_s is given as the average of the values given by both the previous formulas:

$$H_{s3} = (H_{s1} + H_{s2})/2. \quad (8.4)$$

For the case of two wave systems, the second system is only considered, if the normalized energy of the second peak has at least half energy of the main peak.

To summarize the XWAVE algorithm is a seven parameter geophysical two model function based on the analysis of image spectra. It uses coefficients a_1 to a_7 which are determined by fitting using the least squares method, with collocated H_s from *in-situ* buoy wave measurements and the TS-X/TD-X derived parameters E , α , θ and sea surface wind speed U_{10} . The algorithm fitting method, is a linear fitting that uses the least squares method, the parameter E with *in-situ* wave measurements, according to the following:

$$H_{sar} = a\sqrt{E} + b. \quad (8.5)$$

The standard method of least squares (OLS) is conceptually simple and computationally straightforward. The OLS estimates are commonly used to analyse both experimental and observational data. The linear approach for tuning X-band radar data images was successfully applied by [Borges *et al.*, 2004], where in their study, the signal to noise ratio (SNR) of X-band radar images, was linearly fitted with wave height measurements.

The tuning procedure of TS-X/TD-X data with *in-situ* wave measurements is processed as follows; eight sub-scenes are extracted from the middle column of the TS-X/TD-X StripMap VV polarized image data. All the sub-scenes have the same range coordinates (and therefore same incidence angle). The size of each sub-scene is chosen to be 2048 x 2048 pixel of a previously spatial averaged by a factor of 2 (Chapter 7). This means that for StripMap data the pixel spacing is 1.25 m times 2, which results in an analysis box of 5.1 km side-size. The size of the sub-scene is sufficient to resolve longer ocean waves with wavelengths of 600m at least eight times. The sub-scenes are calibrated and the image spectrum is derived using the methodology described in Appendix A. From the average of the eight derived spectrums, the integral is calculated. The result is given as parameter E . The development of the functions and the terms which are taken into account into the algorithm are discussed in the next sections.

8.4 Dependencies taken into account in the algorithm

8.4.1 Incidence angle

The dependencies of the SAR data with the underlying sea state were pursued. Although TS-X/TD-X data is calibrated according to incidence angle (Chapter 5), dependency with the incidence is still observed as there is a decrease of the values of the parameter E with incidence angle (figure 8.5). The variation of the parameter E is better understood for imaged wave fields with a wave height of approximately 2 m, as the wave height is low enough to have less distortion when imaging of ocean waves in high sea state conditions. Imaged wave fields of wave heights of approximately 1 m, have too low distortions, almost linear, difficult for evaluating dependencies.

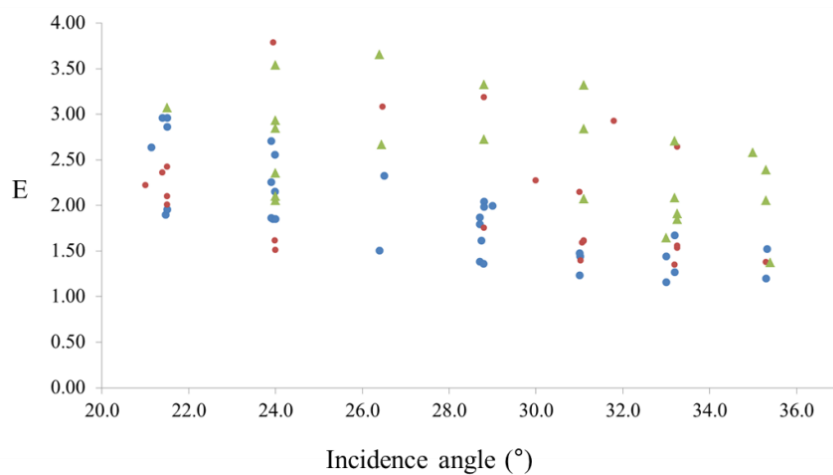


Figure 8.5: Parameter E derived from TS-X/TD-X data acquired at different incidence angles and wave heights. The colours correspond to the different wave height ranges. Blue: wave height: [1.9-2.1] m, red: wave height: [2.9-3.1] m, green: wave height: [3.9-4.1] m.

Considering the variation of the parameter E with incidence angle (figure 8.5), the dependency of the incidence angle can be approximately simplified to $\sqrt{E \cdot \tan\theta_i}$. As a first approach, wave height can be estimated from TS-X/TD-X data assuming only incidence angle dependency as follows:

$$H_s = a \cdot \sqrt{E \cdot \tan\theta_i} + b . \quad (8.6)$$

The linear fitting of (formula 8.6) with the *in-situ* significant wave height measurements is presented in figure 8.6. The linear fitting resulted in a very low correlation with $R = 0.60$ and scatter index $S_i = 0.56$. This poor result is related to another dependency taken into account in the algorithm, the sea surface wind speed, which is described next.

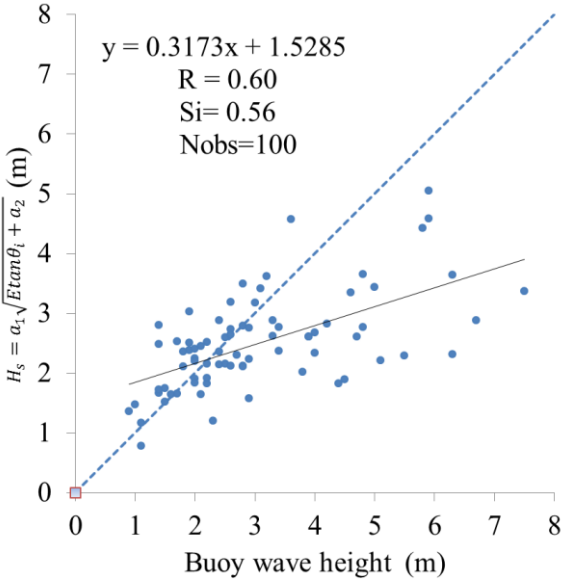


Figure 8.6: Significant wave height estimation using (8.6) with *in-situ* wave data.

8.4.2 Sea surface wind speed U_{10}

Recalling from the last section that the linear fitting of (formula 8.6) showed poor correlation and high scatter index, the bias of the measurements was found to be correlated with the sea surface wind speed (figure 8.7).

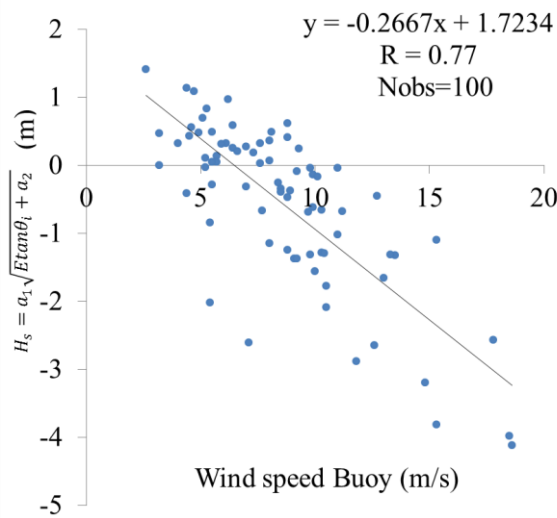


Figure 8.7: Scatterplot with the bias found on the H_s given by the buoy and values of H_s derived by using (formula 8.6).

The correlation observed on figure 8.7 is not high, because different imaged wave fields with different wave heights produce different bias. The wind information is taken into account in (formula 8.7) creating a new function, with a, b, c the fitting coefficients, defined as:

$$H_s = a \cdot \sqrt{E \cdot \tan\theta_i} + v \cdot b \cdot U_{10}xmod + c \tag{8.7}$$

The fitting results of (formula 8.7) proved to improve results (figure 8.8). This is (formula 8.2), the first function of the XWAVE algorithm, intended to be applied for TS-X/TD-X data acquired under moderate sea state conditions ($\sim < 3.5$ m).

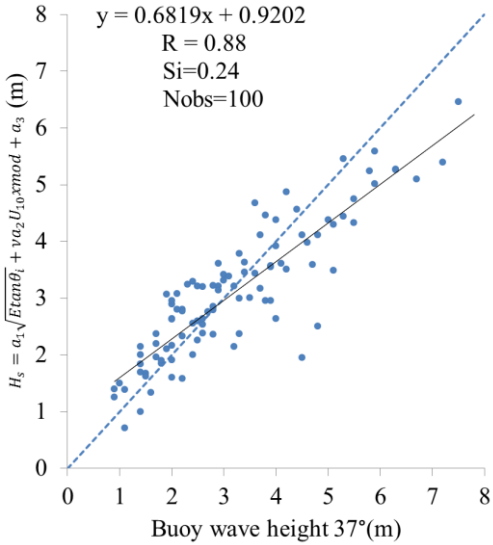


Figure 8.8: H_s derived from TS-X/TD-X data using (8.5) against *in-situ* H_s

The dependence on wind is not only due to the wind wave growth but also to the influence of the wind in the imaging mechanism of the SAR. For the same wave height or wave spectrum, the wave field will be imaged differently according to different wind speeds.

The value of $\sqrt{E \cdot \tan\theta_i}$ will tend to be higher for *swell* waves and lower for *wind sea* waves, being sensitive therefore to the sea type: *swell*, *wind sea*.

It can be concluded, that by taking wind information, correlation was improved, and achieves now a value of about 88%, but some obvious outliers are still present. Some estimations of significant wave height values using (8.13) can be much lower (more than 1 or 2 m difference) that the real wave height, is due to the strong distortion when imaging ocean waves in high sea state conditions, as referred previously. This distortion on the data is related with ocean waves propagating in the satellite path direction (azimuth direction). A method to obtain a better estimation of significant wave height of TS-X/TD-X data acquired under high sea state conditions, although the data is with high distortion is discussed in the next section.

8.4.3 Ocean wave propagation direction in relation to satellite path (azimuth)

In this section the last dependency considered in the algorithm, which is the ocean waves propagation direction in relation to the satellite path (azimuth direction) is discussed.

despite the good performance for imaging stationary targets, it has limitations on the imaging of moving targets, more precisely for targets moving azimuthally. This effect is the so called velocity bunching effect [Alpers *et al.*, 1981], [Alpers *et al.*, 1986]. The distortion caused by higher ocean waves leads to high distortion of the SAR image data (Chapter 7). To assert the dependency of the wave travel direction with respect to satellite heading in the wave height results, the bias of the estimation of wave height according to (formula 8.7) is compared to the relative wave direction to azimuth (figure 8.9). The data is shown for wave heights above 4 m, where the effect was found to exist. It is observed a high bias in significant wave height results estimated using (formula 8.7) for cases where the wave propagation direction in respect to azimuth is less than 40° (figure 8.9). The velocity bunching effect, which is the cause of the observed bias, can be related to a cosine type function [Alpers *et al.*, 1981]. The term $\cos(\alpha)$, where α is the wave field peak propagation direction in relation to azimuth, proved to be able to correct the obvious outliers in the tuning data, which indicated it is probable a suitable choice. Therefore the correction term was chosen to be $\cos(\alpha)$, and the new formula for higher wave heights is modified as follows:

$$H_s = a \cdot \sqrt{E \cdot \tan \theta_i} + v \cdot b \cdot U_{10} x_{mod} + c \cdot \cos(\alpha) + d \quad (8.8)$$

This is (function 8.3), the second function of the XWAVE algorithm. As mentioned before, the coefficients a_4 to a_5 are obtained by linear fitting with *in-situ* wave measurements and wind speed can be obtained by the XMOD algorithm.

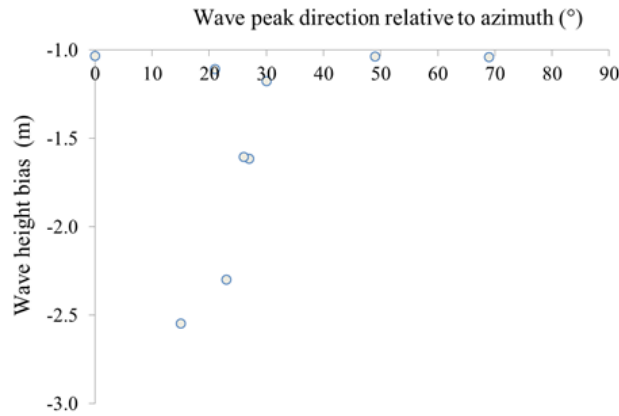


Figure 8.9: Bias of the wave height estimated by (8.5) for ocean waves higher than 4.5 m compared to wave propagation direction relative to the satellite path (azimuth direction).

8.5 Validation of the algorithm

This section presents and describes the results derived from TS-X/TD-X SAR data using the XWAVE algorithm. As for the tuning of the algorithm, the same conditions apply for the validation data. The TS-X/TD-X data must be considered homogenous presenting wind ocean waves; otherwise the results will be unpredictable. The conditions for the verification of the algorithm were also the same for the range of incidence angles, range of wind speed and wave height minimum. Validation of significant wave height derived from TS-X/TD-X against *in-situ* data show a correlation R of 0.91 and a scatter index Si of 0.21 and a bias of 0.01 m when using *in-situ* wave buoy data (figure 8.10).

The algorithm performance was accomplished when using TS-X/TD-X data acquired under specific sea state conditions and limited data-set. The sea type analyzed presents mixed conditions of *swell* and *wind sea* which are typical for open ocean waters. Conditions outside these limits might not provide the expected performance. The wave peak wavelength λ_p and direction θ_p are also compared to the *in-situ* wave measurements. For the comparison of θ_p ,

only 77 out of 100 buoys chosen for validation are directional buoys. The sea state parameters derived from the TS-X/TD-X data are also compared with the results from the WAM wave model running at DWD. Figure 8.11 shows the results from the wave numerical model running at DWD compared to *in-situ* wave measurements. It is visible an underestimation of the values of H_s calculated by the wave model and the *in-situ* wave measurements, which were mostly *swell* condition cases.

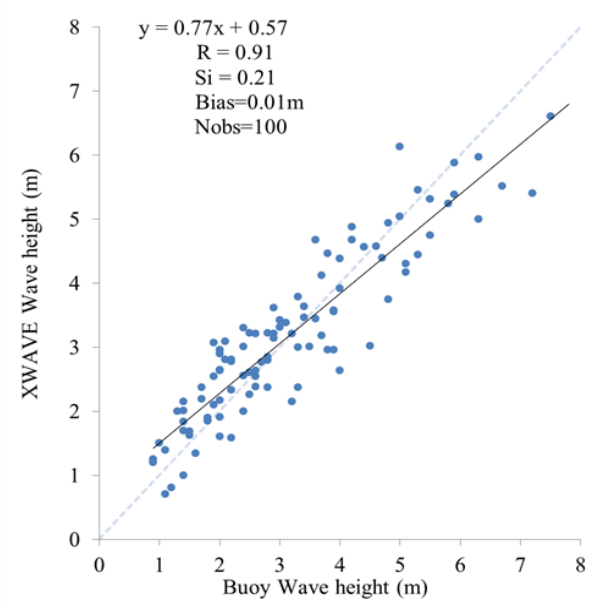


Figure 8.10: Validation of H_s derived from TS-X/TD-X data using the developed empirical algorithm XWAVE against *in-situ* wave measurements. The data used for verification of the algorithm corresponds to 100 homogenous TS-X/ TD-X VV polarized StripMap data acquired with incidence angles between 20° and 37° collocated with buoys with water depth higher than 100 m.

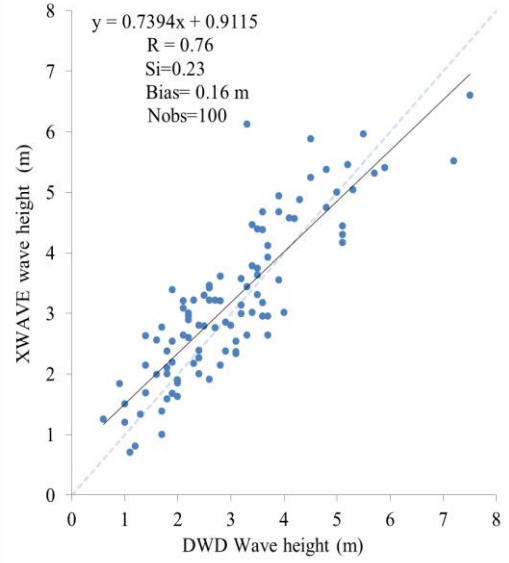


Figure 8.11: Comparison of values of H_s given by the wave model WAM running at the DWD and the values H_s derived from TS-X/TD-X data.

Chapter 9

Case studies

In this chapter, four case studies of TS-X/TD-X VV polarized StripMap data acquired over *in-situ* wave measurements are presented. The common sea state integrated parameters, significant wave height, peak period and direction as are compared to *in-situ* buoy wave measurements and to results of the wave model WAM running at DWD. Additionally also the spectral shape from the image spectrum derived from the SAR data and the buoy wave spectrum are compared.

9.1 Case-studies over *in-situ* wave measurements

The case studies presented here, provide an insight for the wave measurements imaged by the TS-X/TD-X. The cases are taken over buoys under different sea state conditions, with multiple wave systems and with significant wave heights ranging from 2.1 m to 7.5 m.

For each case, the significant wave height, wave peak period and direction given by the buoy and wave model WAM running at the DWD and the derived from the TS-X/TD-X data are presented. Numerical wave model data is useful to assert the wave field direction, for the cases where buoys do not provide ocean wave field directional information. The wind information which is used to force the wave model is also provided for the year of 2011.

Regarding the comparison of the 1D spectrum of TS-X/TD-X and the buoy 1D spectrum, the spectrums are compared graphically, and for each case study, the derived azimuth *cut-off* frequency is also given. The buoy 1D spectrum, commonly known as wave spectrum, has units of m^2/Hz . To enable comparisons between the 1D spectrum derived from TS-X/TD-X data and the buoy spectrum, the derived spectrum needs to be converted/calibrated to the same units of the spectral values.

It was chosen to calibrate the TS-X/TD-X derived 1D spectrum energy density using the significant wave height derived by the empirical algorithm XWAVE as guideline. A short description of the method adopted is given hereafter. First, H_s is derived using the empirical XWAVE algorithm. From this result, the zero momentum is calculated as follows:

$$m_0 = \frac{H_s^2}{16}. \quad (9.1)$$

It was wrong the formula:

Then the zero momentum m_{0x} is calculated from the TS-X/TD-X spectrum by:

$$m_{0x} = \int_{f_{min}}^{f_{max}} S_x * df * f_c . \quad (9.2)$$

Where S_x is the spectrum derived from the SAR data, df is the frequency spacing and f_c is a calibration factor.

The objective is to force m_{0x} to have the same value of m_0 . A new calibrated spectrum can be obtained by multiplying the TS-X/TD-X spectrum with the factor f_c ; $S_w = S_x * f_c \cdot S_w$ the new calibrated spectrum can now be compared to the buoy wave spectrum. The spectrum is calibrated to simulate to have the same units as the real buoy spectrum. Therefore each 1D spectrum derived from TS-X/TD-X data is calibrated according the wave height given by the XWAVE and is compared in each case study to the buoy spectrum.

The case studies presented are taken under different wave climates, with the intention of showing more complex wave conditions rather than simple cases. A summary of the case studies details is given in Table 9.1. The first case study presented here, describes a spectral shape defined three wave system *swell* wave field propagating in range direction, in moderate-low sea state conditions. The second case study is a case taken in very high sea state and wind speed conditions. Very high sea state conditions and additionally high wind speed are the most difficult cases, as the ocean waves are highly distorted. The third case is a complex four wave system wave field acquired under moderate sea state conditions and high wind speed conditions. The fourth case study presents the analysis of an two wave system wave field taken under moderate low sea state conditions, average wind speed and high incidence angle. In this case, the second wave system is only identified in the derived 2D spectrum from the SAR data, as the wave systems have similar wavelengths appearing therefore as a single wave system in the 1D spectrum.

Table 9.1: Summary of the case studies

Case	Wave height (m)			Wind speed (m/s)			Incidence angle (°)			Wave systems		
]2-3[[3-4[[4-8]]3 – 8[[8 -15]	>15	[20:26[[26:33]	[34:38]	1	2	>2
I	x			x			x					x
II			x			x	x					x
III		x			x		x					x
IV	x				x				x			x

Case study I

Range travelling wave field under moderate sea state conditions. A TD-X VV polarized StripMap data image acquired over buoy 51000 (23°33'30" N 153°54'0" W) near the Hawaii Archipelago with center incidence angle 30.9°, ascending path, on November 17, 2010 at 4:14 UTC.

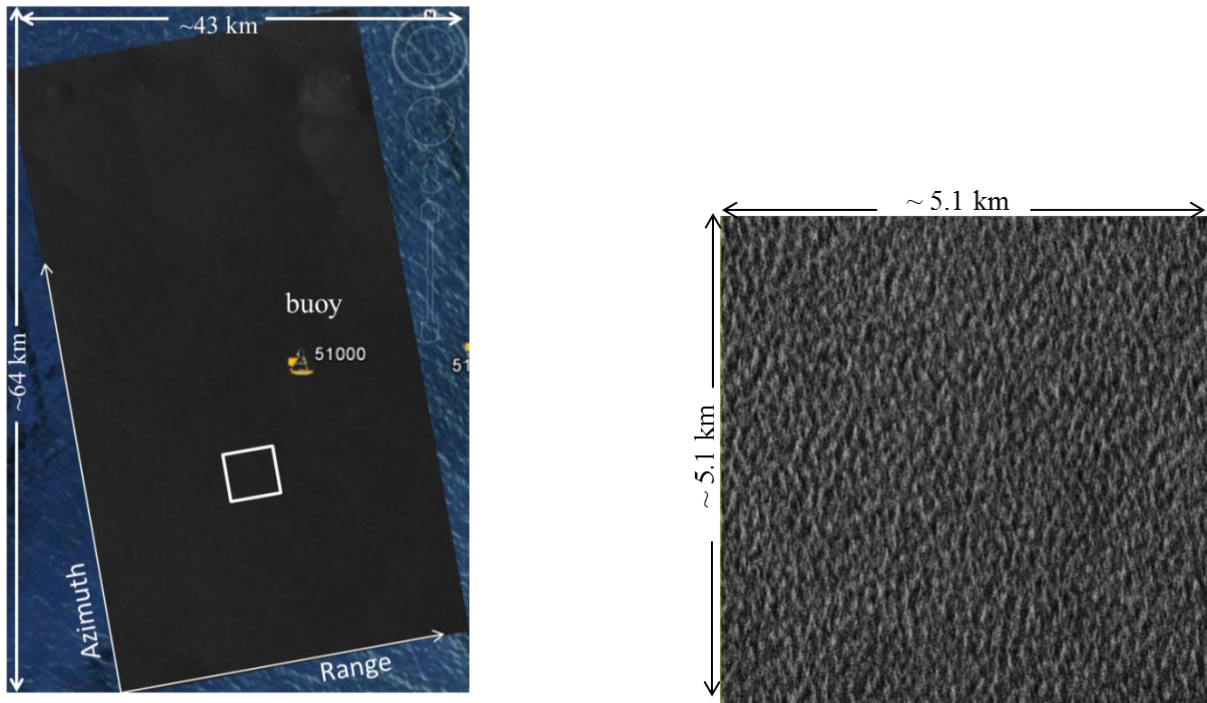


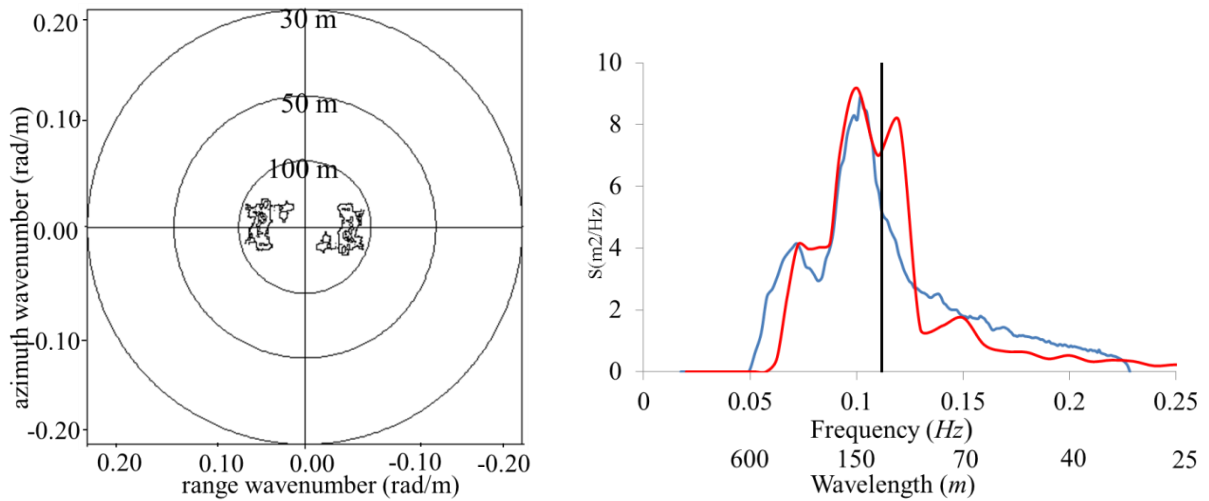
Figure 9.1: TanDem-X VV polarized StripMap image acquired on November 17, 2010 at 4:14 UTC over buoy 51000 near the Hawaii Archipelago in the Pacific Ocean (left). Sub-scene (5.1 x 5.1 km) taken from the left image (right).

The case presented here is the analysis of the TD-X VV polarized StripMap data image acquired over buoy 51000 (figure 9.1). The case is taken under moderate-rough sea state conditions, with a measured buoy wave height of 2.8 m, with equal wave height derived from the TD-X data. The H_s given by the numerical wave model WAM at DWD is 2.5 m, which is underestimated by 0.3 m. An overview of the meteo-marine conditions for the region in question is provided by the wave model WAM at DWD results shown in figure 9.3 and figure 9.4.

The comparison of the peak period shows the same value of peak period (10.0 s) for both TD-X and buoy. The wave peak direction given by the buoy is 73°, which is almost the same as the peak direction derived from TD-X data (74°). A summary of the meteo-marine parameters derived from TD-X data and *in-situ* measurements is given in Table 9.2.

The 2D spectrum derived from the TD-X data (figure 9.2) shows that most of the energy density is located between the 100 m and 300 m wavelengths band of the spectrum. Range travelling ocean waves in respect to the satellite path, which is the case here, present

optimal sea state conditions to be image by the SAR sensor, as the imaging process of these ocean waves is considered mostly linear (Chapter 7). The comparison of the 1D spectral shape (figure 9.2 right) shows a very good fit for the highest energy peak and a good fit for the high frequency peak (~ 0.09 Hz) wave peak. The derived azimuth *cut-off* wavelength is for this case 125m.



The units in the 1D spectrum should be m^2/Hz Figure 9.2: 2D spectrum derived from TS-X VV polarized StripMap image acquired on November 17, 2010 at 4:14 UTC over buoy 51000 (left). Comparison of the 1D spectrum derived from TS-X data (blue) and the buoy 1D spectrum (red). The black vertical line represents the derived *cut-off* frequency: 0.111 Hz (125 m wavelength) (right).

Table 9.2: Sea state parameters provided by buoy 51000, the wave model at DWD, and derived from the collocated TD-X image.

	$H_s(m)$	$T_p(s)$	$\lambda_p(m)$	$\theta_p(^{\circ})$	$U(m/s)$	$Udir(^{\circ})$
DWD	2.5	13.5	285	41	2.5	96
buoy	2.8	10.0	156	73	3.2	99
TS-X	2.8	10.0	156	74	3.9	-

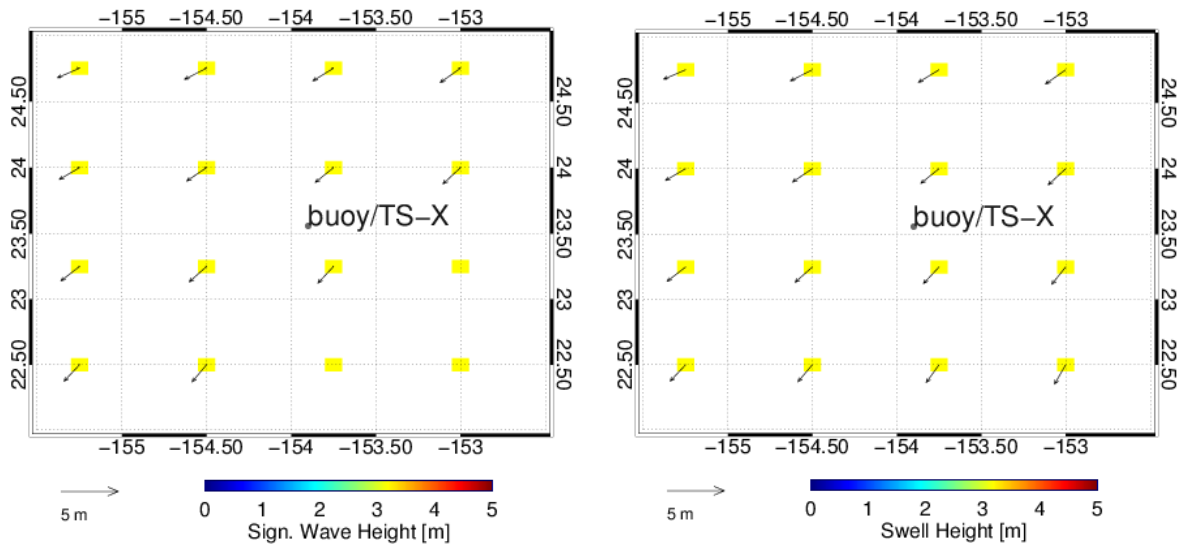


Figure 9.3: H_s wave field (left) and *swell* wave height (right) on November 17, 2010 at 4:14 UTC given by the WAM wave model running at DWD.

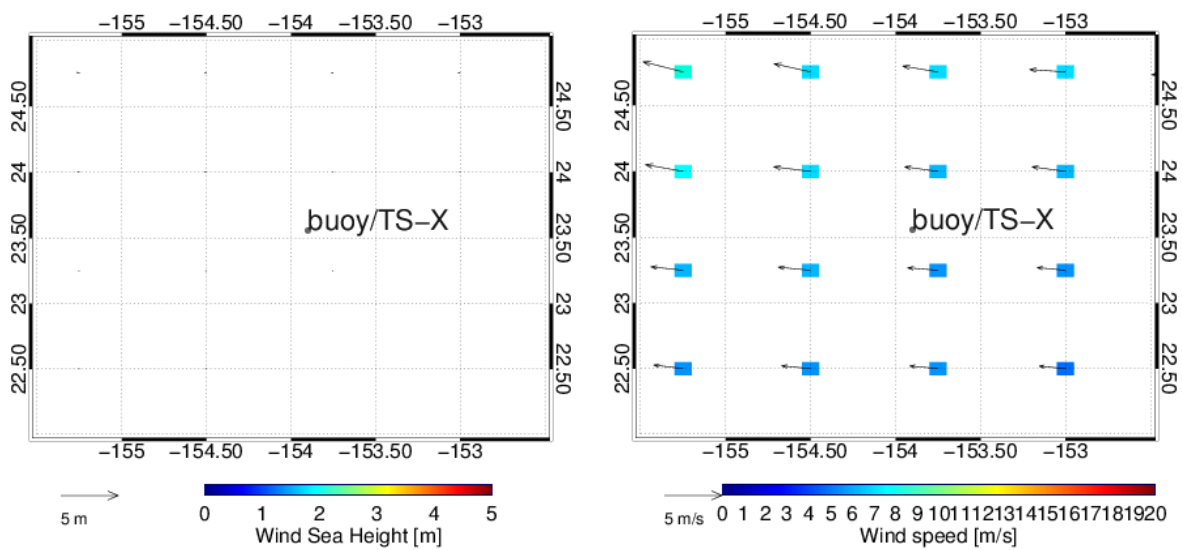


Figure 9.4: *Wind sea* height (left) and wind field (right) on November 17, 2010 at 4:14 UTC given by the WAM wave model running at DWD.

Case Study II

Near-range wave field under high sea state conditions. TD-X VV polarized StripMap data image acquired over buoy 46001 (56.304N 147.92W) with center incidence angle of 26.5° , on November 13, 2011 at 3:23 UTC.

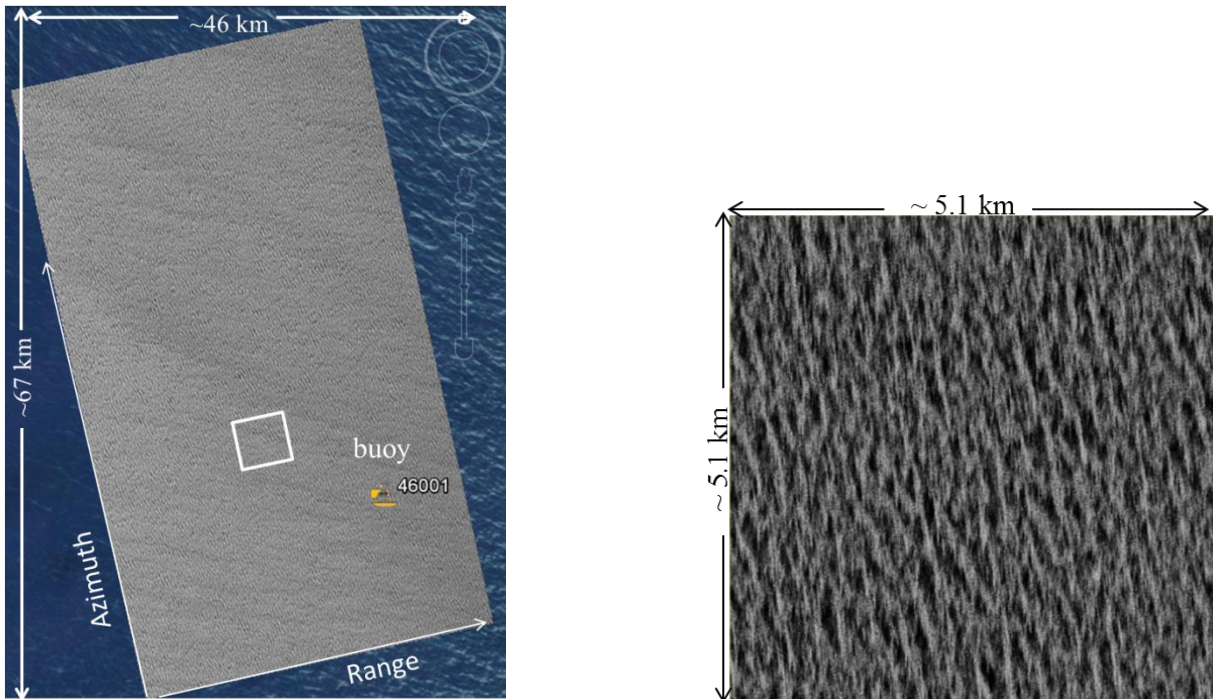
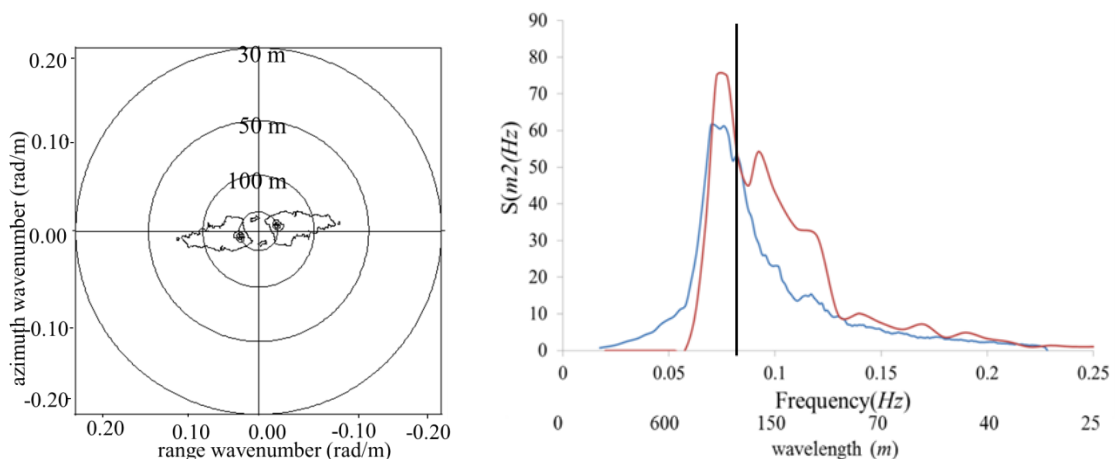


Figure 9.5: TD-X VV polarized StripMap data image acquired on November 13, 2011 at 3:23 UTC over buoy 46001 near the west coast of Canada (left). Sub-scene (5.1 x 5.1 km), taken from the left image (right).



The m^2 is should m^2

Figure 9.6: 2D spectrum derived from TS-X VV polarized StripMap image acquired on November 13, 2011 at 3:23 UTC over buoy 46001 (left). Comparison of the 1D spectrum derived from TD-X data (blue) and the buoy 1D spectrum (red). The black vertical line represents the derived *cut-off* frequency: 0.078 Hz (256 m wavelength) (right).

The case presented here is the analysis of the TD-X VV polarized StripMap data image acquired over buoy 46001 (figure 9.5). The case is taken under high sea state conditions with a measured buoy H_s of 7.5 m and a derived H_s from the TD-X data of 6.6 m. The underestimation of significant wave height by the XWAVE algorithm for this case is of 0.9 m. This underestimation is expected for cases of high sea state conditions, where is more difficult the imaging of ocean waves, even with long wavelengths, by the SAR (Chapter 7).

A summary of the meteo-marine parameters derived from TD-X data and given by the buoy are given in Table 9.3. An overview of the meteo-marine conditions for the region in question is provided by the wave model WAM at DWD results shown in figure 9.7 and figure 9.8.

The comparison of the peak period shows good results, with a TD-X derived peak period of 13.8 s against a peak period of 13.9 s given by the buoy. Although the difficulties of imaging in high sea state conditions, peak information, especially for near range travelling wave fields, is more easily to infer.

The buoy 46001 does not provide information regarding ocean wave's propagation direction for the time in question. Comparison of the wave peak direction is therefore done against the wave model data.

The wave peak direction of the wave model chosen is in fact the wind sea peak direction, as the wave model gives a higher *wind sea* wave height of 7.0 m, against 2.8 m of *swell* wave height. Therefore the comparison of peak period is done against the wind sea peak period of the model. The wind sea peak direction given by wave model is 262° against the TD-X derived peak direction of 240° . The wave peak period for the DWD wave model shown in Table 9.3 corresponds to the *wind sea* peak period. The *swell* peak period given by the model is 14.9 s (~ 350 m) and the wave peak direction of the *swell* is 219° .

This makes the *swell* wave field calculated by the model an azimuthally propagating wave field. However the *swell* field calculated by the model is not observed both TS-X spectrum and buoy spectrum (figure 9.6). More probably the *swell* wave field calculated by the model was overestimated by one second, and the calculated wind sea wave field also, as the 1D spectrum of the buoy also shows two wave systems very close together.

The comparison of the 1D spectrum derived from TD-X data shows a good agreement with the one given by the buoy for lower frequencies (longer wavelengths). For wavelengths below the azimuth *cut-off* wavelength the difference of the spectral shape of both spectrums has significant differences, e.g. the buoy wave spectrum for higher frequencies, (~ 0.09 Hz - 0.13 Hz) has higher values of energy density then the TD-X spectrum.

Table 9.3: Sea state parameters provided by buoy 46001, the wave model at DWD, and derived from the collocated TD-X image

	$H_s(m)$	$T_p(s)$	$\lambda_p(m)$	$\theta_p(^{\circ})$	$U(m/s)$	$Udir(^{\circ})$
DWD	7.5	13.5	285	262	19.7	276
buoy	7.5	13.8	297	-	18.6	280
TS-X	6.6	13.9	302	240	16.4	-

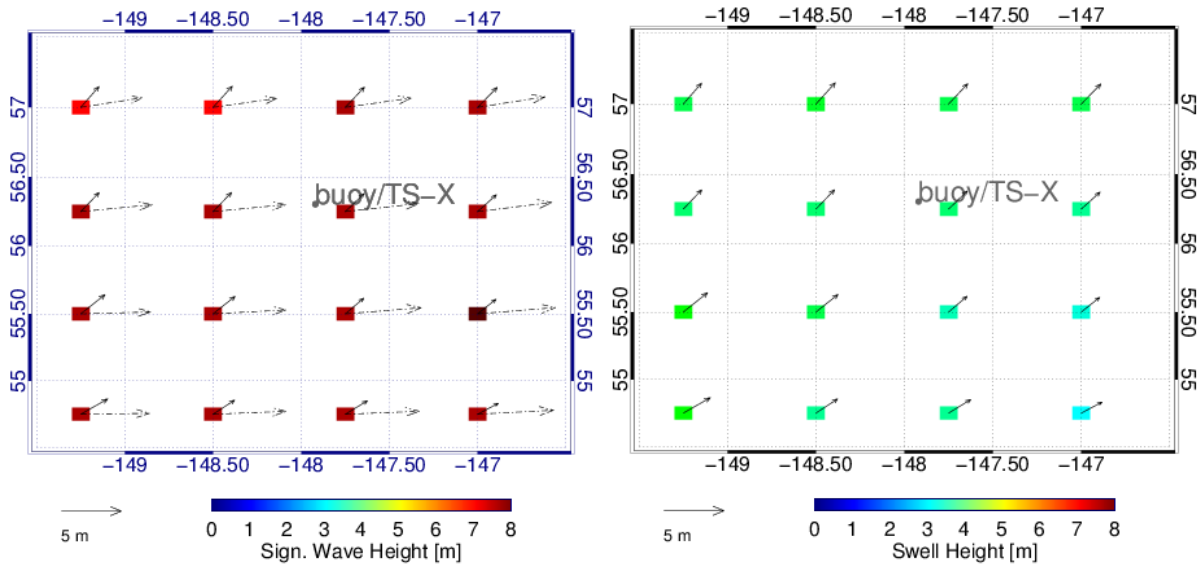


Figure 9.7: H_s wave field (left) and *swell* wave height (right) on November 13, 2011 at 3:23 UTC given by the WAM wave model running at DWD.

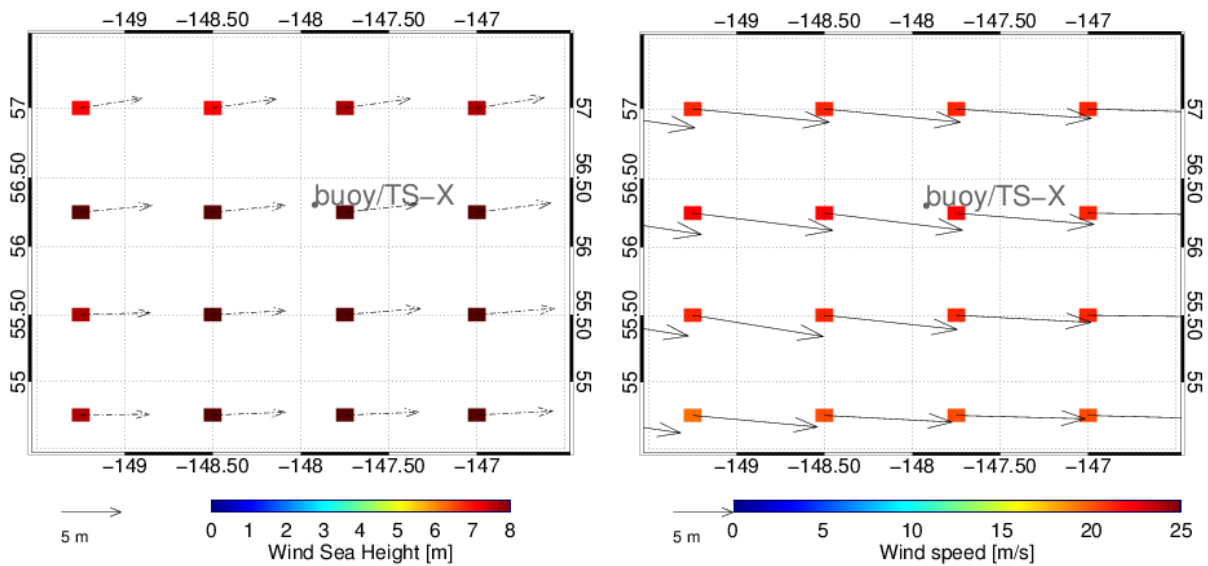


Figure 9.8: *Wind sea* height (left) and wind field (right) on November 13, 2011 at 3:23 UTC given by the WAM wave model running at DWD.

Case study 3:

Four wave system complex wave field, TS-X VV polarized StripMap data image acquired over buoy 46014 (39°14'6" N 123°58'26" W) with center incidence angle of 21.5°, on November 16, 2010 at 14:32 UTC.

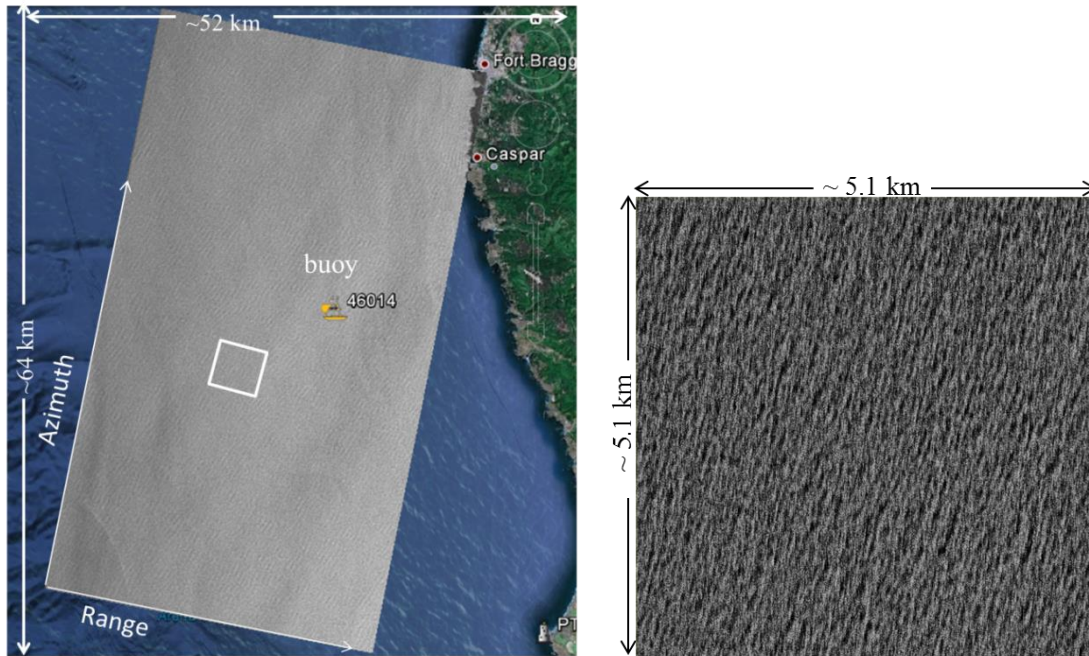


Figure 9.9: TS-X VV polarized StripMap data image acquired on November 16, 2010 at 14:32 UTC over buoy 46014 located near the west coast of USA (left). Sub-scene (5.1 x 5.1 km) taken from the image left (right).

The case presented here is the analysis of the TS-X VV polarized StripMap data image acquired over buoy 46014. This case is taken under rough sea state conditions with a measured buoy H_s of 3.0 m against a derived H_s of 2.7 m from the TS-X data. The XWAVE algorithm underestimated the wave height by 0.3 m. The H_s given by the wave model is for this case 3.5 m, which is overestimated by 0.5m.

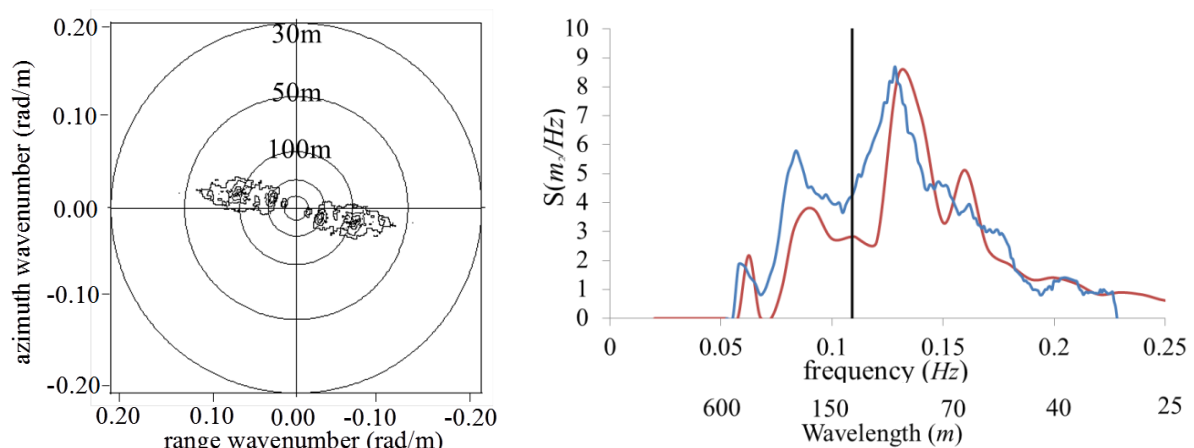
A summary of the meteo-marine parameters derived from the TS-X data and given by the buoy 46014 are given in Table 9.4. An overview of the meteo-marine conditions for the region in question, provided by results from the wave model WAM at DWD, is shown in figure 9.11 and figure 9.12.

The comparison of the peak periods shows similar results with a TS-X derived peak period of 7.9 s against 7.7 s given by the buoy. Given that the buoy 46014 does not provide information regarding the wave field propagation direction, therefore the evaluation of wave peak direction is done using only wave model data. The wave peak direction given by the numerical wave model is 342° against 290° derived from the TS-X data.

However a more detailed analysis of the data provides an explanation for the difference of the ocean wave propagation directions. The buoy spectrum (figure 9.10, right) shows that the imaged wave field is composed of four wave systems with different wavelengths. The 2D spectrum derived from TS-X data (figure 9.10, left) shows that the four wave systems wave fields have different wavelengths but nearly the same wave propagation direction. The wave model peak period is 11.2 s against 7.7 s given by the buoy, which leads to the conclusion that the wave peak direction given by the wave model is not for the same wave system considered to be with highest spectral density (higher peak) by both SAR and buoy.

Therefore in this case we cannot compare the wave peak direction. It is important to note that the spectral shape from the 1D spectrum derived from the TS-X data is similar to the one given by the buoy, which means the SAR data under these moderate conditions is able to image the wave systems without major distortion. The three wave systems are seen in the 1D spectrum as separated wave systems and their peaks match the spectrum peaks of the buoy. The fourth wave system has a frequency of $\sim 0.17 \text{ Hz}$ ($\sim 55\text{m}$) which is not visible in the TS-X derived spectrum.

The derived azimuth *cut-off* wavelength is for this case 131 m. The wave fields observed in the 2D spectrum travel near to range direction which explains why the three of the four imaged wave fields are seen in the 1D spectrum, except the high frequency system at about 0.18 Hz which was not imaged properly.



Its missing the m2 in the 1D spectrum

Figure 9.10: 2D spectrum derived from the TS-X VV polarized StripMap image acquired on November 16, 2010 at 14:32 UTC over buoy 46014 (left). Comparison of the 1D spectrum derived from TS-X data (blue) and the buoy 1D spectrum (red). The black vertical line represents the derived *cut-off* frequency: 0.109 Hz (131 m wavelength) (right).

Table 9.4: Sea state parameters provided by buoy 46014, the WAM wave model at DWD, and derived from the collocated TS-X image.

	$H_s(m)$	$T_p(s)$	$\lambda_p(m)$	$\theta_p(^{\circ})$	$U(m/s)$	$Udir(^{\circ})$
DWD	3.5	11.2	196	342	-	-
buoy	3.0	7.7	93	-	12.0	41
TS-X	2.7	7.9	97	110	10.5	-

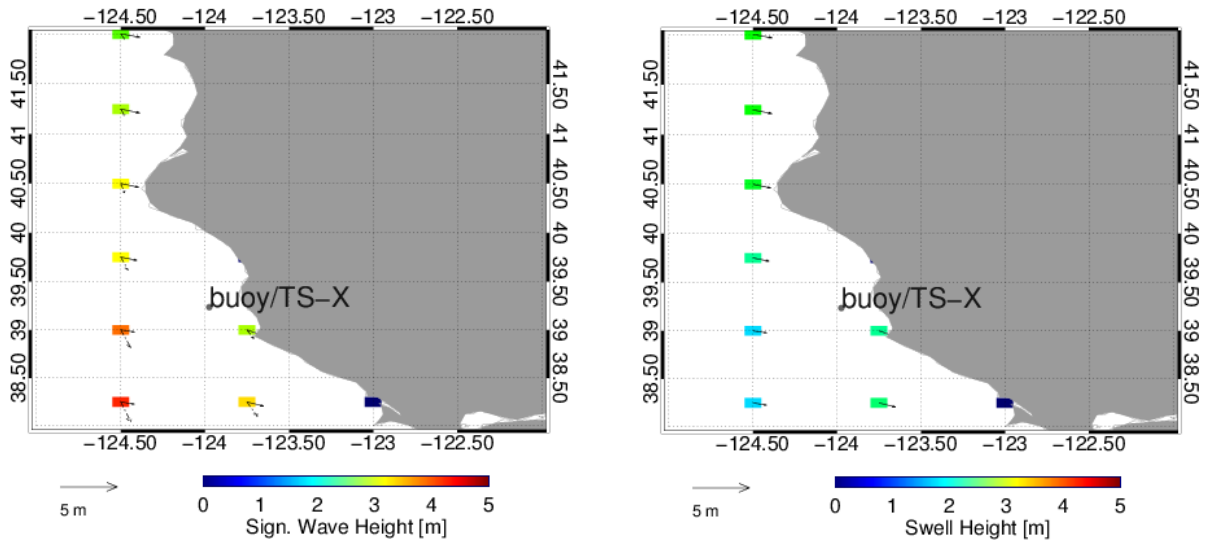


Figure 9.11: H_s wave field (left) and swell wave height (right) on November 16, 2010 at 14:32 UTC given by the WAM wave model running at DWD.

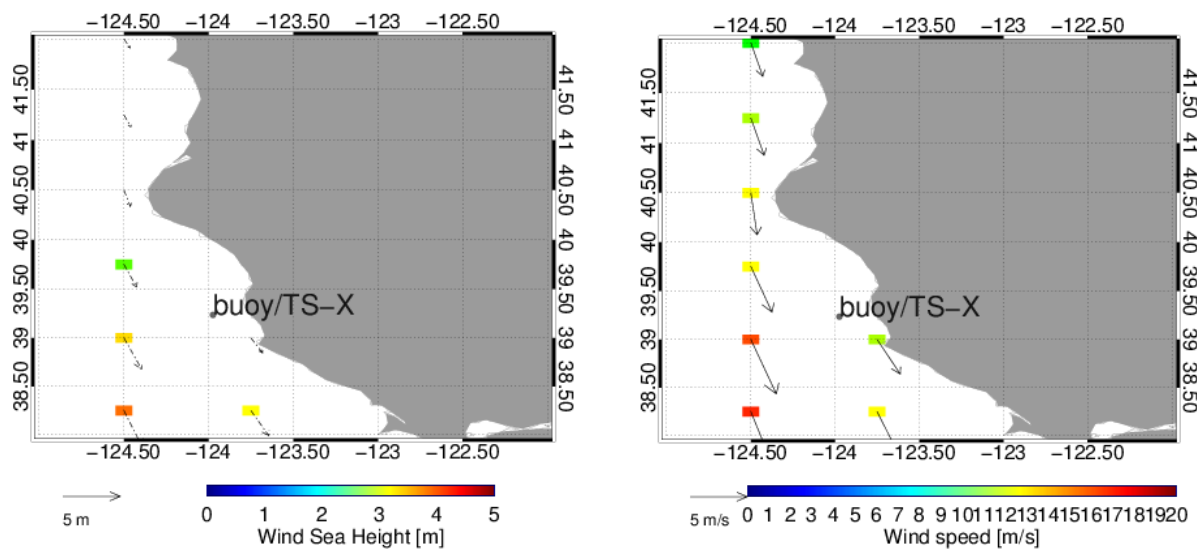


Figure 9.12: Wind sea height (left) and wind field (right) on November 16, 2010 at 14:32 UTC given by the WAM wave model running at DWD.

Case study 4:

The conditions under which this case study was performed are the following: Wave field composed of two wave systems with the same wavelength and different propagating direction. TS-X VV polarized StripMap data image acquired over buoy 42056 with heading of 190° and center incidence angle of 37.2° on July 1, 2010 at 11:36 UTC.

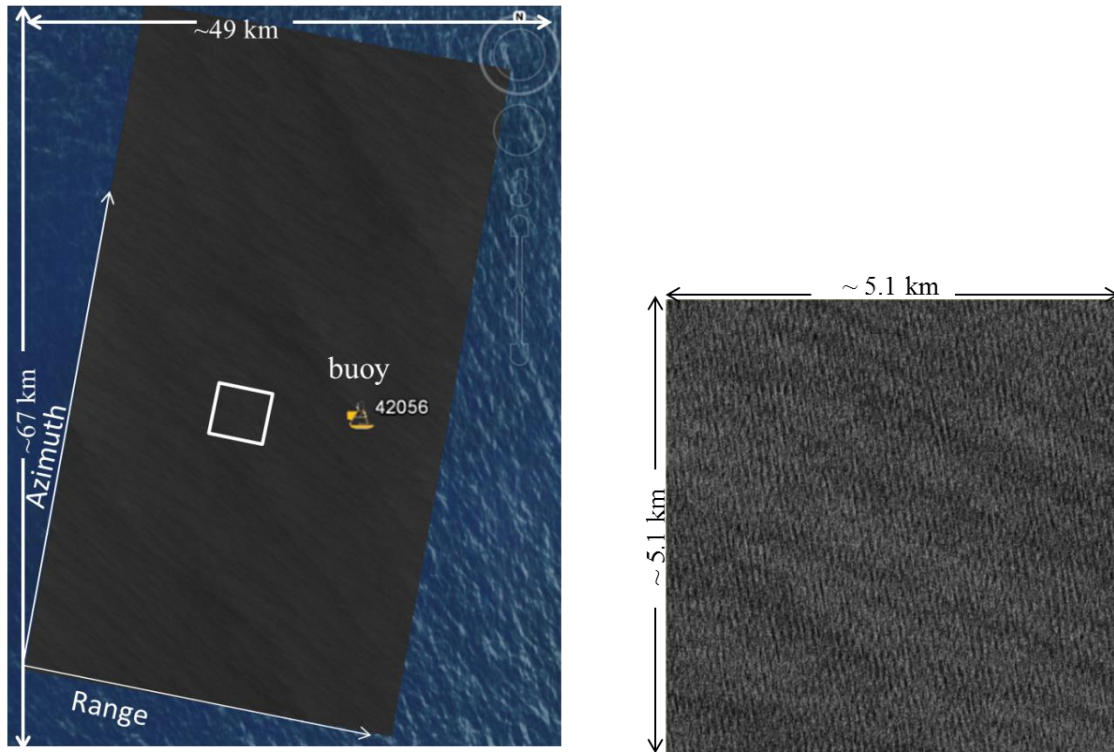


Figure 9.13: TS-X VV polarized StripMap data image acquired on July 1, 2010 at 11:36 UTC over buoy 42056 located near the west coast of Cuba (left). Sub-scene (5,1 x 5.1 km) taken from the left image (right).

The last case presented, is the analysis of the TS-X VV polarized StripMap data image acquired over buoy 42056 near Cuba (figure 9.13) during moderate sea state conditions, with a measured buoy H_s of 2.1 m and a derived H_s from the TS-X data of 1.9 m. The XWAVE algorithm underestimated the wave height by 0.2 m. The calculated H_s by the wave model is 1.7, which is underestimated by 0.4 m.

A summary of the meteo-marine parameters derived from TS-X data and given by the buoy 42056 are given in Table 9.5. An overview of the meteo-marine conditions for the region in question, provided by results from the wave model WAM at DWD, is given in figure 9.15 and figure 9.16.

The comparison of the wave peak period shows the same value (7.7 s) for both TS-X and the buoy. The wave peak direction given by the buoy is of 119° against 93° derived from the TS-X data, which confirms that the imaged wave field is a range propagating wave field. The derived 2D spectrum from the TS-X data (figure 9.14) shows two peaks which correspond

to two wave systems propagating with almost the same wavelength but with different directions. It is probable that the wave peak direction derived from the TS-X data belongs to the second wave system which has approximately the same wavelength and almost the same energy density (figure 9.14). The two peaks are not visible in the 1D spectrum, only visible in the 2D spectrum. The comparison of the spectral shape of the 1D spectrum shows reasonable agreement of the energy peak with the one given by the buoy. The main differences observed in the spectral shape are that the 1D spectrum derived from TS-X data has overestimated energy density in the higher frequencies when comparing to the buoy.

The second difference is that the second peak observed in the buoy 1D spectrum at about 0.16 Hz is not clearly visible in the spectrum derived from the TS-X data. The derived azimuth *cut-off* wavelength is for this case study, 114 m. The imaged wave field is near range travelling wave field, therefore the azimuth *cut-off* wavelength should be negligible for the frequency of the wave peak observed, which explains the good fit of the spectral peak.

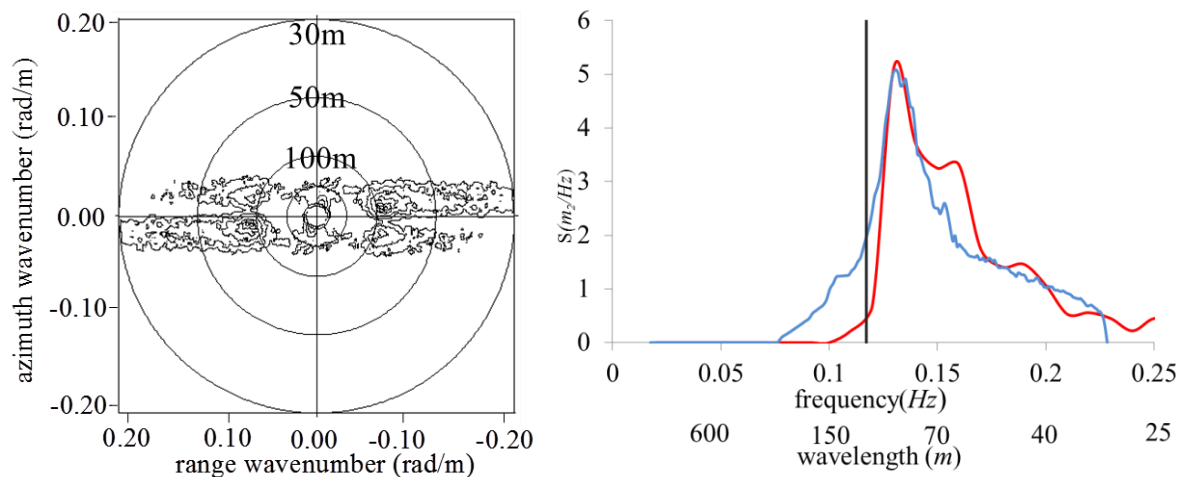


Figure 9.14: 2D spectrum derived from TS-X VV polarized StripMap image acquired on July 1, 2010 at 11:36 UTC over buoy 42056 (left) Comparison of the 1D spectrum derived from TS-X data (blue) and the buoy 1D spectrum (red). The black vertical line represents the derived *cut-off* frequency: 0.117 Hz (114 m wavelength) (right).

Table 9.5: Sea state parameters provided by buoy 42056, the WAM wave model at DWD, and derived from the collocated TS-X image.

	$H_S(m)$	$T_p(s)$	$\lambda_p(m)$	$\theta_p(^{\circ})$	$U(m/s)$	$Udir(^{\circ})$
<i>DWD</i>	1.7	8.4	110	121	-	-
<i>buoy</i>	2.1	7.7	93	119	10.0	130
<i>TS-X</i>	1.9	7.7	93	93	10.2	-

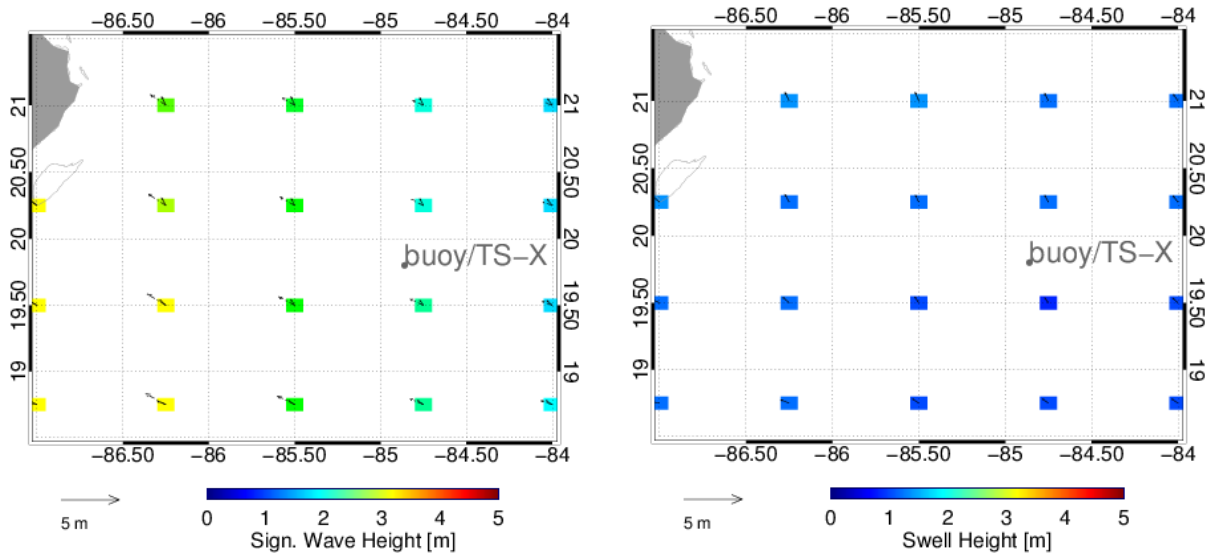


Figure 9.15: H_s wave field (left) and *swell* wave height (right) on July 1, 2010 at 11:36 UTC given by the WAM wave model running at DWD.

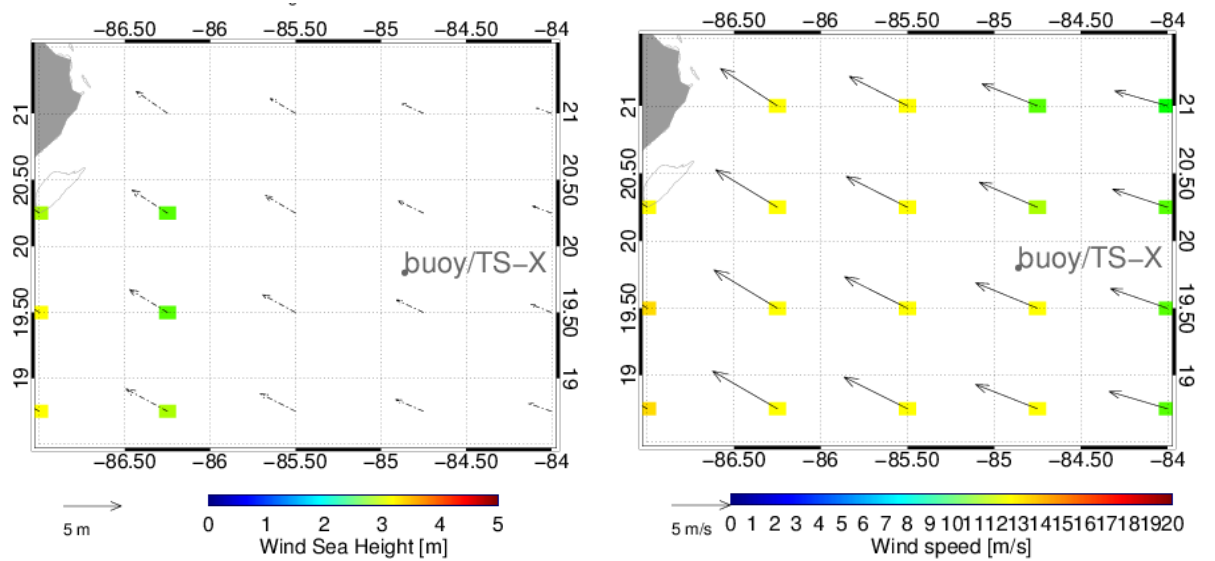


Figure 9.16: *Wind sea* height (left) and wind field (right) on July 1, 2010 at 11:36 UTC given by the WAM wave model running at DWD.

Chapter 10

Extraction of coastal wave field

In this chapter an important application of the empirical algorithm XWAVE is presented. Meteo-marine information is derived from TS-X/TD-X data acquired over coastal areas exploiting the advantage of the high-resolution TS-X SAR. As a result information regarding the spatial variability of significant wave height and ocean waves wavelength present in coastal areas can be obtained. Three case studies of TS-X data imagery acquired over coastal areas and the respective derived significant wave height fields are presented. The results are compared to *in-situ* wave measurements and/or numerical wave model results. Additionally, the corresponding ocean peak wavelength field for each sub-scene analyzed is given. This chapter is based on the published paper [Bruck *et al.*, 2013].

10.1 Coastal wave field extraction using TS-X/TD-X data

In coastal waters, ocean waves properties change considerably, influenced by the underlying bathymetry. Ocean waves in coastal waters normally experience effects such as shoaling, refraction, and diffraction. Additionally, ocean waves are often affected by currents and crossing over from other wave systems, nonlinear wave–wave interaction, and also depth-induced wave breaking. The variation of sea state properties in the spatial domain cannot be measured with a single buoy, as it only provides information on the time domain regarding sea state at its point location. To obtain the spatial variability of the sea state in high variable areas, an array of ocean waves measuring buoys can be used, although this method has limitations. More preferably wave models can be used. In order to accurately predict the wave field in coastal areas models require in addition to good input also up to date bathymetry.

In complex coastal areas, the resolution of the bathymetry should be in the order of a few hundred of meters or less.

Normally bathymetry is obtained by field sensing campaigns. This process takes time, is expensive, and not always is possible to perform. In some locations the bathymetry is rapidly changing in time and becomes out dated and unsuitable very fast because the ground floor is sand or mud and therefore is easily affected by transport and erosion. The bathymetry available might be out dated and not representative of the real bathymetry.

Aside the performance of the model itself, up-to-date fine resolution bathymetry is needed together with quality good resolution (depends on the complexity of the area) initial boundary conditions, i.e. sea-state parameters or spectra, wind fields, wave current field, etc. For the wave and wind conditions at the boundary normally taken from global scale wave models, some inaccurate results can occur, especially in storm situations where models have more difficulty in predicting accurately the correct significant wave height or the time at which the storm occurs. For this reason modeling is not a straightforward task.

An alternative method to obtain information regarding the sea state or wave field is to analyze SAR data. The TS-X/TD-X satellite provides high-resolution SAR images of the ocean surface (up to 1 m), spatial resolution which was not available with the previous conventional C-band satellites, e.g., ERS and ENVISAT missions. This makes TS-X/TD-X data suitable for coastal surface wave field observation, especially to observe the considerably changing sea-state properties.

TS-X/TD-X data acquired over coastal areas cannot be asserted for homogeneity by the homogeneity test (Chapter 7), due to the high sea state variability in the spatial domain, therefore the TS-X/TD-X data needs to be previously inspected visually for disturbances.

10.2 Case studies

In two case studies, wave fields derived using the developed algorithm are applied on TS-X/TD-X data acquired over the complex coastal area near the Elbe Estuary in the North Sea off the coast of Germany. The North Sea area is a shallow water ocean area, with a few hundred meters depth (figure 10.1). The first case study is the analysis of a TS-X StripMap data image taken in this complex coastal area during very high sea state conditions. The second case is the analysis of a TS-X StripMap data image taken during moderate sea state conditions over the Elbe Estuary. This second case is the most challenging, because the Elbe estuary is a highly complex coastal area with rapidly changing bathymetry due to currents and tides that change the underwater topography, which is composed mainly of sand banks. For these two cases, the derived significant wave height and wave peak wavelength wave field using the XWAVE algorithm are compared to numerical wave model results.

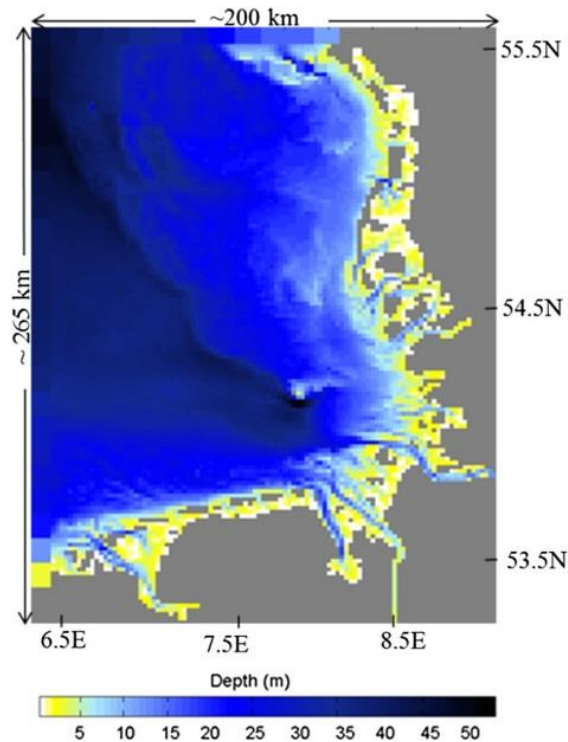


Figure 10.1: Bathymetry with a resolution of 1 nautical mile for the North Sea area near the coast of Germany.

The last case study presents the analysis of a TS-X StripMap data image taken under moderate sea state conditions off the coast of USA. In this case the TS-X image is located between three buoys, which although not collocated, are within very short distance of a few kilometers. Therefore they still provide useful information regarding the variation of the significant wave height in the ocean area covered by the TS-X data image. The conditions of the cases present here are different from the ones tuned in the algorithm, which was tuned using deep water measurements with homogenous wave fields. Therefore these case studies provide an assessment of the performance of the algorithm XWAVE when applied to TS-X/TD-X data acquired in coastal waters with non-homogenous wave fields.

Case study I: Coastal wave field extraction in high sea state conditions

The first case study is the analysis of a TS-X StripMap VV polarized image acquired under high sea state conditions on December 9, 2011 at 5:42 UTC between the Helgoland Island and the Elbe Estuary. The TS-X acquisition is collocated with a buoy (54.02° N, 8.11° E) visible in the middle of the image (see figure 10.2). The water depth of the area of the TS-X acquisition varies between approximately 5 to 40 m (figure 10.3).



Figure 10.2: TS-X VV polarized StripMap image acquired on December 9, 2011 at 5:42 UTC near the island of Helgoland located in the North Sea, near the coast of Germany, Google earth ©.

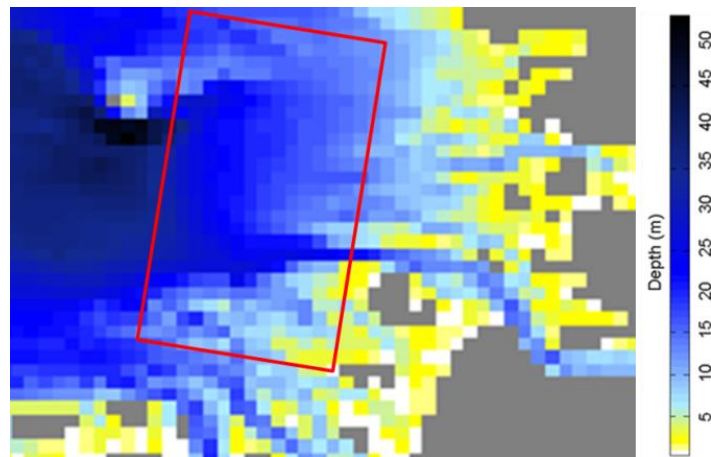


Figure 10.3: View of the respective underlying bathymetry for the same area shown in figure 10.2. The red box corresponds to the area of the TS-X acquisition.

An overview of the meteo-marine conditions predicted by the WAM-DWD wave model results, for the surrounding area of the German Bight is also provided. The H_s field and the *swell* wave height are shown in figure 10.4. The *wind sea* wave height and wind field are shown in figure 10.5. The wave field is propagating towards east, with decreasing wave height from approximately 6 m to approximately 2.5 m as it approaches the east landmass. Given that the *swell* component is below 0.5 m (figure 10.4), the wave field is mainly *wind sea*. The wind fields given by the model in the location of the TS-X image is of 18.5 m/s. The derived wind field from TS-X data gives values of wind speed varying between 20 m/s and 25 m/s. Wave model data provided by the DWD and local buoy data are used to validate the results. The sea state parameters given by the buoy, the wave model results from DWD for the nearest grid

point to the buoy location (54°N , 8.2°E , $dx = \sim 6\text{km}$) and the ones derived from the TS-X sub-scene taken over the position of the buoy are shown in Table 10.1.

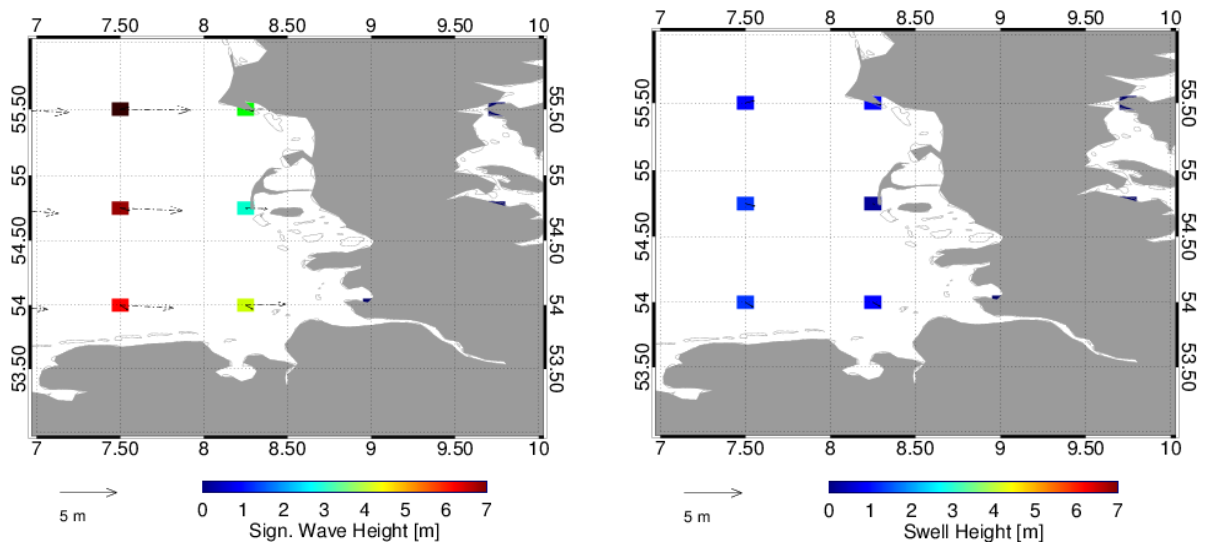


Figure 10.4: H_s wave field (left) and swell wave height (right) given by the WAM wave model at DWD on December 9, 2011 at 6:00 UTC.

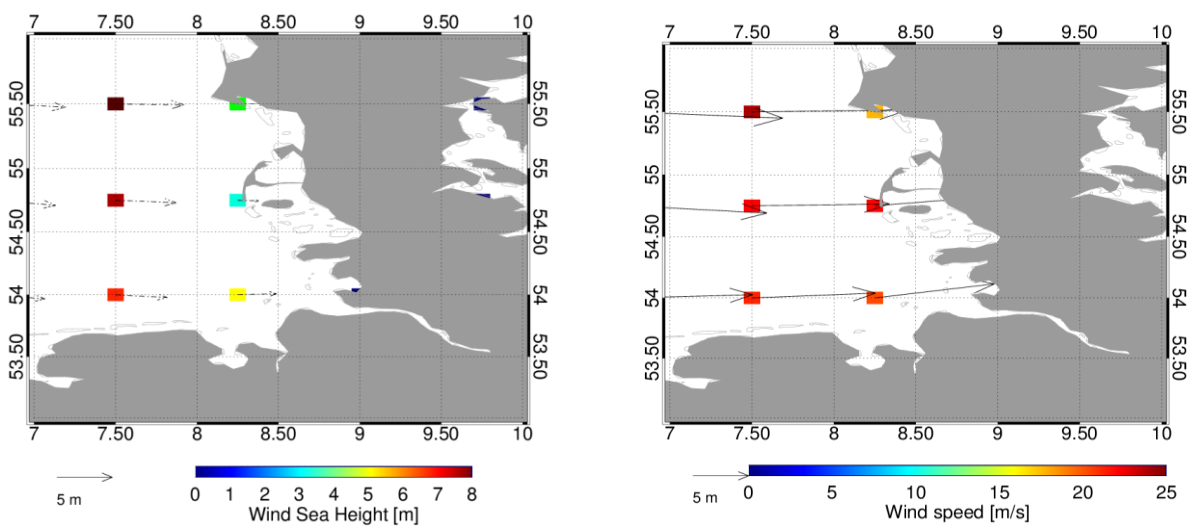


Figure 10.5: Wind sea height (left) and wind field (right) given by the WAM wave model at DWD on December 9, 2011 at 6:00 UTC.

Table 10.1: Sea state parameters given by the buoy, the DWD wave model (grid point 54 N 8.2 E) and derived from the collocated TS-X StripMap image taken on December 9, 2011 at 5:42 UTC.

	$H_s(m)$	$T_p (s)$	$\lambda_p(m)$	$\theta_p(^{\circ})$	$U_{10}(m/s)$	$U_{10}dir(^{\circ})$
<i>DWD</i>	4.1	13.5	285	307	18.5	261
<i>buoy</i>	5.7	11.1	195	-	-	-
<i>TS-X</i>	6.0	11.6	210	298	21.1	260

The significant wave height estimated from TS-X data at the buoy location (6 m) is quite similar to the *in-situ* wave measurements (5.7 m). The significant wave height estimated using the XWAVE algorithm is for this case overestimated by 0.3 m. The significant wave height given by the wave model at DWD is 4.1 m.

The underestimation of the wave model by about 2 m, is probably not due to the too low resolution of the grid (0.75°), more likely is related to a delayed prediction of the incoming high waves due to storm. This assumption resides in the fact that, the next wave model prediction, 3 hours later, shows higher values of significant wave height (5.4 m) closer to the ones derived from TS-X/TD-X data and the buoy. Regarding the comparison of the peak period, (using dispersion relationship in the case of the TS-X), shows a good fit with a TS-X peak period of 11.6 s and a buoy peak period of 11.1 s. The wave model gives for the peak period an overestimated value of 13.5 s.

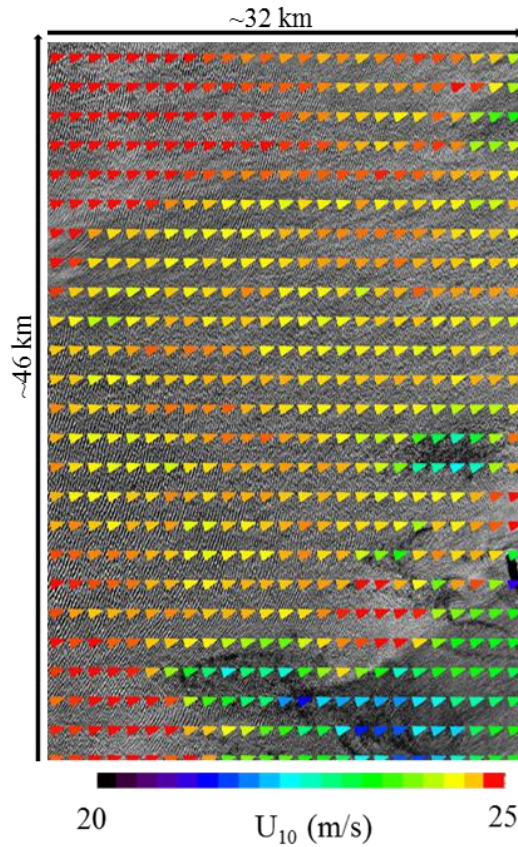


Figure 10.6: Sea surface wind field derived applying the XMOD algorithm on the TS-X VV polarized StripMap acquired on December 9, 2011 at 5:42 UTC.

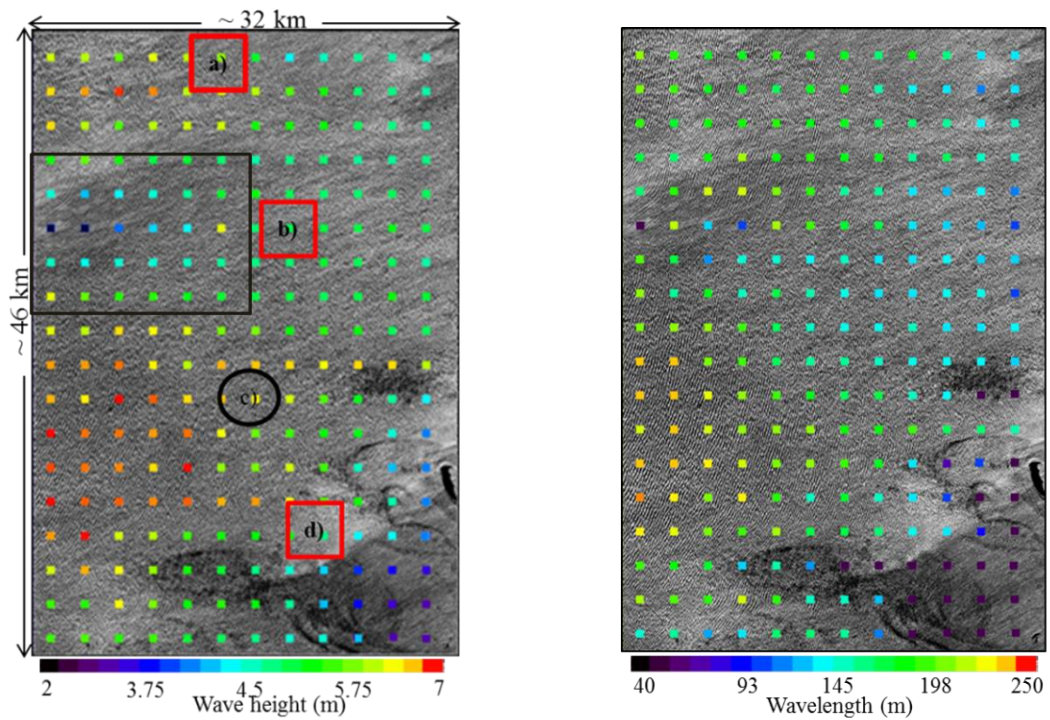


Figure 10.7: H_s wave field (left) and peak wavelength field (right) derived from TS-X VV polarized StripMap image acquired on December 9, 2011 at 5:42 UTC using a 2.6 km x 2.6 km size box. The red boxes and black circle (location of the buoy) are sub-scenes presented in figure 10.8.

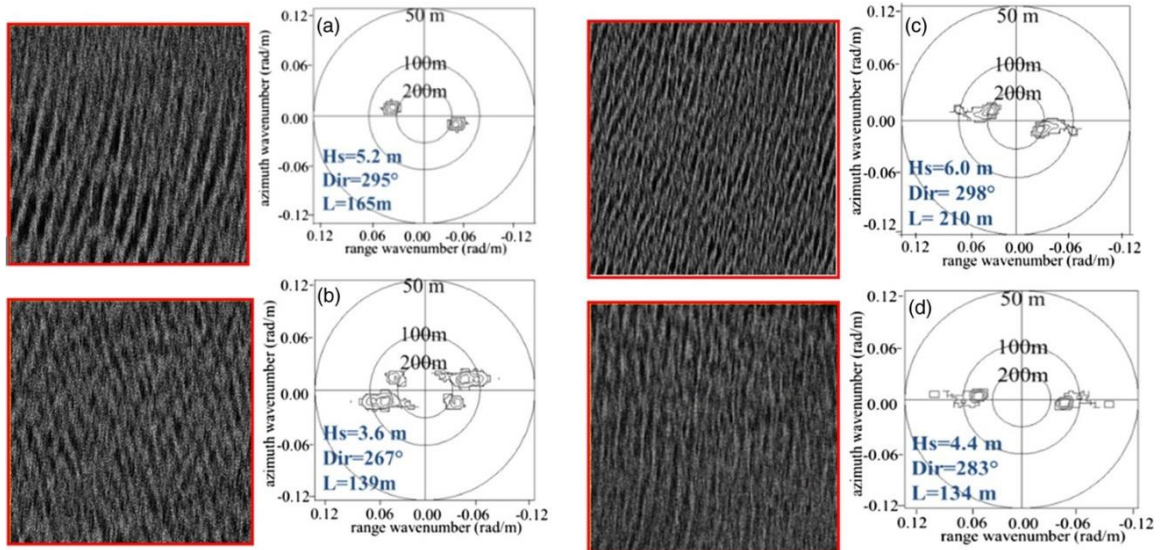


Figure 10.8: Sub-scenes (2.6×2.6) km from the TS-X VV polarized StripMap data image acquired on December 9, 2011, at 5:42 UTC.

Four sub-scenes ($\sim 2.6\text{km} \times \sim 2.6\text{ km}$) taken from different positions of the TS-X data are presented in figure.10.8.

Sub-scene (a) is located in the upper part of the TS-X acquisition (figure 10.7). The derived H_s is 5.1 m and the peak wavelength is 165 m. Only one wave system is detected in the derived 2D spectrum.

Sub-scene (b) is located in the area where the wave fields reunite after being diffracted around the Helgoland Island (figure 10.9). The case presented here, shows cross sea conditions, where two wave systems with different propagating direction can be visualized in the 2D spectrum. The H_s derived from the TS-X data is for this case 3.6 m and the peak wavelength, 139 m.

Sub-scene (c) is located at the position of the buoy. In this case one wave system is detected in the derived 2D spectrum from the sub-scene. The H_s derived from TS-X data, is as mentioned before, 6.0 m. Further details regarding the sea state parameters derived from this sub-scene and the comparison with the buoy results can be seen in Table 10.1.

Sub-scene (d) is located near shallower waters in the bottom part of the TS-X acquisition near the coast. In this case, sea surface signatures caused by the underlying bathymetry can be observed in the SAR data. The derived H_s from TS-X data for this case is 4.4 m. The derived peak wavelength is 134 m, which is the lowest of all the cases. Only one wave system is detected in the derived 2D spectrum.

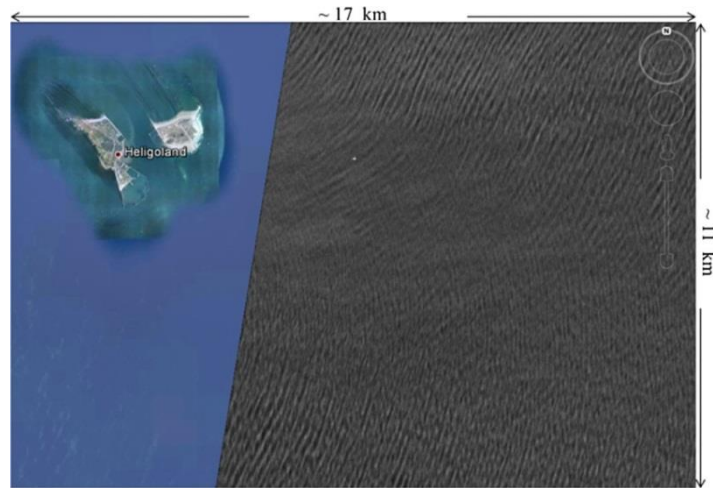


Figure 10.9: Zoom into the TS-X VV polarized StripMap image acquired on December 9, 2011, at 5:42 UTC (black rectangle figure 10.7), shown on Google Earth©

Case study II: Comparison with wave model data

A TS-X StripMap image is acquired over the Elbe estuary during moderate sea state conditions. Two TS-X StripMap data images are taken at different times, one during high tide and the second during low tide (figure 10.10) and (figure 10.11). These images are able to show the complexity of the underlying bathymetry which changes strongly with the tide. This translates into a high variation on the coastline from one case to the other. The underlying bathymetry is composed partially by sand banks which are rapidly changing with the tides and currents. Figure 10.12 shows the bathymetry for an area of the North Sea surrounding the Elbe estuary, and a zoom into the bathymetry.

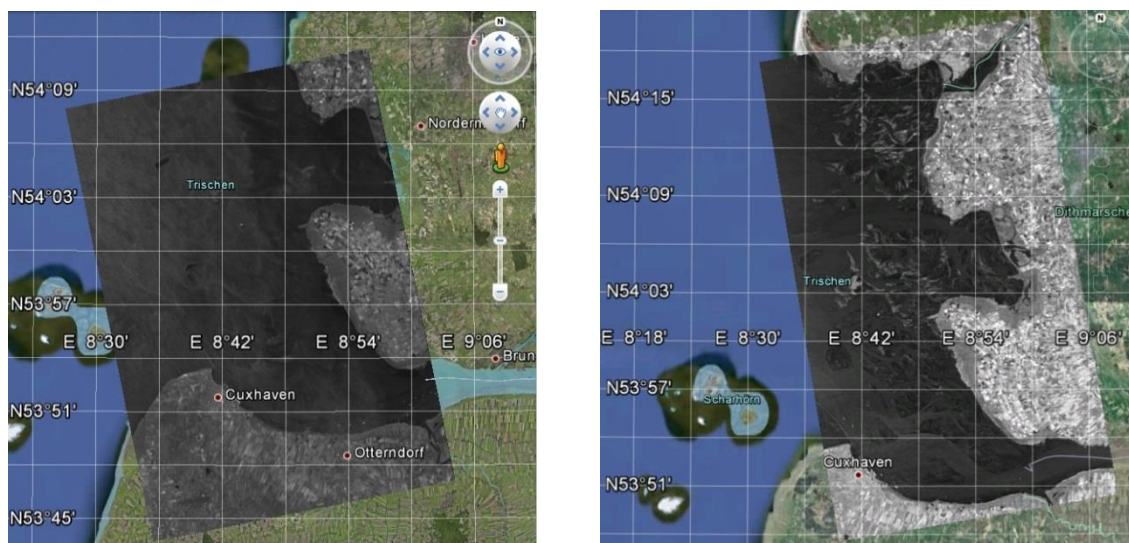


Figure 10.10: High tide situation acquired on TS-X StripMap taken on November 21, 2008 at 17:01 UTC (left). Low tide situation acquired on TS-X StripMap taken on November 26, 2008 at 17:10 UTC (right).

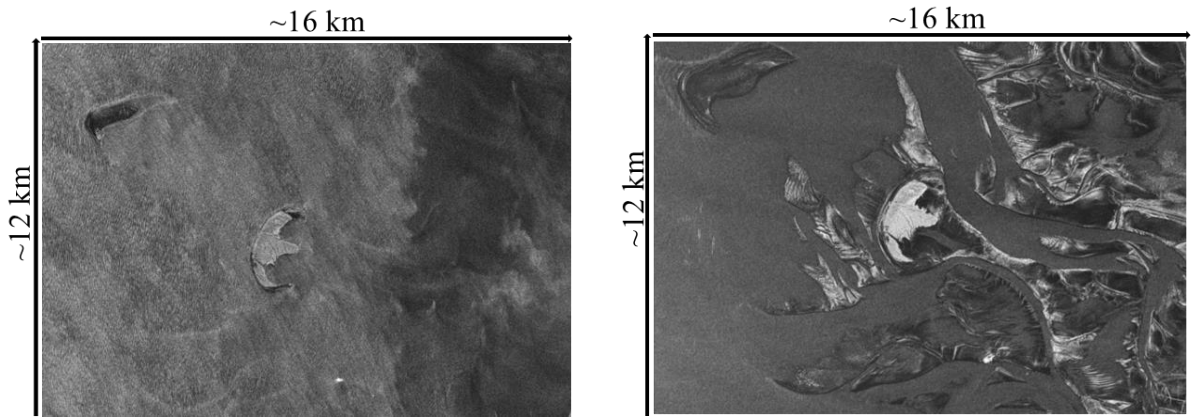


Figure 10.11: TS-X sub-scenes from the TS-X StripMap data taken on November 21, 2008 at 17:01 UTC showing high tide (left) and low tide situation taken on November 26, 2008 at 17:10 UTC (right).

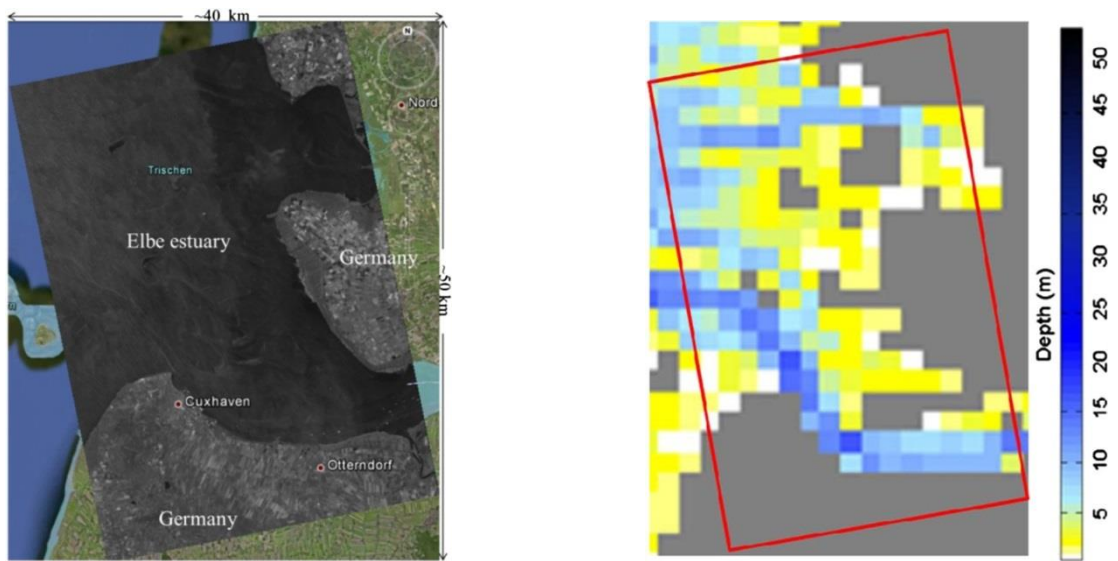


Figure 10.12 TS-X HH polarized StripMap image acquired on November 21, 2008, at 17:01 UTC over the Elbe estuary, and respective underlying bathymetry , Google Earth ©.

The bathymetry shows that the water depth in the Elbe River estuary is in average approximately 10 m and reaches 20 m depth in the deepest locations. The lower the water depth is, the higher the influence on ocean waves, which influences their wavelength and wave height (shoaling).

In this case study sea state information derived from the TS-X data is compared to global and coastal wave numerical models results (k-model and DWD). The bathymetry shown in figure.10.1 is used as the area for the coastal model *K-model*.

At the *k-model* grid boundary input sea state and wind information is given by the WAM wave model (global) running at the DWD. The WAM-DWD wave model results are shown in figure 10.13 and figure 10.14.

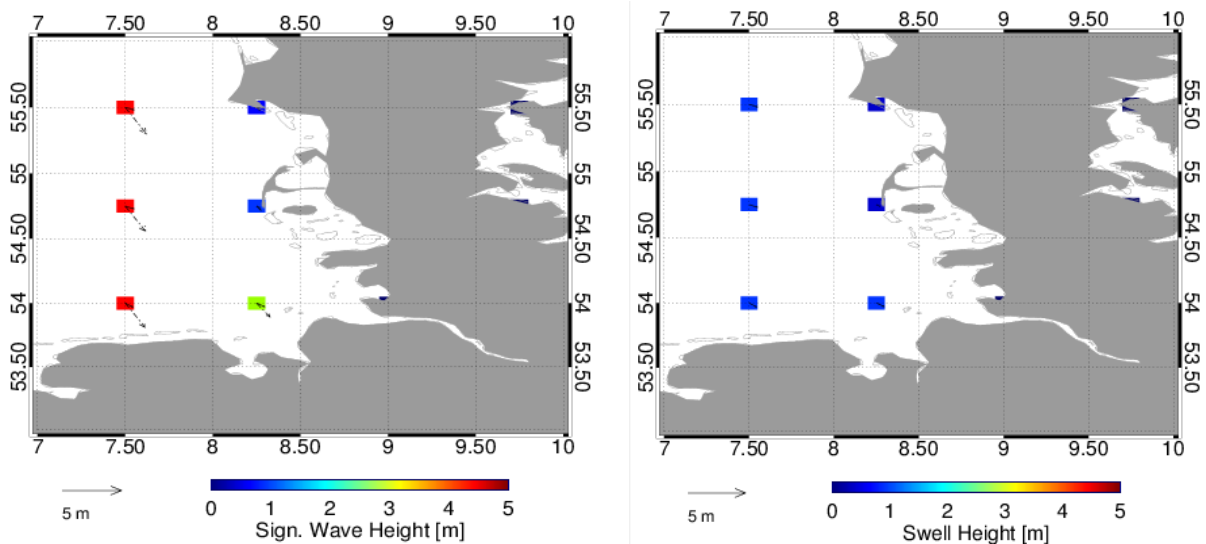


Figure 10.13: H_s wave field (left) and *swell* wave height (right) given by the WAM wave model running at the DWD on November 21, 2008 at 17:01 UTC.

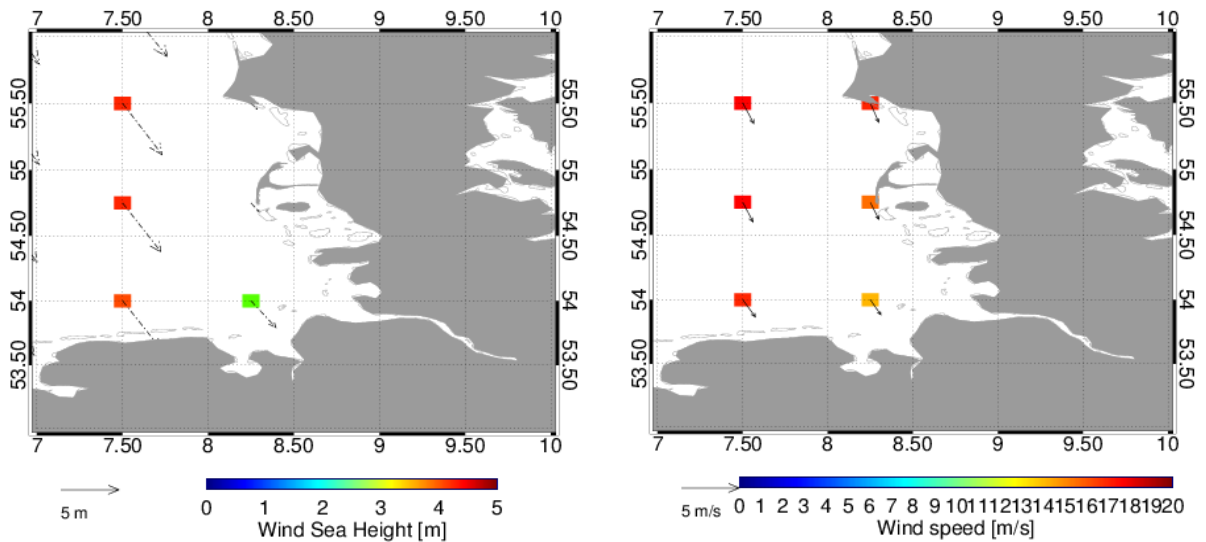


Figure 10.14: Wind sea height (right) and wind field (left) given by the WAM wave model running DWD on November 21, 2008 at 17:01 UTC

The WAM-DWD wave model results show that the computed H_s values decrease from west to east and have its lowest value of 2.4 m at grid point coordinates 54°N 8.25°E, which are the closest to the Elbe estuary. The WAM-DWD wave model data shows the waves on November 21, 2008 at 18:00 UTC are predominantly *wind sea* (figure 10.14).

Wind field data is shown in figure 10.14 right and present high value of wind speed, ranging from 13.2 m/s to 16.7 m/s and the value of wind speed decreases with longitude from 15.3 m/s to 13.2 m/s for the same latitude of 54°N. The wind field derived from TS-X data is shown in figure 10.15. The highest values are of approximately 13 m/s and are in average 9 m/s

in the brighter area of the image and approximately 5 m/s in the darkest area of the image. This change in the wind field is clearly visible in the image and shows an atmospheric front.

The H_s field derived from the TS-X data is for this case study obtained by shifting the analysis box by 1.3 km. The TS-X wave analysis resolution, for this case, is a 1024 pixel box, spatial averaged sub-scene by a factor of 2, which corresponds to an area of approximately 2.6 km. The numerical spectral model *k-model* designed for coastal application was applied for our case (figure 10.16) with resolution of 1 nautical mile (~1.9 km). The H_s wave field derived by the numerical coastal wave model with fine resolution and up-to-date bathymetry is used to assess the stability of the wave height estimation overall the wave field. The TS-X derived wind field is also provided as input for the coastal model. The area of analysis is of approximately 30 km, and the wind speed is in average 12 m/s.

The H_s wave field derived from the TS-X data (figure 10.17) and the H_s results from the numerical model (figure 10.16) follow the same trend of wave height values. With derived values of 2.2 m against values given by wave model of 2.0 m and down to derived values of 0.5 m against values of 0.3 m given by model. The corresponding peak wavelength field of the derived wave height wave field is given in figure 10.17 right.

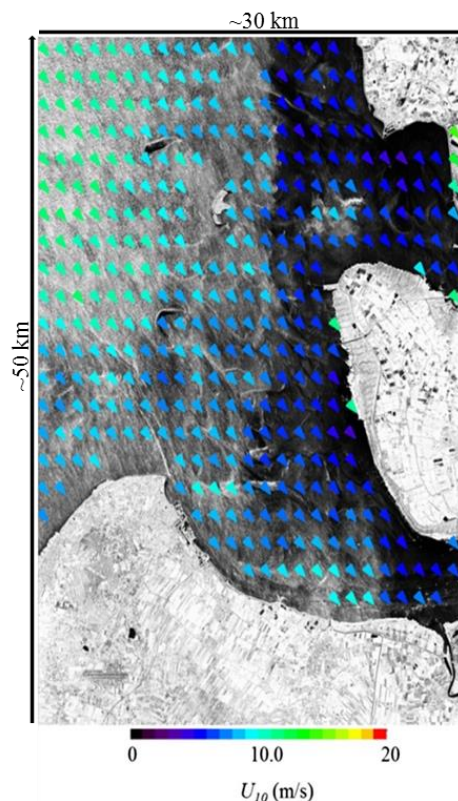


Figure 10.15: Sea surface wind field derived from the TS-X HH polarized StripMap data acquired over the Elbe Estuary on November 21, 2008 at 17:01 UTC.

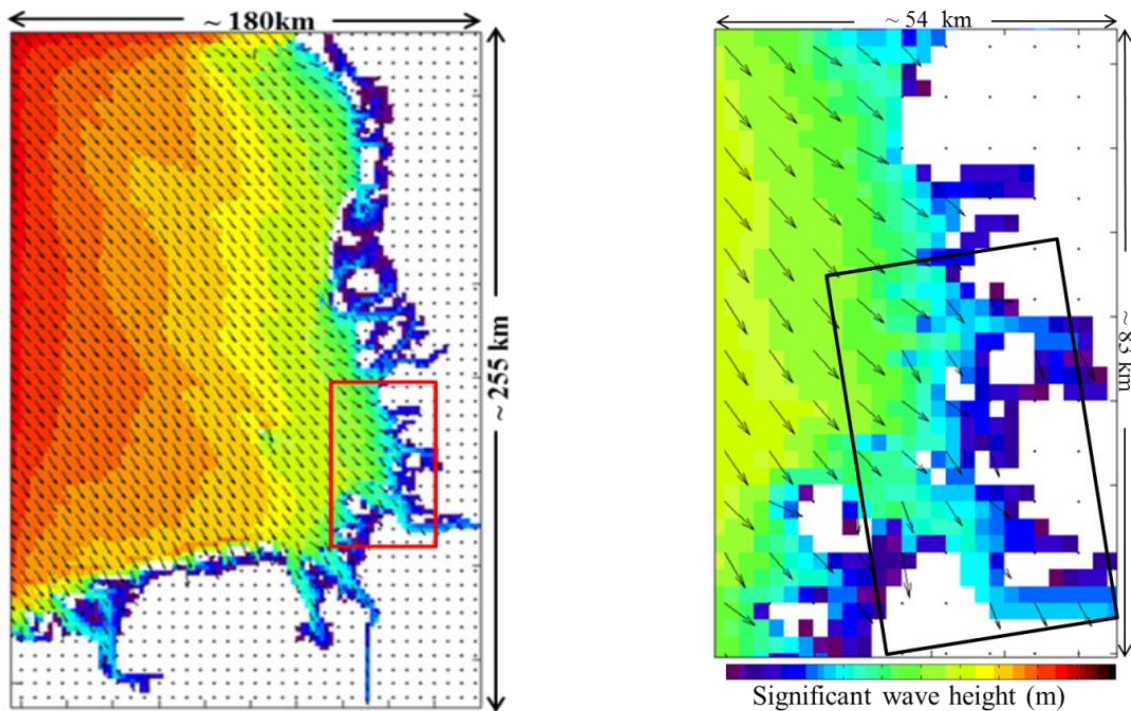


Figure 10.16: Coastal wave model H_s results (K -model) for the North Sea, near the coast of Germany, with a resolution of 1 nautical mile on November 21, 2008 at 18:00 UTC (left). Zoom into the area of the inside the red box shown on the right image, the black box corresponds to the area of the TS-X acquisition (right).

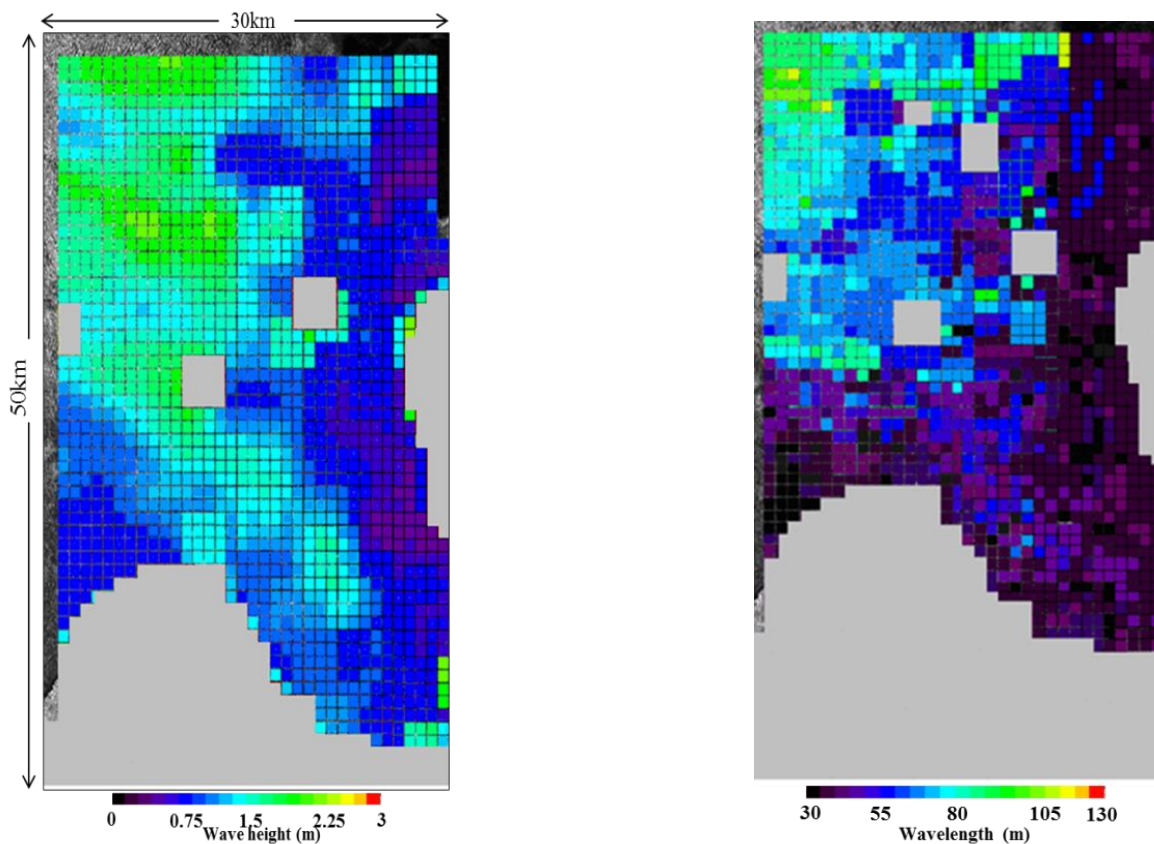


Figure 10.17: Significant wave height wave field derived from the TS-X HH polarized StripMap image acquired over the Elbe estuary on November 21, 2008 at 17:01 UTC (left) and the corresponding peak wave length (right).

Case Study III: Measuring sea state variability on TS-X data, verification with *in-situ* wave measurements.

This case presents the analysis of the TS-X VV polarized StripMap data image acquired in the southwest of USA, near Santa Barbara (California) acquired on April 9, 2012 at 1:51 UTC (figure.10.18).

At the location where the TS-X data image is acquired, spatial variability of sea state is expected. This because, the wave field propagates from Northwest and the cape visible in the figure shadows the northwest wave fields in the south. In this area the variation of significant wave height is measured by three buoys, 46054, 46218 and 46011, (figure 10.18). Buoy 46054 is located about half a kilometer south of the TS-X acquisition boundary. The H_s measured by buoy 46054 at nearest available time; 1:00 UTC is 1.1m. Buoy 46218 is located about 6 km west from TS-X acquisition boundary.

The measured H_s by buoy 46218 at 2:06 UTC time is 1.6 m. Buoy 46011 is located 37 km north of the TS-X acquisition boundary. The measured H_s by buoy 46011 is 1.9 m. The measured buoy wind speed recorded by buoy 46054 is 8.8 m/s at 00:50 UTC. The wind speed measured by station PTCG1 located in the cape (figure 10.18) at 1:50 UTC is of 9.3 m/s.

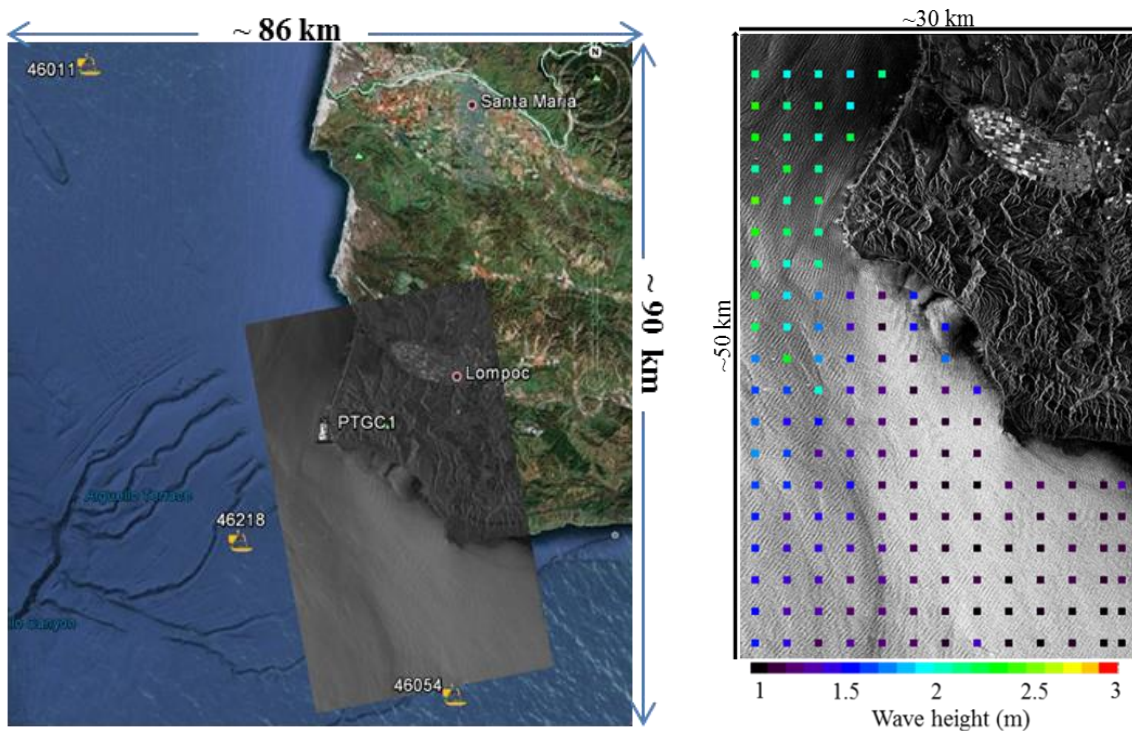


Figure 10.18: TS-X VV polarized StripMap image acquired over the south coast of USA, near Santa Barbara (California) acquired on April 9, 2012 at 1:51 UTC (left). Significant wave height wave field (box size 2.6 km) derived from the image shown left (right).

A summary of the *in-situ* observations available near the TS-X acquisition is shown in Table 10.2. From Table 10.2 it is shown that the variability of H_s in the area covered by the TS-X image is of 0.8 m. The H_s given by buoy 46011 which is located about 40 km north of the TS-X acquisition is of 1.9 m. The H_s values derived from the TS-X image for the upper part area are about 2.0 m, being the highest 2.1 m.

The derived TS-X H_s decreases to values of 1.7 m in the middle of the image, which is similar to the H_s of 1.6 m given by the nearest buoy 46218, at about 6 km from the TS-X acquisition. In the bottom part of the TS-X image, the derived H_s from TS-X data, decreases down to 1.0 m, which is also close to the wave height value of 1.1 m given by buoy 46054, located at about 2.5 km from the TS-X acquisition. These results show that the variability of the wave field derived from TS-X data tend to follow the variability of H_s measured by the buoys.

An interesting point to mention is regarding the wind information, the derived wave height in this case is higher where wind speed is lower and lower where wind speed is higher (Table 10.2). The wave field is mainly *swell* and therefore the spectral parameter E has stronger influence in this case. This case study is a good example that shows the stability between the input parameter sea surface wind speed and the spectral parameter E .

Table 10.2: Summary of *in-situ* data (waves and wind) at the location of the TS-X StripMap data acquired on April 9, 2012 at 1:51 UTC, south coast of USA near Santa Barbara (California).

Station	Position Relative to TS-X image	Dx (km)	H_s (m)	Tp (s)	Dir (°)	Wind speed(m/s)	Wind direction(°)
46218 (waves only)	West	~ 6	1.6	14.3	293	-	-
46054 (waves/wind)	South	~2.5	1.1	14.8		-	-
46011(waves/wind)	North	~40	1.9	13.8	299	5.4	311
PTCG1 (wind only)	center	0	-	-	-	9.3	4
<i>In-situ</i> sea state information: $dt < 30$ min, wind information: $dt < 10$ min.							

Chapter 11

Summary and Conclusions

The aim of this PhD thesis is to develop an algorithm to derive significant wave height, H_s , from TS-X/TD-X SAR data. In order to achieve the main objective, several sub-objectives were successfully accomplished. Those objectives include:

- 1) The development of a method to discard TS-X/TD-X data containing unwanted signatures and retain data with homogenous wind generated ocean wave's wave field.
- 2) Evaluation of the quality of the 2D spectrum derived spectral peak parameters, peak wavelength and direction parameters with *in-situ* wave measurements.
- 3) Determination and evaluation of the minimum measured ocean wave wavelength by the SAR, analysis of the dependency of the azimuth *cut-off* wavelength with the underlying meteo-marine conditions.
- 4) Analysis of TS-X/TD-X SAR data, performing sensitive studies with the aim of pursuing dependencies on parameters derived from SAR data with meteo-marine conditions.
- 5) Tuning and validation of the algorithm with deep water *in-situ* wave measurements.
- 6) Evaluation of the 1D spectral shapes on the basis of comparisons with *in-situ* wave measurements.
- 7) Performance assessment of the ability of developed algorithm, to measure sea state variability in the spatial domain, when applied to coastal TS-X/TD-X data imagery.

- **Conclusions regarding filtering artifacts in the data**

The TS-X/TD-X data considered for the validation/tuning of the algorithm is acquired over homogeneous wave fields, free of phenomena unrelated with wind generated sea surface waves, like internal waves, oil slicks atmospheric disturbances. The method to select homogeneous wave fields in SAR images is based on the spectral analyses of sub-scene. The method basically checks if spectral properties are similar within the sub-scene analyzed. The method proved to be successful in the identification of TS-X/TD-X data with homogenous wind generated ocean waves and to discard data which presents undesirable artefacts.

- **Assessment of the ocean waves peak wavelength and direction**

The verification of peak wavelength and peak direction derived from 200 TS-X/TD-X data using the Fourier analysis with *in-situ* wave measurements showed good results for both parameters. For peak wavelength, the verification resulted in a correlation $R = 0.96$ and a scatter index $Si = 0.13$ and for the peak direction, correlation $R = 0.95$ and scatter index $Si = 0.14$. The shortest peak wavelength measured for the 200 cases analyzed is about 67 m and the longest approximately equal to 591 m.

- **Assessment of the azimuth *cut-off* wavelength**

The evaluation of the azimuth *cut-off* wavelength (minimum measured ocean wavelength in azimuth direction) derived for the TS-X/TD-X showed good correlation with both significant wave height and sea surface wind speed. The dependency of the azimuth *cut-off* wavelength analyzed for 200 TS-X/TD-X with significant wave height resulted in a correlation $R = 0.80$ and with sea surface wind speed, $R = 0.56$. Dependency with *wind sea* wave conditions resulted in a correlation $R = 0.80$ and for *Swell* a correlation $R = 0.74$ was obtained.

Azimuth *cut-off* wavelength was also analyzed for dependency with incidence angle. For incidence angles up to 38° it is possible, depending on meteo-marine conditions, to measure lower values of azimuth wavelength (~ 55 m). For incidence angles exceeding approximately 38° only ocean wavelengths in azimuth direction longer than about 100 m could be detected.

A very important conclusion is that it is possible to measure much lower ocean wavelengths from TS-X/TD-X data than from SAR data provided by e.g. ERS and ENVISAT missions. For ocean waves propagating in azimuth, for which SAR has more imaging limitations, it was possible to measure a case with azimuth wavelength of 46 m. For ERS, ENVISAT data the minimum wavelength limit for measuring azimuth propagating waves is about 150 m.

- **Empirical algorithm XWAVE**

The most important contribution presented in this thesis. The development of the first algorithm to derive sea state parameters from TS-X/TD-X data. The parameters derived are significant wave height, peak wavelength and peak direction. The algorithm proved to be robust, acknowledging the validation results obtained by comparing the algorithm to 100 *in-situ* wave measurements data-points values. The performance achieved is in this validation study is given by the scatter index $Si = 0.21$, the correlation $R = 0.93$ and a bias of 0.02 m.

- **Verification of the 1D spectral shape**

The 1D spectra derived from TS-X/TD-X data was verified with buoy wave spectrum. This was done by visually comparing the plotted spectrum of both. In this first order level of assessment of the case studies analyzed here, there is good agreement between the spectral shape of the spectrum derived from TS-X/TD-X and buoy. This is mainly due to the lower *cut-off* effect influence which leads therefore to less distortion on the spectrum. As expected, the spectrums are more similar in the low frequency band of the spectrum, as longer ocean waves are better imaged by the SAR.

- **Extraction of coastal wave field**

The developed algorithm is applied to TS-X/TD-X data acquired on coastal waters to produce H_s and peak wavelength fields, exploiting the advantage of the high resolution data of the TS-X/TD-X. The results obtained are compared with *in-situ* wave measurements and results of wave models runs. The comparison with *in-situ* and wave models results for the case presented here, showed good agreement with no obvious outliers. The results obtained provide further understanding on sea state spatial variability in coastal areas. Wave fields derived from TS-X/TD-X SAR imagery using the XWAVE algorithm proved to be a useful new tool capable of analyzing the highly variable sea state conditions present in coastal areas.

Outlook

With this work we have identified a number of aspects that require further research. Many aspects of ocean waves and sea state measurement using TS-X/TD-X data were analyzed in the aim of this thesis, but need further and deeper analysis. First, it is recommended that the sea surface data acquired by the TS-X/TD-X needs to be increase in number. Especially cases of higher sea state conditions are needed for analysis. A larger data-set provides a more stable and reliable tuning coefficients. Further work should focus on the analysis of the fitting of the algorithm regarding the different wave climates (*wind sea, swell*). The fitting of data acquired specifically for each wave climate will lead to different algorithm tuning coefficients, and probably optimized new formulas.

Another issue that needs further analysis is the sea surface data taken by the TS-X/TD-X at different incidence angles. For higher incidence angles SAR data loses quality, but for lower incidence angles, fine tuning of the data according to incidence angle can optimize results.

Regarding the spectrum derived from TD-X/TS-X data further analysis is also needed; the spectral shape derived from TS-X/TD-X data in relation to the real wave spectrum should be deeper investigated. The analysis of derived spectrum TS-X/TD-X data together with the buoy spectrum leads to further understanding of the azimuth cut off, improvement in the measurement of short wind waves, which are steps to further optimize the algorithm.

This thesis showed that the XWAVE algorithm seemed at first glance to be suitable for coastal applications. Several case studies were compared with buoy data and numerical wave model data. However derivation of sea state in coastal areas is more complicated then deriving in deep water, so a detailed study including a large number of coastal SAR data images taken in different sea state conditions should be analyzed against high resolution coastal wave models.

The XWAVE algorithm is presented in this thesis with results mainly from StripMap VV polarized data, however analysis was done using other type of TS-X/TD-X data which showed promise results, therefore a further step can be the implementation of the algorithm to the full range of TS-X/TD-X data types.

Other aspects found in the analysis of TS-XTD-X SAR data were found indirectly related to ocean waves but of interesting and important value. Certain atmospheric phenomena signatures were detected in TS-X/TD-X data, which were not visible in C-band SAR data, in TS-X/TD-X data is possible to observe cloud formations besides its signatures in the sea surface. Other signatures visible in the sea surface are high resolution wind streaks. In opposition to C-band

data, where wind streaks signatures were in the order of more than 1000 m apart, the wind streaks observed in the TS-X/TD-X data are suspected to be related to the wind gusts, with sea surface signatures in the order of 100 meters, clearly visible in the TS-X/TD-X data. This effect caused some unforeseen complications on the retrieval of the spectrum from the TS-X/D-X data, where the energy peak related to ocean waves was sometimes confused with the peak related to wind signatures.

The further investigation of the wind gusts suspected signatures is of valuable importance to the evaluation of marine weather, especially in coastal areas, where turbulence can be observed with very high resolution.

Appendix A

This appendix provides additional case studies of TS-X/TD-X data acquired over *in-situ* wave measurements.

Case study A1: Moderate sea state and undefined wave systems: TD-X VV polarization StripMap data image acquired over buoy 46089 (45°53'36" N 125°49'9" W) with centre incidence angle of 21.4° on December 4, 2011 at 2:02 UTC.

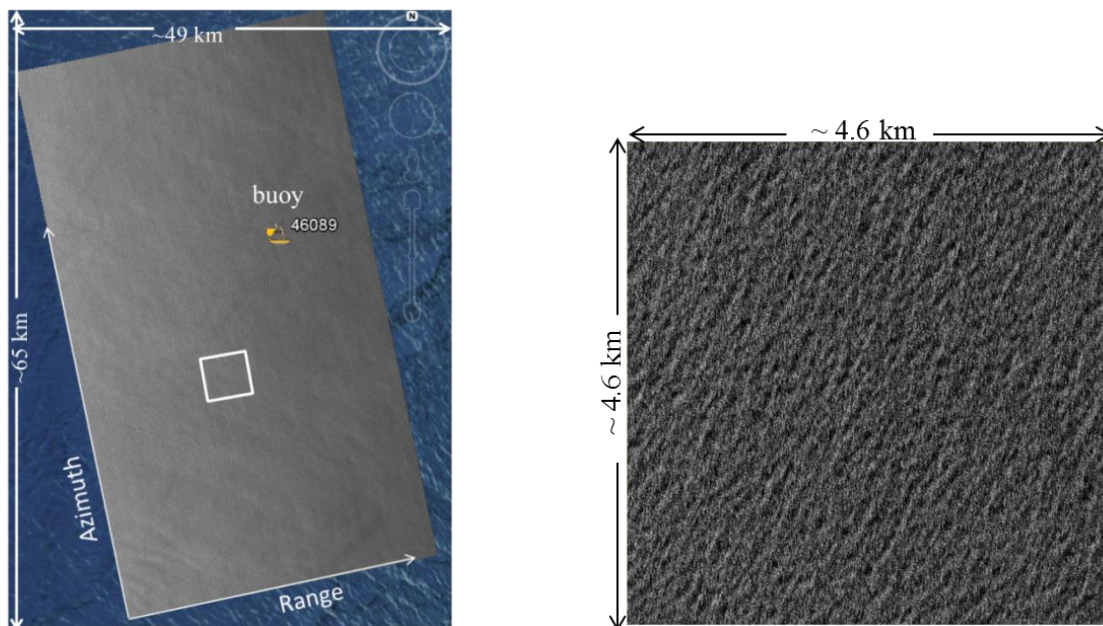


Figure A.1: TD-X VV polarized StripMap data image acquired on December 4, 2011 at 2:02 UTC over buoy 46089 located near the west coast of the USA (left). Sub-scene (4.6 x 4.6 km), taken from the left image (right).

The case presented here is the analysis of the TD-X VV polarized StripMap data image acquired over buoy 46089 under moderate sea state conditions. The H_s derived from the TD-X data is about 2.4m, which is the same as the H_s measured by the buoy. The comparison of the peak period shows almost a perfect match, with a derived peak period from the TD-X data of 10.1 s against 10.0 s given by the buoy. The ocean waves peak direction of 281 ° derived from SAR is a perfect match with the buoy.

A summary of the meteo-marine parameters derived from the TD-X data and measured by the buoy 46089 are given in Table A.1. The derived 1D and 2D spectra from the TD-X data are shown in figure A.2. The wave spectrum given by the buoy has an irregular spectral shape. There are no obvious peaks in the wave spectrum. The spectral shape spectrum derived from TD-X data generally visually approximates, with some differences, the spectral shape of the

spectrum given by the buoy. The major differences are the SAR derived spectrum has higher energy in the lower frequencies than the wave spectrum given by the buoy, and the peak in the higher frequencies after the azimuth cut-off frequency is not observed in the 1D spectrum derived from the SAR data.

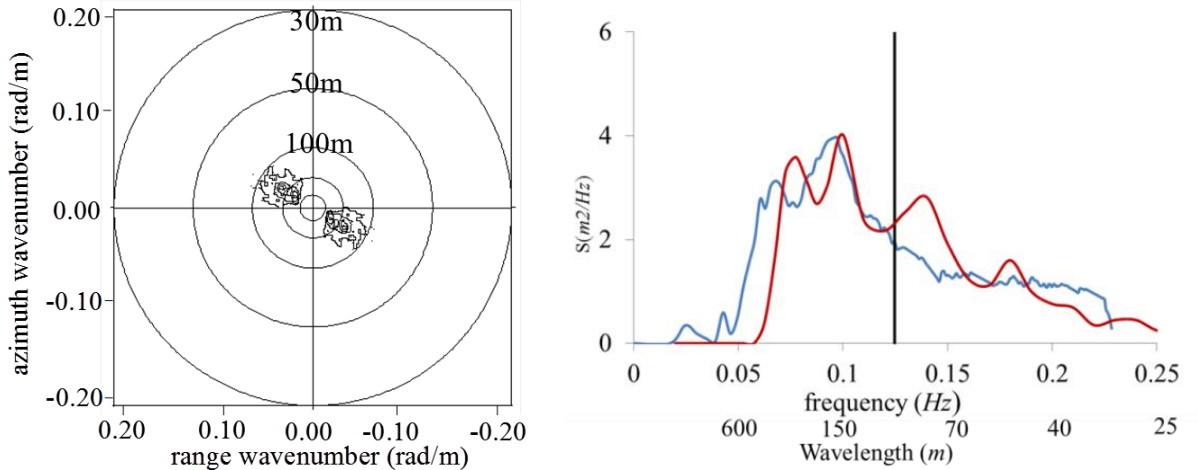


Figure A.2: 2D spectrum derived from TD-X VV polarized StripMap image acquired on December 4, 2011 at 2:02 UTC over buoy 46089 (left). Comparison of the 1D spectrum derived from TD-X data (blue) and the buoy 1D spectrum (red). The black vertical line represents the derived cut-off frequency: 0.124 Hz (102 m wavelength) (right).

Table A.1: Sea state parameters provided by buoy 46089, the WAM wave model at the DWD, and derived from the collocated TD-X image.

	$H_s(m)$	$T_p(s)$	$\lambda_p(m)$	$Dir(^{\circ})$	$U(m/s)$	$Udir(^{\circ})$
<i>DWD</i>	2.4	12.3	236	305	8.2	347
<i>buoy</i>	2.4	10.0	159	281	7.2	348
<i>TD-X</i>	2.4	10.1	156	281	7.0	-

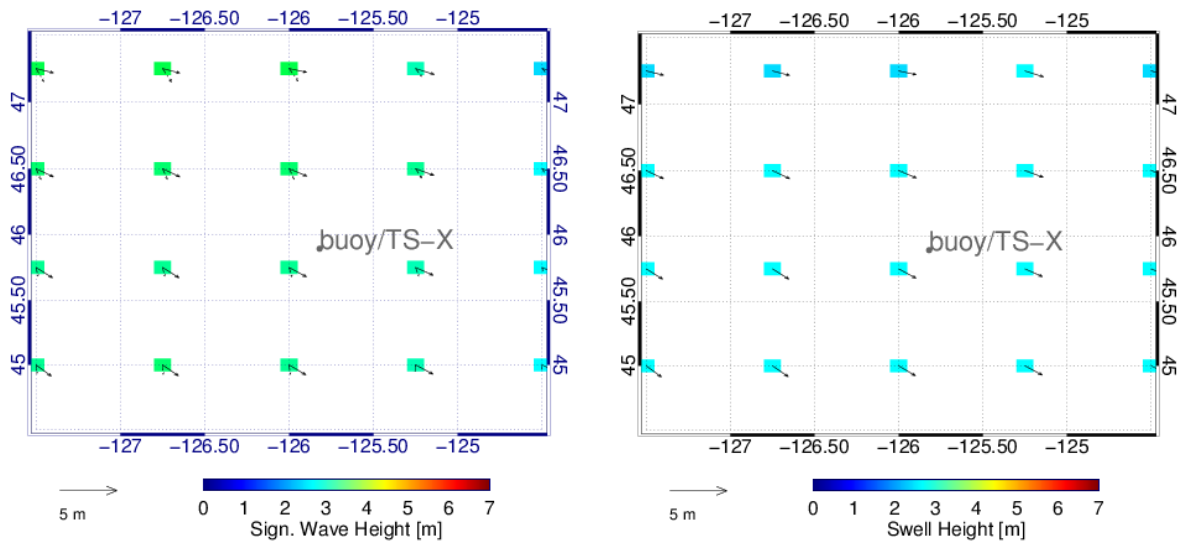


Figure A.3: H_s wave field (left) and *swell* wave height (right) on December 4, 2011 at 2:02 UTC given by the WAM wave model running at the DWD.

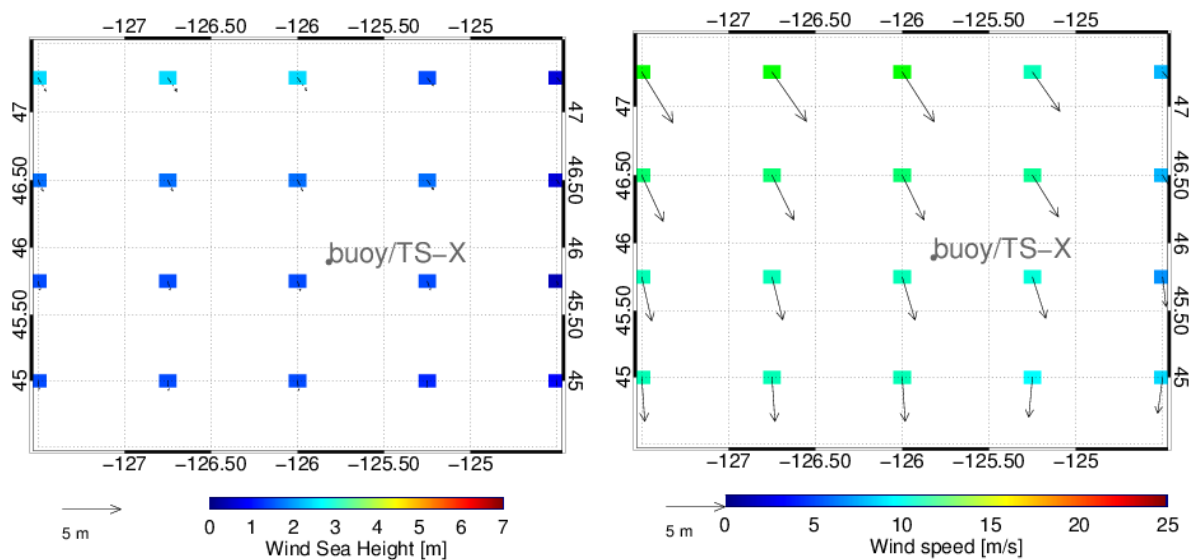


Figure A.4: *Wind sea* height (left) and wind field (right) on December 4, 2011 at 2:02 UTC given by the WAM wave model running at the DWD.

Case study A2: Moderate sea state, one wave system: TS-X VV polarization StripMap data image acquired over buoy 46005 (46°5'59" N 131°0'5" W) with centre incidence angle of 24° on December 4, 2011 at 15:04 UTC.

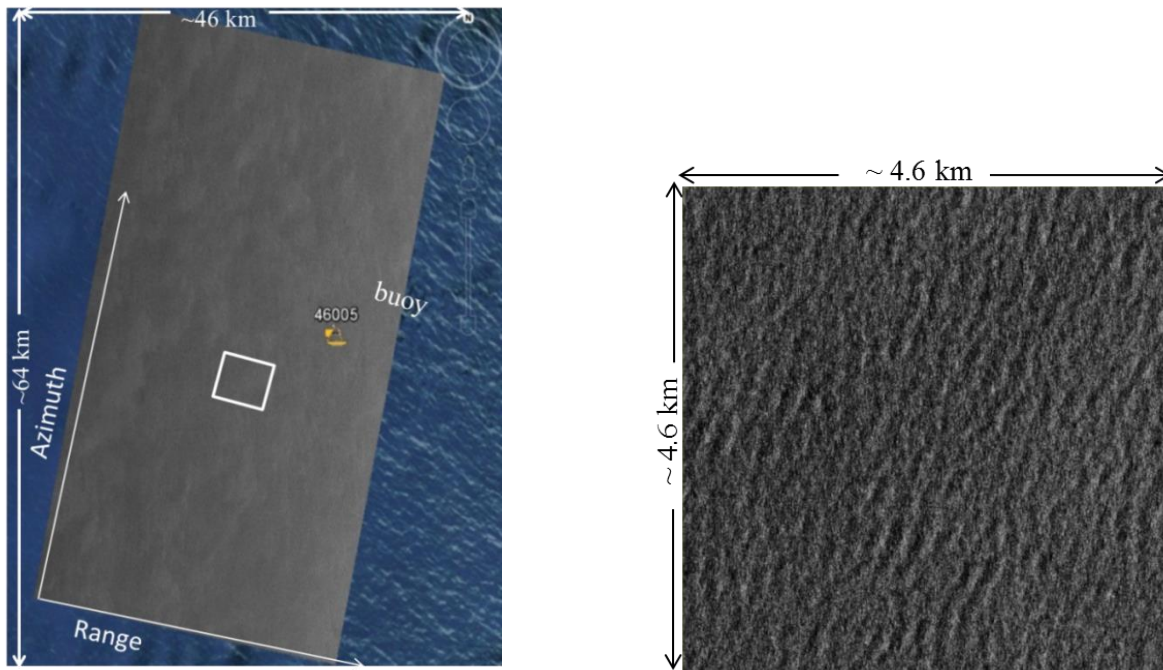


Figure A.5: TS-X VV polarized StripMap image acquired on December 4, 2011 at 15:04 UTC over buoy 46005 (left). Sub-scene (4.6 x 4.6 km) taken from the image left (right).

The case presented here is the analysis of the TS-X VV polarized StripMap data image acquired over buoy 46005 during moderate sea state conditions. The H_s derived from the TS-X data is of about 2.6 m, the same as the H_s measured by the buoy. The H_s estimated by the wave model is underestimated by 0.3 m. The TS-X derived peak period is of 12.4 s against 12.1 s given by the buoy.

This buoy does not provide information regarding ocean waves propagation direction. Therefore the comparison of the ocean waves peak direction is done with wave model data. The waves peak direction given by wave model is of 293° against 301° derived from the TS-X data. The wave direction measured results confirm that the imaged wave field is a range propagating wave field. A summary of the meteo-marine parameters derived from TS-X data and given by the buoy are given in Table A.2.

The derived 1D and 2D spectra from the TD-X data are shown in figure A.6. The derived 2D spectrum from the TS-X data shows a single wave system. The comparison of the 1D spectrum shows a steep energy peak which has a very good fit with the one with one given by the buoy. The derived azimuth *cut-off* wavelength is 127m. The good comparison results are explained by the fact that the imaged wave field is composed of long wavelength ocean waves traveling in range direction, which makes it an optimal case to be imaged by the SAR,

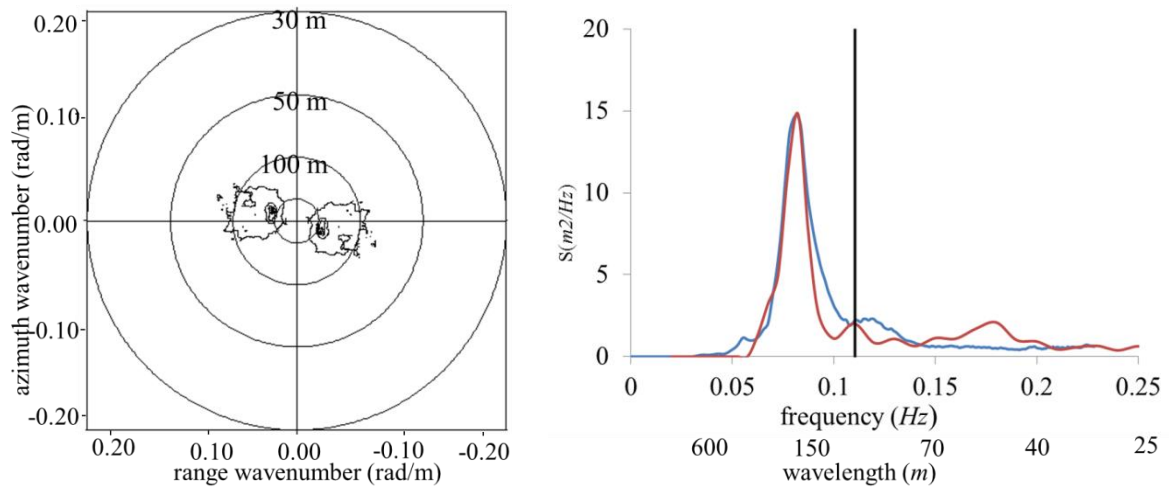


Figure A.6: 2D spectrum derived from TS-X VV polarized StripMap image acquired on December 4, 2011 at 15:04 UTC over buoy 46005 (left). Comparison of the 1D spectrum derived from TS-X data (blue) and the buoy 1D spectrum (red). The black vertical line represents the derived *cut-off* frequency: 0.110 Hz (127 m wavelength) (right).

Table A.2: Sea state parameters provided by buoy 46005, the WAM wave model at DWD, and derived from the collocated TS-X image.

	$H_s(m)$	$T_p(s)$	$\lambda_p(m)$	$Dir(^{\circ})$	$U(m/s)$	$Udir(^{\circ})$
<i>DWD</i>	2.3	13.5	285	293	8.9	357
<i>buoy</i>	2.6	12.1	229	-	8.8	-
<i>TS-X</i>	2.6	12.4	240	301	9.0	-

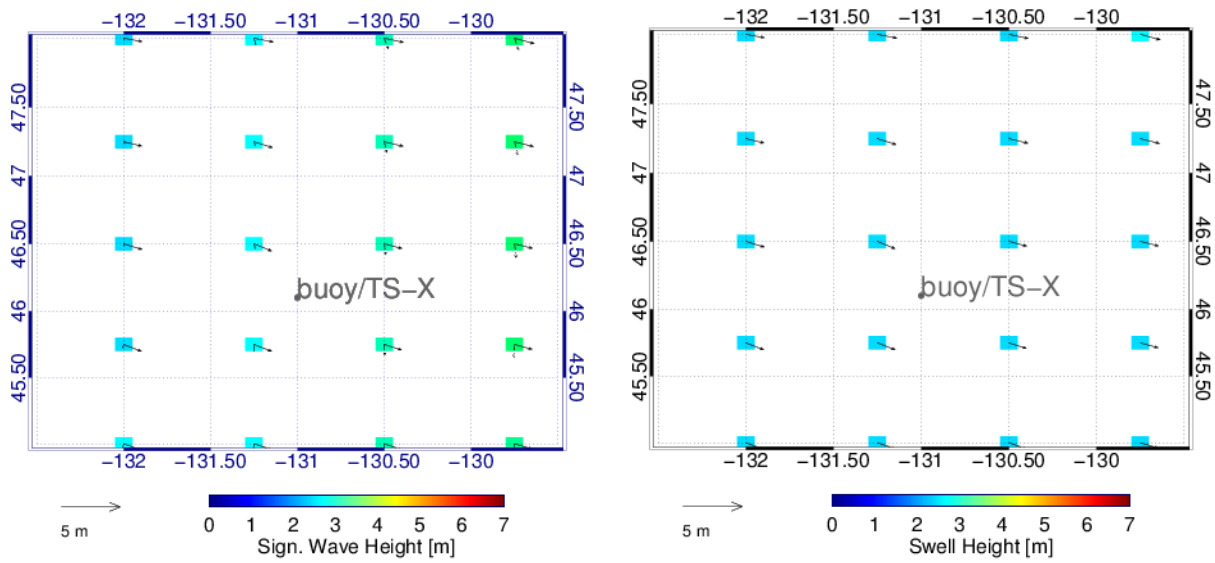


Figure A.7: H_s wave field (left) and *swell* wave height (right) on December 4, 2011 at 15:04 UTC given by the WAM wave model running at DWD.

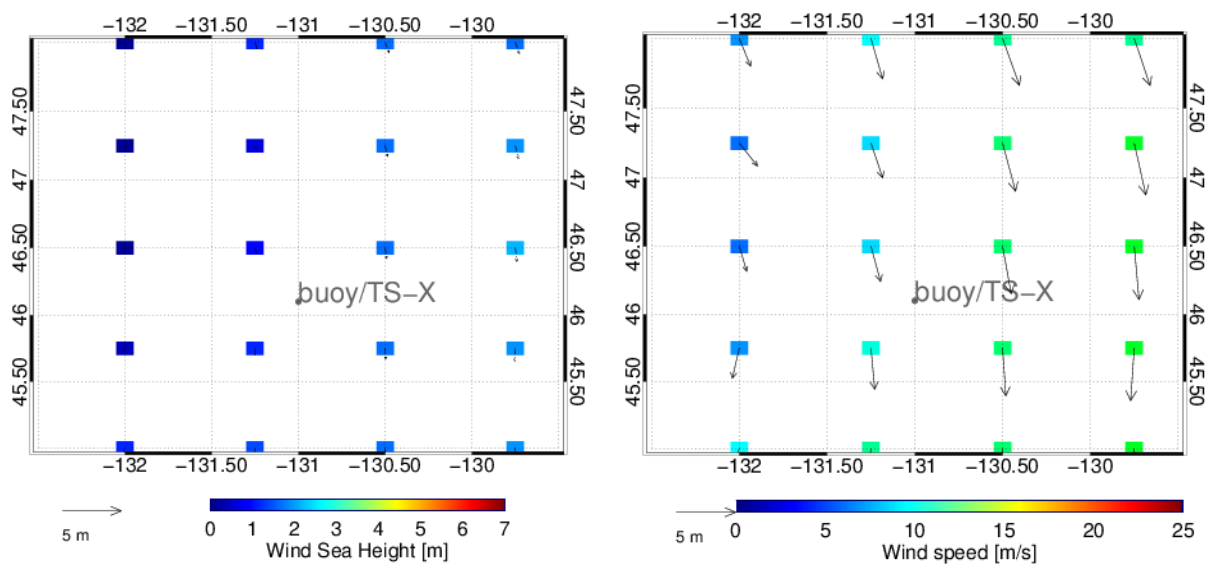


Figure A.8: *Wind sea* height (left) and wind field (right) on December 4, 2011 at 15:04 UTC given by the WAM wave model running at DWD.

Appendix B

2D wave fields derived from TS-X and marine radar WaMoS data

In this appendix some of the results achieved on the project TerraWAM and on the paper [Bruck *et al.*, 2010] are presented and discussed. The objective is the comparison of the 2D spectrum derived from TS-X data and the marine radar WaMoS data, as both instruments are X-band radars able to obtain 2D wave information of the sea surface. The ocean waves peak wavelength and direction are inter-compared and auxiliary verified by *in-situ* wave measurements.

B.1 Marine (X-band) Radar (WaMos II) data



Figure B.1: Marine Radar located at the top of the pole (left) Radar image (right) © DLR.

The **Wave and Surface Current Monitoring System (Wamos II)** [Ziemer *et al.*, 1994] is software-radar system which objective is to analyze X-band marine radar data acquired over the sea surface and provide information regarding sea state. It was developed at the GKSS in the early 80's and has been commercial since 1995 by OCEANWAVES <http://www.oceanwaves.org/start.html>. The software is able to transform a standard marine radar (figure B.1), which is used for detecting targets (ships), and extends its abilities to

measure ocean waves. In order to obtain an estimation of the sea state; significant wave height and peak period, usually a stack of n radar images, taken each 2 s, of the ocean surface is taken for analysis, [Nieto Borges et al., 2004] (figure B.2). This means, that the marine radar WaMoS is able to measure the ocean wave field in the spatial and temporal domain.

The system uses the output from marine X-band radar to determine wave and surface current parameters in near real-time. The measurements are based on the backscatter of radar energy from the ocean surface (sea clutter) [Nieto Borges et al., 2004], [Nieto Borges et al., 2008]. The backscatter, which is visible on the marine radar, shows the wave patterns. The WaMoS II is a software system that from a sequence of X-band marine radar images calculates in real time the two dimensional spectrum. The TS-X/TD-X data and marine radar WaMos data have one important detail in common, they are both radar based sensor and able to measure the wave field in the two dimensional domain. The marine radar, additionally, also measures in the time domain

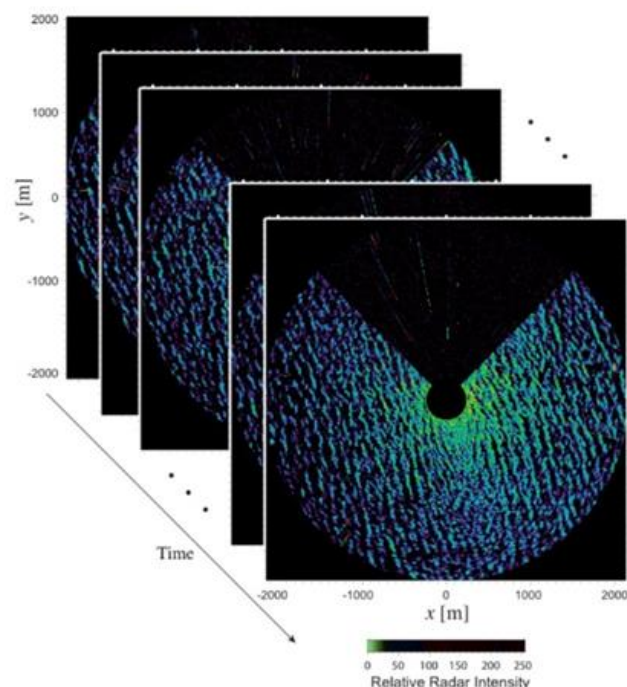


Figure B.2: Sequence of marine radar WaMoS data images of the sea surface taken for the same location over time, as seen in [Nieto Borges et al., 2004].

B.2 Objectives

The marine radar data used for the work presented in this thesis is taken from the WaMoS system installed in the Ekofisk oil platform, located in the North Sea ($56^{\circ}33'N$ $3^{\circ}25'E$) (figure B.3).



Figure B.3: Ekofisk oil platform located the North Sea. The marine radar WaMoS is located in the platform, measuring the sea state conditions of the ocean area surrounding the platform (~5km).

TS-X SAR data is acquired over the Ekofisk oil platform, where the marine radar WaMos is installed. The objective is to inter-compare the sea state information derived from the TS-X data, from radar data acquired by the marine radar WaMos and compare with *in-situ* wave measurements. More precisely, the goal is to check if the 2D wave field imaged by the marine radar WaMoS and the TS-X/TD-X SAR sensor are measured alike.

To assert the measuring capabilities of both sensors, the 2D spectrum derived from both sensors are compared visually and summarized into sea state parameters, H_s , peak period and peak direction for comparison.

Significant wave height is estimated from the marine radar data by taking a sequence of about 20 radar images. This has the advantage that artefacts can be smeared out from the sequences of the sequence of the radar images. The TS-X data can be only taken one time as a photo snapshot. The TS-X sub-scenes are taken from an area about 3 km distance from the Ekofisk oil platform to avoid obvious interference from the structure to the wave field. The distance cannot be larger because, then the TS-X imaged wavefield would not take into account

the partial interference related to the Ekofisk oil platform which the marine radar and the buoy cannot avoid to measure, as they are located there.

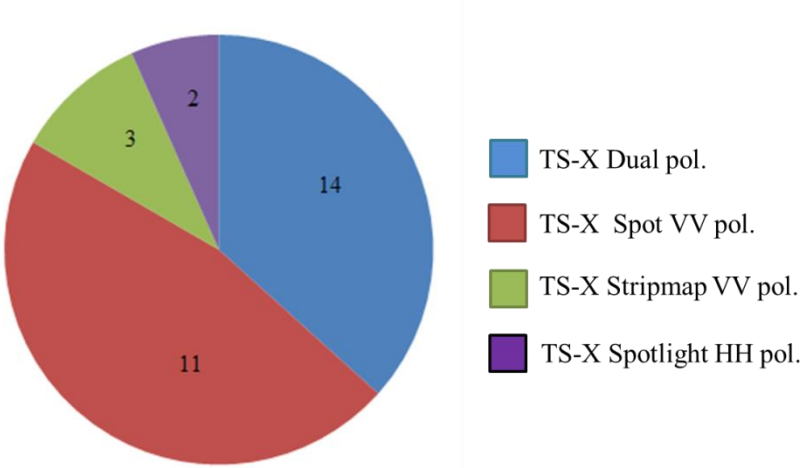


Figure B.4: Distribution of different TS-X data image mode acquired over the Ekofisk oil platform with valid *in-situ* and marine radar WaMoS measurements.

B.3 Inter-comparison *in-situ*/TS-X/marine radar WaMoS data

The XWAVE algorithm is applied for different types of TS-X/TD-X products. The XWAVE algorithm is also tuned with SpotLight data, HH polarized data and dual polarized data, although with a limited data-set. The data is tuned directly with wave measurements from the buoy located at the oil platform Ekofisk. Because the TS-X acquisitions were taken at the same location no incidence dependence is needed. For this study only here TS-X data is acquired.

The marine radar WaMoS covers an ocean area of about 5 km around the Ekofisk oil platform. The Ekofisk oil platform interferes with the surrounding wave field. The wave field by the radar is predicted to be slightly different from the wave field outside the 5 km perimeter analysed. However the buoy is also located in the Ekofisk oil platform, and because it is a point located device is then more probable to measure a wave field disturbed by the platform. Figure.B.5 shows the H_s derived from a single marine radar image, against H_s derived from sequences of marine radar images. It is visible that H_s derived from both is different, but does not change significantly for this case. Figure B.6 shows the comparison of H_s derived from marine radar Wamos and *in-situ* wave measurements. With a good correlation $R = 0.90$ and a scatter index Si of 20. The comparison of significant wave eight derived from TS-X data for the same measurements against *in-situ* wave measurements resulted in a good correlation $R = 0.70$ and a Scatter index $Si = 0.17$, (figure B.7). Comparison of the significant wave height derived

from the marine radar WaMos and the significant wave height derived from TS-X data resulted in a correlation $R = 0.77$ and a Scatter index $Si = 0.30$ (figure B.8). The comparison of the wave peak period derived from TS-X data with *in-situ* wave measurements is given in figure B.9. The comparison of the peak period derived from TS-X data compared to the peak period derived from the marine radar Wamos is shown in figure B.10. And finally, the comparison of the peak wave direction derived from TS-X data with the peak direction derived from the marine radar WaMos data is given in figure B.11.

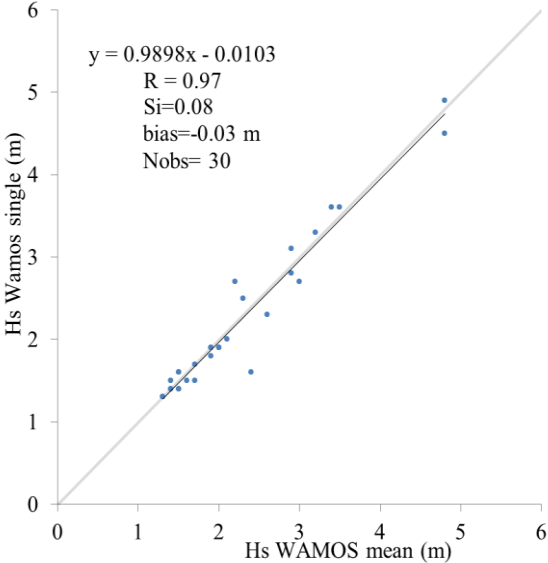


Figure B.5: Comparison of H_s derived from a single marine radar image with H_s derived from marine radar WaMoS images.

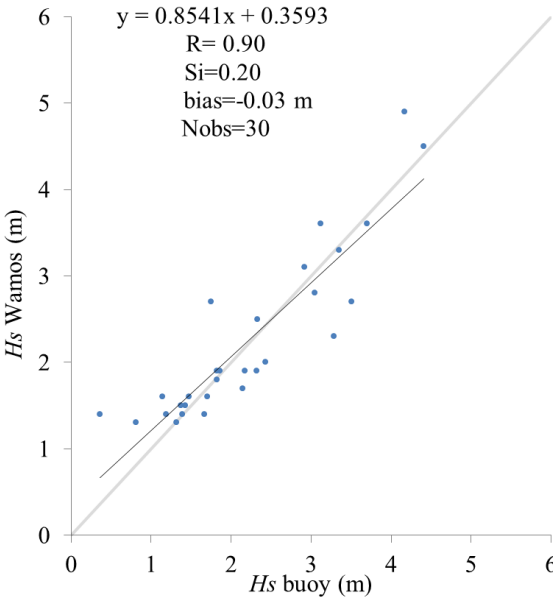


Figure B.6: Comparison of H_s given by the marine radar WaMoS with *in-situ* buoy wave measurements.

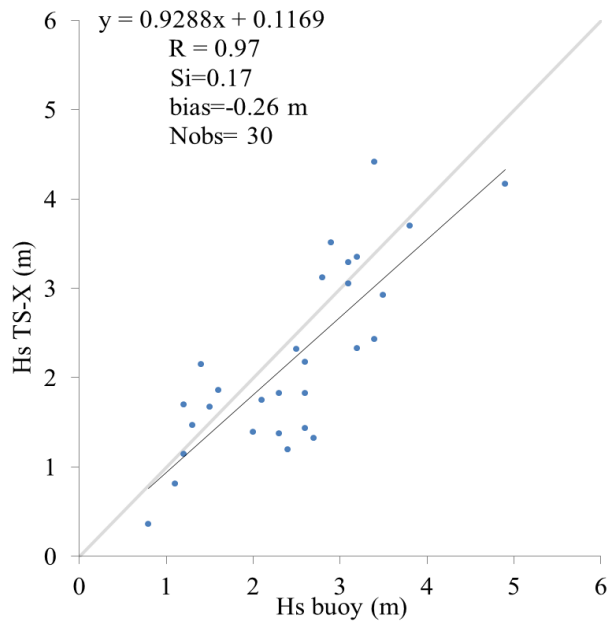


Figure B.7: Comparison of H_s derived from TS-X data with *in-situ* buoy wave measurements.

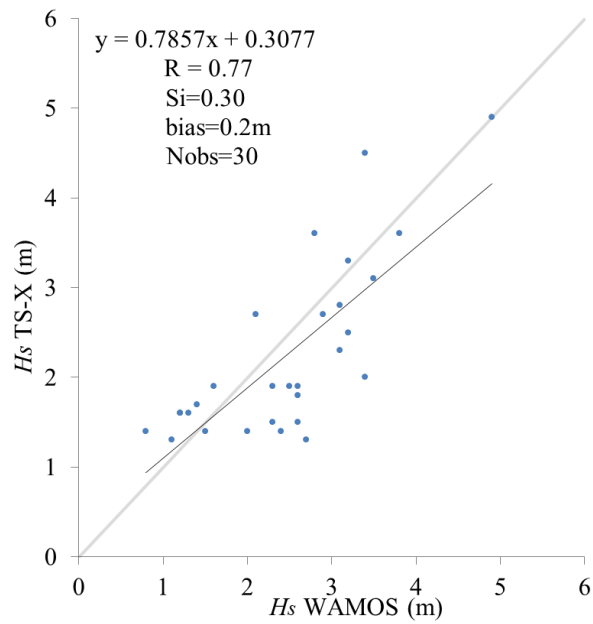


Figure B.8: Comparison of H_s derived from TS-X data with H_s given by the marine radar WaMoS.

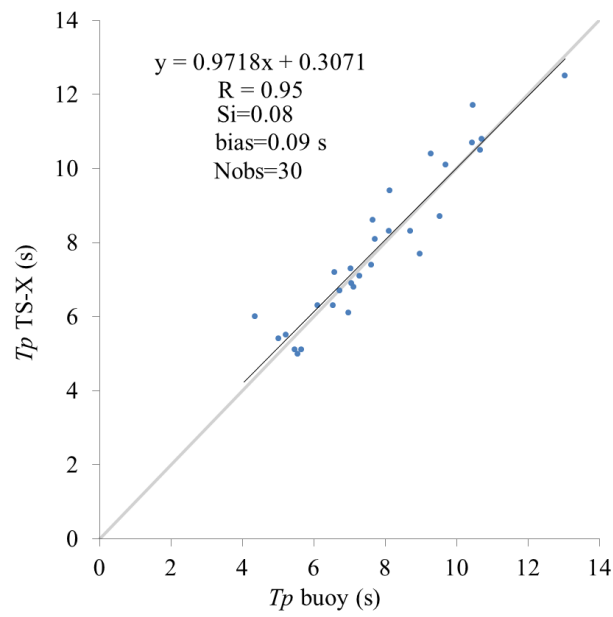


Figure B.9: Comparison of the peak period derived from the TS-X data against the peak period given by the buoy.

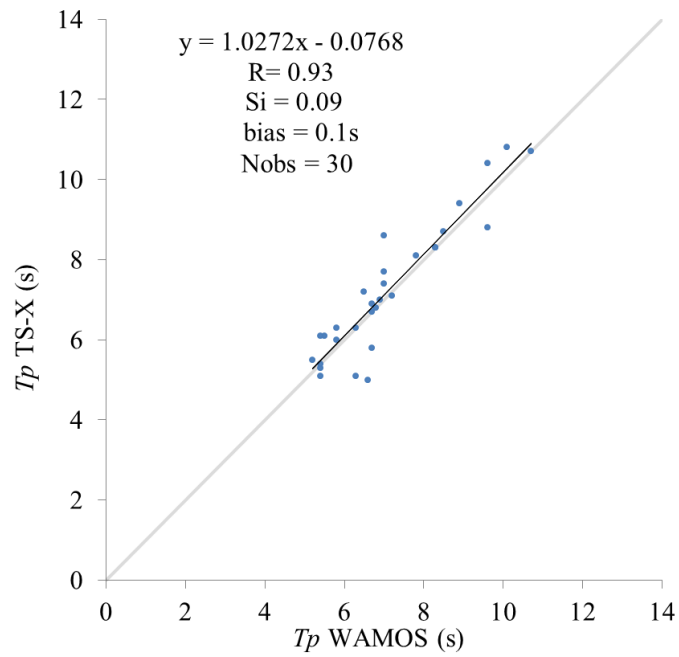


Figure B.10: Comparison of the peak period derived from TS-X data against the peak period measured by the marine radar WaMos.

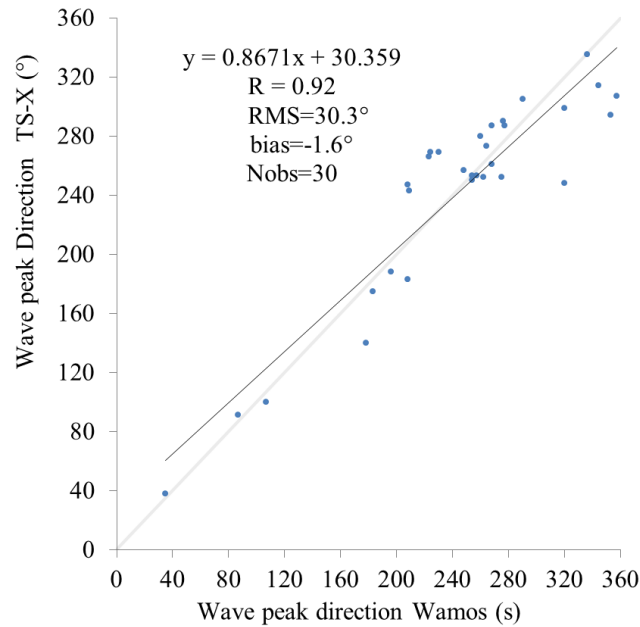


Figure B.11: Comparison of the peak wave direction derived from TS-X data against the wave peak direction derived from the marine radar WaMoS data.

B.4 Case studies

In this sub-section, three case studies of analysis done on TS-X data taken over the Ekofisk oil platform are presented. The first two cases are TS-X SpotLight mode acquisitions and the third case is a dual polarized StripMap TS-X data image. For the dual polarized data case, only the results for VV polarized data is presented. For each case study the derived 2D spectrum from both the TS-X and the marine radar data are shown. Sea state parameters are derived from both radar systems and compared to *in-situ* wave measurements.

Case study I

TS-X VV polarized SpotLight data image acquired on 15 May, 2009 at 17:19 UTC.

Main details:

- TS-X SpotLight VV pol data.
- moderate–high sea state conditions
- two wave systems

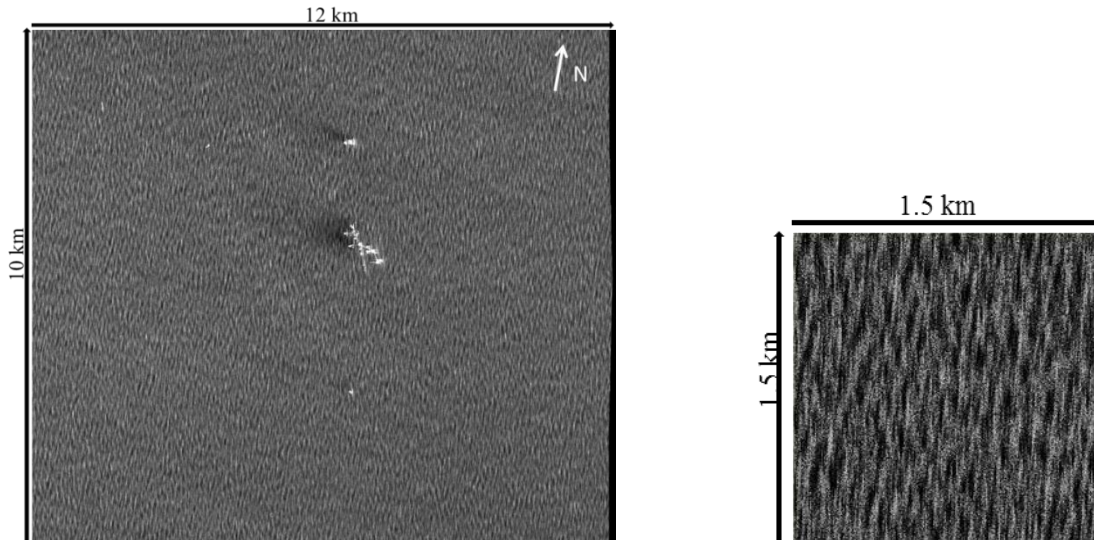


Figure B.12: TS-X VV polarized SpotLight data image taken over Ekofisk oil platform on May 15, 2009 at 17:19 UTC (left). Sub-scene from image showed left (right).

The first case presented here, is the analysis of a sub-scene taken from the TS-X SpotLight acquisition taken over Ekofisk oil platform on the 15th May 2009 under rough sea state conditions (figure B.12). The 2D spectrum derived from both the SAR and the marine radar WaMoS data are shown in figure B.13.

There are differences visible between both the 2D spectra. In the spectrum derived from TS-X data the *cut-off* effect signature is visible. This signature is seen as a spreading of the energy spectral values along the range axis (Chapter 7). Despite the influence of the *cut-off* effect, the quality of the derived peak parameters is good. The peak wavelength derived from the SAR spectrum is in good agreement with the *in-situ* value and with the WaMos. However the wave peak direction does not match. This is due to the fact that the imaged wave field is composed of two wave systems with same wavelength but different propagating directions. Therefore the SAR and WaMoS radar systems assume differently which one is the most energetic wave system. As there is no information available regarding ocean waves propagation direction, it is not possible to verify which one of the systems is correctly obtaining the wave direction.

The significant wave height derived from the SAR data using the XWAVE algorithm is slightly underestimated by about 0.2 m. The significant wave height derived from the marine radar WaMoS data is slightly underestimated by 0.1 m. A summary of the sea state parameters given by the three measurements devices is shown in Table B.1.

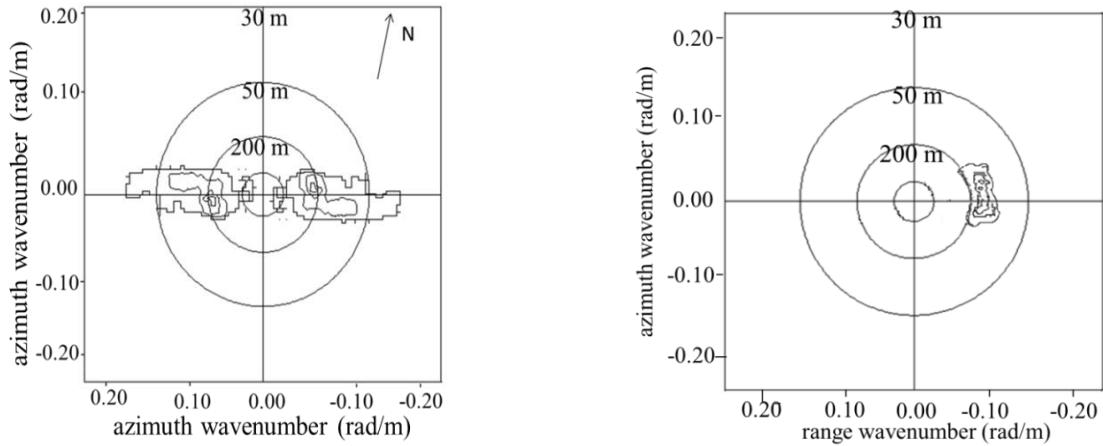


Figure B.13: 2D spectrum derived from the image data sub-scene (figure 11.10 right) (left) 2D spectrum derived from marine radar WaMoS data on May 15, 2009 at 17:19 UTC (right).

Table B.1: Sea state parameters given by the buoy, the WaMoS and derived from the collocated TS-X SpotLight data taken on May 15, 2009 at 17:19 UTC.

	$H_s(m)$	$T_p(s)$	$\lambda_p(m)$	$Dir(^{\circ})$
<i>Buoy</i>	3.7	8.7	119	-
<i>WaMoS</i>	3.6	8.3	108	291
<i>TS-X</i>	3.5	8.3	108	267

Case study II

TS-X HH polarized StripMap data image acquired on May 4, 2009 at 17:19 UT

Main details:

- TS-X StopLight VV pol data.
- moderate sea state conditions
- two wave systems

The second case presented here, is the analysis of a sub-scene taken from the TS-X SpotLight acquisition taken over Ekofisk oil platform on the 4th 2009, under moderate sea state conditions, (figure B.14). The 2D spectrum derived from the SAR and the marine radar WaMos data are shown in figure B.15. Also in this case it is observed in the 2D spectrum derived from the SAR data the *cut-off* effect signatures. Despite the presence of *cut-off* effect signatures, the peak wavelength and direction derived from the SAR spectrum are in good agreement with *in-situ* wave measurements and with the WaMos derived parameters. A summary of the sea state parameters given by the three measurements devices is shown in Table B.2.

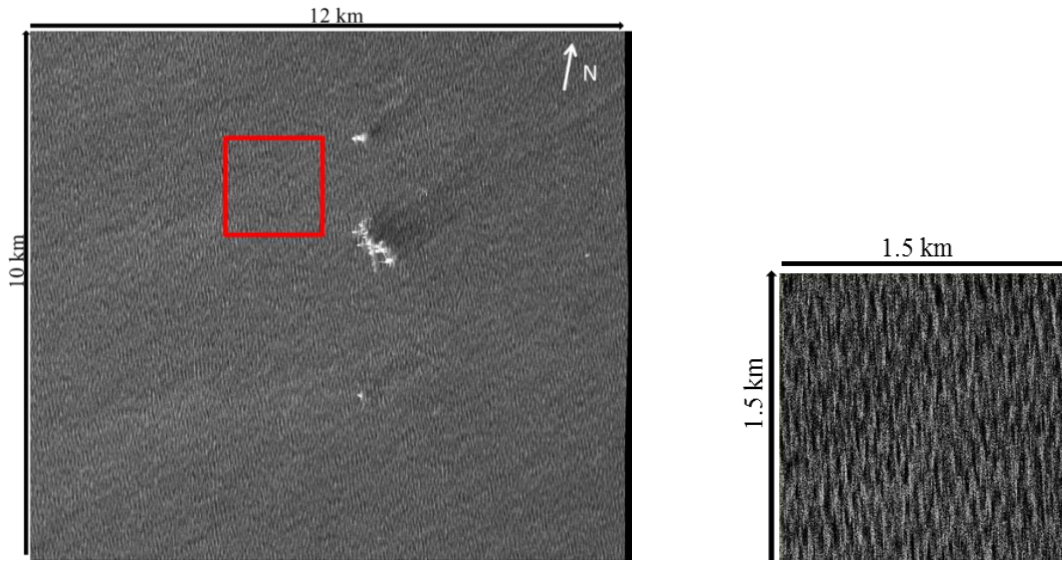


Figure B.14: TS-X VV polarized SpotLight image data taken over Ekofisk oil platform on May 4, 2009 at 17:19 UTC (left). Sub-scene from image showed left (right).

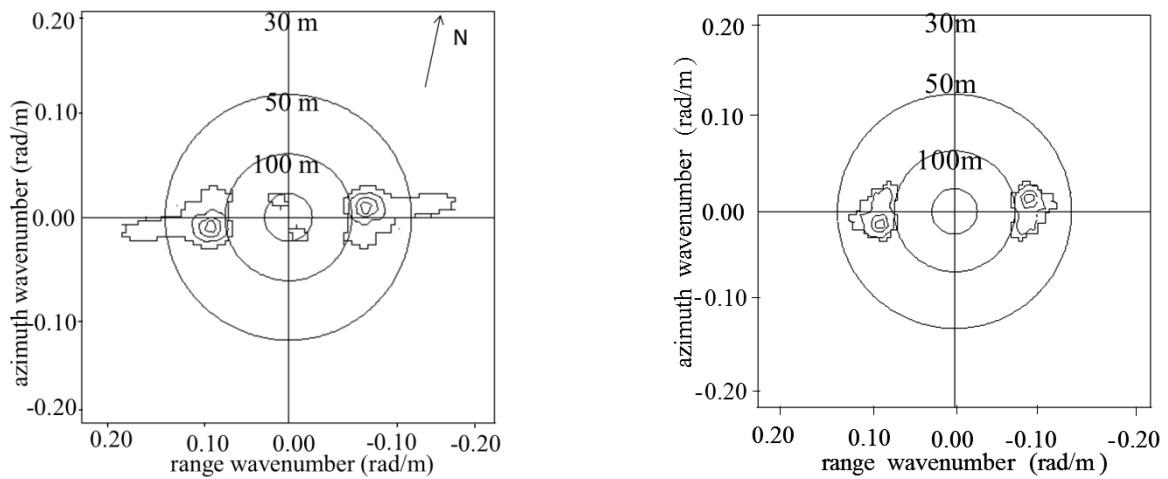


Figure B.15: 2D spectrum derived from sub-scene in figure B.14 (left). 2D spectrum derived from marine radar WaMoS data on May 4, 2009 at 17:19 UTC (right).

Table B.2: Sea state parameters given by the buoy, the WaMoS and derived from the collocated TS-X SpotLight data taken on May 4, 2009 at 17:19 UTC.

	$H_S(m)$	$T_p(s)$	$\lambda_p(m)$	$Dir(^{\circ})$
<i>Buoy</i>	2.4	6.7	70	-
<i>WaMoS</i>	2.0	6.7	70	248
<i>TS-X</i>	2.4	7.2	81	249

Case study III

TS-X dual polarized StripMap data acquired on August 16, 2009 at 17:27 UTC

Main details:

- TS-X dual polarized StripMap data
- Near range Wave field
- Moderate sea state conditions

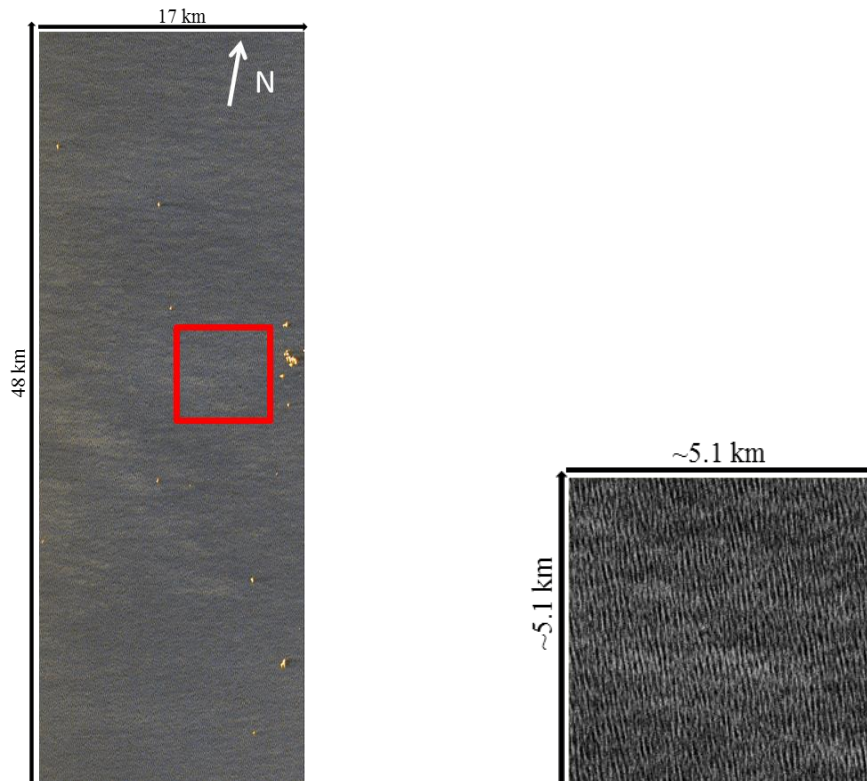


Figure B.16: TS-X dual polarized (HH-VV) StripMap image data taken over Ekofisk oil platform on August 16, 2009 at 17:27 UTC (left). TS-X Sub-scene from image showed left (right).

The third case presented here, is the analysis of the TS-X dual polarized StripMap data image taken on the August 16, 2009 over Ekofisk oil platform under moderate sea state conditions (figure B.16). The results presented here are for the TS-X VV polarized data. The 2D spectrum derived from both the SAR and the marine radar WaMos data are shown in figure B.17. The derived peak information, peak wavelength and direction from the SAR spectrum, are in good agreement with *in-situ* wave measurements and with the WaMos derived parameters. The significant wave height given by the buoy is of 3.4 m. The estimation of significant wave height by the XWAVE algorithm is slightly overestimated by 0.2 m. The estimation of wave height by the marine radar WaMos is overestimated by about 0.1 m. A summary of the sea state parameters comparison between the three measurements devices for this case is given in Table B.3.

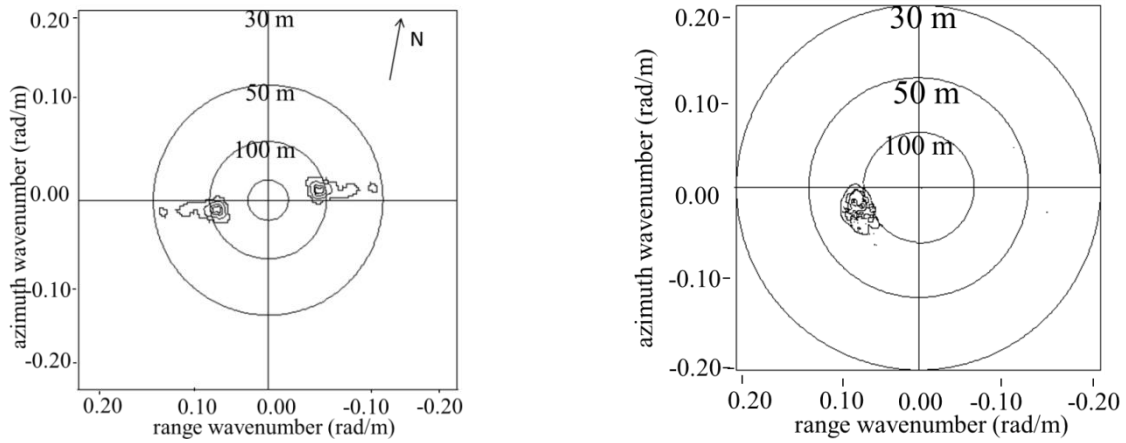


Figure B.17: 2D spectrum derived from sub-scene from TS-X dual polarized StripMap on August 16, 2009 at 17:27 UTC (figure 10.13) (left). 2D spectrum derived from marine radar WaMoS data for the same date and time (right).

Table B.3: Sea state parameters given by the buoy, the WaMoS and derived from the collocated TS-X StripMap data taken on August 16, 2009 at 17:27 UTC.

	$H_S(m)$	$T_p(s)$	$\lambda_p(m)$	$Dir(^{\circ})$
<i>Buoy</i>	3.4	8.1	102	-
<i>WaMoS</i>	3.3	8.3	108	254
<i>TS-X</i>	3.6	8.6	116	251

Appendix C

In this appendix the algorithm to derived sea surface wind speed (XMOD) is described and discussed. Also included in this appendix, is the comparison of sea surface wind speed estimated using the XMOD to *in-situ* wind speed measurements.

C.1 Sea surface wind speed at 10 m height (U_{10})

The sea surface wind speed U_{10} is essential as input for the XWAVE algorithm. An X-Band Geophysical Model Function (GMF) algorithm was established for VV and HH polarized TS-X and TD-X data to obtain the wind fields (XMOD-algorithm) [Ren *et al.*, 2012]. The GMF relates sigma naught σ_0 , incidence angle θ and wind direction ϕ . The XMOD linear model function is defined as

$$\sigma_0 = x_0 + x_1 v + x_2 \sin(\theta) + x_3 \cos(2\phi) + x_4 v \cos(2\phi) \quad (\text{C.1})$$

where σ_0 is NRCS, U is the wind speed, θ is the incidence angle and ϕ is the radar azimuth relative to wind direction. The constants x_0 to x_4 now tuned using data from the space-borne Imaging Radar-C/X (SIR-C/X) mission in 1994 and the European Center (ECMWF) reanalyzed ERA-40 wind fields (ECMWF: Re-Analysis of the global atmosphere and surface conditions for 45-years). Wind speed from TS-X data can be retrieved using this model accurately between 2 m/s and 25 m/s for incidence angles θ between $20^\circ \sim 55^\circ$.

The wind direction is given by weather numerical models or derived directly from the SAR image, by analyzing wind related signatures (e.g wind streaks) visible on SAR data images. These signatures are produced by airflow over the sea surface, which interaction of the wind with the sea surface is visible in the SAR images as wind streaks (Chapter 6). In coastal areas the wind shadowing structures in SAR images are indicator of the wind direction. Additionally, the local gradient method [Koch W., 2004] or Fourier analyses can be implemented [Alpers *et al.*, 1994] to determine the wind direction. Other sources of wind direction input are given by wind models (recall Chapter 8). The dependency of sigma naught and the wind direction is shown in figure C.1. For the validation of the XMOD algorithm results, the wind direction used as input is the one measured by the anemometers. This is done to avoid a source error related to the derivation of the wind direction from SAR data. This makes the XMOD wind speed results only dependent on the performance of the model.

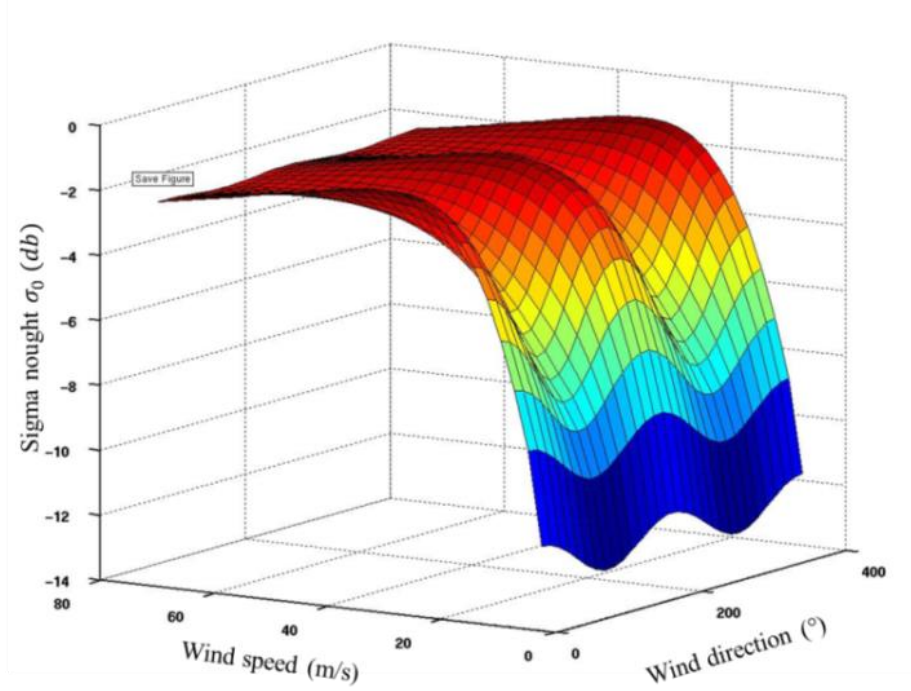


Figure C.1: Graphic representation of the sea surface wind speed U_{10} estimation from TS-X/TD-X SAR data by the XMOD function [Ren et al., 2012].

C.2 Validation of the sea surface wind speed U_{10} algorithm XMOD

Wind speed can have high variation on the area covered by the TS-X/TD-X StripMap image (30km x50 km). The wind speed high variation named as wind gusts are related with atmospheric instability. An example case of the XMOD algorithm applied on TD-X data is shown in figure C.2.

The XMOD algorithm is applied to TS-X/TD-X VV polarized StripMap data collocated with buoys (wave measurements devices). The sea surface wind speed U_{10} derived by the XMOD algorithm is compared with the wind speed measured by the anemometers located at the wave measurement devices. The values of wind speed obtained with the XMOD algorithm, are derived from a sub-scenes of about 5.1 km side length, collocated with the anemometer/buoy position. The performance of the XMOD algorithm on a data-set of 100 TS-X/TD-X Stripmap VV polarized data images collocated with *in-situ* wind observations resulted on good results with a correlation R of 0.93 and a scatter index Si of 0.15 and a bias of -0.25 m/s (figure C.3).

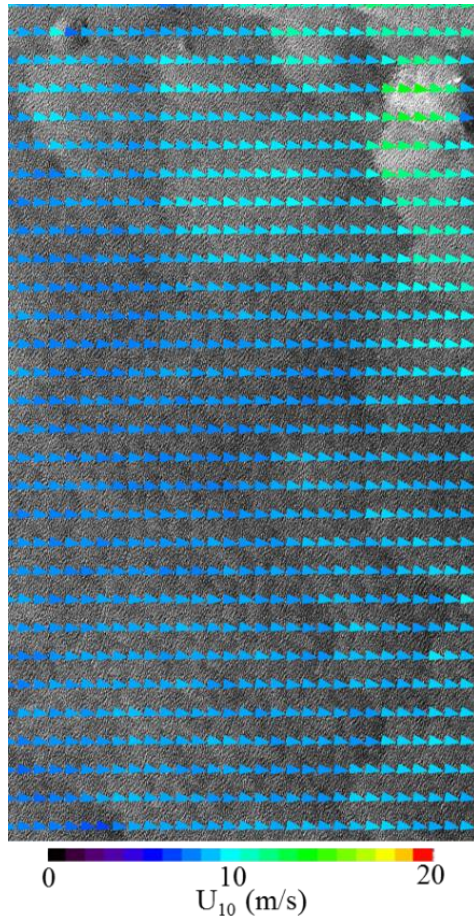


Figure C.2: Sea surface Wind fields U_{10} derived by the XMOD algorithm on the TanDEM-X VV polarized StripMap data image acquired on November 17, 2010 at 4:14 UTC over buoy 51000 near the Hawaii Archipelago.

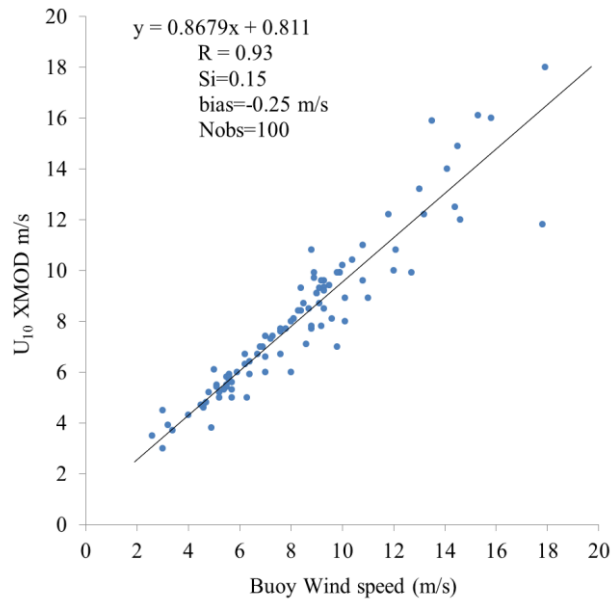


Figure C.3: Comparison of the derived sea surface wind speed at 10 m height, U_{10} , given by the XMOD algorithm and wind speed measured by anemometers.

Appendix D

In this appendix, it is presented a case study example of ocean waves analysis performed using TD-X Stripmap VV polarization data in deep water. The case provides an insight on the variation of sea state properties in the spatial domain in deep water. The variation is analyzed for different neighboring locations by selecting different sub-scenes inside the StripMap image. The variation of the sea state properties is also analyzed by selecting different sub-scene size. The TD-X image data analyzed is the TD-X Stripmap VV polarized data image taken on November 17, 2010 at 4:14 UTC over the buoy 5100, near the Hawaii Archipelago (figure D1). The different size sub-scenes taken from different locations in the TD-X data image are analyzed.

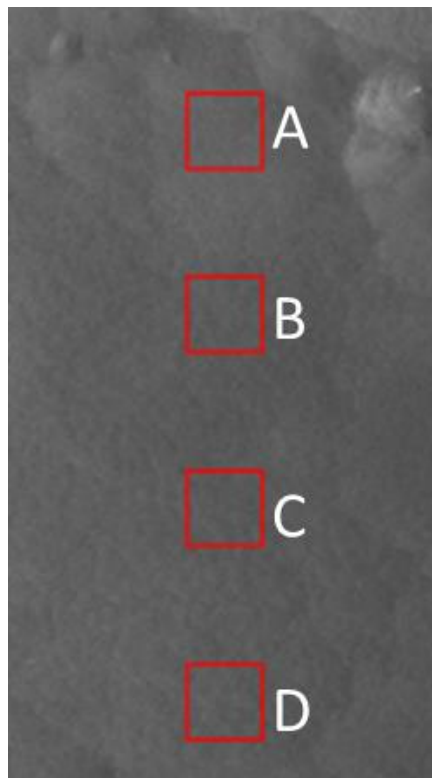


Figure D.1: TanDEM-X VV polarized StripMap image acquired on November 17, 2010 at 4:14 UTC over buoy 51000 near the Hawaiian Archipelago. Sub-scenes are analysed and results are shown in Table D.1 and from figure D.2 to figure D .5

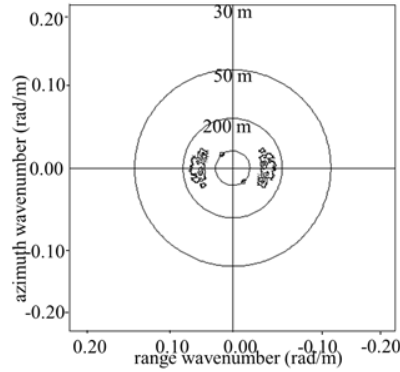
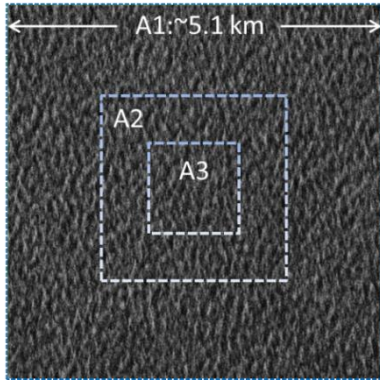
The TD-X data image is not considered homogeneous for the full area, but the area where sub-scenes are extracted it is defined as homogenous by the methodology described in Chapter 7. For each sub-scene the 2D spectrum and the sea state parameters are derived. The larger the sub-scene size chosen, the more ocean waves it contains, and it provides a closer

result to the average sea conditions. However it can be computationally inefficient or undesirable to analyze larger areas. For smaller sub-scenes the difference of the statistical results becomes more erratic, as the number of waves inside the sub-scene is less, and this leads to higher probability that the average value is influenced by the exceptions as freak waves, single waves, wave groups, etc. A 2048 pixel sided sub-scene is equivalent to about 5.1 x 5.1 km, 1024 pixel sided sub-scene is equivalent to about 2.6 x 2.6 km area, and a 512 pixel sided sub-scene is equivalent to about to about 1.3 x 1.3 km. The results for image data and using different box sized are shown in figure D.2, figure D.3, figure D.4 and figure D.5. The results are summarized in Table D.1.

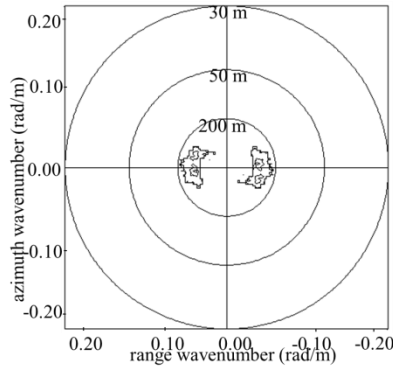
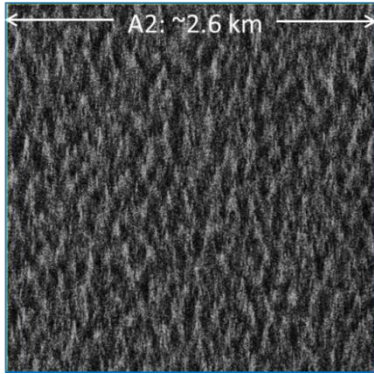
Table D.1: Summary of the sea state parameters results obtained for the different sized sub-scenes from the TD-X data acquired on November 17, 2010 at 4:14 UTC over buoy 51000 near Hawaii Archipelago.

	H_s (m)		T_p (s)		θ_p ($^\circ$)		U_{10} (m/s)	
	$\overline{H_s}$	stdv	$\overline{T_p}$	stdv	$\overline{\theta}$	stdv	$\overline{U_{10}}$	stdv
A	2.5	0.10	9.8	0.31	255	4.4	4.1	0.64
B	2.6	0.1	9.5	0.23	270	14.9	3.8	0.12
C	2.8	0.05	10.2	0.83	273	11.2	4.1	0.0
D	2.9	0.10	9.2	0.15	273	10.4	4.1	0.0

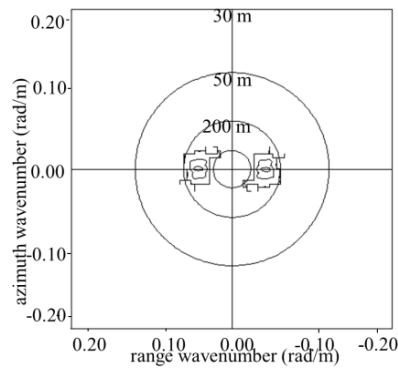
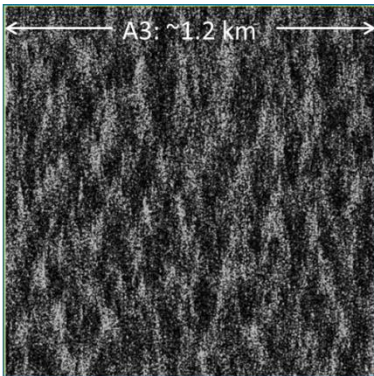
A



A1	~5.1km
H_s	2.6
T_p	9.9
θ	253
U_{10}	4.5



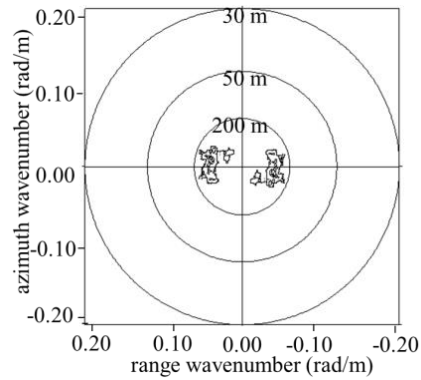
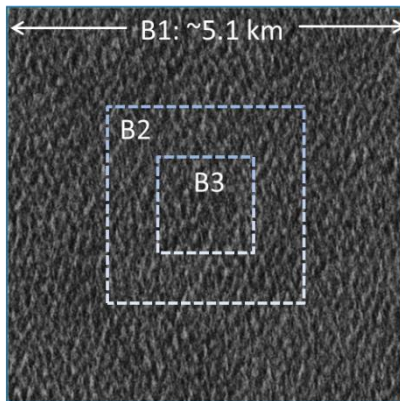
A2	~2.6 km
H_s	2.4
T_p	10.1
θ	252
U_{10}	3.4



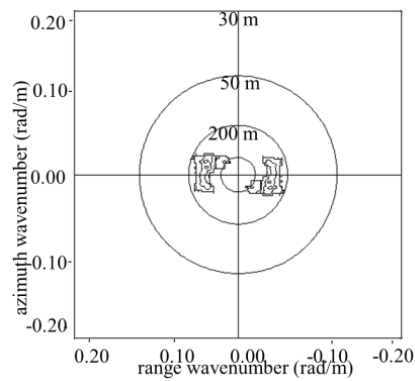
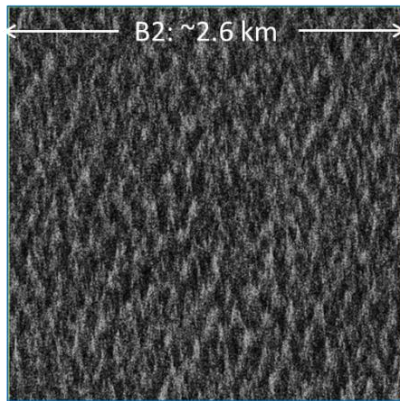
A3	~1.2 km
H_s	2.5
T_p	9.5
θ	260
U_{10}	4.5

Figure D.2: Sub-scenes from the TanDEM-X StripMap VV polarized image acquired on November 17, 2010 at 4:14 UTC over buoy 51000 near the Hawaii Island at position A and their respective derived 2D image spectrum and the meteo-marine parameters. On top the 2048 pixel sub-scene results are shown, in the centre a 1024 pixel sub-scene results are shown and on the bottom a 512 pixel sub-scene results are shown.

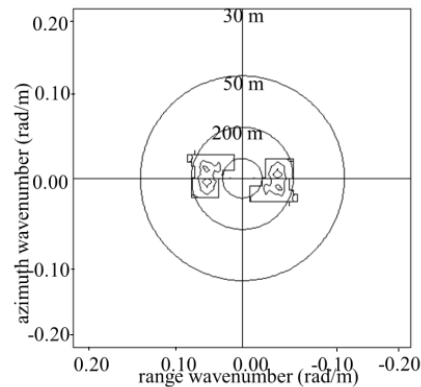
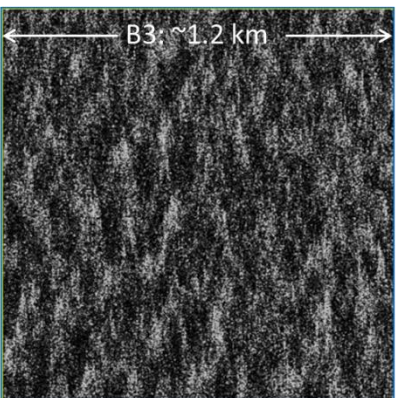
B



B1	~5.1 km
H_s	2.7
T_p	9.6
θ	276
U_{10}	3.9



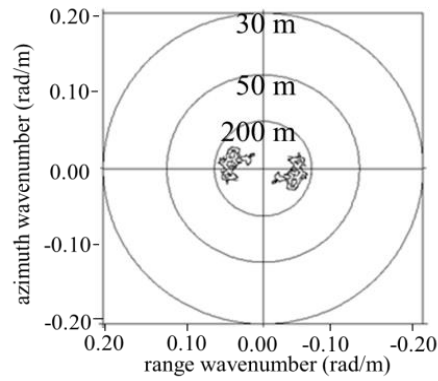
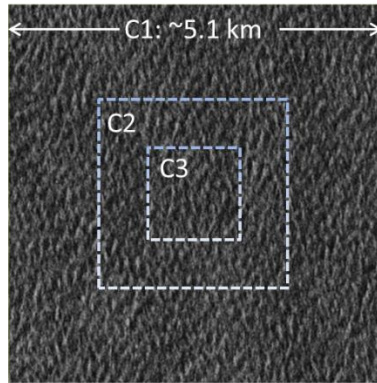
B2	~2.6 km
H_s	2.7
T_p	9.4
θ	281
U_{10}	3.7



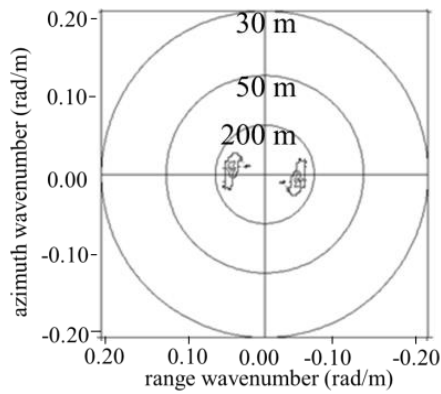
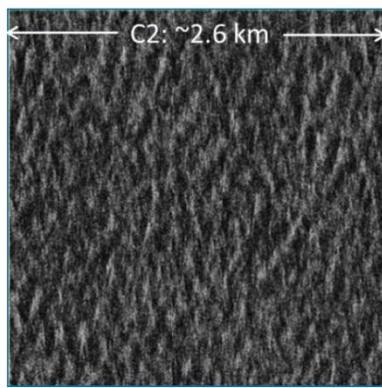
B3	~1.2 km
H_s	2.3
T_p	9.5
θ	253
U_{10}	3.7

Figure D.3: Sub-scenes from the TanDEM-X StripMap VV polarized image acquired on November 17, 2010 at 4:14 UTC over buoy 51000 near the Hawaii Island at position B and their respective derived 2D image spectrum and the meteo-marine parameters. On top the 2048 pixel sub-scene results are shown, in the centre a 1024 pixel sub-scene results are shown and on the bottom a 512 pixel sub-scene results are shown.

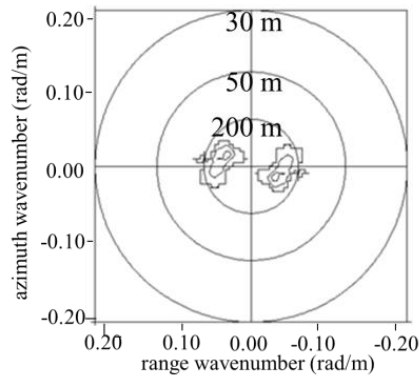
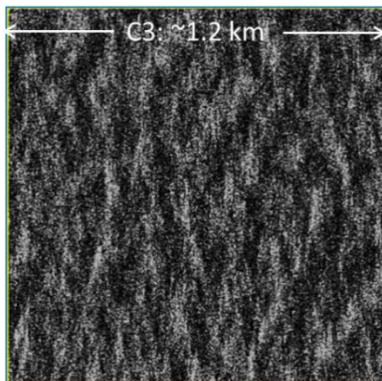
C



C1	~5.1 km
H_s	2.7 m
T_p	9.9 s
θ	265 °
U_{10}	4.0 m/s



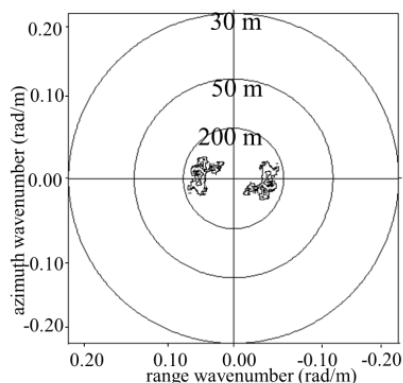
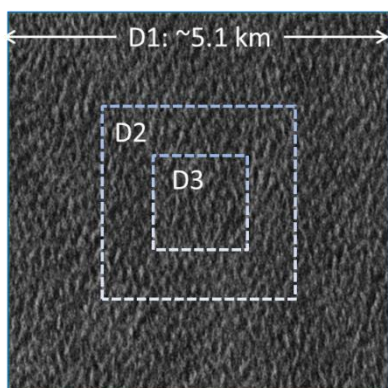
C2	~2.6 km
H_s	2.8 m
T_p	9.5 s
θ	269 °
U_{10}	4.0 m/s



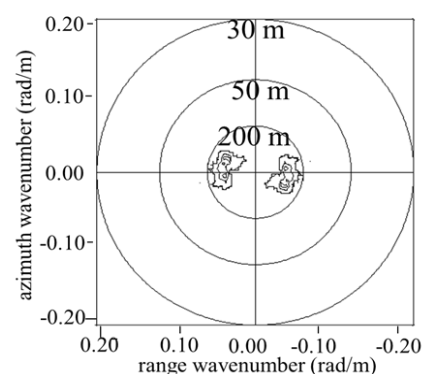
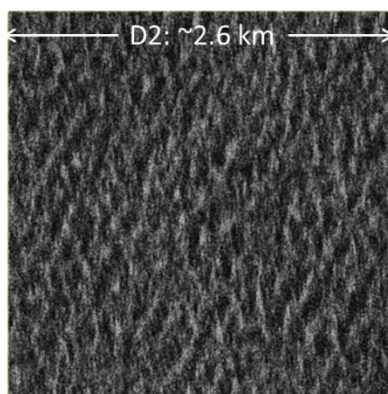
C3	~1.2 km
H_s	2.8 m
T_p	11.1 s
θ	286 °
U_{10}	4.0 m/s

Figure D.4: Sub-scenes from the TanDEM-X VV polarized StripMap data image acquired on November 17, 2010 at 4:14 UTC over buoy 51000 near the Hawaii Island at position C and their respective derived image spectrum and the meteo-marine parameters. On top the 2048 pixel sub-scene results are shown, in the centre a 1024 pixel sub-scene results are shown and on the bottom a 512 pixel sub-scene results are shown.

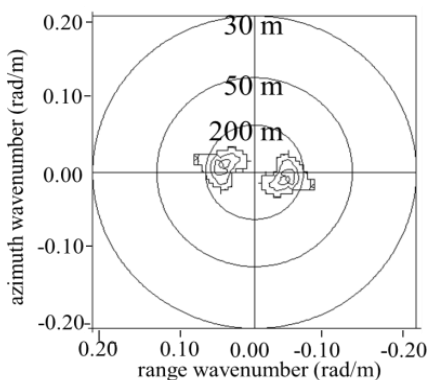
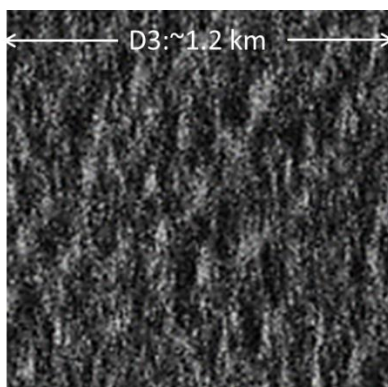
D



D1	~5.1 km
H_s	2.9 m
T_p	9.2 s
θ	270 °
U_{10}	4.1 m/s



D2	~2.6 km
H_s	2.8 m
T_p	9.3 s
θ	285 °
U_{10}	4.1 m/s



D3	~1.2km
H_s	2.9 m
T_p	9.0 s
θ	265 °
U_{10}	4.1 m/s

Figure D.5: Sub-scenes from the TanDEM-X VV polarized StripMap data image acquired on November 17, 2010 at 4:14 UTC over buoy 51000 near the Hawaii Island at position D and their respective derived image spectrum and the meteo-marine parameters. On top the 2048 pixel sub-scene results are shown, in the centre a 1024 pixel sub-scene results are shown and on the bottom a 512 pixel sub-scene results are shown.

References

- ASAR Product Handbook - ESA, <https://earth.esa.int/handbooks/asar/>.
- Abdalla, S., J.-R. Bidlot, and P. Janssen, 2006, Global validation and assimilation of ENVISAT ASAR wave mode spectra, In *Proceedings of the 2006 SEASAR Workshop, Eur. Space Agency, Frascati, Italy*.
- Alpers, W. and B. Brümmer, 1994, Atmospheric boundary layer rolls observed by synthetic aperture radar aboard the ERS-1 satellite, *J. Geophysical Res.*, 99, 12613-12621, doi: 10.1029/94JC00421
- Alpers, W. and K. Hasselmann, 1982, Spectral signal to clutter and thermal noise properties of ocean wave imaging synthetic aperture radars, *Int. J. Rem. Sens.*, 3, 423-446, doi: 10.1080/01431168208948413
- Alpers, W.R. and C. Brüning, 1986, On the relative importance of motion related Contributions to the SAR imaging Mechanism of Ocean surface waves, *IEEE Trans. On Geosci. and Rem. Sens.*, 24, 873-885; doi: 10.1109/TGRS.1986.289702.
- Alpers, W. R., D.B. Ross and C.L. Ruffenach, 1981, On the detectability of ocean surface waves by real and synthetic aperture radar, *J. Geophys. Res.*, **86**, 6481–6498, doi: 10.1029/JC086iC07p06481.
- Bamler, Richard and Schättler, Birgit, 1993, *SAR Data Acquisition and Image Formation*. In: *Geocoding: ERS-1 SAR Data and Systems*, Wichmann-Verlag Wichmann-Verlag. pp. 53-102.
- Beal, D.G. Tilley and F.M. Monaldo, 1983, Large and small-scale spatial evolution of digitally processed ocean surface wave spectra from SEASAT synthetic aperture radar, *Int. J. of Rem. Sens.*, **88**, 1761-1778, doi: 10.1029/JC088iC03p01761.
- Breit, H., T. Fritz, U. Balss, M. Lachaise, A. Niedermeier, A. and M. Vonaka, 2010, TerraSAR-X SAR Processing and Product, *IEEE Trans. On Geosci. and Rem. Sens.*, **48**, doi: 10.1109/TGRS.2009.2035497.
- Brown, R., Baker, J., McCall, J., 1996, Nondirectional and directional Wave data analysis Procedures, NDBC Technical Document 96-01, Stennis Space Center.
- Bruck, M. and S. Lehner, 2010, Extraction of wave field from TerraSAR-X data, In *Proceedings of SEASAR 2010 Workshop, Frascati, Italy*, ISBN 9789292212438.
- Bruck, M., and S. Lehner, 2014, TerraSAR-X/TanDEM-X Sea State Measurements Using the XWAVE Algorithm, *Int. J. Remote Sens.*, accepted.

- Bruck, M., and S. Lehner, 2013, Coastal wave field extraction using TerraSAR-X data, *Journal of Applied Remote Sensing*, **7**(1), 073694, doi: 10.1117/1.JRS.7.073694.
- Bruck, M. Pontes, M.T., Azevedo, E. and Lehner, S., 2011, *Study of Sea-State Variability and Wave Groupiness Using TerraSAR-X Synthetic Aperture Radar Data*. In: Proceedings of EWTEC 2011 on CD, pp. 1-7. 9th EWTEC 2011, 5 - 9 September 2011, Southampton, UK.
- Brusch, S., P. Held, Lehner, S., Rosenthal, W. and A. Pleskachevsky, Underwater Bottom-Topography in coastal areas from TerraSAR-X data, *Int. J. of Rem. Sens.*, 2010, doi: 10.1080/01431161.2010.489063.
- Brusch, S., S. Lehner, T. Fritz, M. Soccorsi, A. Soloviev, and B. van Schie, Ship Surveillance With TerraSAR-X, 2011, *IEEE Trans. On Geosci. and Rem. Sens.*, **49**, (3), pp. 1092-1103, doi: 10.1109/TGRS.2011.2117471, ISSN 0196-2892.
- Booij, N., Ris R.C. and Holthuijsen L.H., 1999, A third-generation wave model for coastal regions, *J. Geophys. Res.*, **104**, 7649-7681, doi: 10.1029/1998JC900123.
- Collard, F., Ardhuin, F., and Chapron, B., 2005, Extraction of coastal ocean wave fields from SAR images, *IEEE Journal of Oceanic Engineering*, **30**, 3, pp. 526–533, doi: 10.1109/JOE.2005.857503.
- Cumming, I., Wong F., 2004, *Digital Signal Processing of Synthetic Aperture Radar Data: Algorithms and Implementation*, Artech House , ISBN: 978-1-58053-058-3.
- Curlander, J., 1991, *Synthetic aperture radar: Systems and signal processing*, John Wiley and Sons, Inc, New York.
- Diaz Méndez, M. G., Lehner, S., Ocampo-Torres, F.J., Li, Bruschi S., Wind and wave observations off the south Pacific Coast of Mexico using TerraSAR-X imagery, 2010, *Int. J. Remote Sens.* **31**(17), 4933–4955, doi: 10.1080/01431161.2010.48521.
- Engen, G. and H. Johnson, 1995, SAR-ocean wave inversion using image cross spectra, *IEEE Trans. On Geosci. and Rem. Sens.*, **33**, 1047-1056, doi: 10.1109/36.406690.
- Günther, H., S. Hasselmann and P.A.E.M., Janssen, 1992, The WAM model cycle 4 (revised version), Technical report, Deutsches Klimarechenzentrum (DKRZ), Hamburg, Germany.
- Goda, Y., *Random Seas and Design of Marine Structures*, 1985, University of Tokyo Press, Japan.
- Hasselmann, S., K. Hasselmann, J.H. Allender and T.P. Barnett, 1985, Computations and parameterizations of the nonlinear energy transfer in a gravity wave spectrum, part 2: Parameterizations of the nonlinear energy transfer for application in wave models. *J. Phys. Oceanogr.* **15**, 1378-139.

- Hasselmann, K. and S. Hasselmann, 1991, On the nonlinear mapping of an ocean wave spectrum into a synthetic aperture radar image spectrum, *J. Geophys. Res.*, **96**, 10713–10729, doi: 10.1029/91JC00302.
- Hasselmann, S., C. Brüning, K. Hasselmann, and P. Heimbach, 1996, An improved algorithm for the retrieval of ocean wave spectra from Synthetic aperture radar image spectra, *J. Geophys. Res.*, **101**, 16615–16629, doi: 10.1029/96JC00798.
- Hasselmann K., T.P. Barnett, E. Bouws, H. Carlson, D.E. Cartwright, K. Enke, J.A. Ewing, H. Gienapp, D.E. Hasselmann, P. Kruseman, A. Meerburg, P. Miller, D.J. Olbers, K. Richter, W. Sell, and H. Walden, 1973, Measurements of wind-wave growth and swell decay during the Joint North Sea Wave Project (JONSWAP), *Deustches. Hydrogr. Z., Suppl.*, **A(8)**, 12, p.95.
- Heimbach, P., S. Hasselmann, and K. Hasselmann, 1998, Statistical analysis and inter comparison with WAM model data of three years of global ERS-1 SAR wave Mode Spectral retrievals, *J. Geophys. Res.*, **103**, 7931–7977, doi: 10.1029/97JC03203.
- Johnsen, H., G. Engen, B. Chapron, N. Walker, and Y.-L. Desnos, 2002, The ASAR Wave Mode: Level 1 and 2 Algorithms and Products, *In ENVISAT Calibration Review, 9-13 September 2002*, Eur. Space Agency, Noordwijk, Netherlands.
- Johnsen, H., G. Engen, F. Collard, V. Kerbaol, and B. Chapron, 2006, Envisat ASAR wave mode products — Quality assessment and algorithm upgrade, *In Proceedings of SEASAR 2006*, Eur. Space Agency Spec.Publ., ESA SP-613.
- Koch, W., Directional Analysis of SAR Images Aiming at Wind Direction, 2004, *IEEE Trans. On Geosci. and Rem. Sens.*, **42**, no 4,702-710, doi: 10.1109/TGRS.2003.818811.
- Kerbaol, V., B. Chapron, and P.W. Vachon, 1998, Analysis of ERS-1/2 synthetic aperture radar wave mode imaggettes, *J. Geophys. Res.*, **103**, 7833-7846, doi: 10.1029/97JC01579.
- Komen, G.J., L. Cavaleri, M. Donelan, K. Hasselmann, S. Hasselmann, and P. Janssen, 1994, *Dynamics and Modelling of Ocean Waves*, Cambridge University Press, Cambridge, UK.
- Krogstad, H., 1992, A simple derivation of Hasselmann's nonlinear ocean synthetic aperture radar transform, *J. Geophys. Res.*, **97**, 873–885, doi: 10.1029/91JC03010.
- Lehner, S., J. Schulz-Stellenfleth, J. B. Schättler, H. Breit H, and J. Horstmann, 2000, Wind and wave measurements using complex ERS-2 wavemode data, *IEEE Trans. On Geosci. and Rem. Sens.*, **38**, 2246–2257, doi: 10.1109/36.868882.
- Lehner, S., A. Pleskachevsky, and M. Bruck, 2012, High resolution satellite measurements of coastal wind field and sea state, *Int. J. Remote Sens.*, **33**, issue 23, doi: 10.1080/01431161.2012.685975.

- Li, X., Lehner, S., 2013, Algorithm for sea surface wind retrieval from TerraSAR-X and TanDEM-X data, *IEEE Trans. On Geosci. and Rem. Sens.*, **52**, 5, 2928 – 2939, doi: 10.1109/TGRS.2013.2267780.
- Li. X., S. Lehner S., and W. Rosenthal, 2010, Investigation of Ocean Surface Wave Refraction Using TerraSAR-X Data, *IEEE Trans. On Geosci. and Rem. Sens.*, **48**, 2, 830 – 840, doi, 10.1109/TGRS.2009.2033177.
- Li, X.-M., S. Lehner, and T. Bruns, 2010, Ocean wave integral parameters measurements using Envisat ASAR wave mode data, *IEEE Trans. On Geosci. and Rem. Sens.*, **49**, 1, 155 – 174, doi: 10.1109/TGRS.2010.2052364.
- Lyzenga, D. R., R. A. Shuchman, and J. D. Lyden, 1985, SAR imaging of waves in water and ice: evidence for velocity bunching, *J. Geophys. Res.*, **90**, C1, 1031–1036, doi: 10.1029/JC090iC01p01031.
- Mastenbroek, C. and C.F. de Valk, 2000, A semi-parametric algorithm to retrieve ocean wave spectra from synthetic aperture radar, *J. Geophys. Res.*, **105**, C2, 3497-3516, doi: 10.1029/1999JC900282.
- Massonnet, D., Souyris, J.C., 2008, *Imaging with Synthetic Aperture Radar*, EPFL Press, ISBN 9780849382390 - CAT# EF8239.
- Munk, W .H., 1950, Origin and generation of waves, in *Proceedings of the 1st Conf. Coastal Engineering (Long Beach)*, New York, ASCE, doi: <http://dx.doi.org/10.9753/icce.v1.1>.
- Nieto Borge, J.C., Hessner, K., Jarabo-Amores P. and de la Mata-Moya D., 2008, Signal to noise ratio analysis to estimate ocean wave heights from X-band marine radar image time series, *IET Radar Sonar Navigation*, 2, 1, pp. 35-41, doi: 10.1049/iet-rsn:20070027.
- Nieto Borge, J. C., G. R. Rodriguez, K. Hessner, and P.I. González, Inversion of Marine Radar Images for Surface Wave Analysis, 2004, *J. of Atmos. and Oceanic Technol.*, **21**, 1291-1300, doi: [http://dx.doi.org/10.1175/1520-0426\(2004\)021<1291:IOMRIF>2.0.CO;2](http://dx.doi.org/10.1175/1520-0426(2004)021<1291:IOMRIF>2.0.CO;2).
- Pierson, W. J., G. Neumann and R. W. James, 1955, *Practical Methods for Observing and Forecasting Ocean Waves by Means of Wave Spectra and Statistics*, Washington, U.S Navy Hydrographic Office, Publication No. 603 (reprinted 1960), pp. 284.
- Pierson, W.J. Jr., Moskowitz, L., 1964, A proposed spectral form for fully developed wind seas based on the similarity theory of S.A. Kitaigorodskii, *J. Geophys. Res.* **69**, 24, 5181–5190, doi: 10.1029/JZ069i024p05181.
- Ren Y. Z., S. Lehner, S. Brusch, X-M. Li, and M.-X. He, 2012, An algorithm for the retrieval sea surface wind fields using X-band TerraSAR-X data, *Int. J. Remote Sens.*, 33, 23, doi :10.1080/01431161.2012.685977.

- Schmidt, R., 1995, Bestimmung der Ozeanwellen-Radar-Modulations Übertragungs Funktion aus der Abbildung der Ozeanwellenfeldes durch Flugzeuge getragene Radar Systeme mit syndetischer Apertur, PhD Thesis, Universität Hamburg, Germany.
- Schneggenburger, C., 1998, Spectral wave modeling with non-linear dissipation. Helmholtz-Zentrum Geesthacht, Ph.D. Thesis, University of Hamburg, Germany.
- Schneggenburger, C., H. Günther and W. Rosenthal, 2000, Spectral wave modelling with non-linear dissipation: validation and applications in a coastal tidal environment, in: *Coast Eng.*, **41**, 201–235, doi:10.1016/S0378-3839(00)00033-8.
- Schulz-Stellenfleth, J., T. König, and S. Lehner, 2007, An empirical approach for the retrieval of integral ocean wave parameters from synthetic aperture radar data, *J. Geophys. Res.*, **112**, C3, doi: 10.1029/2006JC003970, 2007.
- Schulz-Stellenfleth, J., S. Lehner, S., and D. Hoja, 2005, A parametric scheme for the retrieval of two-dimensional ocean wave spectra from synthetic aperture radar look cross spectra, *J. Geophys. Res.*, **110**, C05 004.1–C05 004.17, doi: 10.1029/2004JC002822.
- Schulz-Stellenfleth, J., Lehner S, 2004 Measurement of 2-D sea surface elevation fields using complex synthetic aperture radar data, *IEEE Transactions on Geoscience and Remote Sensing*, **42**, 6, pp. 1149 – 1160, doi: 10.1109/TGRS.2004.826811.
- Snyder, R.L, F.W., Dobson, J.A. Elliot, and R.B. Long, 1981, Array measurements of atmospheric fluctuations above surface gravity waves, *J.Fluid Mech.*, **102**, 1-59, doi: <http://dx.doi.org/10.1017/S0022112081002528>.
- Steele, K.E. and T.R. Mettlach, 1993, NDBC wave data - current and planned. Ocean Wave Measurement and Analysis – In *Proceedings of the Second International Symposium. ASCE*, 198-207.
- Steele, K.E., Teng, C-C., and D. W-C. Wang, 1992, Wave direction measurements using pitch and roll buoys, *Ocean Engineering*, **19**, 4, pp. 349-375, doi:10.1016/0029-8018(92)90035-3.
- Steele, K.E., D.W. Wang, M.D. Earle, E.D. Michelena, R.J. Dagnall, 1998, Buoy pitch and roll computed using three angular rate sensor, *Coastal Engineering*, **35**, Issues 1-2, October 1998, pp. 123-139, doi:10.1016/S0378-3839(98)00025-8.
- Tolman, H. L., 2002, User manual and system documentation of WAVEWATCH-III version 2.22. NOAA / NWS / NCEP / OMB technical note, 222, 133.
- Tolman, H. L., 1989, The numerical model WAVEWATCH: a third generation model for the hindcasting of wind waves on tides in shelf seas, *Communications on Hydraulic and Geotechnical Engineering*, Delft Univ. of Techn., ISSN 0169-6548, Rep. no. 89-2, 72 pp.

- Vachon P.W., H.E. Krogstad, and J. S. Paterson, 1994, Airborne and space-borne synthetic aperture radar observations of ocean waves, *Atmosphere-Ocean*, 32:1, 83-112, doi :10.1080/07055900.1994.9649491
- Van der Westhuysen, A. J., 2007, Advances in the spectral modelling of wind waves in the near shore, Ph.D. Thesis, Fac. of Civil, Engineering, Delft University of Technology, Netherlands.
- Vesecky, J. and R. Stewart, 1982, The observation of ocean surface phenomena using imagery from the Seasat synthetic aperture radar, *J.Geophys. Res.*, 87, 3397–3430, doi: 10.1029/JC087iC05p03397.
- Ziemer, F., and H. Günther, 1994, A system to monitor ocean wave fields, *Proc. Second Int. Conference on Air–Sea Interaction and Meteorology and Oceanography of the Coastal Zone*, Amer. Meteor. Soc., 18–19., Lisbon, Portugal.
- WAMDI Group: Hasselmann, K., Hasselmann, S., Janssen, P.A.E.M., Komen, G.J., Bertotti, L., Lionello, P., P., Guillaume, A., Cardone, V.C., Greenwood, J.A., Reistad., M., Zambresky, L. and Ewing, J. A., 1988, The WAM model - a third generation ocean wave prediction model. *Journal of Physical Oceanography*, **18**, pp. 1775-1810, [http://dx.doi.org/10.1175/1520-0485\(1988\)018<1775:TWMTGO>2.0.CO;2](http://dx.doi.org/10.1175/1520-0485(1988)018<1775:TWMTGO>2.0.CO;2).

List of Symbols

a	<i>Amplitude of linear ocean wave</i>
A	<i>Area</i>
α_r	<i>Azimuth resolution</i>
R_r	<i>Range resolution</i>
G_r	<i>Ground range resolution</i>
H	<i>Height of linear ocean wave</i>
h	<i>Water depth</i>
θ_i	<i>Incidence angle</i>
θ_p	<i>Wave peak direction</i>
θ	<i>Direction</i>
H_s	<i>Significant wave height</i>
λ_p	<i>Peak wavelength</i>
T_p	<i>Peak period</i>
U	<i>Wind speed</i>
U_{dir}	<i>Wind speed direction</i>
U_{10}	<i>Sea surface wind speed at 10 m height</i>
π	<i>Pi</i>
σ	<i>Radar cross section</i>
σ_0	<i>Sigma naught (normalized radar cross section)</i>
λ	<i>Wavelength</i>
T	<i>Period</i>
f	<i>Frequency</i>
c_{light}	<i>Speed of light</i>
c_g	<i>Group velocity</i>
ω	<i>Angular frequency</i>
k	<i>Wavenumber</i>
k_x	<i>Azimuth wavenumber</i>
k_y	<i>Range wavenumber</i>
L	<i>Length of the antenna</i>
c	<i>Phase speed</i>
g	<i>Gravity</i>

R	<i>Slant range</i>
V	<i>Platform (satellite) velocity</i>
η	<i>Sea surface elevation</i>
$S(f)$	<i>One dimensional wave frequency spectrum</i>
$S(f, \theta)$	<i>Two dimensional wave frequency spectrum</i>
α	<i>Wave peak direction in relation to satellite path (azimuth)</i>
P	<i>Power spectrum</i>
E	<i>Integrated energy from SAR spectrum</i>
X_{SAR}	<i>TS-X/TD-X measurement</i>
R	<i>Correlation</i>
S_I	<i>Scatter index</i>

List of acronyms

ASAR - Advanced Synthetic aperture Radar on-board ENVISAT

DWD - Deutsches Wetter Dienst - German Weather Center

DLR - Deutsches Zentrum für Luft und Raumfahrt – German Aerospace Center

ENVISAT - Environmental satellite launched by ESA

ESA - European Space agency

ECMWF - European Center for Medium-Range weather forecast

ERS - European Remote sensing satellite

FFT - Fast Fourier Transform

NRCS - Normalized Radar Cross Section

RAR - Real Aperture Radar

RMS - Root Mean Square

SAR - Synthetic Aperture radar

TS-X – TerraSAR-X satellite

TD-X -TanDEM-X satellite

UTC - Universal time Coordinates

WAM - Third generation Numerical wave model